Relation between microstructure and properties in magnetic shape memory alloys studied by neutron diffraction

Natalia A. Río López

2024

Supervisors:

Jose María Porro

Fernando Plazaola

Este trabajo de investigación para optar al Grado de Doctora por la Universidad del País Vasco (UPV/EHU) se ha realizado en colaboración entre el Basque Center for Materials, Applications and Nanostructures (BCMaterials) y el Departamento de Electricidad y Electrónica de la Facultad de Ciencia y Tecnología.

Adicionalmente, ha sido posible gracias a la financiación obtenida desde diferentes fuentes. A nivel regional, el Departamento de Educación del Gobierno Vasco, mediante la concesión de la beca predoctoral (PREB_2020_1_0002) en la categoría específica de neutrónica y aceleración de partículas y el Departamento de Educación y de Industria, financiando actividades experimentales a través de los programas IKUR, ELKARTEK y PIBA. A nivel nacional, el ministerio de Ciencia, Innovación y Universidades, mediante los Proyectos de Generación del Conocimiento y Retos

ZTF-FCT
Zientzia eta Teknologia Fakultatea
Facultad de Ciencia y Tecnología

Agradecimientos

Todo aquel que hace una tesis lo describe como una montaña rusa, con subidas y bajadas. Cuando tienes con quien compartirlas, la experiencia es infinitamente mejor. Por eso, quiero agradecer a aquellos que han formado parte de esta experiencia.

En primer lugar, evidentemente, a mis directores, que tanta dedicación han puesto en esta tesis. A Txema, por la oportunidad de empezar esta investigación, por todo el tiempo invertido en formarme y enseñarme tanto, y, sobre todo, por confiar en mí y mi tesis más de lo que yo misma lo hacía. A Fernando, por la ayuda prestada siempre que he necesitado, y la motivación tras cada reunión. A Patricia, que, sin ser directora (al menos sobre el papel), ha jugado un papel indispensable. Sin todos tus conocimientos de cristalografía y magnetismo, y tu gran disposición a transmitírmelos, esta tesis no hubiera sido posible.

Tampoco hubiera sido posible sin mis profesores del instituto y la universidad, que me motivaron a seguir estudiando ciencia. Gracias a vosotros también. Y a Ismael, el primer científico que conocí, y la primera persona que me hizo plantearme la posibilidad de ser doctora.

I would also like to thank Ross Colman and his group at Universita Karlova, in Prague, for their invaluable ability growing single crystals, willingness to share knowledge, and fruitful scientific discussions. The knowledge I acquired there really made a difference in this PhD. Thanks also to the Group of Magnetic Shape Memory materials at the Institute of Physics of the Czech Academy of Sciences, for the opportunity to spend a research stay there and for all the learning I took home.

And, of course, to the Magnetic Materials Lab at Boise State University: Peter, Aaron, Ammon, John and Nicolas. Thank you for welcoming to your lab so warmly and for sharing with me your vast knowledge regarding single crystals and mechanical properties. Your ideas and suggestions have been really valuable for me and my work.

No puedo no mencionar a los “local contact” y trabajadores del ILL, a los que tan agradecida estoy por su contribución en la (amplia) parte de neutrónica de esta

tesis. Sobre todo, a Alberto, por la inestimable ayuda en los experimentos y la paciencia y disposición con mis muchas dudas sobre el posterior análisis.

Gracias también a todas las personas del BCM y la UPV/EHU que me han prestado su apoyo técnico cuando no era capaz de hacer funcionar correctamente algún equipo, o cuando necesitaba cortar metales con la cizalla. Y a los colaboradores que me han proporcionado muestras con las que trabajar, o datos que analizar.

Y especialmente, gracias a todos esos compañeros de trabajo, ahora amigos, que han hecho de estos más de cuatro años una etapa inolvidable. A Leire, mi compañera de desayunos, faltadas, charlas filosóficas, alegrías y crisis existenciales. Empezamos juntas, y no hubiera terminado de no ser por ti. A Ainara, referente en cómo hacer una tesis (y todo el papeleo que conlleva) y amistad indispensable para charlas, desahogos, cervezas y risas. A mis hermanos científicos, Aritz, Dani, Mikel, por todos los buenos (y malos) ratos que compartimos, la ayuda mutua, y, sobre todo, por vuestra habilidad de hacerme ver la vida desde la perspectiva correcta. A Elena y Elvira, por toda la alegría que habéis aportado a la sala en mis largos días de escritura. A Pello, Paula, Vera, Vanessa, Josu, Ane, Marcos, Corina, Bruno….

Sin olvidar a esos amigos de fuera del trabajo, mi cuadrilla de Gernika, que, con los muchos chistes, fiestas, bromas, y risas en general, me han hecho desconectar cuando más lo necesitaba. Y, especialmente, a Bisko, por ser una constante inyección de felicidad.

Por supuesto, gracias a mi familia, mis padres, Luis María y Maricarmen y hermano, Álvaro, que no dejan de apoyarme incondicionalmente ni a 500km de distancia. Aunque estéis lejos, seguís muy cerca.

Y, por último, pero no menos importante, gracias a Joseba, por estar siempre ahí y sacar lo mejor de mí. Dos masters, (casi) dos tesis y una vida a la par.

ESKERRRIK ASKO DANORI!

Contents

RESUMEN i
LABURPENA vii
ABSTRACT ix
LIST OF PUBLICATIONS xi
Part of the thesis xi
Other publications xii
CHAPTER 1 1
1.1. ACTIVE MATERIALS 1
1.2. SHAPE MEMORY ALLOYS: MARTENSITIC TRANFORMATION, MT 2
1.2.1. Martensitic Transformation, MT 2
1.2.2. Shape Memory Effect, SME. 3
1.3. MAGNETIC SHAPE MEMORY ALLOYS AND EXPLOITATION OF THE PROPERTIES OF THE MT. 5
1.3.1. Magnetic Field induced Strain, MFIS 6
1.4. CANONICAL MSMA SYSTEMS 9
1.4.1. Ni-Mn-Ga systems. Physical properties. 9
1.5. OBJECTIVES AND STRUCTURE OF THE THESIS 12
1.6. BIBLIOGRAPHY 13
CHAPTER 2 21
2.1. ALLOY SYNTHESIS TECHNIQUES 21
2.1.1. Polycrystalline alloys 21
2.1.2. Single crystal alloys 24
2.2. STRUCTURAL AND COMPOSITIONAL CHARACTERIZATION OF MSMAs 26
2.2.1. Energy Dispersive X-Ray Spectroscopy (EDX) 26
2.2.2. X-Ray Fluorescence spectroscopy (XRF) 26
2.2.3. Laue diffraction 27
2.2.4. Differential Scanning Calorimetry (DSC) 29
2.3. MAGNETIC CHARACTERIZATION OF MSMAs 30
2.3.1. Vibrating Sample Magnetometer (VSM) 30
2.3.2. Superconductive Quantum Interference Device (SQUID) 31
2.4. MECHANICAL PROPERTIES CHARACTERIZATION 33
2.4.1 Micromechanical testing device 33
2.4.2. Micropeening station 33
2.5. BIBLIOGRAPHY 34

CHAPTER 3 37
3.1 INTRODUCTION TO NEUTRON SCATTERING 37
3.2 NEUTRON DIFFRACTION EXPERIMENTS 44
3.2.1. Introduction to Neutron Diffraction 44
3.2.2. Powder Neutron Diffraction, PND 46
3.2.3 Single Crystal Neutron Diffraction, SCND 49
3.4. NEUTRON DIFFRACTION DATA ANALYSIS 51
3.4.1. Nuclear structure analysis 51
3.4.2. Magnetic structure analysis 53
3.5. BIBLIOGRAPHY 54
CHAPTER 4 59
4.1. INTRODUCTION 59
4.2. EXPERIMENTAL PART 60
4.2.1 Fabrication of Ni-Mn-Sn-Co powders 60
4.2.2. Heat treatments 61
4.2.3. Characterization Techniques 61
4.3. STRUCTURAL BEHAVIOUR 62
4.3.1. Composition and transformation characteristics 62
4.3.2. Powder neutron diffraction 64
4.4. MAGNETOCALORIC EFFECT 74
4.5 SUMMARY AND CONCLUSIONS 75
4.6. BIBLIOGRAPHY 77
CHAPTER 5 83
5.1. INTRODUCTION 83
5.2. EXPERIMENTAL PART 84
5.2.1. Fabrication of Ni-Mn-Ga-Cu alloys 84
5.2.2. Characterisation techniques 85
5.3. STRUCTURAL BEHAVIOUR 85
5.3.1. Composition and transformation characteristics 85
5.3.2. Powder neutron diffraction 87
5.4. MAGNETIC INTERACTIONS AND STRUCTURE 94
5.5. SUMMARY AND CONCLUSIONS 99
5.6. BIBLIOGRAPHY 100
CHAPTER 6 105
6.1. INTRODUCTION 105
6.2. EXPERIMENTAL PART 106

6.2.1. Fabrication of Ni-Mn-Ga-Co-In-Fe alloys 106
6.3. STRUCTURAL BEHAVIOUR 107
6.3.1. Composition and transformation characteristics 107
6.3.2. Powder neutron diffraction 109
6.4. RELATION BETWEEN MAGNETIC INTERACTIONS AND STRUCTURE 113
6.5. SUMMARY AND CONCLUSIONS 120
6.5. BIBLIOGRAPHY 121
CHAPTER 7 127
7.1. INTRODUCTION 127
7.2. EXPERIMENTAL PART 128
7.2.1. Fabrication of Ni-Mn-Ga-Co-(In,Fe) master alloys 128
7.2.2. Growth of Ni-Mn-Ga-Co-(In,Fe) single crystals 129
7.2.3 Structural and magnetic characterization techniques 129
7.2.4 Surface patterning and single crystal mechanical testing 130
7.3. STRUCTURAL BEHAVIOUR 131
7.3.1. Composition and transformation characteristics 131
7.3.2. Single crystal neutron diffraction 134
7.4. EFFECT OF TRAINING ON THE MARTENSITIC ELASTICITY 140
7.5. EFFECT OF PATTERNING ON THE ELASTICITY OF THE MARTENSITE 144
7.6. SUMMARY AND CONCLUSIONS 147
7.6. BIBLIOGRAPHY 148
CHAPTER 8 153
8.1. CONCLUSIONS 153
8.2. FUTURE WORK 155
Appendix – Supporting Images 159
A.1. CHAPTER 4 SUPPORTING IMAGES 159
A.2. CHAPTER 5 SUPPORTING IMAGES 163
A.3. CHAPTER 6 SUPPORTING IMAGES 166
A.4. CHAPTER 7 SUPPORTING IMAGES 172

RESUMEN

Desde tiempos prehistóricos, el descubrimiento y posterior entendimiento y empleo de los materiales ha marcado el paso entre diferentes eras. Sin embargo, la revolución industrial supuso un cambio de tendencia, debido al surgimiento de materiales específicamente diseñados para mostrar unas propiedades concretas, dependientes de la aplicación buscada. Es decir, actualmente los materiales son diseñados y fabricados para cubrir las necesidades concretas de una aplicación, lo que contrasta significativamente con el previo descubrimiento y posterior implementación, característico de la metodología anterior.

El creciente y exhaustivo estudio de estos nuevos materiales ha propiciado un desarrollo exponencial de los denominados materiales activos o inteligentes. Definidos como aquellos materiales con la capacidad de modificar sus propiedades físicas en respuesta a la aplicación de un estímulo externo, se clasifican en dos grupos, en función de la naturaleza de la respuesta (señal, deformación mecánica). Dentro del conjunto de materiales exhibiendo una deformación mecánica como respuesta se encuentran las aleaciones con memoria de forma (SMAs, por sus siglas en inglés).

Las aleaciones con memoria de forma son aquellas que reaccionan al previamente mencionado estímulo externo (temperatura, tensión, campo magnético) recuperando su forma original, perdida tras una deformación pesudo-plástica. Esta propiedad deriva de la denominada transformación martensítica (MT, por sus siglas en inglés), una transición entre dos fases sólidas: una de alta temperatura y simetría (austenita) y otra de baja temperatura y menor simetría (martensita). Puesto que se trata de una transición de primer orden, sin difusión atómica, los átomos se desplazan una distancia menor que la distancia interatómica, reteniendo así sus posiciones relativas. Por consiguiente, ambas fases poseen la misma composición, aunque exhiben una estructura distinta. La temperatura a la que se produce esta transición estructural se conoce como temperatura de transición martensítica (T_M) en el caso del proceso directo, y temperatura de transición austenítica (T_A), para el proceso inverso.

El proceso de recuperación de forma, llamado efecto de memoria de forma (SME, por sus siglas en inglés) se resume de la siguiente manera: la temperatura desciende por debajo de T_M, dando lugar a una martensita maclada, con variantes cristalográficas idénticas orientadas de forma aleatoria. Al aplicar un estrés de magnitud suficiente, las variantes se orientan, dando lugar a una deformación macroscópica, de modo que el material adquiere la llamada forma temporal. Al incrementar la temperatura por encima de T_A, la transición austenítica (de martensita a austenita) genera una nueva deformación macroscópica por la que el material recupera la forma original.

La orientación de las maclas en la martensita no se conserva al repetir el proceso de transformación martensítica, mientras que la austenita presenta la misma estructura en cada ciclo, razón por la que se conoce como memoria de forma unidireccional o *one-way*, por su nombre en inglés. Para retener la estructura martensítica y originar en el material la denominada memoria de forma bidireccional o *two-ways*, base de la mayoría de aplicaciones, la aleación debe entrenarse. Tradicionalmente, esto implica varios ciclos de inducción de la MT con una carga aplicada, proceso que genera defectos cristalográficos que actúan como puntos de nucleación, favoreciendo una orientación determinada de las variantes martensíticas.

Determinadas aleaciones con memoria de forma, las conocidas como aleaciones con memoria de forma magnética (MSMAs, por sus siglas en inglés) combinan esta capacidad de recuperación de forma con propiedades magnéticas. Por tanto, además de la ya mencionada transición estructura, presentan una transición magnética de segundo orden de una fase no magnética o magnética débil a otra fase ferromagnética (o viceversa). La temperatura a la que ocurre se denomina temperatura de Curie (T_C). Dependiendo de si la transformación estructural involucra un cambio en el comportamiento magnético o no, las MSMAs se dividen en dos grupos, las aleaciones con memoria de forma metamagnética (MMSMAs) y las aleaciones con memoria de forma ferromagnética (FSMAs), respectivamente.

Las FSMAs se caracterizan por tener un momento magnético distinto de cero en la martensita. En ausencia de un campo magnético externo, las variantes presentan una orientación aleatoria, con la anisotropia magnetocristalina característica

describiendo un eje fácil a lo largo de la variante. Los dominios magnéticos presentes en las variantes se alinean con el campo magnético externo cuando éste es aplicado, provocando su rotación y, como resultado, una deformación macroscópica. Este es el efecto conocido como deformación inducida por campo magnético (MFIS, por sus siglas en inglés). Las FSMAs, cuyo principal representante son las aleaciones Ni-Mn-Ga, son especialmente interesantes para su uso como sensores o actuadores.

La propiedad más característica de las MMSMAs es el efecto magnetocalórico, derivado de la transformación martensítica inducida por campo magnético. El cambio de entropía asociado a este proceso crea un aumento o disminución de la temperatura del material, en función de si el cambio entrópico es negativo o positivo, respectivamente. Dentro del amplio rango de MMSMAs que se están estudiando, principalmente por su interés como refrigeradores en estado sólido, destacan los sistemas Ni-Mn-Sn o Ni-Mn-Ga dopados con Cu, Co o In.

Puesto que las aplicaciones de las MSMAs dependen de una deformación inducida como respuesta a la aplicación de un campo magnético externo, ya sea por inducción de la MT o por reorientación de variantes, las temperaturas de transición estructural y magnética son claves para determinar el rango de actuación de estos materiales en potenciales aplicaciones. Un gran número de estudios previos han correlacionado las microestructuras austenítica y martensítica con la evolución de ambas temperaturas. Siguiendo esa línea de investigación, esta tesis se centra en el efecto que la variabilidad de un factor (composición, tratamiento térmico) tiene en la estructura de varias series de aleaciones con memoria de forma metamagnética. Mediante el empleo de diversas técnicas de difracción de neutrones, se resuelve la estructura atómica de dichas aleaciones, permitiendo correlacionarla tanto con las propiedades magnéticas como con la evolución de las temperaturas de transición característica.

Como punto de partida de esta tesis, se establece el impacto de distintos tratamientos térmicos en la estructura y la transición estructural de una serie de aleaciones Ni-Mn-Sn-Co. Para ello, se seleccionan tres muestras de idéntica composición y se les somete a procesos distintos: sin tratar, tratamiento térmico completo y tratamiento térmico intermedio. Este último consiste en calentar la

muestra a 1173K durante una hora, para su posterior templado con agua a 273K, mientras que para el tratamiento térmico completo se realiza un calentamiento adicional a 723K seguido de templado. Durante el análisis de la muestra no tratada, se observa la presencia de austenita retenida en el rango de temperatura de la martensita, lo que se atribute a la obstaculización de la transición martensítica por parte de las tensiones inducidas en el material durante la fabricación. La ausencia de austenita en este rango térmico en las muestras tratadas evidencia la relajación de estas tensiones, permitiendo conectarlo con una transición estructural más barata, energéticamente hablando y resultando en una menor T_M.

Adicionalmente, dos muestras de composición ligeramente distinta son sometidas al tratamiento térmico completo. La comparación de la ocupación de sus sitios atómicos permite correlacionar dicha ocupación con el tipo de interacciones magnéticas interatómicas, que a su vez se asocian con la evolución de la T_C. Para terminar este estudio, la actuación magnetocalórica de las aleaciones es evaluada mediante el cálculo de su cambio de entropía, demostrando así una mejora en las propiedades magnetocalóricas de las aleaciones tras los tratamientos térmicos.

La siguiente parte, dividida en dos capítulos, aborda la interdependencia entre composición, estructura y propiedades magnéticas. En el primero de ellos se analiza el efecto de la sustitución de Mn por Cu en una aleación Ni-Mn-Ga-Cu. Tras la resolución estructural de todas las muestras de la serie, mediante el empleo de difracción de neutrones en polvo, la mayor distorsión de la martensita generada por un mayor contenido de cobre se asocia una mayor necesidad energética para inducir la transición estructural, explicando así la creciente T_M. Partiendo de la estructura resuelta, se calcula el momento magnético teórico total empleando varios posibles modelos de interacciones magnéticas entre los átomos, dependiendo de su distancia interatómica. La comparación de estos momentos teóricos con los medidos experimentalmente permite deducir el tipo de acoplamiento magnético en la celda unidad y, por tanto, la evolución de la T_C.

En el segundo de los capítulos dedicados a la variabilidad composicional, una aleación Ni-Mn-Ga-Co-In-Fe es dopada con distintos porcentajes de Fe, sustituyendo al Mn. De forma análoga al estudio del efecto del dopaje con cobre, la estructura de

todas las muestras de la serie se estudia empleando difracción de neutrones en polvo, permitiendo conectar una mayor distorsión estructural de la martensita con un mayor valor de T_M. Basándose en dependencia entre el tipo de acoplamiento magnético y la distancia interatómica establecida en el capítulo anterior, se deduce el porcentaje de interacciones ferromagnéticas y antiferromagnéticas en cada una de las muestras, con el objetivo de explicar la evolución de la T_C observada en la serie De esta forma, se demuestra la correlación entre la composición, la estructura y las propiedades magnéticas tanto en este sistema como en el anterior Ni-Mn-Ga-Cu.

Aunque la mayor parte de los estudios presentados en esta tesis han sido realizados empleando muestras policristalinas por razones de simplicidad y accesibilidad en lo que se refiere al crecimiento de las muestras, la presencia de límites de grano es un elemento limitante en sus potenciales aplicaciones. Para ello, se emplean aleaciones monocristalinas, en las que se centra la última parte de este trabajo. Dos aleaciones monocristalinas, Ni-Mn-Ga-Co-In y Ni-Mn-Ga-Co-Fe, seleccionadas en base al estudio del efecto de Fe como dopante, son estudiadas mediante difracción de neutrones en monocristales. El empleo de haces de neutrones tanto polarizados como sin polarizar permite la determinación de la distribución de momento magnético en cada una de las posiciones atómicas. Siguiendo un enfoque similar al de las secciones previas, se determina el mecanismo detrás de la dependencia entre el tipo de acoplamiento magnético y las propiedades magnéticas, así como con la temperatura de transición magnética.

Como se ha mencionado previamente, la mayoría de las aplicaciones potenciales requieren de la memoria de forma *two-ways*, una propiedad introducida en la aleación mediante entrenamiento. Con el objetivo de determinar las condiciones de entrenamiento idóneas para la obtención de una martensita maclada, se estudia la movilidad de las variantes martensíticas obtenida mediante el enfriamiento de la muestra desde la austenita con distintas cargas aplicadas en su superficie. Este movimiento es estudiado antes y después del patronado de la superficie de la aleación con *micropeening*, a modo de técnica de generación de defectos que actúen como puntos de nucleación de movimiento de variantes.

A modo de conclusión final de esta tesis, se ha observado una evidente dependencia entre la microestructura y las interacciones magnéticas interatómicas en múltiples aleaciones con memoria de forma magnética. Esto contribuye a un mejor entendimiento de los mecanismos en los que radica la explicación de la correlación entre la estructura y las propiedades magnéticas, así como de la evolución de las temperaturas de transición determinantes del rango de actuación del material.

LABURPENA

Historiaurreko garaietatik, materialen aurkikundea, beraien propietateak ulertzeak eta horren ondoriozko erabilerak aro batetik besterako aldaketa ekarri du. Hala ere, azken hamarkadetan aldaketa handia gertatzen ari da: propietate jakin batzuk lortzeko fabrikatutako materialen garapena. Hau da, desiratutako aplikaziorako materialak sortzea, aurreko planteamenduaren kontran, non lehengo materialak aurkitzen ziren eta hurrengo(ondoren), erabilerak.

Garapen arlo handi honetan, Forma Magnetiko Memoriadun Aleazioek (MSMAs, bere ingelesezko siglen arabera) interesa sortu dute, eremu magnetikoek eragindako kontaktu gabeko deformazio makroskopikoagatik. Prozesu hau gertatzen den tenperatura kontrolatzea garrantzitsua da erabilera potentzialetarako (adibidez, sentsoreak, eragingailuak eta solido-egoerako hozkailuak). Tenperatura hau, egitura trantsizio eta trantsizio magnetikoen tenperaturak definitzen dute. Trantsizio tenperatura hauek aleazioaren martensita eta austenita mikroegituren menpe daudenez gero,ondoriozta daiteke egitura garrantzitsua dela erabilera potentzialetarako.

Tesi honetan aurkeztutako lana hurrengoan oinarritzen da,zenbait faktorek , bereziki tratamendu termikoek eta konposizio aldaketek, hautatutako MSMAen austenita eta martensita egituran duten eragina aztertzea. Neutroi difrakzio teknikak baliatuz, beraien atomo-egitura ebazten da, egitura hauen eta propietate magnetikoen arteko korrelazioa ezartzen ahalbidetzen du, beraien trantsizio-tenperatura (T_C eta T_M) aldaketez gain.

Tesi honen abiapuntua Co dopatutako Ni-Mn-Ga aleazioen tratamendu termiko jakin batzuen arteko alderaketa da. Helburu horrekin, konposizio berdina eta tratamendu termiko ezberdina duten hiru aleazio hautatu ziren: tratatugabea, bitarteko tratamenduarekin (HT1) eta tratamendu osoarekin (HT2). Fabrikazioan induzitutako tentsioak tratamendu termiko biekin erlaxazioa egiazten da, eta egitura-trantsizio erraztuarekin lotzen da. Beraz, T_M-ren eboluzioa azaltzen da. Gainera, tratamendu termiko berdindun eta konposizio desberdindun aleazio bi alderatzen dira atomo-egitura eta elkarrekintza magnetiko motak erlazionatzeko. T_C-ren aldaketa erlazio

honekin elkartzen da. Azterketa honetan amaitzeko, aleazioen errendimendu magnetokalorikoa bere entropiaren aldaketa kalkulatzen ebaluatzen da, tratamendu termikoen hobekuntza frogatuz.

Hurrengo partean konposizio, egitura eta propietate magnetikoen mendekotasuna ebaluatzen da. Mn-, Cu- edo Fe-ren ordezkapenak Ni-Mn-Ga edo Ni-Mn-Ga-Co-In sistemetan, hurrenez hurren, duen efektua austenita-egituran eta martensita-egituran agertzen da. T_M handiagoa martensita-egitura distortsionatuagoarekin eta MT energia handiagoarekin lotzen da. Aleazio bakoitzaren atomo-egitura ebatziz, atomoen arteko elkarrekintza magnetiko motak ondorioztatzen dira. Hau portaera magnetikoaren oinarria da, Curie tenperatura barne. Hortaz, T_C -ren eboluzioa eta aleazioen propietate magnetikoen aldaketa egitura eta konpontzio aldaketarekin batzen da, Cu edo Fe-dopaketarengatik.

Tesi honen azken atala monokristalen esplorazioan datza, erabilera gehigarriak lortzeko bide bezala. Aurreko lanekin koherentzia mantenduz, Ni-Mn-Ga-Co-In eta Ni-Mn-Ga-Co-In-Fe kristal bana hautatzen da lan honetan. Neutroi polarizatuen difrakzioko emaitzek austenita-egituren momentu magnetikoaren banaketa ematen du. Tesiko aurreko kapituluen antzera, egitura magnetiko hauetan T_C-rekin eta propietate magnetikoen arteko zerikusia ezarri da. Desiratutako aplikazioetarako maklen mugimenduaren garrantzia ikusita, martensita maklatuaren lorbidean askotariko prestakuntza baldintzak probatu dira. Gainazaleko *patterning*-a jasan aurreko eta osteko higidura hau ikertzen da.

Ikuspegi orokor bezala, tesi honetan hainbat MSMAen mikroegituraren eta atomoen arteko elkarrekintza magnetikoen arteko korrelazioa ezartzen da. Erlazio honek propietate magnetikoak eta trantsizio tenperaturen eboluzioa hobeto ulertzea eta lan-tartea zehaztea ahalbidetzen du.

ABSTRACT

Since prehistoric times, the discovering, understanding of the properties and subsequent increased use of different materials have marked the pass between ages. Over the past few decades, however, a notable shift has taken place: the development of materials specifically engineered to exhibit desired properties. In other words, materials are now tailored to meet specific application needs, contrasting with the former approach of discovery followed by implementation.

Within this vast field of development, an interest on Magnetic Shape Memory Alloys (MSMAs) has surged, due to the contactless, magnetic field-induced macroscopical deformation they undergo. For the potential, real-world implementations, such as sensors, actuators or solid-state refrigerators, controlling the temperature at which this process occur is particularly compelling. Being this temperature dependant on the structural and magnetic transition temperatures, that, in turn, are heavily influenced by the austenitic and martensitic structures, one can deduce the crucial role the structure plays on the potential applications of these materials.

This thesis focuses on analysing the impact of various factors, specifically post-annealing heat treatments and compositional modifications, have on the structure and magnetism of selected Ni-Mn-based MSMAs. By different neutron scattering techniques, their atomic ordering is solved, enabling the establishment of a correlation between the structure and the magnetic properties, in addition to the variation of the characteristic transition temperatures (T_C and T_M).

The starting point of this dissertation is the comparation of different post annealing heat treatments on Co-doped Ni-Mn-Sn alloys. With this aim, three same-composition different-heat treated samples are selected: non-treated, with intermediate heat treatment (HT1) and with complete heat treatment (HT2). The relaxation of the stresses induced during the fabrication process upon both treatments is evidenced and connected with a facilitated structural transition. Hence, the evolution of the T_M is explained. Additionally, two same-heat treatment different-

composition samples are compared as a way to correlate the atomic site occupancies and the type of magnetic exchange interactions. The variation of T_C is associated with this correlation. To conclude this study, the magnetocaloric performance of the alloys is evaluated by the calculation of their entropy change, demonstrating an improvement of the magnetocaloric response upon the post annealing treatments.

The following part is directed to the evaluation of the interdependence between composition, structure and magnetic properties. The effect Mn substitution by Cu or Fe has in the austenitic and martensitic structure of a Ni-Mn-Ga or Ni-Mn-Ga-Co-In system, respectively, is manifested. An increased T_M is accordingly associated with a more distorted martensite and a consequent more energy-demanding martensitic transformation. By solving the atomic structure of each alloy, the relevant type of magnetic coupling between atoms is inferred. The latter is found to be the basis of the magnetic behaviour of the alloys, including the evolution of their T_C. Thus, the evolution of T_C and T_M and the change in the magnetic properties are correlated with the compositional and structural change as a function of Cu or Fe doping.

The last part of this dissertation is dedicated to the exploration of single crystal MSMAs, as a path towards further applicability of these alloys. For the sake of consistency with prior studies, a Ni-Mn-Ga-Co-In and a Ni-Mn-Ga-Co-Fe crystals are selected for this study. The results from polarized neutron diffraction studies led to the determination of the magnetic moment distribution in the different unique sites of the austenite structures. In a similar manner to the previous part of the thesis, the dependence of these magnetic structures with the T_C and the magnetic properties is established. The impact of various training conditions on the obtention of a twinned martensite is tested, given the significance of the twin variants movement in the desired applications. This movement is examined prior and following to undergoing specific surface patterning processes.

As a general overview, this thesis establishes a correlation between the microstructure and the interatomic magnetic exchange interactions of multiple MSMAs, contributing to a further understanding of the mechanisms behind both the magnetic properties and the evolution of the transition temperatures determining the actuation range.

LIST OF PUBLICATIONS

Part of the thesis

- B. Rodríguez-Crespo*, N.A. Río-López*, P. Lázpita, S. Ceballos, M. Ríos, D. Domenech, J.A. Rodríguez-Velamazan, J. López-García, V. Chernenko, J.M. Porro, D. Salazar. Impact of magnetic, atomic and microstructural ordering on the magnetocaloric performance of powdered NiCoMnSn metamagnetic shape memory ribbons. *Materials and Design*. 2024, 245, 113279. Doi: 10.1016/j.matdes.2024.113279

- N.A. Río-López, P. Lázpita, D. Doménech, J.A. Rodriguez-Velamazan, V.A. Chernenko, F. Plazaola, C. Seguí, J.M. Porro. Tuning magnetic interactions between elements in Cu-doped Ni-Mn-Ga alloys: a neutron diffraction study. Journal of alloys and compound – *Manuscript under journal review*

- N.A. Río-López, P. Lázpita, J.A. Rodriguez-Velamazan, V.A. Chernenko, F. Plazaola, J.M. Porro. Antiferromagnetic to ferromagnetic coupling crossover upon Fe-doping in NiMnGaCoIn alloys – *Manuscript under preparation*

- N.A. Río-López, R. Colman, A. Smith, P. Lázpita, J.A. Rodriguez-Velamazan, V.A. Chernenko, O. Heczko, F. Plazaola, P. Müllner, J.M. Porro. Correlation between magnetic struct7ure and mechanical properties in Fe- and In-doped NiMnGaCo single crystals – *Manuscript under preparation*

- N. A. Río-López, P. Lázpita, D. Salazar, V. I: Petrenko, F. Plazaola, V. Chernenko, J. M. Porro. Neutron scattering as a powerful tool to investigate magnetic shape memory alloys: A review. *Metals*. 2021, 11, 1–21. Doi:10.3390/met11050829.

Other publications

- J. M. Porro, A. Villar, C. Redondo, N. A. Río-López, A. Lasheras, D. Salazar, R. Morales, E. Fernández-Martín. Competition of Magnetic Anisotropies in Permalloy Antidot Lattices. *Magnetochemistry*. 2022; 8(5):55. Doi: 10.3390/magnetochemistry8050055

- A. Valverde, N. A. Río-López, G. I. Tovar, D. Torres, M. Rosales, S. Wuttke, A. Fidalgo-Marijuan, J. M. Porro, M. Jiménez-Ruiz, V. García-Sakai, A. García, J. M. Laza, J. L. Vilas-Vilela, L. Lezama, M. I. Arriortua, G. J. Copello, R. Fernández de Luis. Designing Metal-Chelator-like Traps by Encoding Amino Acids in Zirconium-Based Metal–Organic Frameworks. *Chemistry of Materials*. 2022, 34(21), 9666-9684. Doi: 10.1021/acs.chemmater.2c02431

- A. Valverde, , E. Alkain, N. A. Rio-López, L. Lezama, A. Fidalgo-Marijuan, J. M. Laza, S. Wuttke, J. M. Porro, I. Oyarzabal, M. Jiménez-Ruiz, V. García-Sakai, P.L. Aria, I. Agirrezabal-Telleria, R.Fernández de Luis. Enzyme-mimicking of copper-sites in metal–organic frameworks for oxidative degradation of phenolic compound. *J. Mater. Chem. A.* 2024, 12, 4555-4571. Doi: 10.1039/D3TA06198A

CHAPTER 1
Introduction

1.1. ACTIVE MATERIALS

In the past few decades, there has been a significant surge in the search for new materials with tailored properties, driven by their vast range of potential applications. Within this promising field of development, one category outstands: smart or active materials, defined as those that exhibit the ability to modify their physical properties as a response to external stimuli. Being the stimulus a physical or chemical signal, the response can be manifested as a mechanical deformation or another type of signal.[1–4]

Active materials with mechanical properties are particularly interesting for their prospective use as sensors and actuators, besides the widely studied complex mechanisms underlying their behaviour. In this group, we can find the shape memory alloys (SMAs), characterized by their ability to recover their original form after being subjected to certain external stimulus, such as strains or magnetic fields[5–7]. This unique effect, known as shape memory effect (SME) was firstly observed by Arne Ölander in 1932 when studying an Au-Cd alloy[8]. In 1965, William Buehler, Frederick Wang and Stanley Pickart discovered the most widely used and studied shape memory alloys, NiTi[9]. Their SME and the up to 12% recoverable volume deformation they can undergo, along with their interesting mechanical properties, have led to their use in microsystems, industrial applications, biomedical and automotive industries, etc.[10]

Since the early 90´s, Heusler type alloys, such as Ni_2MnGa or Ni_2MnSn, have been gaining interest as the most potential shape memory alloys with magnetic properties: these are the so-called Magnetic Shape Memory Alloys (MSMAs)[11–15]. Being these alloys the focus of the work presented in this dissertation, they will be extensively introduced in the next sections, including their shape memory effect, actuation mechanisms, crystal structure, mechanical and magnetic properties

1.2. SHAPE MEMORY ALLOYS: MARTENSITIC TRANFORMATION, MT

1.2.1. Martensitic Transformation, MT

The distinctive properties exhibited by the SMAs steam from a process called martensitic transformation, a first-order transition between two solid-state phases. These phases are a high-temperature, high-symmetry one, known as the austenite or austenitic phase, and a low temperature, low symmetry one, referred to as the martensite or martensitic phase. Due to the diffusion-less character of the transformation, the atoms move less than their interatomic distances, retaining their relative positions upon undergoing the phase transition and leading to structurally different but same-composition phases[16,17].

This transformation can be direct (austenite to martensite) or inverse (martensite to austenite), also simply denoted martensitic and austenitic transformations, respectively. These transformations take place within a range of temperatures, having starting (T_M^S, T_A^S) and finish (T_M^F, T_A^F) temperatures, and often showing a thermal hysteresis between them (see **Figure 1.1**). During the span of this dissertation, the martensitic (T_M) and austenitic (T_A) transformation temperatures will be taken as the average between their respective starting (T_M^S, T_A^S) and finishing (T_M^F, T_A^F) temperatures.

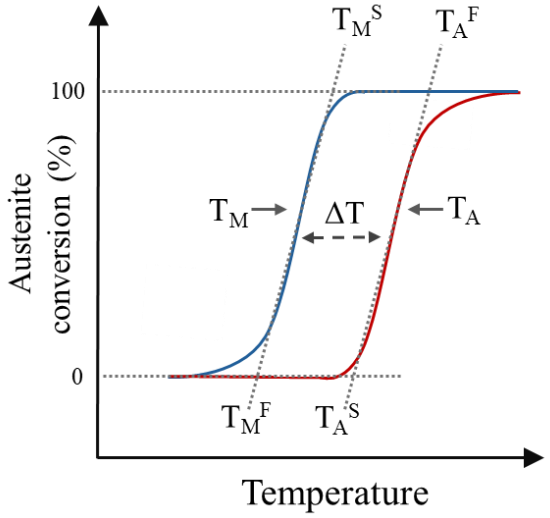

Figure 1.1. *Sketch of the thermal hysteresis loop of the direct (blue) and inverse (red) martensitic transformation, showcasing the characteristic transformation temperatures (T_M^S, T_A^S, T_M^F, T_A^F)*

When the martensite is obtained upon cooling from the austenite phase, a stressed structure is obtained. The crystal matrix elastically absorbs these stresses by a twinning process, leading to the formation of twin variants, which are defined as crystallographic equivalent structures with different orientations (see **Figure 1.2**), that are separated by crystallographic planes known as twin boundaries. In the absence of an external applied force, they are randomly oriented, resulting in a very small macroscopic deformation[17,18].

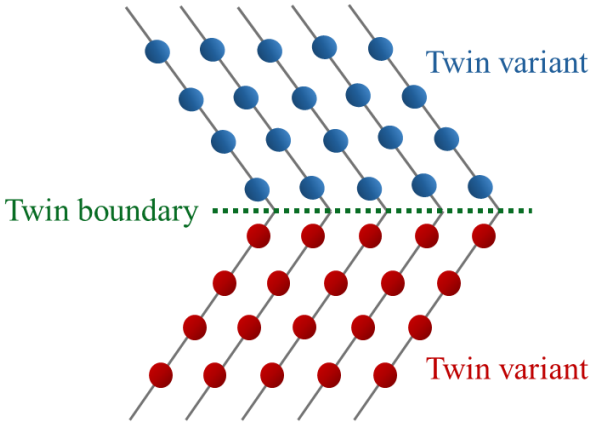

Figure 1.2. *Schematic representation of twin variants, separated by a twin boundary (green dashed line).*

The martensitic transformation can be induced not only by temperature, but also by stress. When a load is applied above T_M^S, the martensite starts to form with a preferential growth of one of the variants, defined by the direction of the application of the strain induced by the load, due to the defects created by the stress acting as nucleation points. The release of the stress induces the transition to the high temperature (austenite) phase, involving a macroscopic change in the shape. This is the so-called superelastic effect.[19,20]

1.2.2. Shape Memory Effect, SME.

The previously introduced shape memory effect (SME) [17,18,21,22] originates from a thermally induced martensitic transformation. The SME, schematized in **Figure 1.3**, can be explained as a three-step process as follows:

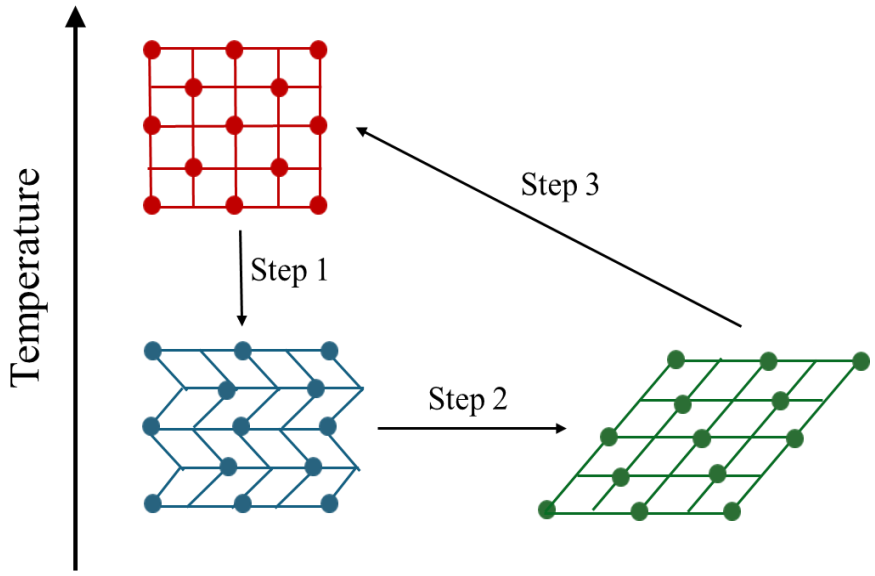

Figure 1.3. *Scheme showing the shape memory effect, with the corresponding structures present in the different stages of the transformation.*

- Step 1: Starting from the alloy in its austenitic phase, the temperature decreases below T_M, and a twinned martensite is formed.
- Step 2: The randomly oriented twin variants induced after the martensitic transformation are aligned upon the application of a certain stress, known as the twinning stress (σ_{TW}). As a result of the orientation of the variants and the formation of a de-twinned martensite, a macroscopical deformation is obtained. In opposition to the superelastic effect, this de-twinned martensite is retained after releasing the stress.
- Step 3: As the temperature is increased above T_A, the austenitic phase is induced, and the alloy recovers the original macroscopic shape.

Being the austenite the less energetic crystal structure of the alloy, the same structure is obtained after every austenitic transformation, hence the macroscopic shape associated to the austenitic phase can be considered to be remembered. Nevertheless, and due to the twin variants being randomly oriented after each heating-cooling cycle across the MT, the martensitic shape is not retained. Consequently, this is the phenomenon referred to as the *one-way* shape memory effect.

For a SMA to exhibit the process known as the *two-ways* shape memory effect, both the austenitic and the martensitic phases must be retained. Since retaining the crystal shape of the martensite is not an intrinsic property of the shape memory alloys,

it can only be induced through a training process, which typically involves several cycles of inducing the martensitic transformation by decreasing the temperature while applying a load to the SMA[23,24]. The crystallographic defects this load generates in the alloy act as nucleation points for the twin variants to grow with a specific orientation, so a detwinned martensite is formed. The defects are maintained as the temperature increases and, in turn, acquired by the austenite. Upon thermally reinducing the martensitic transformation, the defects act again as nucleation points, leading to the re-formation of the previous martensite. As a result, the transition between the austenite and the martensite phases with oriented twin variants is obtained solely by temperature change.[25–28] The most common application of the shape memory alloys, which is their use as sensors and actuators, is based on this *two-ways* shape memory effect.

1.3. MAGNETIC SHAPE MEMORY ALLOYS AND EXPLOITATION OF THE PROPERTIES OF THE MT.

A particularly interesting class of shape memory alloys is magnetic shape memory alloys, MSMAs, as they combine the distinctive shape memory effect with magnetic properties. Hence, they display two transformations, the structural (MT) phase transition and a magnetic one, which is a second order phase transition. The latter is a weak magnetic or paramagnetic-to-ferromagnetic (or vice versa) transition, occurring at a characteristic temperature, the Curie temperature (T_C). Based on this transition occurring either in the austenitic or martensitic phases, it is commonly referred to as the austenitic or martensitic Curie temperature (T_C^A or T_C^M, respectively).[29–31]

Depending on whether the structural transition also involves a change in the magnetic behaviour of the alloy, MSMAs can be classified as ferromagnetic shape memory alloys (FSMAs) or metamagnetic shape memory alloys (MMSMAs). While in FSMAs the martensitic transformation does not change the ferromagnetic behaviour of the alloy, MMSMAs are characterized by a ferromagnetic austenite to weak- or non-magnetic martensite phase transformation.[7,32]

The ability of MSMAs to undergo macroscopical deformations upon the application of external magnetic fields can arise from two different phenomena: a magnetic field induced strain, MFIS, and a magnetic field induced martensitic transformation. These effects are the distinctive feature of FSMAs and MMSMAs, respectively.

1.3.1. Magnetic Field induced Strain, MFIS

Ferromagnetic shape memory alloys, as every ferromagnetic material, are characterized by possessing a non-zero net magnetic moment in the martensite, commonly known as saturation magnetization (μ_{sat}). In the absence of an external applied magnetic field, the crystallographic martensitic structure of the alloys can be described as a randomly oriented twinned one, as discussed in the previous section. The magnetocrystalline anisotropy describes an easy axis along each variant. If the variants are randomly oriented, there are multiple easy axis, while single-variant crystal present a sole easy direction of magnetization. [33,34]

The application of an external magnetic field to the ferromagnetic martensite with strong magnetocrystalline anisotropy results in the competition between two different energy terms: the Zeeman energy and the magnetocrystalline anisotropy energy. The first is responsible for the rotation of the magnetization in the direction to the applied field, and can described by **Equation 1.1,**

$$E_{Zeeman} = -\mu_0 \overrightarrow{H} \cdot \overrightarrow{M_S} \qquad \textbf{\textit{Equation 1.1}}$$

where μ_0 is the magnetic permeability of free space, $\vec{H}$, the applied magnetic field, and $\overrightarrow{M_S}$, the spontaneous magnetization. The magnetocrystalline anisotropy energy, which opposes the magnetization to move out of the easy direction, can be expressed as **Equation 1.2** for the simplest case of uniaxial anisotropy:

$$E_{anisotropy} = K_u \cdot sin^2\theta \qquad \textbf{\textit{Equation 1.2}}$$

where *Ku*, is the magnetocrystalline anisotropy constant, and θ is the angle formed by the magnetization vector and the easy direction of magnetization (easy axis).[35,36]

Given a sufficiently strong magnetocrystalline anisotropy, the Zeeman energy generated on the twin boundaries renders the reorientation of the twin variants more favourable than the rotation of the magnetic moments. Therefore, the variants with the magnetic moments aligned with the external magnetic field grow, by rotating the variants perpendicular to it, until a single variant state is obtained, and a macroscopical strain is observed in the alloy (see **Figure 1.4**).

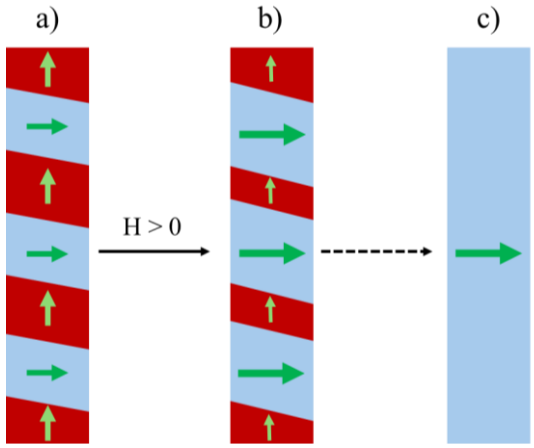

***Figure 1.4**. Schematic of the process of magnetic field induced strain and subsequent mechanical reset of the sample in a ferromagnetic shape memory alloy. a) The sample in a self-accommodated martensite phase without applying any magnetic field. b) Growing of the variants with the magnetic moments along the applied field. c) Single variant martensite.*

This reversible, contactless mechanical deformation, known as Magnetic Field Induced Strain (MFIS), makes FSMAs highly promising for magnetostrictive related applications. However, it is highly dependent on the structure, requiring a low symmetry martensite and twin variants with a low twinning stress, to ensure they are highly mobile. A certain magnetostress needs to be reached within the martensite, in order to induce twin variants reorientation upon the application of an external magnetic field.[37,38] The value of the magnetic stress can be calculated as shown in **Equation 1.3,**

$$\sigma_{mag} = (1 - a/c)^{-1} K_u \qquad \textbf{\textit{Equation 1.3}}$$

being *c/a* the relation between the martensitic cell parameters (see **Section 3.2**). The obvious important role this relation plays not only in σ_{mag}, but also in the maximum theoretical deformation archivable by SMAs (1- *c/a*)[38] implies a strong correlation between the potential magnetostrictive-related applications of MSMAs

and the crystal structures of the alloys. Therefore, the crystal structures of the austenite and martensite phases of MSMAs will be analysed in detail in **Section 1.4**.

It must be noted that for the martensitic twin variants to reorient under the influence of an external magnetic field, the alloy must be in its ferromagnetic martensitic state, signifying below the structural (T_M) and magnetic (T_C) transition temperatures. Therefore, these temperatures are a key factor for the optimization of magnetostrictive-related applications of MSMAs.

1.3.1. Magnetocaloric Effect, MCE.

The magnetocaloric effect is an interesting phenomenon consisting of a material changing its temperature when exposed to a magnetic field[39,40]. The induced alignment and reorientation of the magnetic moments of a material leads to a variation of its entropy (ΔS), causing the aforementioned temperature change. Upon removal of the magnetic field, the magnetic moments return to their disordered state, making the effect reversible.[41]

In the particular case of metamagnetic shape memory alloys, the magnetocaloric effect arises from the previously mentioned magnetic field-induced MT. As previously introduced, MMSMAs are characterized by a ferromagnetic austenite to a weak-magnetic martensite transformation. Therefore, the resultant significant entropy change, ΔS, is a combination of the structural (ΔS_{str}) and magnetic (ΔS_{mag}) entropy changes (see **Equation 1.4**).

$$|\Delta S| = |\Delta S_{str}| \pm |\Delta S_{mag}| \qquad \textit{Equation 1.4}$$

The positive or negative sign of the total entropy value provides valuable information about the type of magnetocaloric effect. The conventional or Direct Magnetocaloric Effect (MCE) is associated with a temperature increase upon the application of the magnetic field, and, therefore, to $\Delta S<0$. The Inverse Magnetocaloric Effect (IMCE), however, is related to $\Delta S>0$ and a decrease in temperature. The rapid and sharp magnetic field-induced austenite-to-martensite transformation results in a less symmetrical martensite structure and, hence, in $\Delta S_{str}<0$. Additionally, the associated ferromagnetic-to-weak magnetic transition implies a less magnetically order structure, increasing ΔS_{mag}.

Since the absolute value of the entropy is positive, MMSMAs decrease their temperature when a magnetic field is applied at temperatures close to T_M, making these alloys highly promising for solid state refrigeration applications[42,43]. It is worth mentioning that the change in the transformation temperature (dT_M) induced by the (I)MCE is described by **Equation 1.5**,

$$\frac{dT_M}{dH} = -\mu_0 \frac{\Delta M}{\Delta S} \qquad \textit{Equation 1.5}$$

where ΔM is the induced change in magnetization, μ_0 is the vacuum magnetic permeability and dH is the applied field. Therefore, it can be concluded that the MCE is significantly dependant on the nature of the MT (through ΔM), T_M and T_C.[44–47]

1.4. CANONICAL MSMA SYSTEMS

1.4.1. Ni-Mn-Ga systems. Physical properties.

For a full understanding of the martensitic transformation and the properties arising from it, such as the MFIS and the magnetocaloric effect, a deeper insight into the austenitic and martensitic structure is necessary. As previously introduced, the austenitic phase exhibits a high symmetry, whereas the martensitic phase displays a lower one.

All the alloys studied in the work presented in this thesis are based on intermetallic Heusler compounds with X_2YZ composition (Ni_2MnGa, Ni_2MnSn), in which the high temperature austenitic phase presents a cubic *Fm-3m* crystal phase with a $L2_1$ ordering. This structure can be described as four interpenetrating face centered cubic (*fcc*) sublattices. In an ideal ordered case, Y and Z atoms take the (0, 0, 0) and (0.5, 0.5, 0.5) positions, respectively, leaving the remaining equivalent (0.25, 0.25, 0.25) and (0.75, 0.75, 0.75) sites for the X atoms. These positions are widely referred to as Wyckoff positions 4a, 4b and 8c, being this the denotation employed across this dissertation when referring to specific crystal lattice atomic sites. In the particular case of Ni-Mn-Ga alloys, this cubic structure is transformed to tetragonal or orthorhombic crystal structures in the martensite phase. While the cubic austenite is characterized by the lattice parameter a and the angle β = 90º, the tetragonal and

orthorhombic structures are characterized by the lattice parameters *a* and *c*, or *a*, *b* and *c* parameters, respectively, in addition to β = 90º (see **Section 3.2** for further information).[3,11,48,49]

In the most widely studied Heusler SMA, the stoichiometric Ni_2MnGa, the martensitic structure is described as a tetragonal phase with a non-modulated *I4/mmm* symmetry. As pictured in **Figure 1.5**, this martensitic unit cell is related to the parent phase by a 45º rotation around the (001) axis, implying that the austenitic and martensitic lattice parameters (*a* and *a´*, respectively) are correlated as $\frac{\sqrt{2}}{2}$a = a´. This structure can also be described as a *fcc* lattice, related to the austenitic structure by the elongation or contraction of the *c* axis.[13,50]

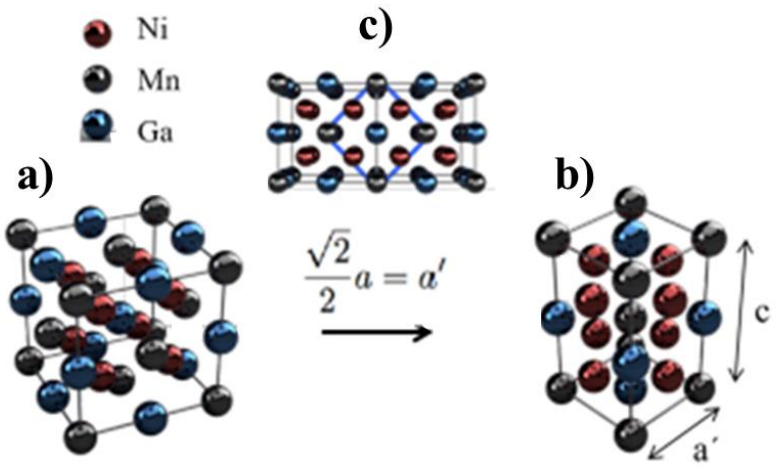

Figure 1.5. *a) austenitic and b) martensitic structures, along with c) the relation between both structures by a 45º rotation around the (001) axis. Figure adapted from*[51]

Nevertheless, in non-stoichiometric or doped Ni-Mn-Ga alloys different martensitic structures can be found, such as tetragonal, orthorhombic and/or modulated cells. Analogously to the tetragonal martensite, the orthorhombic one can be described with a *Immm* symmetry, also related to the parent phase by a 45º rotation around the (001) axis.[51] The modulated cells means that their atomic arrangement shows a repetitive, periodic pattern of slight distortions, known as modulations.[18]Since the MT is a first-order, diffusionless phase transition, the relative positions of the atoms remain invariable, even though their absolute positions are altered between the martensite and austenite phases. **Table 1.1** correlates the

austenitic atomic sites within the crystal lattice (space group *Fm-3m*) with their equivalent ones in the most prevalent resultant orthorhombic (space group *Immm*) or tetragonal (space group *I4/mmm*) martensites. Both the tetragonal and orthorhombic structures can show a shifting along the (110) system of planes. Generally, the modulation periods are five or seven (110) planes, being that the reason for the 5M and 7M denotation, respectively. The low twinning stresses associated with a modulated martensite make the MFIS more energetically viable, resulting in theoretical deformations up to 6 and 10% for the 5M and 7M modulated martensites, respectively.[1,52]

Table 1.1. *Wyckoff site denotations in the cubic (space group Fm-3m), tetragonal (I4/mmm) and orthorhombic (Immm) unit cells, and their corresponding equivalences.*

Fm-3m		**I4/mmm**		**Immm**	
Position - Wyckoff site		Position - Wyckoff site		Position - Wyckoff site	
(0.25, 0.25, 0.25) (0.75, 0.75, 0.75)	8c	(0, 0.5, 0.25) (0, 0.5, 0.75)	4d	(0, 0.5, 0.25) (0, 0.5, 0.75)	4j
(0, 0, 0)	4a	(0, 0, 0)	2a	(0, 0, 0)	2a
(0.5, 0.5, 0.5)	4b	(0, 0, 0.5)	2b	(0.5, 0.5, 0) (0, 0, 0.5)	2c

It should be mentioned that, besides the MFIS Ni-Mn-Ga systems can display, a notable magnetocaloric effect is observed in off-stoichiometric and (Cu,Co,In)-doped MMSMAs. In this dissertation, Ni-Mn-Ga alloys doped with different elements will be studied in order to optimise their properties towards the exploitation of these characteristic features.

1.4.2. Ni-Mn-Sn systems. Physical properties.

As extensively described in the previous section, the magnetocaloric effect Heusler alloys arises from the nature of the MT and, in turn, from the characteristics of the austenite and martensite phases. For years, Ni-Mn-Sn alloys have attracted significant attention due to their remarkable magnetocaloric effect[53]. Analogously to the Ni-Mn-Ga alloys, the interesting properties these systems exhibit originate from the martensitic transformation and, in turn, from the austenitic and martensitic structures.[54,55]

While their high symmetry austenite *Fm-3m* cubic phase displays the already detailed $L2_1$ ordering, common to every Heusler alloy, the MT leads to a complex microstructure. The off-stoichiometric and doped martensite structure can be described as 3M, 5M, 7M or 4O, with a tetragonal (*I4/mmm*), orthorhombic (*Pmma*) or monoclinic (*P2/m*) symmetry, with M meaning modulation every certain number of planes and O, modulation every certain number of unit cells.[26,56]

This exceptional variability in the crystal structure of the martensite phase and, hence, on the MT, as a direct consequence solely of compositional modifications (i.e. off-stoichiometric and/or doped alloys) makes these alloys highly promising for magnetocaloric related applications upon proper tuning of their properties.

1.5. OBJECTIVES AND STRUCTURE OF THE THESIS

The main goal of the work presented in this dissertation consists in the design and study of new ferromagnetic and metamagnetic Heusler alloys, whose practical implementations are based on magnetic field induced strain or magnetocaloric effect. In this introduction, we have explained the crucial importance of the dependence of both the MFIS and the (I)MCE on the structural (T_M) and magnetic (T_C) transition temperatures, as well as on the behaviour of the MT, that, in turn, is conditioned by the crystal structures of the austenite and martensite phases. Moving forward within this line, this thesis aims to analyse the effect compositional changes and fabrication alterations have on the resultant structures and properties of the studied alloys.

More specifically, Chapter 4 focuses on the effect post-annealing heat treatments have on the martensitic transformation and the magnetocaloric effect of Co-doped Ni-Mn-Sn alloys. Chapters 5 and 6 explore the effect Cu- and Fe- doping, respectively, have on the characteristic transition temperatures and crystal structures of Ni-Mn-Ga-based alloys, while Chapter 7 aims to expand the Fe-doping study employing single crystals. In each study and system of alloys, the microstructure is closely related to the magnetic properties of the alloys and, consequently, with the practical implementations

Complementing these experimental chapters two more sections related with the employed characterization techniques are presented hereafter. Since neutron diffraction techniques are a key tool for drawing the connection between the macroscopic properties and the microstructure of the alloys, they are detailed in Chapter 3. Finally, Chapter 2 comprises an introduction to the fabrication and magnetic characterisation techniques employed to describe the experimental results presented in this dissertation.

1.6. BIBLIOGRAPHY

1. Acet M, Mañosa L, Planes A. Magnetic-Field-Induced Effects in Martensitic Heusler-Based Magnetic Shape Memory Alloys. *Handb Magn Mater*. 2011;19(C):231-289. doi:10.1016/B978-0-444-53780-5.00004-1

2. L'vov VA, Chernenko VA, Barandiaran JM. Magnetic shape memory materials with improved functional properties: Scientific aspects. In: *Springer Series in Materials Science*. Vol 231. .) Novel f. Springer International Publishing; 2016:1-40. doi:10.1007/978-3-319-26106-5_1

3. Río-lópez NA, Lázpita P, Salazar D, et al. Neutron scattering as a powerful tool to investigate magnetic shape memory alloys: A review. *Metals (Basel)*. 2021;11(5):1-21. doi:10.3390/met11050829

4. Heczko O, Scheerbaum N, Gutfleisch O. Magnetic shape memory phenomena. In: *Nanoscale Magn. Mater. Appl.* ; 2009:399-739.

5. Chowdhury P, Sehitoglu H. Deformation physics of shape memory alloys – Fundamentals at atomistic frontier. *Prog Mater Sci*. 2017;88:49-88. doi:10.1016/j.pmatsci.2017.03.003

6. Petrini L, Migliavacca F. Biomedical Applications of Shape Memory Alloys. *J Metall*. 2011;2011(Figure 1):1-15. doi:10.1155/2011/501483

7. Chernenko VA, L'vov VA, Cesari E, Barandiaran JM. Fundamentals of magnetocaloric effect in magnetic shape memory alloys. In: *Handbook of Magnetic Materials*. Vol 28. Elviser; 2019:1-45.

doi:10.1016/bs.hmm.2019.03.001

8. Ölander A. Cadmium-gold alloys solid. *J Am Chem Soc*. 1932;54(10):3819-3833.

9. Wang FE, Buehler WJ, Pickart SJ. Crystal structure and a unique “martensitic” transition of TiNi. *J Appl Phys*. 1965;36(10):3232-3239. doi:10.1063/1.1702955

10. Mohd Jani J, Leary M, Subic A, Gibson MA. A review of shape memory alloy research, applications and opportunities. *Mater Des*. 2014;56:1078-1113. doi:10.1016/j.matdes.2013.11.084

11. Brown PJ, Crangle J, Kanomata T, et al. The crystal structure and phase transitions of the magnetic shape memory compound Ni2MnGa. *J Phys Condens Matter*. 2002;14(43):10159-10171. doi:10.1088/0953-8984/14/43/313

12. Cong DY, Wang YD, Lin Peng R, et al. Crystal structures and textures in the hot-forged Ni-Mn-Ga shape memory alloys. *Metall Mater Trans A Phys Metall Mater Sci*. 2006;37(5):1397-1403. doi:10.1007/s11661-006-0084-0

13. Richard ML, Feuchtwanger J, Allen SM, et al. Chemical order in off-stoichiometric Ni-Mn-Ga ferromagnetic shape-memory alloys studied with neutron diffraction. *Philos Mag*. 2007;87(23):3437-3447. doi:10.1080/14786430701297582

14. Webster PJ, Ziebeck KRA, Town SL, Peak MS. Magnetic order and phase transformation in Ni2MnGa. *Philos Mag B Phys Condens Matter; Stat Mech Electron Opt Magn Prop*. 1984;49(3):295-310. doi:10.1080/13642817408246515

15. Graf T, Felser C, Parkin SSP. Simple rules for the understanding of Heusler compounds. *Prog Solid State Chem*. 2011;39(1):1-50. doi:10.1016/j.progsolidstchem.2011.02.001

16. Otsuka K, Ren X. Martensitic transformations in nonferrous shape memory alloys. *Mater Sci Eng A*. 1999;273-275:89-105. doi:10.1016/S0921-

5093(99)00291-9

17. Kohl M, Krevet B, Ohtsuka M, Brugger D, Liu Y. Ferromagnetic shape memory microactuators. *Mater Trans*. 2006;47(3):639-644. doi:10.2320/matertrans.47.639

18. Otsuka K, Wayman C. *Shape Memory Materials*. Cambridge University Press; 1999.

19. Auricchio F, Taylor RL, Lubliner J. Auricchio, F., Taylor, R. L., & Lubliner, J. (1997). Shape-memory alloys: macromodelling and numerical simulations of the superelastic behavior. Computer methods in applied mechanics and engineering, 146(3-4), 281-312. *Comput Methods Appl Mech Engrg*. 1997;146:281-312.

20. Miyazaki S, Kim HY, Hosoda H. Development and characterization of Ni-free Ti-base shape memory and superelastic alloys. *Mater Sci Eng A*. 2006;438-440(SPEC. ISS.):18-24. doi:10.1016/j.msea.2006.02.054

21. Soderberg O, Aaltio I, Ge Y, Heczko O, Hannula S. Ni – Mn – Ga multifunctional compounds. 2008;482:80-85. doi:10.1016/j.msea.2006.12.191

22. Müllner P, King AH. Deformation of hierarchically twinned martensite. *Acta Mater*. 2010;58(16):5242-5261. doi:10.1016/j.actamat.2010.05.048

23. Müllner P, Chernenko VA, Kostorz G. Large cyclic magnetic-field-induced deformation in orthorhombic (14M) Ni-Mn-Ga martensite. *J Appl Phys*. 2004;95(3):1531-1536. doi:10.1063/1.1639144

24. Chmielus M, Chernenko VA, Knowlton WB, Kostorz G, Müllner P. Training, constraints, and high-cycle magneto-mechanical properties of Ni-Mn-Ga magnetic shape-memory alloys. *Eur Phys J Spec Top*. 2008;158(1):79-85. doi:10.1140/epjst/e2008-00657-3

25. Asadian M, Seyedein SH, Aboutalebi MR, Maroosi A. Optimization of the parameters affecting the shape and position of crystal-melt interface in YAG single crystal growth. *J Cryst Growth*. 2009;311(2):342-348. doi:10.1016/j.jcrysgro.2008.10.045

26. Chulist R, Czaja P. On the role of atomic shuffling in the 4O, 4M and 8M martensite structures in Ni-Mn-Sn single crystal. *Scr Mater*. 2020;189:106-111. doi:10.1016/j.scriptamat.2020.08.007

27. Chernenko VA, Villa E, Besseghini S, Barandiaran JM. Giant two-way shape memory effect in high-temperature Ni-Mn-Ga single crystal. *Phys Procedia*. 2010;10:94-98. doi:10.1016/j.phpro.2010.11.081

28. Zheludev A, Shapiro S, Wochner P, Tanner L. Precursor effects and premartensitic transformation inMnGa. *Phys Rev B - Condens Matter Mater Phys*. 1996;54(21):15045-15050. doi:10.1103/PhysRevB.54.15045

29. Porro Azpiazu JM, Petrenko V, Rodriguez Crespo B, Rodriguez Velamazan JA, Salazar D. Magnetic, structural and atomic ordering insight of metamagnetic shape memory alloys. Published online 2021. doi:10.5291/ILL-DATA 5-31-2804

30. Dunand DC, Müllner P. Size Effects on Magnetic Actuation in Ni-Mn-Ga Shape-Memory Alloys. Published online 2011. doi:10.1002/adma.201002753

31. Suzuki S, Takagi T, Tani J. Structural and magnetic phase transitions in shape-memory alloys (formula presented). *Phys Rev B - Condens Matter Mater Phys*. 1999;59(2):1113-1120. doi:10.1103/PhysRevB.59.1113

32. Murray SJ, Marioni M, Allen SM, Handley RCO. in ferromagnetic Ni – Mn – Ga. *Appl Phys Lett*. 2000;77(6):886-888. doi:10.1063/1.1306635

33. Bozorth RM. *Ferromagnetism*.; 1993.

34. Faran E, Shilo D. Ferromagnetic Shape Memory Alloys—Challenges, Applications, and Experimental Characterization. *Exp Tech*. 2016;40(3):1005-1031. doi:10.1007/s40799-016-0098-5

35. Rameš M, Heczko O, Sozinov A, Ullakko K, Straka L. Magnetic properties of Ni-Mn-Ga-Co-Cu tetragonal martensites exhibiting magnetic shape memory effect. *Scr Mater*. 2018;142:61-65. doi:10.1016/j.scriptamat.2017.07.034

36. Likhachev AA, Sozinov A, Ullakko K. Modeling the strain response, magneto-mechanical cycling under the external stress, work output and energy losses in

Ni-Mn-Ga. *Mech Mater*. 2006;38(5-6):551-563. doi:10.1016/j.mechmat.2005.05.022

37. Zelený M, Sozinov A, Straka L, Björkman T, Nieminen RM. First-principles study of Co- and Cu-doped Ni2MnGa along the tetragonal deformation path. *Phys Rev B - Condens Matter Mater Phys*. 2014;89(18):1-9. doi:10.1103/PhysRevB.89.184103

38. Straka L, Drahokoupil J, Pacherová O, et al. The relation between lattice parameters and very low twinning stress in Ni50Mn25+xGa25-x magnetic shape memory alloys. *Smart Mater Struct*. 2016;25(2). doi:10.1088/0964-1726/25/2/025001

39. Umetsu RY, Xu X, Kainuma R. NiMn-based metamagnetic shape memory alloys. *Scr Mater*. 2016;116:1-6. doi:10.1016/j.scriptamat.2016.01.006

40. Liang X, Zhang C, Bai J, et al. Manipulation of magnetocaloric and elastocaloric effects in Ni–Mn–In alloys by lattice volume and magnetic variation: Effect of Co and Fe co-doping. *J Mater Sci Technol*. 2024;172:156-165. doi:10.1016/j.jmst.2023.06.044

41. Pecharsky VK, Gschneidner KA. Magnetocaloric effect from indirect measurements: Magnetization and heat capacity. *J Appl Phys*. 1999;86(1):565-575. doi:10.1063/1.370767

42. Sandeman KG. Magnetocaloric materials: The search for new systems. *Scr Mater*. 2012;67(6):566-571. doi:10.1016/j.scriptamat.2012.02.045

43. Stevens E, Kimes K, Salazar D, et al. Mastering a 1.2 K hysteresis for martensitic para-ferromagnetic partial transformation in Ni-Mn(Cu)-Ga magnetocaloric material via binder jet 3D printing. *Addit Manuf*. 2021;37(August 2020). doi:10.1016/j.addma.2020.101560

44. Nambiar SS, Murthy BRN, Sharma S, Prasanna AA, Chelvane AJ. Microstructure and Mechanical Properties of Annealed Quinary Ni-Mn-Sn-Fe-In Heusler Alloy. *Eng Sci*. 2022;17:303-308. doi:10.30919/es8d632

45. Esakki Muthu S, Rama Rao N V., Manivel Raja M, Raj Kumar DM, Mohan

Radheep D, Arumugam S. Influence of Ni/Mn concentration on the structural, magnetic and magnetocaloric properties in Ni50-xMn37+xSn13 Heusler alloys. *J Phys D Appl Phys*. 2010;43(42). doi:10.1088/0022-3727/43/42/425002

46. Zhukova V, Ipatov M, Granovsky A, Zhukov A. Magnetic properties of Ni-Mn-In-Co Heusler-type glass-coated microwires. *J Appl Phys*. 2014;115(17):10-13. doi:10.1063/1.4868919

47. Seguí C, Torrens-Serra J, Cesari E, Lázpita P. Optimizing the caloric properties of Cu-doped Ni-Mn-Ga alloys. *Materials (Basel)*. 2020;13(2). doi:10.3390/ma13020419

48. Krenke T, Acet M, Wassermann EF, Moya X, Mañosa L, Planes A. Martensitic transitions and the nature of ferromagnetism in the austenitic and martensitic states of Ni-Mn-Sn alloys. *Phys Rev B - Condens Matter Mater Phys*. 2005;72(1):1-9. doi:10.1103/PhysRevB.72.014412

49. Ayuela A, Enkovaara J, Ullakko K, Nieminen RM. Structural properties of magnetic Heusler alloys. *J Phys Condens Matter*. 1999;11(8):2017-2026. doi:10.1088/0953-8984/11/8/014

50. Tickle R, James RD, Shield T, Wuttig M, Kokorin V V. Ferromagnetic shape memory in the NiMnGa system. *IEEE Trans Magn*. 1999;35(5 PART 3):4301-4310. doi:10.1109/20.799080

51. Pérez-Checa A. *Development of New Ni – Mn – Ga Based High Temperature Shape Memory Alloys*. Universidad del País Vasco/Euskalherriko Unibertsitatea; 2019.

52. Zheng H, Wang W, Xue S, Zhai Q, Frenzel J, Luo Z. Composition-dependent crystal structure and martensitic transformation in Heusler Ni-Mn-Sn alloys. *Acta Mater*. 2013;61(12):4648-4656. doi:10.1016/j.actamat.2013.04.035

53. Sozinov A, Likhachev AA, Ullakko K. Crystal structures and magnetic anisotropy properties of Ni-Mn-Ga martensitic phases with giant magnetic-field-induced strain. *IEEE Trans Magn*. 2002;38(5 I):2814-2816. doi:10.1109/TMAG.2002.803567

54. Rodríguez-Crespo B, Río-López N., Lázpita P, et al. Impact of magnetic, atomic and microstructural ordering on the magnetocaloric performance of powdered NiCoMnSn metamagnetic shape memory ribbons. *Mater Des*. Published online 2024:113279. doi:10.1016/j.matdes.2024.113279

55. Helmholdt RB, Buschow KHJ. Crystallographic and magnetic structure of Ni2MnSn and NiMn2Sn. *J Less-Common Met*. 1987;128:167-171.

56. Sánchez-Alarcos V, Pérez-Landazábal JI, Recarte V, Lucia I, Vélez J, Rodríguez-Velamazán JA. Effect of high-temperature quenching on the magnetostructural transformations and the long-range atomic order of Ni-Mn-Sn and Ni-Mn-Sb metamagnetic shape memory alloys. *Acta Mater*. 2013;61(12):4676-4682. doi:10.1016/j.actamat.2013.04.040

57. Li XZ, Zhang WY, Valloppilly S, Sellmyer DJ. New Heusler compounds in Ni-Mn-In and Ni-Mn-Sn alloys. *Sci Rep*. 2019;9(1):1-7. doi:10.1038/s41598-019-44179-2

CHAPTER 2
Experimental Methods

2.1. ALLOY SYNTHESIS TECHNIQUES

2.1.1. Polycrystalline alloys

A. Induction Furnace

An induction furnace is a widely used tool for the preparation of polycrystalline alloys. It consists of a coil and an electronic oscillator that passes a high-frequency alternating current through the coil. This magnetic field penetrates the object and generates electric eddy currents inside the conductor, which heat the material due to the Joule effect induced by the currents flowing through their resistance. This particular heating process leads to a very rapid melting process and homogeneous melt, due to the high-frequency magnetic field serving as stirring. It was used to cast the shape memory alloys' polycrystalline rods.[1]

This casting process starts by weighing the different chemical elements that will conform the alloys according to the desired composition before placing them on the ceramic crucible. The crucible is placed inside the furnace, which is purged until a non-reactive atmosphere is created. Then, the metallic pieces are molten due to the heat created by the eddy currents[2]. Once the aforementioned homogeneous melt is created, the ceramic piece covering the hole of the crucible is removed, allowing the melt to fall into the cooper mould, quickly solidifying and, hence, creating the polycrystalline rod.

The equipment used were a commercial induction furnace model Induret Compact made by REITEL Feinwerktechnik GmbH (**Figure 2.1**), located at the Faculty of Science and Technology of the University of the Basque Country, and a homemade vertical induction furnace, available at the faculty of Mathematics and Physics of the Universita Karlova in Prague, Czech Republic.

Figure 2.1. *Reitel Induret Compact induction furnace, crucible and cooper mold used for polycrystalline rods production. Figure taken from*[3]

B. Arc-melting furnace

The arc-melting is another technique extensively used for the fabrication of polycrystalline alloys. It is based on the application of a high voltage and the subsequent creation of an electric arc between a cooper surface and a tungsten tip under argon atmosphere. This arc reaches up to 3273K, what allows to melt the metallic pieces placed on the cooper surface. Before performing the melting, an argon atmosphere is created inside the furnace, to avoid oxidation or contamination of the sample. With every purging/melting cycle, an increasingly homogeneous metallic piece is obtained.[4,5]

As a consequence of the huge differences in the melting temperatures between metallic elements, the obtained composition can differ from the desired calculated one. Due to this, along with the impossibility of obtaining alloy pieces heavier than 10 grams, we decided not to fabricate the alloys from their metallic precursors directly by arc-melting. Instead, this tool was used to re-melt the polycrystalline rods obtained via induction furnace, allowing us to obtain more homogeneous polycrystalline alloys.

consistenThe arc-melting furnace employed is an Edmund Bühler Compact Arc Melter MAM-1 located at BCMaterials (**Figure 2.2**).

***Figure 2.2**. Edmund Bühler Compact Arc Melter MAM-1, cooper surface and tungsten tip used for the polycrystalline alloys re-melting and homogenization.*

C. Melt-spinning

Melt-spinning is a widely used preparation technique for polycrystalline ribbons due to the easy processability of the alloys. The working principle consists of placing the polycrystalline mass into a quartz tube with an 0.75 mm diameter ejection hole at the bottom. The alloy is then induction melted and ejected into a copper wheel moving at a defined angular speed. The higher is the wheel speed, the higher the quenching rate, as less material per unit of length is deposited on the copper wheel. This high quenching rate facilitates the retention of the austenitic and martensitic phases and prevents the formation of precipitates, what lead to an alloy with improved magnetic properties.[6–8]

For the polycrystalline ribbons used in this work, an Edmund Bühler Melt Spinner MSP10, located at BCMaterials, was used (**Figure 2.3**).

***Figure 2.3**. Edmund Bühler Melt Spinner MSP10. Figure taken from*[9]

2.1.2. Single crystal alloys

A. Modified optical floating zone furnace

The floating zone furnace is a single crystal growth technique based on the zone melting method. A polycrystalline rod is placed vertically on top of a single crystal seed with a desired known crystalline phase and orientation (the one we expect our polycrystalline rod to adopt). The seed is mounted on a shaft, allowing them to displace vertically alongside the furnace, and the whole system is under vacuum or under an inert gaseous atmosphere. A set of four halogen lamps focused on the junction zone between the polycrystal and the seed is employed to heat the zone up to 2000 ºC and create the molten zone, thanks to a strong thermal current. When the molten zone is stable, the lamps are swept at a constant rate along the sample to melt the polycrystal seed at the top. As the polycrystalline rod sweeps vertically across the focal zone of the lamps, the re-solidification as a single crystal at the bottom of the melting zone occurs. The obtained single crystal inherits the crystallographic orientation and crystal phase of the single crystal seed.[10,11]

As previously mentioned, in an optical floating zone furnace the heat used for the melting process is produced by light from halogen or xenon lamps, focused on a

small section of the crystal by 4 ellipsoidal mirrors. In the classical modified optical floating zone method, the precursors are mounted on a moving shaft placed on the bottom of the chamber, but floating otherwise. In the employed modified optical floating zone furnace, a sapphire tube is also mounted on the shaft, with the polycrystalline rod and the single crystal seed inside it (**Figure 2.4**). The quartz tube is transparent to the employed infrared radiation and chemically inert, and is used to avoid the bouncing movement between the precursors, as well as the possible subsequent multigrain crystallization or volume changes.

The growth of all single crystals was achieved by using a FZ-T-12000-X-VP-CR, Crystal Systems Ltd optical floating zone furnace, located at the faculty of Mathematics and Physics of the Charles University. After a long optimization process of the growth parameters; i.e. the growing pressure and the rod sweep velocity, a 0.25MPa high purity argon atmosphere and a 2mm/hour speed were the selected conditions for the growth.

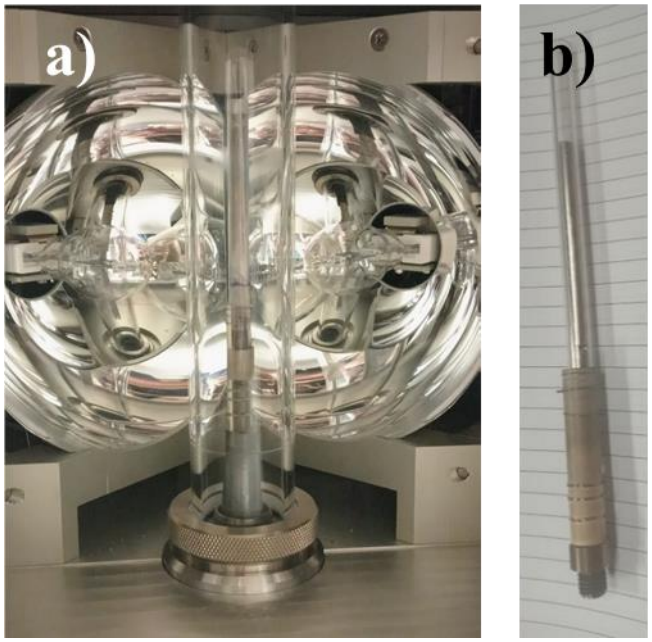

***Figure 2.4**. a) Ellipsoidal crystal mirrors from the FZ-T-12000-X-VP-CR, Crystal Systems, Ltd, optical floating zone furnace and sapphire tube. (b)Single crystal seed and polycrystalline master rod.*

2.2. STRUCTURAL AND COMPOSITIONAL CHARACTERIZATION OF MSMAs

2.2.1. Energy Dispersive X-Ray Spectroscopy (EDX)

Energy Dispersive X-Ray Spectroscopy is a technique widely used for the chemical analysis of a material. X-Rays are a type of monochromatic electromagnetic radiation typically produced when a primary electron beam reaches the material and causes the ejection of an inner shell electron from it. As a result, an outer shell electron transits to fill the inner shell vacancy, producing a monochromatic photon in the X-ray wavelength regime whose energy corresponds to the energy difference between the two electron orbitals involved. This radiation emitted by the sample hits a detector, where the X-ray photon energies and intensities are measured, which will correspond to the energy spectrum from the material, from which its elementary composition is determined.[3,9]

The most usual ways to generate the electron beam used for EDX are thermionic emission from a W or LaB_6 filament or field emission guns. The latter releases the electrons by an electric potential in a cold W cathode or a thermally assisted Schottky type W-ZrO_2 emitter. In both situations, the generated electrons are accelerated and focused into the sample by electromagnetic lenses located within the column and traced along the sample surface by scan coils.[12]

A Hitachi TM300 desktop Scanning Electron Microscope equipped with an energy-dispersive X-Ray detector, located at the Faculty of Science and Technology of the University of the Basque Country, was used to determine the composition of the polycrystalline alloys presented in this thesis.

2.2.2. X-Ray Fluorescence spectroscopy (XRF)

X-Ray Fluorescence is a technique for elemental analysis based on the emission of fluorescent (or secondary) X-Rays from a material. Fluorescent or secondary X-Rays are the names given to those photons emitted by a sample as a result of its excitation by either high-energy X-rays or Gamma Rays, while fluorescence is a phenomenon in which the absorption of an incident radiation,

coincident with the energy of certain electronic transitions of an element, results into the emission of radiation with different energy.[13]

When a sample is bombarded with X-Rays or Gamma Rays with energies higher than the ionization energy of an element, the ionization process results in the ejection of one or more electrons from the inner orbitals of the atom. In order to keep the stable electronic structure of the atom, electrons from outer orbitals jump to occupy the vacant inner orbitals, releasing energy equal to the energy difference between the two orbitals involved. This energy is usually released by photons and collected by a detector. Each atom has its characteristic ionization energy, and hence, the radiation emitted by the sample is dependent on the type and number of atoms present in the material.[14] A schematic picture of this process, alongside with the EDX process, is shown in **Figure 2.5**

A Rigaku ZSX Primus IV X-Ray fluorescence spectrometer, located at the Institute of Physics of the Czech Academy of Sciences, was used for the elemental characterization of the Single Crystal samples presented in this thesis.

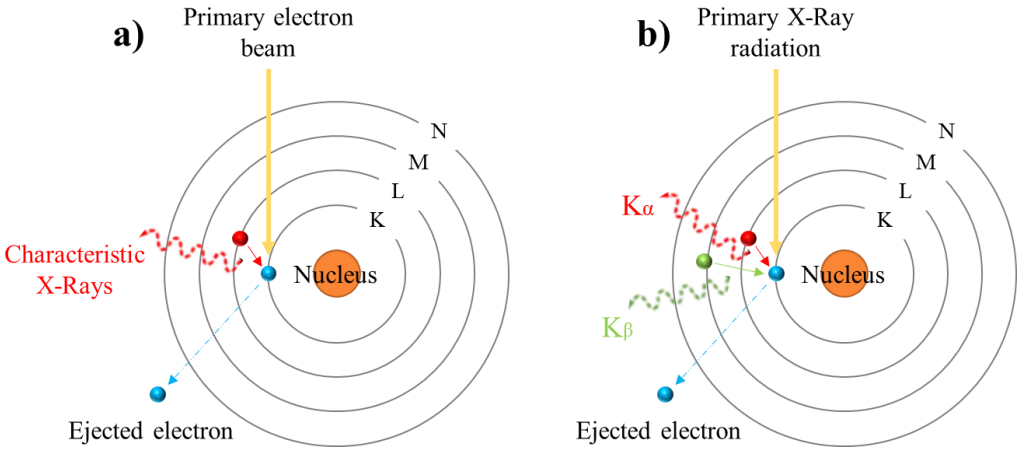

Figure 2.5. *Comparation between the X-Rays emission process in a) Energy Dispersive X-Ray Spectroscopy and b) X-Ray Fluorescence.*

2.2.3. Laue diffraction

Laue diffraction is a type of diffraction usually employed for the structural orientation of single crystals. This technique allows to obtain the reciprocal space map of the crystal, providing information about the orientation, the presence of twin variants and/or defects of the crystals. A it is schematized in **Figure 2.6**, in an X-ray

Laue diffractometer, the X-Ray beam passes through a stationary single crystal (the sample) mounted on a goniometer, which diffracts the beam following Bragg's law (**Equation 2.1**), where n is an integer, λ is the wavelength, d corresponds to the interplanar distance and θ, to the angle between the beam and sample.

$$n\lambda = 2dsin\theta \qquad \textbf{\textit{Equation 2.1}}$$

Contrary to other X-Ray based characterization techniques, Laue diffraction uses a polychromatic X-Ray beam with multiple wavelengths, also known as white beam, and a unique θ. When the Bragg reflection produced by each set of crystal planes reaches the detector, a Laue pattern, characteristic to the symmetry of the crystal, is created, as shown in **Figure 2.6**. By moving the goniometer, the crystal orientation can be tuned, leading to a different part of the crystal been parallel to the beam. If this part corresponds to a symmetry plane, a high symmetry pattern is obtained.[15,16]

A PhotonicScience Laue diffractometer, located at Universita Karlova, Prague, Czech Republic, was used for the orientation of the single crystal alloys presented in this thesis, in addition to the Instrument Orient express at ILL, Grenoble, France.

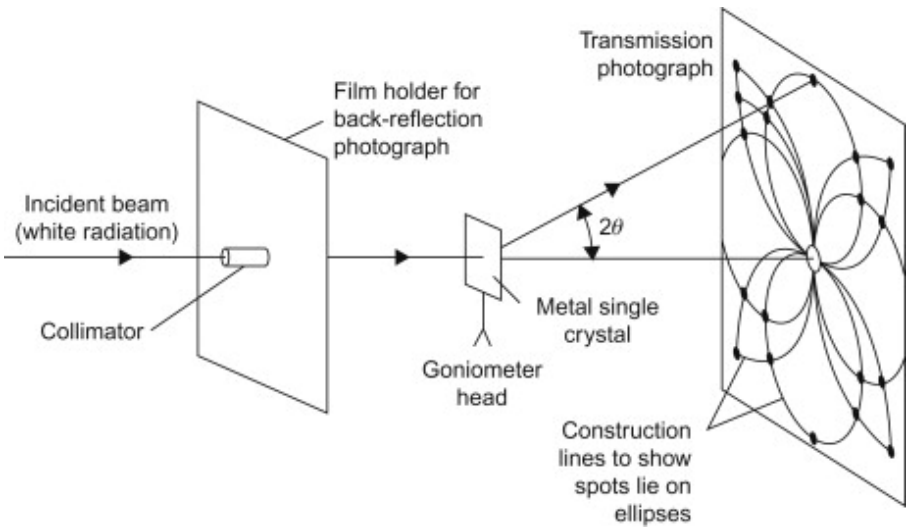

***Figure 2.6**. Schematic image of the X-Ray diffraction process by Laue method. Figure adapted from*[16]

2.2.4. Differential Scanning Calorimetry (DSC)

Differential Scanning Calorimetry is a structural characterization technique based on the measurement of the difference in the heat flow rate between a reference sample (or the environment) and the measured sample. Depending on the signal measured, two basic types of DSCs can be distinguished: the heat flux DSC and the power-compensated DSC.

In the heat flux DSC, the heat exchange between the measured sample and the environment (or the reference sample) is measured via a heat conduction path with a given thermal resistance. The heat flow rate is proportional to the intensity of the heat exchange, which is determined by the temperature difference. The measuring system in the power-compensated DSC, where the heat flow is compensated with energy provided by electric current, consists of two identical microfurnaces, each one with a temperature sensor, located inside a thermostated aluminium block. To follow the specific heating rate, the same heating power is supplied to both of them, so that when a phase transition occurs, a temperature difference between the microfurnaces is appreciated. This temperature difference is due to both the measurement signal and the input signal of a second control circuit, which compensates most of the heat flow rate. This is achieved by increasing or decreasing the power supplied to the sample furnace with a heating power proportional to the remaining temperature difference. [3,17]

The DSC technique has been used to determine the two types of phase transition temperatures of the samples. First order phase transitions, involving structural transformations, are seen in the heat flow – temperature curve as a peak, whose area corresponds to the heat gained or lost by the sample. The magnetic phase transitions, which are second order phase transitions, lead to a change in the baseline of the curve.

The equipment used is a DSC 2920, TA Instruments, New Castle, DE, USA, located at the Universitat de les Illes Balears, in Mallorca, Spain.

2.3. MAGNETIC CHARACTERIZATION OF MSMAs

2.3.1. Vibrating Sample Magnetometer (VSM)

A Vibrating Sample Magnetometer (VSM) is a device for magnetic characterization based on the detection of the dipolar magnetic moment induced in a material in the presence of an even magnetic field. If the sample is vibrating with a specific sinusoidal motion, a sinusoidal electric signal is induced in the detection coils (the pickup coils) with the same vibration frequency of the sample. Its amplitude is proportional to the magnetic moment, the amplitude and the relative position of the sample and the detection coils. These magnetometers are regularly used to measure the magnetic moments of the sample as a function of the temperature and the applied magnetic field. Their popularity is attributed to their high sensitivity to magnetization changes while allowing for a quick and easy measurement of a wide variety of magnetic samples. [9,18]

The experimental set-up (pictured and schematized in **Figure 2.7**) consists in a vibrating sample fixed to a non-magnetic sample holder placed in the airgap of an electromagnet, with four detection (pickup) coils situated at the poles of the magnetic field generator. The sample holder is attached to an electromechanical transductor, responsible of generating the vibration of the sample. Its movement is controlled by an oscillator and translated to the sample holder by a transducer assembled in a vertical position, perpendicular to the magnetic field. Therefore, the sample vibrates with a given frequency and amplitude, inducing a voltage in the aforementioned coils. This induced voltage signal is described by **Equation 2.2**,

$$V = -NS\frac{dB}{dT} = -NS\frac{d(B_{ext}+g(t)\Delta_m)}{dt} \qquad \textit{Equation 2.2}$$

where *g(t)* is a function related to the position of the sample, *N* is the number of wire turns in the coil, *T*, the temperature, *S* is the transversal coil area, *m* corresponds to the magnetic moment of the sample, *B* to the applied external magnetic field, and *t* to the time.

The detected voltage signal is measured through a differential amplifier, followed by a tuned amplifier and, finally, through a lock-in amplifier using the voice coil drive signal as reference. The outcome signal of this last amplifier, a direct current

signal exclusively proportional to the magnetic moment of the sample, corresponds to the outcome signal of the magnetometer.[3,9,18]

For the experimental part of this thesis, two different Vibrating Sample Magnetometers were used: a homemade one (**Figure 2.7**) and a commercial one. The homemade VSM, located at the Science and Technology Faculty of the University of the Basque Country, works with a frequency of 63Hz and can apply magnetic fields up to 1.8T. The temperature can be varied from 123 to 773 K by a heating electric resistance and a cooling system consisting on a continuous N2 gas flux circulating through a liquid N2 vessel. The temperature control system is analogous to the commercial one, a MicroSense Inc Vibrating Sample Magnetometer, located at BCMaterials. This equipment can apply magnetic fields up to 2T and operate in a 100-500 K temperature range.

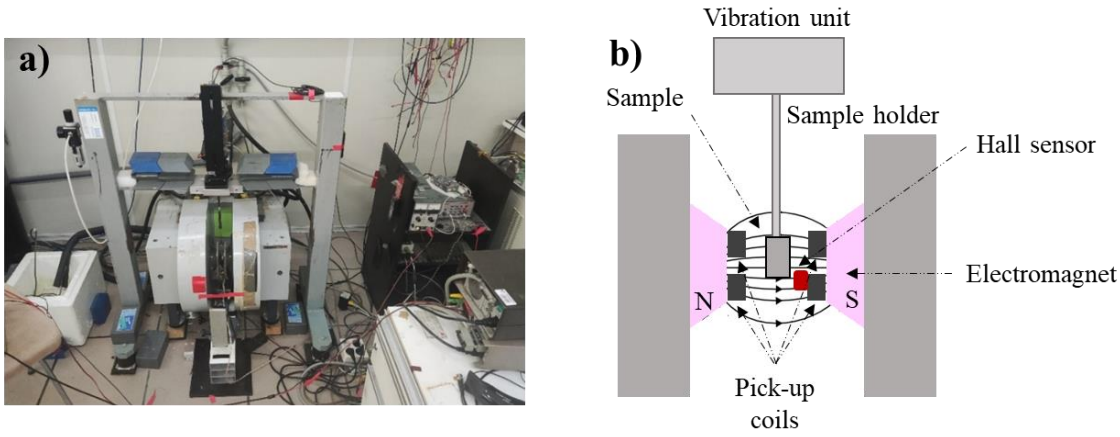

Figure 2.7. *a) Homemade Vibrating Sample Magnetometer and b) schematic image of the operational set-up.*

2.3.2. Superconductive Quantum Interference Device (SQUID)

A Superconductive Quantum Interference Device (SQUID) magnetometer is a very sensitive magnetometry tool based on superconducting loops containing Josephson junctions. The measurement procedure is based on the extraction technique, and starts with a sample placed in the centre of a detection coil which moves following a vertical path, causing a change in the voltage running through the coil. The supercurrent created in this detector coil as a result of the Cooper pairs going through the loops by tunnel effect crosses another coil, known as the entrance coil,

inducing a magnetic flux that is measured by the SQUID magnetometer. Therefore, small changes in the magnetic behaviour of the sample can be detected. The high sensitivity is the main advantage of the SQUID compared to the VSM, 10^{-8} vs 10^{-6} emu.[3,9,18]

The aforementioned created supercurrent is described by **Equation 2.3**, being δ the phase difference between the wave function describing the quantum behaviour of the pairs in each side of the juncture.

$$J = J_0 sin\delta \qquad \textbf{\textit{Equation 2.3}}$$

While J_0 is only dependant on the juncture structure, the phase difference δ depends on the potential applied to each end, following the **Equation 2.4**. The current, J, can be independent of the time or related following a periodic modulation, resulting in $V = 0$ (Josephson DC effect) or $V \neq 0$ (Josephson AC effect), respectively.

$$\frac{d\delta}{dt} = \frac{2eV}{\hbar} = \frac{2\pi V}{\phi_0} \qquad \textbf{\textit{Equation 2.4}}$$

The current passing through the junctures is periodically related to the magnetic flux in the loops (**Equation 2.5**).

$$J = J_0 sin\delta cos\left(\frac{e\phi}{\hbar}\right) + \frac{2V}{R} \qquad \textbf{\textit{Equation 2.5}}$$

Therefore, the I - V curves depend on the magnetic flux. The most widely used SQUID, the SQUID DC, consists in a fixed current, I_0, going through the device, while the change in the voltage as a function of the magnetic flux is measured. I_0 is selected to maximize the voltage amplitude.[3,9,18]

In this thesis a Quantum Design MPMS-7 SQUID, belonging to the General Research Services (SGIKER) of the University of the Basque Country, was employed, allowing to measure in a 1.7 - 400 K temperature range and with applied fields up to 7T.

2.4. MECHANICAL PROPERTIES CHARACTERIZATION

2.4.1 Micromechanical testing device

A micromechanical testing device is designed to measure the force and displacement induced in a sample that undergoes compression tests. The sample is placed in between a sensor and a plate. This plate is moved by an electric motor, and the sample is compressed while pushing the plate. The sensor allows to measure the force of the compression, while the micrometer attached to the motor measures the displacement undergone by the plate with high precision. Therefore, the stress and strain induced and suffered by the sample can be correlated.

All the stress-strain curves presented in this thesis were obtained employing a homemade device, pictured in **Figure 2.8** and located at the Boise State University, in Idaho, USA.

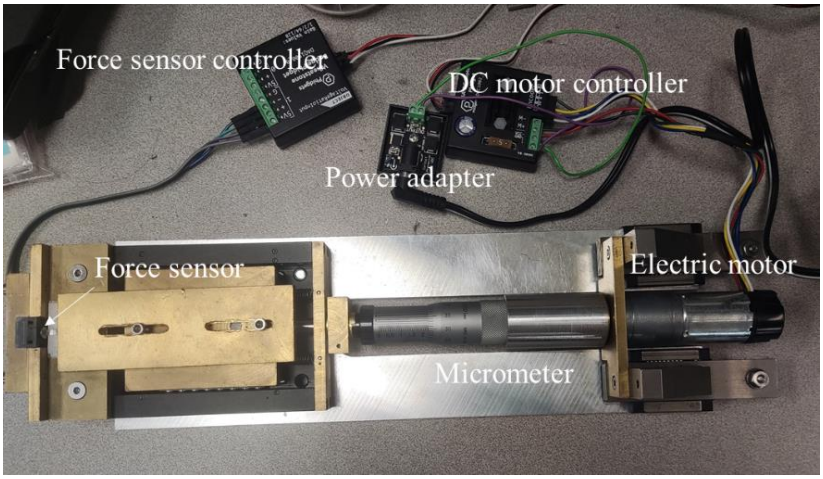

Figure 2.8. *Micromechanical testing device and its key parts.*

2.4.2. Micropeening station

The micropeening station is an equipment employed for the patterning or treatment of a surface via glass nanoparticles, known as the peening media. The set-up (**Figure 2.9**) consists of a sand-blasting cabinet containing a motorized linear stage, where the sample holder is located, and a small air eraser device, combined with the peening media holder. When a pneumatic valve is opened, the air eraser atomizes a hopper of the media, so the glass nanoparticles pass through the nozzle and reach the stage. The

sample is attached to a magnet placed in this stage. Then, a lineal movement is drawn by a motor, so that the stage is moved, and the air stream reaches the sample.

By a regulator control, the pressure supplied to the air eraser can be controlled and, hence, the force the particles hit the sample with, modified. Since the sample is magnetically linked to the stage, the sample needs to be below its Curie temperature to ensure that it remains unmovable, limiting the maximum temperature that the sample can reach during this process. A Peltier module and a NI-TC01 thermocouple are placed inside the cabinet to control and measure the stage temperature, respectively.

The work presented in this dissertation was carried out by employing a homemade micropeening station, located at the Boise State University, in Idaho, USA.

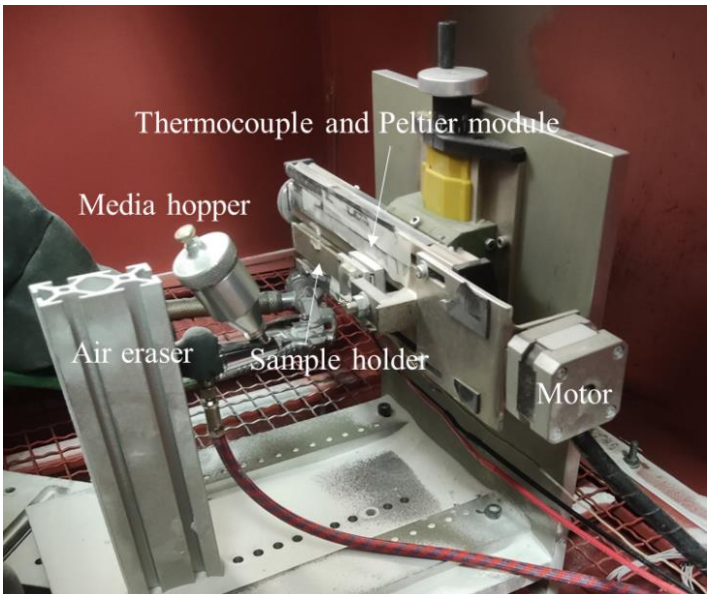

***Figure 2.9**. Homemade micropeening station and its key part*

2.5. BIBLIOGRAPHY

1. Frenzel J, Zhang Z, Neuking K, Eggeler G. High quality vacuum induction melting of small quantities of NiTi shape memory alloys in graphite crucibles. *J Alloys Compd*. 2004;385(1-2):214-223. doi:10.1016/j.jallcom.2004.05.002

2. Davies EJ. *Conduction and Induction Heating*. IET; 1990. doi:10.1049/PBPO011E

3. Pérez-Checa A. *Development of New Ni – Mn – Ga Based High Temperature Shape Memory Alloys*. Universidad del País Vasco/Euskalherriko Unibertsitatea; 2019.

4. Arun S, Radhika N, Saleh B. Advances in vacuum arc melting for high entropy alloys: A review. *Vacuum*. 2024;226(January):113314. doi:10.1016/j.vacuum.2024.113314

5. Tatar C, Acar R, Qader IN. Investigation of thermodynamic and microstructural characteristics of NiTiCu shape memory alloys produced by arc-melting method. *Eur Phys J Plus*. 2020;135(3):1-11. doi:10.1140/epjp/s13360-020-00288-w

6. Rodríguez-Crespo B, Río-López N., Lázpita P, et al. Impact of magnetic, atomic and microstructural ordering on the magnetocaloric performance of powdered NiCoMnSn metamagnetic shape memory ribbons. *Mater Des*. Published online 2024:113279. doi:10.1016/j.matdes.2024.113279

7. Rong C, Shen B. Nanocrystalline and nanocomposite permanent magnets by melt spinning technique. *Chinese Phys B*. 2018;27(11). doi:10.1088/1674-1056/27/11/117502

8. Budhani RC, Goel TC, Chopra KL. Melt-spinning technique for preparation of metallic glasses. *Bull Mater Sci*. 1982;4(5):549-561. doi:10.1007/BF02824962

9. Rodríguez-Crespo B. *Development of Heusler-Alloy-Based Magnetoaloric Inks for 2D-3D Printing*. University of the Basque Country; 2024.

10. Cejpek P, Straka L, Veis M, et al. Rapid floating zone growth of Ni2MnGa single crystals exhibiting magnetic shape memory functionality. *J Alloys Compd*. 2019;775:533-541. doi:10.1016/j.jallcom.2018.10.113

11. Vlášková K, Proschek P, Pospíšil J, Klicpera M. Low-temperature study of an Er2Ti2O7 single crystal synthesized by floating zone technique and simplified feed rod preparation route. *J Cryst Growth*. 2020;546(May). doi:10.1016/j.jcrysgro.2020.125783

12. Abd Mutalib M, Rahman MA, Othman MHD, Ismail AF, Jaafar J. *Scanning Electron Microscopy (SEM) and Energy-Dispersive X-Ray (EDX) Spectroscopy*. Elsevier B.V.; 2017. doi:10.1016/B978-0-444-63776-5.00009-7

13. Brouw P. *Theory of XRF*.; 2010.

14. Li F, Ge L, Tang Z, Chen Y, Wang J. Recent developments on XRF spectra evaluation. *Appl Spectrosc Rev*. 2020;55(4):263-287. doi:10.1080/05704928.2019.1580715

15. Helliwell JR, Harrop S, Habash J, et al. Instrumentation for Laue diffraction (invited). *Rev Sci Instrum*. 1989;60(7):1531-1536. doi:10.1063/1.1140977

16. Amorós J., M.J B, Canut de Amorós M. *The Laue Method*. Acadedemic Press; 1975.

17. Janovszky D, Sveda M, Sycheva A, et al. Amorphous alloys and differential scanning calorimetry (DSC). *J Therm Anal Calorim*. 2022;147(13):7141-7157. doi:10.1007/s10973-021-11054-0

18. Lázpita P. *Transiciones Magnéticas y Estructurales En Aleaciones Ferromagnéticas Con Memoria de Forma*. Universidad del País Vasco/Euskalherriko Unibertsitatea; 2008.

CHAPTER 3
Neutron Diffraction Techniques

3.1 INTRODUCTION TO NEUTRON SCATTERING

Neutron scattering techniques are widely used in materials science due to their versatility and multidisciplinary character. The basis of neutron scattering consists on the measurement of the intensity of a scattered neutron beam after it has passed through the sample. Due to having no charge and an electric dipole equal to zero, the neutron is non-destructive and penetrates deeply into matter. The fact that they interact with the atomic nuclei via short-range nuclear forces, rather than electric forces, allows them to scatter light elements with a measurable scattering cross-section and to differentiate isotopes and elements with similar atomic numbers (see **Figure 3.1**). As a result, neutron scattering techniques present an advantage over other techniques based on charged particles and electric forces' interactions (X-Rays, electron diffraction, etc).

In addition, neutrons can probe not only the nuclear structure of materials, but also their magnetic properties. This is a consequence of neutrons havimg a net magnetic moment, what causes magnetic interactions with the magnetic moments created by unpaired electrons in the sample, resulting in magnetic scattering events.[1–3]

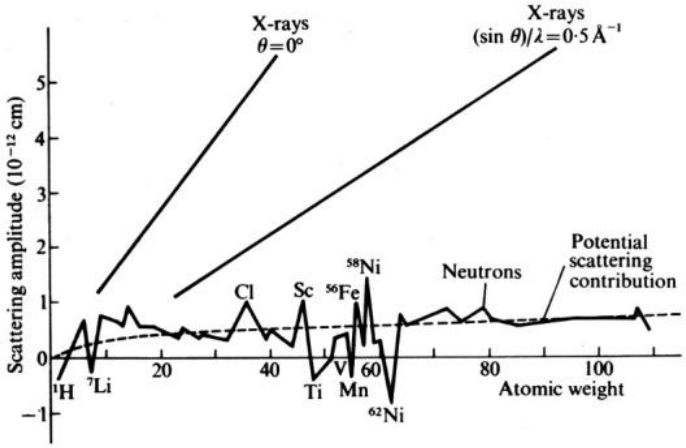

Figure 3.1. *Correlation between the scattering amplitude of neutrons and x-rays and the atomic weight of the atoms from which they are scattered. Figure adapted from*[4]

Neutrons possess not only the characteristics readily associated with particles (mass, charge, spin, magnetic moment), but also the attributes of a wave (such as wavelength and frequency). Following the quantum physics theory and the correlated wave-particle duality,[5,6] those properties can be combined to describe the moving wavelength, as shown in **Equation 3.1**, where λ is the wavelength, m, the mass of the neutron, v corresponds to the velocity of the neutron and $\hbar$ is the reduced Planck constant.

$$\lambda = \frac{2\pi\hbar}{mv} \qquad \textit{Equation 3.1}$$

This wavelength relates to the neutron energy by the Planck-Einstein equation (**Equation 3.2**, where h is the Planck constant and c, the speed of light), since the theory of neutron scattering from condensed matter is developed assuming a monochromatic beam. Neutrons that have reached thermal equilibrium at room temperature present kinetic energies comparable with typical thermal ejections of atoms in condensed matter, making them a powerful tool to study both the atomic-scale structure and the atomic-scale dynamics in a wide-range of materials.[6–9]

$$E = \frac{hc}{\lambda} \qquad \textit{Equation 3.2}$$

Two main groups are usually employed to classify the neutron scattering facilities: fission reactors and spallation sources (see **Figure 3.2**). The first ones are based on the nuclear fission process, where a heavy nucleus, typically ^{235}U, absorbs a neutron and, as a consequence, splits into two lighter nucleus and releases an average of 2.4 neutrons of about 2 MeV each. Due to the arrangement of the core of a nuclear reactor, these released neutrons induce additional fission processes by colliding with other nuclei, creating a chain reaction. In order to employ these neutrons in a scattering experiment, their energy is reduced to less than 1eV via collisions with a moderator substance until thermal equilibrium is reached. Therefore, their kinetic energy is determined by the nature (e.g. material) and temperature of the moderator, and the neutrons emerging from them are named cold, thermal and hot depending on their final energy after leaving the moderator (see **Table 3.1**). To determine the wavelength of the outcoming flux, a monochromator is used, such as Ge(311) at D1B or Cu(200)

at D20, which are neutron diffractometers located at the Institute Laue-Langevin (ILL), in Grenoble, France, which is one of the best-known reactor sources.[6,7,10]

Table 3.1. *Classifications of the neutrons, depending on their energy, temperature and wavelength.*

Neutrons	Energy (meV)	Temperature (K)	Wavelenght (Å)
Cold	0.1 - 10	1 -120	4 - 30
Thermal	5 -100	60 - 1000	1 - 4
Hot	100 - 500	1000 - 6000	0.4 -1

Spallation sources, on the other hand, produce neutrons by bombarding a heavy nucleus with high energy protons. These protons are produced by an ion source, fed with both hydrogen gas and hot caesium vapour, forming a discharged plasma as a result. The caesium cations are attracted towards the cathode surfaces, acting as electron donors to the positively charged hydrogen ions, thus enhancing H- ion production[11]. Pulses of protons are then extracted and accelerated by a synchrotron, cyclotron or linear accelerator, travelling at speeds close to the speed of light until they reach the spallation target. This target, made of a heavy metal with high neutron yield upon being hit by an accelerated proton, such as lead, mercury or tungsten, is put on a temporary highly excited state upon being hit by the protons, which rapidly decays. The de-excitation process results into several decay products, including lighter nuclei and neutrons. The energy associated to the resultant neutron beam is reduced in moderators, as previously mentioned. Unlike reactor sources, where a continuous flux of neutrons is produced, spallation sources produce ~100μs pulses of neutrons with a 10-60 Hz frequency, depending on the specific neutron source. This variety of frequencies results into a spread of energies and speeds, with the faster neutrons arriving to the detector before the slower ones. The speed of the neutrons is measured by the measurement of their flight time over a known distance. This is the method employed by the ISIS Neutron and Muon Source, located in Oxfordshire, UK.[6,7,10,11]

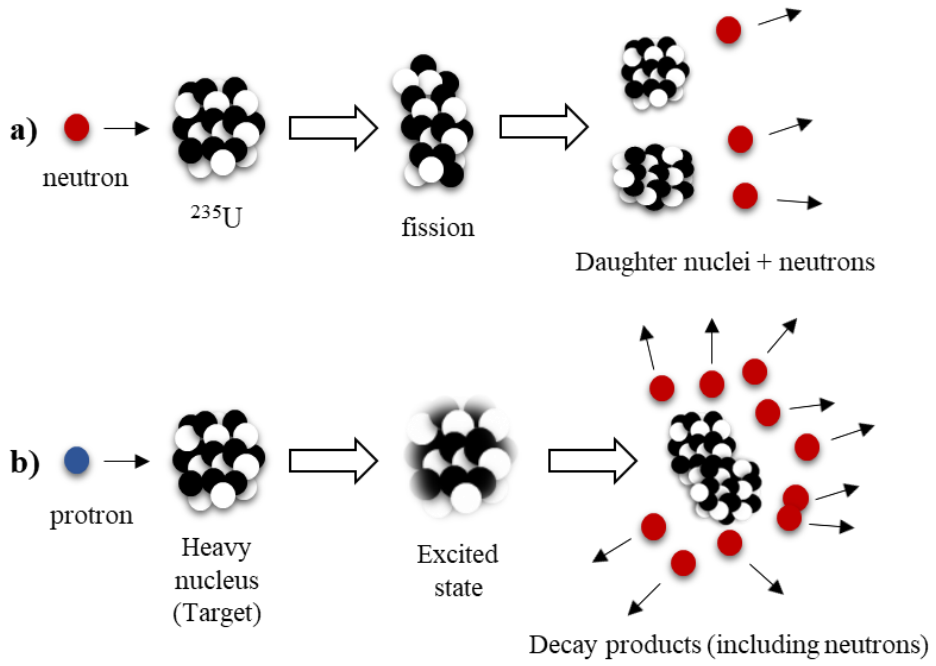

***Figure 3.2**. Visual representation of the two main methods of neutron production: a) fission reactors and b) spallation sources.*

Neutron scattering events can be classified into two main groups depending on the presence of energy transfer to the atoms: elastic and inelastic, employed to study the structure and the lattice dynamics of the materials, respectively. When a neutron with initial wavevector $\boldsymbol{k}_i$ and energy E_i is scatters under an angle 2θ with the material (see **Figure 3.3**), their wavevectors and angle change to $\boldsymbol{k}_f$ and E_f, respectively. The momentum transfer vector, $\boldsymbol{Q}$, can be expressed as **Equation 3.3**, while the energy transfer is described by **Equation 3.4** as follows:

$$\boldsymbol{Q} = \boldsymbol{k}_i - \boldsymbol{k}_f \qquad \textit{Equation 3.3}$$

$$\hbar w = E_i - E_f \qquad \textit{Equation 3.4}$$

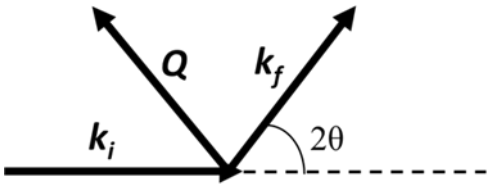

***Figure 3.3.** Representation of the moment transfer **Q** and its relation with the initial ($\boldsymbol{k}_i$) and final ($\boldsymbol{k}_f$) moments.*

A scattering process is elastic if $E_i = E_f$, and inelastic if $E_i \neq E_f$. Elastic scattering is used to unravel the structure of the sample, and the change in the trajectory of the beam upon being scattered from the sample is analysed. Inelastic scattering provides information about the dynamic processes present in the sample, associated with specific changes in energy. In this thesis we will focus on elastic scattering processes and, more specifically, in diffraction processes. The lack of energy exchange in the materials can be explained by considering the neutrons to be scattered by an isolated nucleus rigidly bound to its surroundings. When the incident neutron beam reaches the fixed nuclei, neutron-nucleus interactions happen and a scattered wave (beam) is produced. This wave is considered to be spherical due to the nuclear force being strong, isotropic, short-range, and the incident neutrons' wave is practically unaffected by the interaction[6,12].

To characterize the structure of the material by means of an elastic neutron scattering process, the measurement of the intensity of the scattered neutron beam with high precision is mandatory. The easiest and most common way to calculate absolute intensities is to express the scattering process as a *cross-section*, which can be defined as the effective area of the material that the neutrons must hit in order for a particular scattering process to take place. The terms *Total scattering cross-section* and *differential scattering cross section* are used to express the ability of a particular atom to scatter a neutron beam, being the former the probability of neutrons to change their energy or direction in any way (**Equation 3.5**) and the latter, the scattering in a given direction (**Equation 3.6)**:

$$\sigma_s = \frac{total\ number\ of\ neutrons\ scattered\ per\ second}{\phi_0} \qquad \textbf{Equation 3.5}$$

$$d\sigma_s = \frac{number\ of\ neutrons\ scattered\ per\ second\ into\ \mathrm{d}\Omega\ about\ a\ given\ direction}{d\Omega} \qquad \textbf{Equation 3.6}$$

Where ϕ_0 is the incident neutron flux and $d\Omega$, the solid angle, a three-dimensional analogous of the scattered angle. As previously mentioned, the scattered waves (beams) are considered to be spherical. Therefore, the scattered cross-section equals to 4π multiplied by the square of the scattering length density, b, being this a

very extended way to express the scattering ability of the neutron beam by a particular atom. It is characteristic of the nucleus, being different for different isotopes of the same element. Moreover, it is independent of *Z*, the number of protons of the atom, and is tabulated.[13] While this scattered cross-section definition is widely used, it only applies to coherent scattering, that will be described hereafter.

The second possible classification of neutron scattering processes arises from the nature of the neutron beam: coherent and incoherent scattering. In the former, the neutrons of a beam dispersed by the atoms are in phase and interfere with each other, while in the latter they are randomly distributed. Hence, coherent scattering depends on the position of the atoms relative to each other, providing information about the structure of the sample, while incoherent scattering is only affected by the nature of the atoms that are present, and not by their spatial distribution. While inelastic scattering is highly employed for molecular dynamics studies, it can be disregard in the majority of experiments aiming structural determination.[6,14]

While so far only nuclear interactions with matter have been described, the magnetic moment of the neutrons triggers the possibility to investigate magnetic interactions between the neutron and the electron clouds of the sample. Consequently, the magnetization distribution of the studied samples can be investigated. More specifically, complex magnetic structures can be unravelled by coherent elastic scattering, while the coherent inelastic scattering contains information about the collective magnetic excitations, the magnons.[15–17]

The characteristic magnetic dipole moment, μ_n, of the neutron is described by **Equation 3.7**, where s_n is the spin quantum number, μ_N = 5.051 x 10-27J·T^{-1} is the nuclear magneton and the constant γ equals to 1.913

$$\mu_n = -2\gamma\mu_N s_n \qquad \textit{Equation 3.7}$$

Since neutrons have a spin quantum number s_n = ½, the allowed values of spin angular momentum in quantum mechanics are +½ħ (or "*spin up"*) and -½ħ (or "*spin down"*), which define the polarization states of the neutron. If the spins of a neutron beam are randomly oriented, the beam is unpolarised, while if their spin direction is

fixed, as determined by an applied external magnetic field, it is polarized. The polarization of the beam is described by the vector ***P***, whose component *Pα* isdescribed following **Equation 3.8**, and depends on the number of spin up and spin down neutrons (n_α and $n_{\bar{\alpha}}$, respectively) with respect to the α direction.

$$P_\alpha = \frac{n_\alpha + n_{\bar{\alpha}}}{n_\alpha - n_{\bar{\alpha}}} \qquad \textit{Equation 3.8}$$

The polarization is a consequence of the presence of a magnetic field of flux density ***B***, that exerts a torque ***T*** on the magnetic moment of the neutron**.** As it can be deduced from **Equation 3.9**, if the magnetic field is parallel to the magnetic dipole, the latter is unaffected by the field, and a polarized beam is obtained.[6]

$$\boldsymbol{T} = \mu_n \, x \, \boldsymbol{B} \qquad \textit{Equation 3.9}$$

With the so-called *flipping ratio* measurement method, the beam is polarized either parallel or antiparallel to the vertical axis of the sample and, therefore, two different scattering intensities, I^+ and I^- are obtained, instead of an integrated intensity. The flipping ratio is the ratio between them, calculated as shown in **Equation 3.10** and its simplified version, **Equation 3.11**.

$$R(Q) = \frac{I^+}{I^-} = \frac{F_N^2 + 2Pq^2F_NF_M + q^2F_M^2}{F_N^2 - 2Pq^2F_NF_M + q^2F_M^2} \qquad \textit{Equation 3.10}$$

$$R(Q) = A\left(\frac{F_M}{F_N}\right)^2 + B\frac{F_M}{F_N} + C \qquad \textit{Equation 3.11}$$

where *R(Q)* are the experimentally measured flipping ratios and *A*, *B* and *C* are coefficients derived from transforming **Equation 3.10** into **Equation 3.11.** F_N and F_M correspond to the nuclear and magnetic structure factors, respectively, defined as the sum of the contribution from all the atoms to the scattering of the beam in nuclear and magnetic scattering events, respectively. If the nuclear structure factors are known from an unpolarized neutron diffraction experiment, the magnetic structure factors can be extracted from the measured flipping ratios upon finding the correct fitting models.[17–19]

3.2 NEUTRON DIFFRACTION EXPERIMENTS

3.2.1. Introduction to Neutron Diffraction

Elastic neutron scattering techniques can be classified into three subgroups: neutron imaging, large scale structures and neutron diffraction. In this thesis, we will focus on neutron diffraction techniques, which are based on coherent elastic scattering events, both employing polarised and unpolarised neutron beams. Depending on the state of the sample, the diffraction techniques can be distinguished as Powder Neutron Diffraction, PND, and Single Crystal Neutron Diffraction, SCND.

The theory of neutron diffraction techniques is intimately linked to the elementary concept of crystallography. For the sake of simplicity, the static approximation, i.e. the structures are perfectly rigid and there is no energy transfer, is applied. Considering a crystalline sample, its "rigid" atoms are arranged following a periodic structure. The repeating periodic arrangement of atoms is known as the unit cell, and it can be characterized by three lattice parameters (*a*, *b*, *c*) and three angles (α, β, γ), as it is visually depicted in **Figure 3.4**. As shown in **Table 3.2**, the relationships between them lead to different types of unit cells, also known as lattice systems.

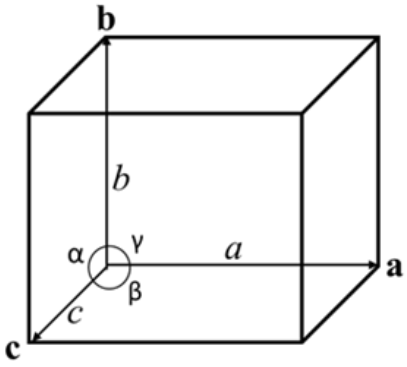

***Figure 3.4**. Parallelepiped-shaped unit cell and its unit cell features.*

***Table 3.2**. Lattice systems, along with the features of the lattice parameters of their unit cells.*[6]

Lattice system	Lattice parameters	
Triclinic	$a \neq b \neq c$	$\alpha \neq \beta \neq \gamma$
Monoclinic	$a \neq b \neq c$	$\alpha = \gamma = 90°, \beta \neq 90°$
Orthorombic	$a \neq b \neq c$	$\alpha = \beta = \gamma = 90°$
Tetragonal	$a = b \neq c$	$\alpha = \beta = \gamma = 90°$
Rhombohedral	$a = b = c$	$\alpha = \beta = \gamma \neq 90°$
Hexagonal	$a = b \neq c$	$\alpha = \beta = 90°, \gamma = 120°$
Cubic	$a = b = c$	$\alpha = \beta = \gamma = 90°$

To describe the position of an atom in the unit cell (*x*, *y*, *z*) coordinates are used, meaning that the atom is displaced from the origin by the vector $x\mathbf{a} + y\mathbf{b} + z\mathbf{c}$. Since these atoms are periodically arranged, crystallographic planes can be described. The Miller indices (*hkl*) represent a set of planes intersecting the characteristic unit cell axes (**a**, **b**, **c**) at *a/h*, *b/k*, *c/l*, respectively (**Figure 3.5**).

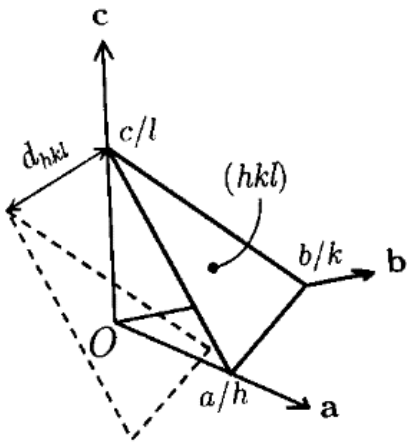

***Figure 3.5.** Representation of crystal planes and inter-planar spacing by Miller indices (hkl).Figure taken from*[6]

Considering a set of crystallographic planes with Miller indices *hkl*, the space between adjacent planes can be described as $d_{hkl.}$ When a neutron beam reaches a crystalline material, the planes scatter the incident neutron beam with an angle equivalent to the incident neutron beam angle, θ_B (see **Figure 3.6**). When the path differences between reflected waves are a whole number *n* of incident neutron beam

wavelengths, λ, the reflected waves interfere in a constructive manner, and the Bragg law (**Equation 3.12**) is fulfilled.

$$n\lambda = 2d\ sin\theta \qquad \textbf{Equation 3.12}$$

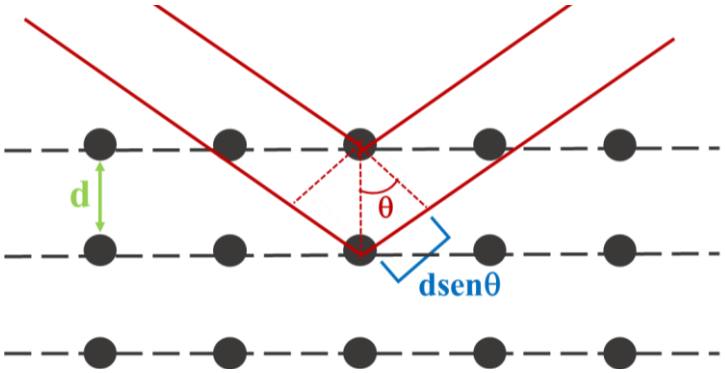

***Figure 3.6**. Diffraction of an incident neutron beam by a set of parallel planes separated a distance* d *between them.*

Polarized neutron diffraction allows to separate nuclear and magnetic scattering and, hence, the determination of the magnetic crystal structure. Since a magnetic structure is a periodic arrangement of magnetic dipole moments, there is some kind of directionally-favoured magnetic coupling, and a magnetic unit cell can be described.[7,10]

3.2.2. Powder Neutron Diffraction, PND

Powder Neutron Diffraction is a neutron diffraction technique performed on polycrystalline samples, either in powder or small crystals shape, with the individual micro crystals being oriented in every possible direction with equal probability (in the ideal case of non-textured samples). The neutron beam reaches the sample and is reflected following the Bragg law, forming to the so-called Debye-Scherrer rings on a two-dimensional detector. A cut through these rings results into a one-dimensional powder diffractogram (**Figure 3.7**), whose analysis allows for a quantitative study of several different crystal phases and to determine the crystal structures, atomic substitutions and vacancies, together with phase transformations and other related crystal structure properties. The position of the Debye-Scherrer rings gives information about the unit cell and its symmetry, while the intensity of the reflections is linked to the contents (atomic species) of the unit cell.[21,22]

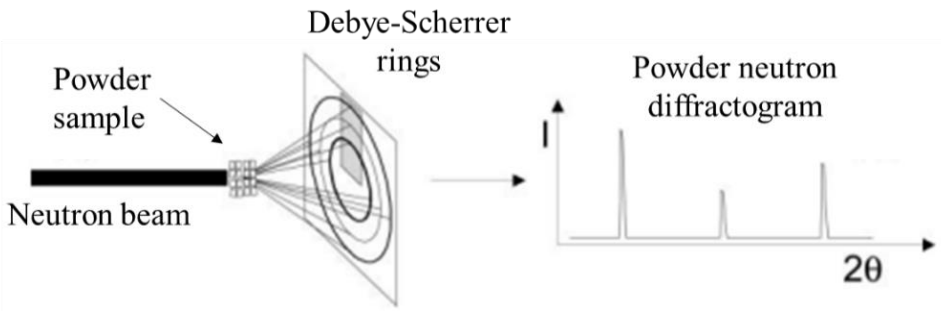

Figure 3.7. *Diffraction from a polycrystalline sample with the cross-section of the Debye-Scherrer rings. Figure taken from*[21]

Even though there are many different powder neutron diffraction set-ups, all of them share some common features, and typically employ neutron beam wavelengths between 0.1 and 5 Å, comparable to the spacings between lattice planes in crystals. Below, the different powder neutron diffractometers employed in the thesis work presented are described.[4,6,23,24]

D1B – HIGH INTENSITY TWO-AXIS POWDER DIFFRACTOMETER (ILL)

D1B is a two-axis diffractometer (**Figure 3.8**) employed for experiments aiming to determine atomic and magnetic crystal structures, which is located at the Institute Laue-Langevin (ILL). The dedicated sample environment available to measure at D1B, and in particular the set of cryostats and furnaces available through the sample environment team at the ILL, allows the user to measure samples in temperatures between 1.5 and 1200 K.

During a experiment, a white thermal neutron beam is diffracted by the monochromator, therefore obtaining a monochromatic beam with a fixed neutron wavelength. Depending on the monochromator used, Germanium (311) or pyrolytic graphite (002), D1B can provide with either 1.28 Å or 2.52Å neutron wavelenghts, rspectively. Once monochromatized, the beam reaches the vanadium can containing the powder sample and is diffracted by it. The resulting Bragg reflections are measured by a multidetector and a diffraction pattern is collected. The parasitic diffraction beams from sample enviroment devices are eliminated thanks to the Radial Oscillating Collimator (ROC) situated in between the sample and the detector.[25,26]

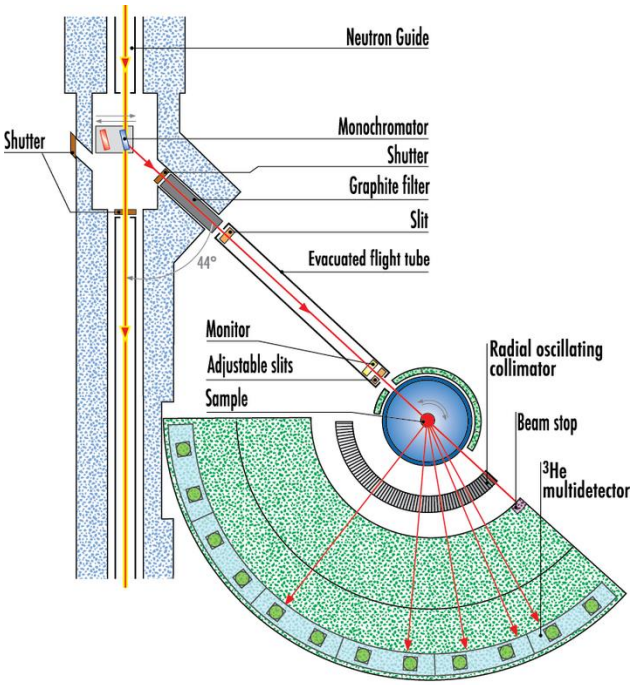

***Figure 3.8**. High Intensity Two-Axis Powder Diffractometer D1B located at the Institute Laue-Langevin, Grenoble, France.*[26]

D20 - HIGH INTENSITY TWO-AXIS DIFFRACTOMETER WITH VARIABLE RESOLUTION (ILL)

D20 is a two-axis diffractometer with a exceptionally high neutron flux, which allows for real-time experiments on very small samples (**Figure 3.9**). Among its advantages, the possibility to measure a complete high resolution diffraction pattern as a function of temperature or pressure oustands. The dedicated sample environment available is similar to that explained in the previous section for D1B, allowing the user to perform experiments in a wide range of temperatures, as previously discussed.

In this instrument, the monochromators available give the user the possibility to choose between four differenet wavelenghts, depending on the monochromator used: pyrolitrix graphite HOPG (002) to obtain a neutron beam with a wavelength of 2.4Å; Cu (200) for 1.3Å, Cu (200) in trasnmission geometry for 0.82 Å, 0.88 Å or 0.94Å, and Germanium (113) for variable waveleghts, depending on the take-off angle. The monochromatic beam is diffracted by the powder sample and the resulting Bragg reflections reach a large microstrip multidetector. The collected data is used to obtain a diffraction pattern. [26–28]

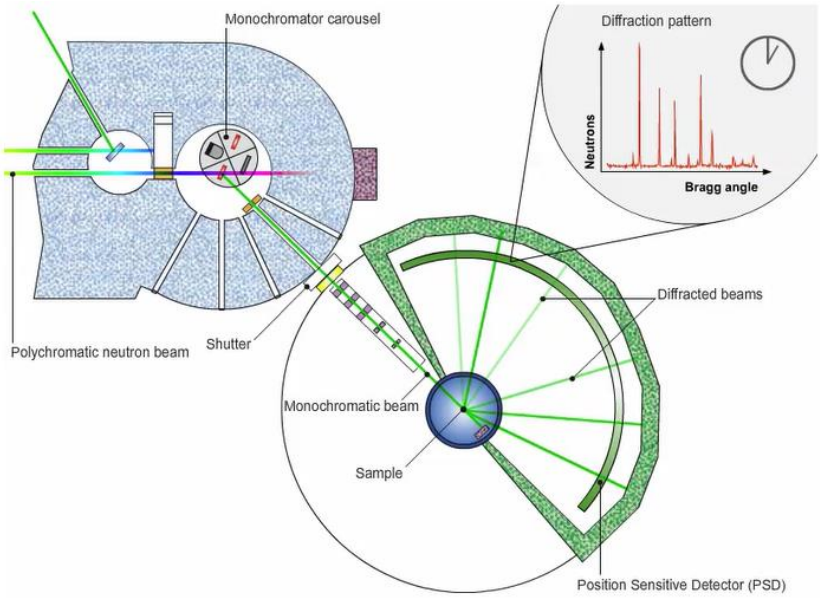

***Figure 3.9**. High Intensity Two-Axis Powder Diffractometer D20 located at the Institute Laue-Langevin, Grenoble, France.*[26]

3.2.3 Single Crystal Neutron Diffraction, SCND

This technique is employed to measure singe crystals, in which each set of planes from the sample diffracts in certain characteristic directions, and there is only one reflection for a plane set. In order to determine every set of planes of the crystalline structure, either an area detector can be employed, or the sample has to be rotated around one crystallographic axis when using a point detector.[1,29,30]

As well as with powder diffraction, the unit cell, space group, positions of the atomic nuclei, site occupancies and magnetic contribution to the Bragg peaks can be determined with this technique, being the latter a consequence of magnetic scattering events, as previously discussed.[6,31] For the single crystal structural analysis performed in this thesis, two different single crystal diffractometers of the ILL have been used: D9, for the atomic structure analysis, and D3 in its flipping ratios configuration, for the magnetic structure analysis.

D9 – HOT NEUTRON FOUR-CYCLE DIFFRACTOMETER (ILL)

This single crystal neutron diffractometer is used for precise and accurate measurements of Bragg intensities of single crystals up to very high momentum transfer, allowing for a detailed study of the atomic structure.

D9 presents a so-called standard "four-cycle geometry", which is based on an asymmetric full circle cradle sample holder, known as Eulerian cradle. Two circles (angles), φ and χ, are used to adjust the crystal orientation relative to the diffractometer axes. A third circle (angle), ω, sets the orientation of the crystal lattice planes to the diffraction position. Finally, the fourth circle (angle), 2θ, rotates the detector to the diffracted beam. A Cu(200) monochromator is employed to obtain a 0.83Å neutron wavelength. To measure at different temperatures, a furnace was mounted on the φ circle[26] (see **Figure 3.10**).

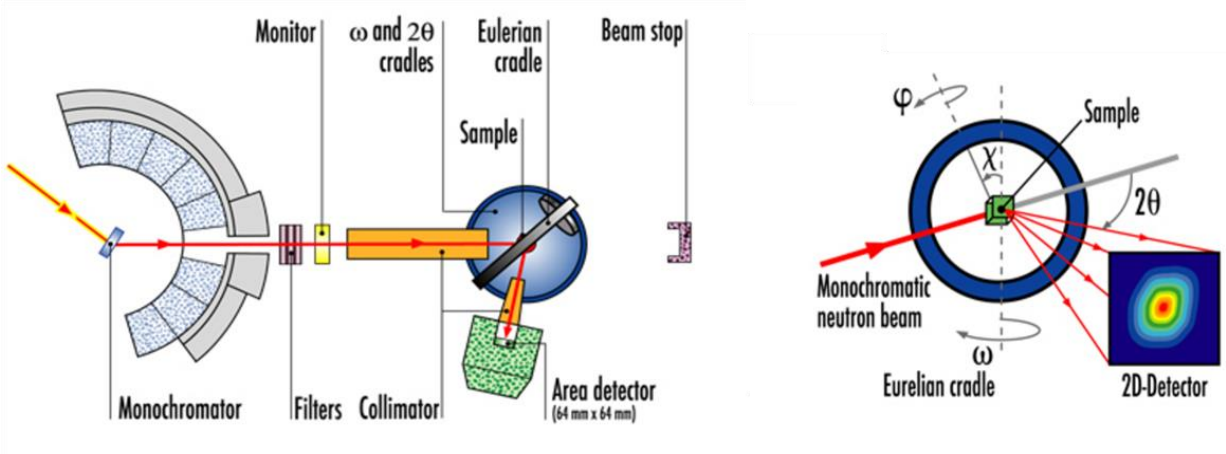

Figure 3.10 *a) Hot neutron four-cycle D9 located at the Institute Laue-Langevin, Grenoble, France. b) Schematics of the detector and the Eulerian cradle sample holder.*[26]

D3 – SPIN POLARIZED HOT NEUTRON BEAM DIFFRACTOMETER (ILL)

This diffractometer, depicted in **Figure 3.11**, offers three different set-ups (high-field, zero-field and non-polarized), making it a very versatile tool for magnetic structure analysis. The high-field configuration allows to determine magnetic form factors and magnetisation distributions, while the zero-field configuration is used to determine non-collinear magnetic structures and antiferromagnetic form factors. The last configuration is employed for the analysis of samples in hydrogenous liquids.

For the analysis displayed in this thesis, the high field set-up was used, where the sample is placed in a high magnetic field and its temperature is controlled by a cryostat. To obtain the selected wavelength, 0.83Å, and a stable polarization, a polarizing monochromator is used. This monochromator consists on exchangeable CoFe and Heusler polarizing monochromators displaced in a symmetric Laue geometry, while the polarization reversal is obtained by a cryoflipper. Therefore, two intensities are obtained for each Bragg reflection, each of them measured with one of the two polarization states of the beam, and the Fourier component of the magnetization distribution in the crystal is obtained from them. The obtained data is presented as flipping ratios, as described in **Section 3.1**. [2,26]

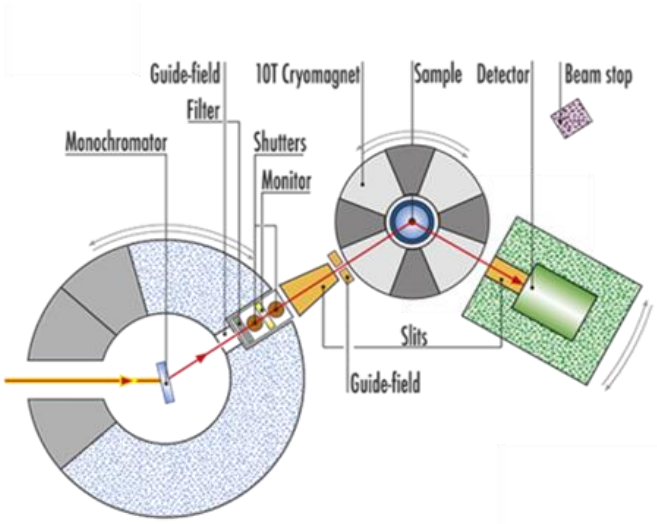

Figure 3.11 *Spin polarized hot neutron beam single crystal diffractometer D3 located at the Institute Laue-Langevin, Grenoble, France.*[26]

3.4. NEUTRON DIFFRACTION DATA ANALYSIS

3.4.1. Nuclear structure analysis

All the structural data presented in this thesis was obtained by refining unpolarized neutron diffraction data. Fullprof Suite[32], a program developed at the ILL for the refinement of diffraction data, was exclusively employed for this purpose.

To accomplish the refinements, the procedure requires two types of input files. The first one, a .dat or .int file, is the processed data obtained from the experiment ("clean" data from the diffractometers, in which data reduction has already been performed), while the second, a .pcr file, contains necessary information for the

analysis (measurement backgrounds, space groups, lattice parameters, resolution parameters, etc). A third input file, an .irf file containing information about the resolution parameters of the instrument, is desirable to be used, as it accounts for the specific data resolution associated with a particular diffractometer. With the help of a tool for visual representation, WinPLOTR, the processed data is represented as a relationship between the intensities and the measured diffraction angle (for PND) or diffraction planes (for SNCD), alongside with the diffractogram calculated based on the input parameters in the .pcr file. The refinement process is repeated by modifying specific input parameters until the represented diffractogram matches the experimental one. The quality of the fitting is generally expressed by the $\chi 2$ statistics parameter, which is reduced to a minimum value once the refinement process is good enough to match the experimental diffractogram. [32]

The data was analysed both via profile (pattern) matching and Rietveld analysis. The former, also known as the LeBail method, allows the determination of the lattice parameters, unit cells and space groups, with the approximate unit cell and resolution parameters as the sole starting information, while by the Rietveld analysis the atomic site occupancies and thermal parameters are also considered for the fitting.

The LeBail method fits the angular positions of the peaks displayed in the diffractogram using a least squares analysis. In opposition to the peak positions, that are constrained by the unit cell parameters, intensities are not affected by it. Therefore, they are calculated by **Equation 3.13**, where $y_i(obs)$ and $y_i(calc)$ are the observed and calculated intensities at each measured point, respectively, while I_{obs} corresponds to the total intensity of the peak.

$$I_{obs} = \frac{\sum y_i(obs) y_i}{y_i(calc)} \qquad \textbf{\textit{Equation 3.13}}$$

To start the calculation of the intensities, an arbitrary intensity starting value is established. After the first calculation is done, the refinement process continues by employing the obtained calculated factor as the experimental one. By this method, resolution parameters, peak widths and shapes, backgrounds and crystal unit cells are obtained.[24,32,33]

Rietveld analysis is a technique extensively used for the analysis of a crystallographic structure. Alongside with the parameters also determined via LeBail analysis, it is possible to determine the coordinates of every atom in the unit cell. It employs the non-lineal least squares method, requiring a good approximation of the starting parameter values to be fitted in order to avoid divergences when trying to fit them.

The powder neutron diffraction data refinements performed in this thesis consisted in fitting resolution parameters, peak widths and shapes, backgrounds and crystal unit cells via LeBail refinements, and atomic site occupancies via Rielveld refinements, using as starting points for each of them the corresponding successful LeBail refinements.[32,34] Nevertheless, there is no backgrounds or peak widths and shapes to be adjusted in SCND data, due to its characteristics. In an analogous way to PND, unit cell parameters and atomic site occupancies are acquired by fitting the positions of the reflections and their intensities.

3.4.2. Magnetic structure analysis

Once the nuclear structure is solved by Rietveld refinement, the magnetic structure may be resolved. In this dissertation, two different processes were employed for this goal: fitting data acquired at a phase presenting magnetic behaviour with a non-polarised beam, and fitting polarized neutron diffraction data acquired in the aforementioned D3 diffractometer. The first one was employed for powder alloys and the latter, for single crystals.

The magnetization densities in each atomic site of the crystal lattice of powder alloys are obtained by performing Rietveld refinements using Fullprof. In a similar fashion to the nuclear structure refinement, the refinement process of the magnetic structure of an alloy consists of modifying specific input parameters until the represented diffractogram matches the experimental one. The .pcr files contains, in addition to the necessary information for the nuclear data analysis, the information for the magnetic phase, such as magnetic space groups, magnetic form factors and values of the magnetic densities in each atomic site.

In order to determine the single crystal magnetic structure Mag2Pol[35] software was employed. To treat data obtained by the flipping ratio method, this program employs the least-squares method. Assuming spherical magnetization densities as a first approximation, the magnetization density in each atomic position is obtained by solving **Equation 3.11.** The structural form factors, F_N, are calculated by the program as an output from the Rietveld refinements performed to obtain the crystal structure of the sample, while the magnetic form factors, F_M, are the Fourier transformations of the magnetic scattering events between the neutrons and the the electron clouds of the sample. A physically meaningful solution to the latter is employed to extract the intensities and obtained the refined magnetic structure, via Fourier inversion, in an analogous way to the nuclear diffraction process. It must be mentioned that, opposite to the case of nuclear scattering, the magnetic scattering amplitude decays with 2θ (or with Q) due to the fact that the interaction potential is spread in space, what implies a non-constant Fourier transformation in Q-space, but instead decaying at high Q.[19,36,37] The quality of the refinement is expressed by the $\chi 2$ statistics parameter, in a similar way to Fullprof.

3.5. BIBLIOGRAPHY

1. Río-lópez NA, Lázpita P, Salazar D, et al. Neutron scattering as a powerful tool to investigate magnetic shape memory alloys: A review. *Metals (Basel)*. 2021;11(5):1-21. doi:10.3390/met11050829

2. Pérez-Checa A. *Development of New Ni – Mn – Ga Based High Temperature Shape Memory Alloys*. Universidad del País Vasco/Euskalherriko Unibertsitatea; 2019.

3. Bailey IF. A review of sample environments in neutron scattering. *Zeitschrift fur Krist*. 2003;218(2):84-95. doi:10.1524/zkri.218.2.84.20671

4. Bacon GE. *Neutron Diffraction*. Claredon Press; 1975.

5. Feynman RP, Leighton RB, Sands M, Lindsay RB. *The Feynman Lectures on Physics, Vol. 3: Quantum Mechanics* . Vol 19.; 1966. doi:10.1063/1.3047826

6. Boothroyd AT. *Principles of Neutron Scattering from Condensed Matter*. Oxford University Press; 2020.

7. Pynn R. *Neutron Scattering Primer*. Vol 19. Los Álamos Neutron Science Center; 1990.

8. Hippert F, Geissler E, Hodeau JL, Lelièvre-Berna E, Regnard JR. *Neutron and X-Ray Spectroscopy*.; 2006. doi:10.1007/1-4020-3337-0

9. Baruchel, J.; Hodeau, J.L.; Lehmann, M.S.; Regnard, J.R.; Schlenker C. *Neutron and Synchrotron Radiation for Condensed Matter Studies*. EDP Sciences - SPRINGER-VERLAG; 1994. doi:10.1007/978-3-662-22223-2

10. Willis BTM, C.J.Carlile. *Experimental Neutron Scattering*. Vol 39. Oxford University Press; 2009.

11. Www.isis.stfc.ac.uk. Webpage ISIS Neutron and Muon Source.

12. Casten RF. *Nuclear Structure From : Build Complex Structures*.

13. Ncnr.nist.gov. Website NIST Center for neutron Research.

14. Pynn R. The Mathematical Foundations of Neutron Scattering. *Neutron Scatt Prim*. Published online 1990:28-31.

15. Stewart JR, Ehlers G, Wills AS, Bramwell ST, Gardner JS. Phase transitions, partial disorder and multi-k structures in Gd 2Ti2O7. *J Phys Condens Matter*. 2004;16(28). doi:10.1088/0953-8984/16/28/L01

16. Fennell T, Bramwell ST, McMorrow DF, Manuel P, Wildes AR. Pinch points and Kasteleyn transitions in kagome ice. *Nat Phys*. 2007;3(8):566-572. doi:10.1038/nphys632

17. Stewart R. Polarized Neutrons - Lecture Notes. Published online 2013.

18. Ressouche E. Polarized neutron diffraction. *École thématique la Société Française la Neutron*. 2014;13:02002. doi:10.1051/sfn/20141302002

19. López-Garcia J, Recarte V, José C, Velamazán AR. Influence of microstructure in the martensitic transformation and in the physical and magnetic properties in metamagnetic shape memory alloys.

20. Pederson BA. Structure and Regulation of Glycogen Synthase in the Brain. *Adv Neurobiol*. 2019;23(January 2010):83-123. doi:10.1007/978-3-030-27480-1_3

21. Fucke K, Steed JW. X-ray and neutron diffraction in the study of organic crystalline hydrates. *Water (Switzerland)*. 2010;2(3):333-350. doi:10.3390/w2030333

22. Evans JSO, Evans IR. Beyond classical applications of powder diffraction. *Chem Soc Rev*. 2004;33(8):539-547. doi:10.1039/b316901b

23. Kisi, E.H. and Howard CJ. *Applications of Neutron Powder Diffraction*. Oxford Scinece Publications; 2012.

24. Dinnebier, R.E and Billinge SJL. Powder Diffraction: Theory and Practice. In: RSCPublishing; 2008.

25. Orench IP, Clergeau JF, Martínez S, Olmos M, Fabelo O, Campo J. The new powder diffractometer D1B of the Institut Laue Langevin. *J Phys Conf Ser*. 2014;549(1):1-6. doi:10.1088/1742-6596/549/1/012003

26. Http//www.ill.eu/fr. Website Institute Laue Langevin - Neutrons for science. http//www.ill.eu/fr.

27. Hansen TC, Henry PF, Fischer HE, Torregrossa J, Convert P. The D20 instrument at the ILL: A versatile high-intensity two-axis neutron diffractometer. *Meas Sci Technol*. 2008;19(3). doi:10.1088/0957-0233/19/3/034001

28. Lázpita P. *Transiciones Magnéticas y Estructurales En Aleaciones Ferromagnéticas Con Memoria de Forma*. Universidad del País Vasco/Euskalherriko Unibertsitatea; 2008.

29. Chmielus M. *Composition, Structure and Magneto-Mechanical Properties of Ni-Mn-Ga Magnetic Shape-Memory Alloys*. Technische Universität Berlin; 2010. doi:http://dx.doi.org/10.14279/depositonce-2738

30. Goldman AI. Neutron Techniques. In: Kaufmann EN, ed. *Characterization of Materials*. John Wiley & sons; 2002:2192-2204. doi:10.1002/0471266965.com098

31. Molnár P, Šittner P, Novák V, Lukáš P. Twinning processes in Cu-Al-Ni

martensite single crystals investigated by neutron single crystal diffraction method. *Mater Sci Eng A*. 2008;481-482(1-2 C):513-517. doi:10.1016/j.msea.2007.01.189

32. Rodríguez-Carvajal J. FullProf. Published online 2001.

33. Le A. Whole powder pattern decomposition methods and applications : Published online 2005:316-326. doi:10.1154/1.2135315

34. Rietveld HM. A profle refinement method for nuclear and magnetgic structures. *J Appl Cryst*. 1969;2:65-71. doi:10.1107/S0021889869006558

35. Qureshi N. Mag2pol: A program for the analysis of spherical neutron polarimetry, flipping ratio and integrated intensity data. *J Appl Crystallogr*. 2019;52:175-185. doi:10.1107/S1600576718016084

36. Rodríguez-Carvajal J. Recent advances in magnetic structure determination by neutron powder diffraction. *Phys B Phys Condens Matter*. 1993;192(1-2):55-69. doi:10.1016/0921-4526(93)90108-I

37. Papoular RJ, Gillon B. Maximum entropy reconstruction of spin density maps in crystals from polarized neutron diffraction data. *Epl*. 1990;13(5):429-434. doi:10.1209/0295-5075/13/5/009

CHAPTER 4

Effect of heat treatments on polycrystalline Co-doped Ni-Mn-Sn alloys

4.1. INTRODUCTION

Ni-Mn-X (X = In, Sn, Sb, Ga…) Heusler alloys have been widely studied as possible materials for promising applications, such as, e.g., solid state refrigeration materials, due to the fact that they are rare-earth-free and non-toxic.[1–3] Among the potential refrigeration-related applications, one outstands: their use as a feedstock material in the additive manufacturing of 3-D printed magnetic regenerators with enhanced thermal transfer. This potential application arises from the inverse magnetocaloric effect they present, which, as explained in **Section 1.3.1**, is greatly dependant on the induced entropy change, ΔS, associated to the abrupt change in magnetization, ΔM, they present.[4–7] Being ΔS related to the magnetic-field induced MT (see **Equation 4.1**), it can be concluded that the magnetocaloric effect is greatly dependant on the nature of the MT (through ΔM), T_M and T_C.[8–10] Since they are conditioned by the structure and atomic composition of the alloy, a deep understanding of the crystal structure of these alloys is required in order to optimise their properties towards the exploitation of all their functionalities[6,11].

$$\frac{dT_M}{dH} = -\mu_0 \frac{\Delta M}{\Delta S} \qquad \textbf{\textit{Equation 4.1}}$$

In previous works,[12–19]stochiometric Ni-Mn-X Heusler alloys, as mentioned in **Section 1.4**, have been proven to have a $L2_1$-ordered face centered cubic structure (*fcc*), presenting a *Fm-3m* symmetry at high temperature, in the austenite phase. In an ideal ordered case, 4a and 4b Wyckoff sites are occupied by Mn and X atoms, respectively, while Ni takes the remaining 8c sites. In off-stoichiometric and/or doped

alloys, a certain percentage of Ni, Mn, X and doping atoms may occupy the available atomic sites randomly, creating a more disordered crystal structure. Nevertheless, post annealing processing and different cooling rates can lead to an increase in the atomic ordering (*B2, $L2_1$*), and/or to the (dis)appearance of secondary phases, and hence, to improved magnetic properties and mechanical behaviour.[4,20]

More in particular, Co-doped Ni-Mn-Sn Heusler alloys are attracting interest since, upon a specific adjustment of their stoichiometry, they have the MT at room temperature. It was previously proven[21] that, while non-doped Ni-Mn-Sn alloys present an antiferromagnetic coupling between the Mn moments on 4a and 4b sites, this same interactions are ferromagnetic in the Co-doped ones, concluding that this stronger ferromagnetic behaviour was due to the change of the crystalline and magnetic structure by substituting Ni for Co. Since, as previously stated, the performance of the materials is conditioned by heat treatments, studying the effect different post synthesis heat treatments have on the magnetic behaviour of Ni-Mn-Sn-Co alloys is of great interest.

In the present chapter we describe a study to understand the effect of post-synthesis heat treatments on the magnetocaloric performance and the structural transformation of two powder alloys with compositions close to the nominal $Ni_{43}Mn_{39}Sn_{11}Co_7$ one. A relationship between their magnetic behaviour (including their magnetocaloric performance) and atomic and magnetic structure was established.

4.2. EXPERIMENTAL PART

4.2.1 Fabrication of Ni-Mn-Sn-Co powders

The fabrication of the $Ni_{43}Mn_{39}Sn_{11}Co_7$ (nominal composition, at.%) polycrystalline master alloys was done in collaboration with colleagues from BCMaterials and the UPV/EHU The selected fabrication method was induction melting from pure constituent elementsunder argon atmosphere and employing a quartz crucible. Approximately 5g of the bulk piece were melted, also under argon atmosphere, and then ejected onto a rotating copper wheel. By employing an Edmund-

Buhler melt-spinning system, two batches of melt-spun ribbons were fabricated. The conditions employed to fabricate these melt-spun ribbons (0.75 mm ejection orifice in the quartz crucible and a 30 $m \cdot s^{-1}$ linear speed of the copper wheel) were selected to optimize their magnetocaloric performance.[4]

To fabricate the powders, the melt-spun ribbons were grinded using an agate mortar and pestle tool. In order to minimize the phase degradation during the process, the ribbons were grinded using liquid Nitrogen, so that they are at 77K, in their low-symmetry martensitic phase[22]. The resultant powders were then sieved with a 100 μ 0m orifice mesh, to obtain grains with a homogeneous size and to avoid bigger grains with less homogeneous properties and with a higher probability of presenting textures.

4.2.2. Heat treatments

It is well known[23,24] that when the alloys undergo specific heat treatments these influence the crystal structure, and that they can lead to surface and internal stresses relaxation, and even modify the presence of defects. In this particular work, we have observed that crystal disorder and residual stresses can be induced in the crystal structure by the fabrication and grinding processes, affecting the magnetic properties of the alloys. In an attempt to relieve them, two specific thermal annealing processes successfully implemented in previous works[4] were selected:

- HT1: heating to 1173K for 1h + ice water quench

- HT2: heating to 1173K for 1h + ice water quench followed by heating to 723K for 30 min + ice water quench

Both heat treatments were carried out by sealing the powders in Argon purged quartz ampoules, to avoid oxidation during heating, and placing them in a high temperature furnace, followed by quenching the alloys in the ampoules in iced water. The aim of this last part of the heat treatment was avoid the formation of intermediate phases while cooling, leading to an enhanced martensitic transformation[25,26]

4.2.3. Characterization Techniques

EDX measurements were carried out to obtain the average composition of the alloys in at.%. The calorimetric measurements were performed by DSC, while the

magnetic properties of the powered samples were studied using VSM and SQUID magnetometers. To calculate the magnetic field-induced entropy changes, thermomagnetization curves (obtained at 0.01-7 T applied magnetic field) and Maxwell relationships were employed, as will be discussed in **Section 4.4**.

The crystal structure was determined by powder neutron diffraction. The experiment[27] was carried out at the D20 instrument of the Institute Laue-Langevin neutron source (Grenoble, France), with a monochromatic neutron beam of $\lambda = 1.54$ Å. High resolution isothermal diffractograms were obtained at 123, 203, 323 and 423 K for the studied powders, corresponding to the ferromagnetic martensite, weak-magnetic martensite, ferromagnetic austenite and paramagnetic austenite phases, respectively.

From the obtained data, the crystal structures (lattice parameters and atomic orderings) were determined via Lebail refinements, and the residual stresses, atomic orderings and magnetic structures were obtained via Rietveld refinements. FullProf suite software was used for the analysis

4.3. STRUCTURAL BEHAVIOUR

4.3.1. Composition and transformation characteristics

As previously stated, the goal of the work presented in this chapter was to study the effect of post-annealing treatments on the magnetocaloric performance and the structural transformation of metamagnetic shape memory alloys that underwent different heat treatments. With this aim, four samples were prepared and their structure and magnetic behaviour, studied.

Table 4.1 summarizes the denomination, measured composition and heat treatment of each sample, alongside with their T_C, T_A and T_M values. The temperature dependence of the low-field magnetization, *M(T)*, shown in **Figure 4.1**, was used to determine these characteristic temperatures, employing the derivative method, i. e., calculating the derivative curve of *M(T)*, and selecting the maxima, where the greatest change of magnetization occur, as the transition temperature. Since only austenitic

magnetic transition was observed in this system of alloys, T_C will be used as a equivalent to T_C^A along the chapter.

Table 4.1. *List of samples studied, including their composition, heat treatmen and characteristic transformation temperatures, obtained employing the derivative method in the low magnetic field thermomagnetization curves.*

Alloy	Composition	Heat treatment	T_C (K)	T_A (K)	T_M (K)
A1 noHT	$Ni_{43.3}Mn_{39.2}Sn_{10.1}Co_{7.4}$	noHT	388	275	248
A1 HT1	$Ni_{43.3}Mn_{39.2}Sn_{10.1}Co_{7.4}$	HT1	393	296	270
A1 HT2	$Ni_{43.3}Mn_{39.2}Sn_{10.1}Co_{7.4}$	HT2	391	296	273
A2 HT2	$Ni_{43.3}Mn_{39.8}Sn_{10.3}Co_{6.6}$	HT2	397	298	277

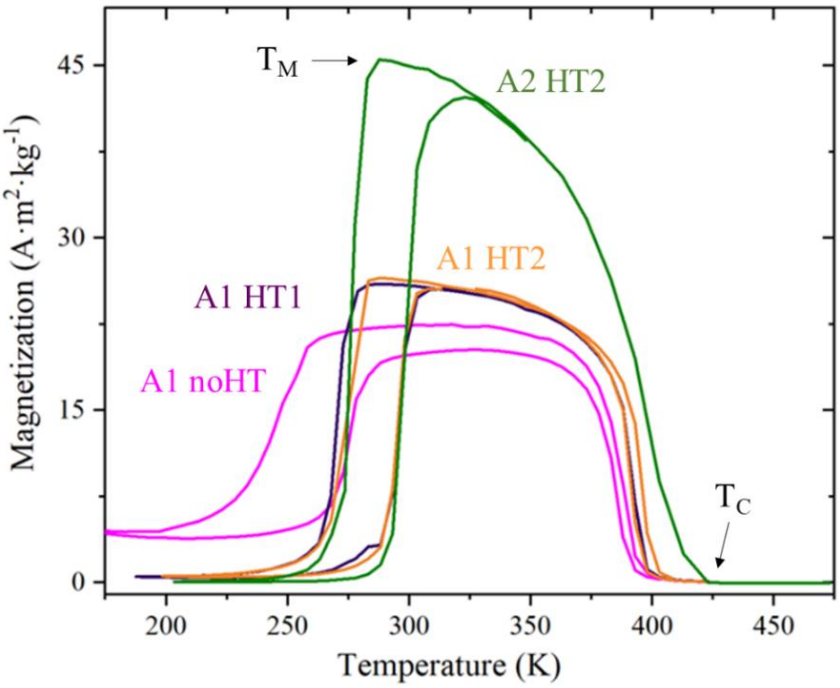

Figure 4.1. *Magnetization versus temperature (M(T)) curves for the studied powders, measured at low magnetic fields (0.01 T), alongside with an example of the approximate positions of T_C and T_M for the A2 HT2 powder.*

The dependence of the magnetization with the heat flow observed in **Figure 4.1** infers a strong effect of the different heat treatments on the transformation behaviour and on the magnetic properties of the martensite and austenite phases of the alloys. In particular, two main observations can be deduced as follows:

- Both heat treatments produced changes on the characteristic structural and magnetic transformation temperatures, as well as a reduction of the thermal hysteresis of the MT.
- The sample A2, which has a different composition than the other ones studied, doubles the magnetization value to its analogously heat-treated A1 sample. This can be attributed to the presence of anisotropic effects induced by the grinding process, a hypothesis supported by the fact that both samples show similar magnetization saturation values at high magnetic fields, when the magnetocrystalline anisotropy is overcome by the field (see **Figure 4.2**).

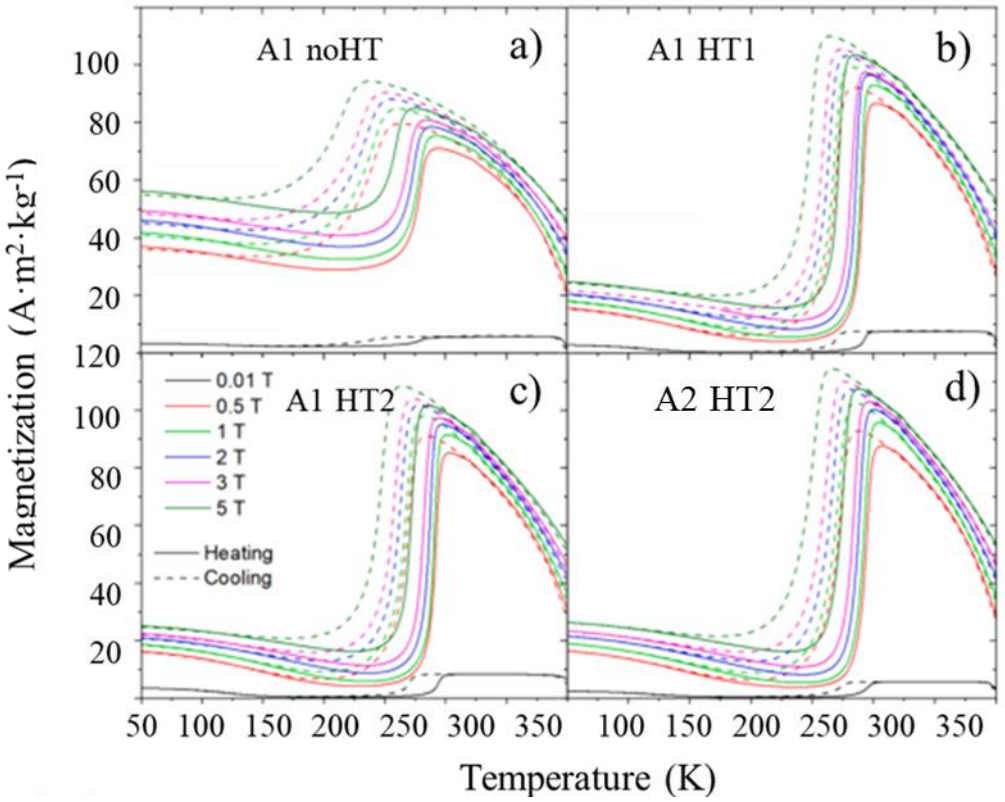

Figure 4.2. *Thermomagnetization curves at different magnetic fields for the a) A1 NoHt, b) A1 HT1, c) A1 HT2 and d) A2 HT2 powders.*

4.3.2. Powder neutron diffraction

Neutron diffraction patterns of each of the four powders were measured at selected temperatures (123, 203, 323 and 423 K), as previously mentioned, in order to keep track of the temperature evolution of the different structural and magnetic phases present in the alloy. With the aim of unravelling the austenitic and martensitic

crystalline structures, pattern-matching LeBail refinements were performed in the highest and lowest temperature diffractograms. These fittings are display in the annex, (**Figures A.1.1 – A.1.4**), to avoid overcrowding the discussion with figures, and in **Figure 4.3**, as a representative.

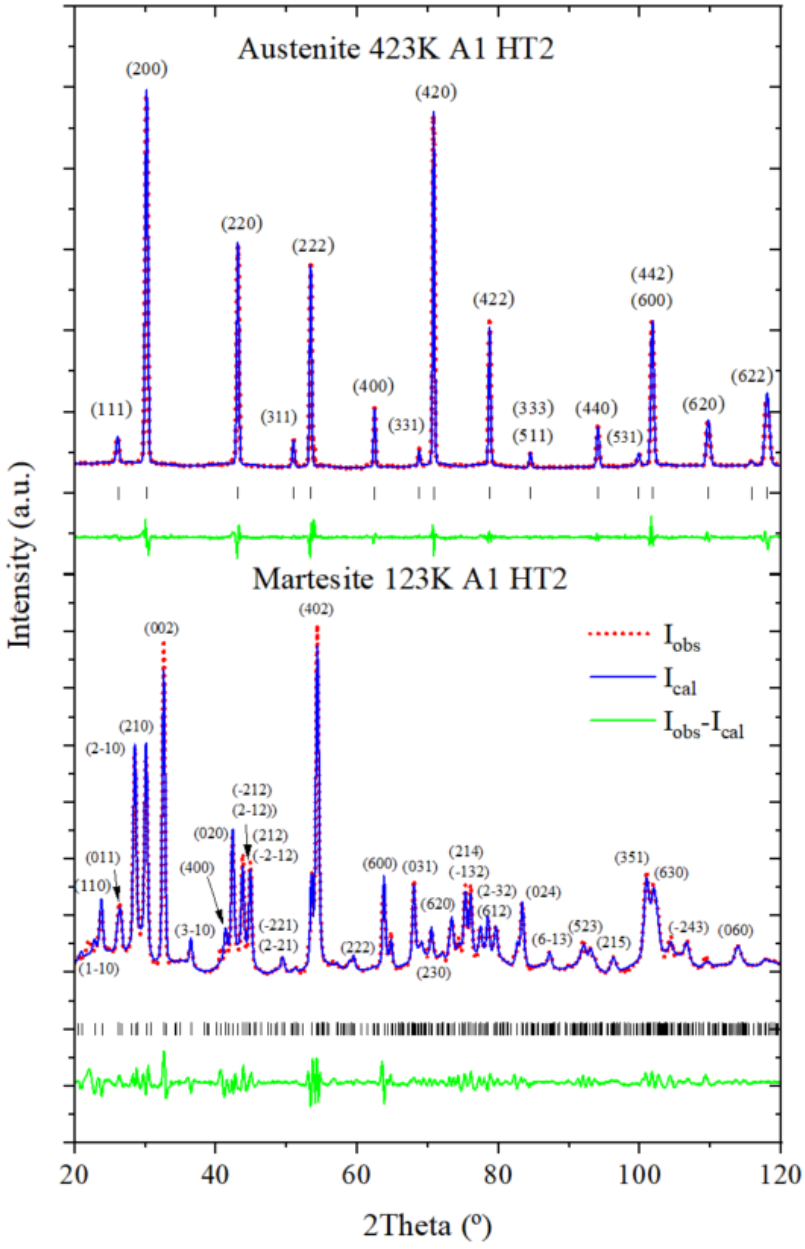

Figure 4.3: *LeBail refinements at 423 and 123 K of the A1 HT2 alloy. Red dots represent experimental points; blue lines are the LeBail fittings; and green lines correspond to the difference between the measurements and the fittings. The Miller indices corresponding to each reflection are indicated with a black line and shown above each peak.*

Table 4.2 summarizes the results of the pattern matching fittings, depicting the space groups and lattice parameters of the four samples studied at their highest

(austenite) and lowest (martensite) temperatures. All the samples present a *Fm-3m* cubic symmetry in the austenitic phase and a 3M modulated *P2/m* monoclinic structure in the martensitic one, what leads to conclude that there are no changes in the crystal symmetries associated with the heat treatments. Nonetheless, a slight change in the cell parameters (increment of a_A and c_M and decrease of β) for the HT2 alloys is observed, which is related to the relaxation of the structure.

It should also be mentioned that neither the HT1-treated sample nor the HT2-treated ones present any phase coexistences at low temperatures, implying that an incomplete martensitic transformation only happens in the non-treated sample.

Table 4.2. *Space groups and lattice parameters of the austenite (at 423 K) and martensite (at 123 K) phases in the studied powder alloys.*

Alloy	T = 423K		T = 123K	
	Symmetry	**Lattice (Å)**	**Symmetry**	**Lattice (Å / º)**
A1 noHT	*Fm-3m*	a = 5.97	*P2/m* *Fm-3m*	a = 4.40, b = 5.54, c = 4.29, β = 93.17 a = 5.96
A1 HT1	*Fm-3m*	a = 5.97	*P2/m*	a = 4.40, b = 5.53, c = 4.29, β = 93.20
A1 HT2	*Fm-3m*	a = 5.98	*P2/m*	a = 4.40, b = 5.53, c = 4.30, β = 93.22
A2 HT2	*Fm-3m*	a = 5.98	*P2/m*	a = 4.40, b = 5.53, c = 4.30, β = 93.04

Besides the study of the crystal phases presented in **Table 4.2**, the existence of internal stresses in the non-heat-treated sample can also be inferred after a careful analysis of the diffractogram peaks corresponding to the cubic austenite phase. As it can be appreciated in **Figure 4.4,** which displays the 423 K (austenite) patterns of the three A1 samples, the non-heat-treated one exhibits noticeably wider peaks. This is associated with a more stressed structure, since the presence of tensions and stresses affect the interplanar distances between some planes, affecting the peak width[28–30]. Hence, the narrower peaks in the other samples can be attributed to stress relief. This phenomenon is more noticeable at higher angles, as it is exemplified with the zoomed peaks. In the low angle (200) peak the width difference is barely noticeable, as opposed to the situation in the (331) and (420) peaks corresponding to *B2* and $L2_1$ ordering, respectively. There is no apparent difference between the effect of heat treatments HT1 and HT2 in the internal stresses, as the aforementioned peaks do not reveal noticeable differences.

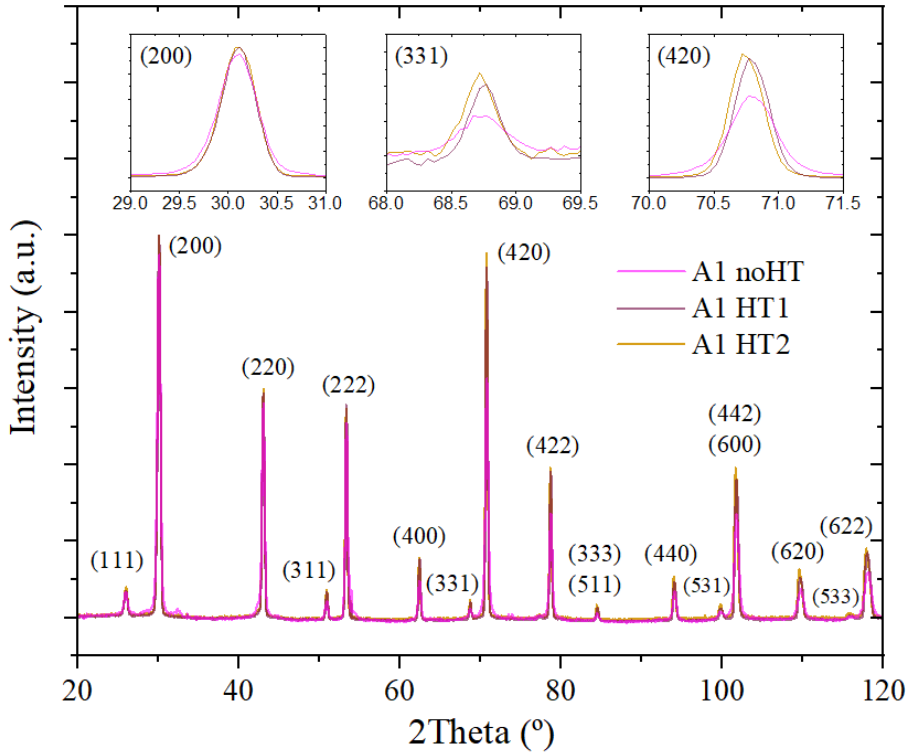

Figure 4.4. *Powder neutron diffractograms obtained at 423K for the A1 noHT (pink), A1 HT1 (purple) and A1 HT2 (orange) samples, alongside with zoomed-in plots of the (200), (331) and (420) peaks. For the sake of comparison, the background in all the patterns was subtracted and their intensity normalized.*

While comparing the higher temperature diffractograms of the different alloys studied revealed the existence of stresses, the comparison of their lowest temperature diffractograms gives us a deeper understanding of the effect they may have on their crystal structure and atomic ordering. **Figure 4.5** show the 123 K patterns of A1 noHT and A1 HT2 alloys, where the coexistence of martensitic and austenitic phases in the former is evidenced by the higher intensity of those peaks present in both phases (marked with an asterisk).

This allows us to conclude that the presence of these internal stresses results in an incomplete structural martensitic transformation during cooling. As a result of the alloy undergoing a heat treatment, the stresses are relieved, hence favouring the completion of the martensitic transformation.

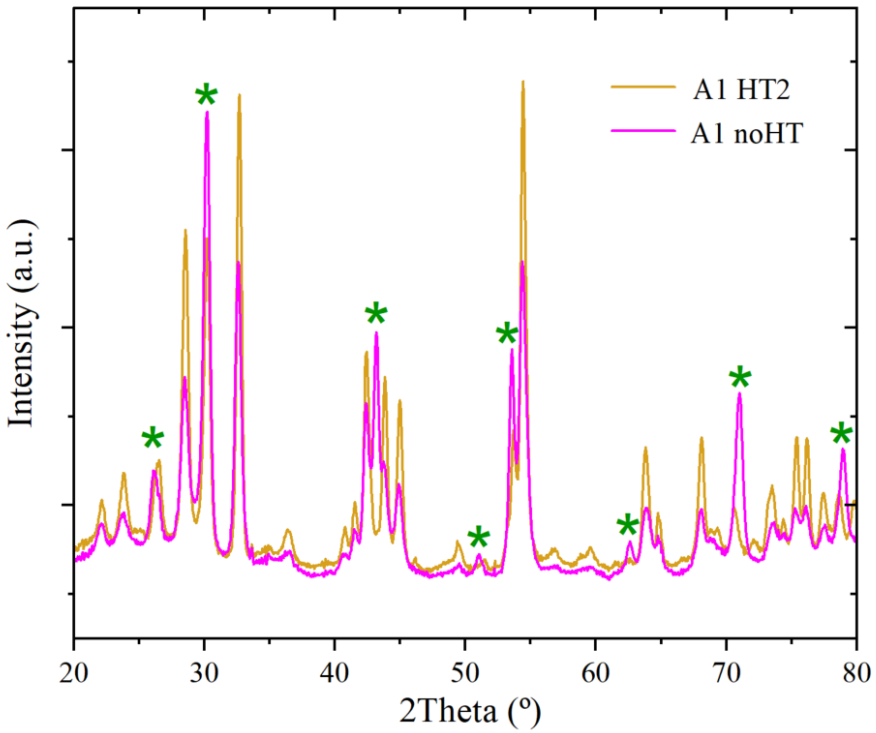

Figure 4.5. *Powder neutron diffractograms obtained at 123K for the A1 noHT (pink) and A1 HT2 (orange) samples. The peaks corresponding to the Fm-3m austenitic phase are marked with a green asterisk.For the indexation of the pekas see Figures A.1.1 and A.1.3.*

From the 423 K diffractograms the atomic orderings in the crystal lattices of the austenite phases of the four alloys were determined by Rietveld refinements; they are presented in **Table 4.3**. Even though the analysis was performed in the austenite (see **Figure 4.6**), as the martensitic transformation is a first-order diffusionless phase transition, the atomic site occupancies of the martensite phase are the non-displaced equivalent ones to these obtained in the austenite phase. The results are similar for the non-heat-treated and HT2 samples, which implies no changes in the atomic ordering related to the manufacturing process. As it was previously reported[21,31,32], in an ideal situation, the dopant Co atoms should occupy 8c Wyckoff sites only. In the alloys studied here, the amount of Mn is higher than 25%, implying that the Mn in excess of 25%, up to which Mn would occupy 4a sites, needs to go elsewhere in the crystal lattice. This, combined with the low amount of Co, leads to a tendency of the Co atoms to occupy all the sites in the unit cell, displacing Mn to 8c positions.

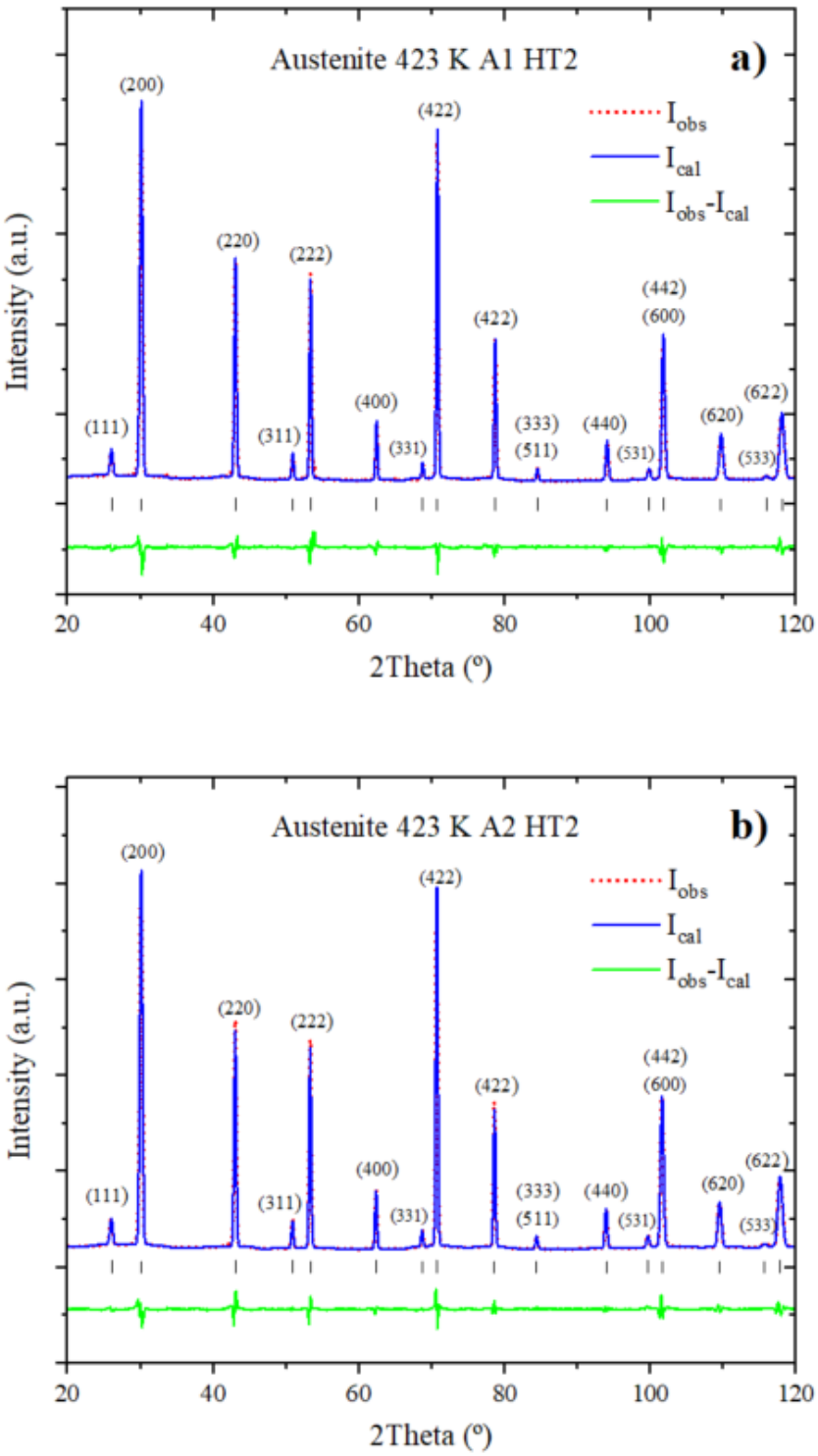

Figure 4.6 *Rietveld refinements at 423 K of the a) A1 HT2 and b) A2 HT2 alloys. Red dots represent experimental points; blue lines are the Rietveld fittings; and green lines correspond to the difference between the measurements and the fittings. The Miller indices corresponding to each reflection are indicated with a black line and indexed above each peak.*

Table 4.3. *Atomic site occupancies (at%) of the studied alloys obtained via Rietveld refinements.*

Alloy	Position	Ni	Mn	Sn	Co
A1 HT2	(0.25, 0.25, 0.25) - 8c	43.3	–	–	6.7
	(0, 0, 0) - 4a	–	25.0	–	–
	(0.5, 0.5, 0.5) - 4b	–	14.0	10.5	0.5
A2 HT2	(0.25, 0.25, 0.25) - 8c	43.3	1.5	–	5.2
	(0, 0, 0) - 4a	–	24.7	–	0.3
	(0.5, 0.5, 0.5) - 4b	–	13.6	10.3	1.1

While most of the information in this work is provided by comparing same-composition different-heat-treatment alloys, from the comparison of the same-heat-treatment (HT2) different-composition (A1 and A2) alloys we can also draw valuable conclusions. The patterns obtained at 423 K for A1 HT2 and A2 HT2 samples are compared in **Figure 4.7.** Due to the different unit cell parameters (see **Table 4.2**), the diffraction peaks of each alloy are slightly displaced, as evidenced in the peaks presented as insets in that figure, selected for the sake of comparison with **Figure 4.4**. The differences in the peak heights for each alloy are related to differences in the atomic orderings of the alloys (see **Table 4.3**). Since the same heat treatment was applied to both samples, the residual internal stresses were equally relieved, whereby leading to similar peak widths.

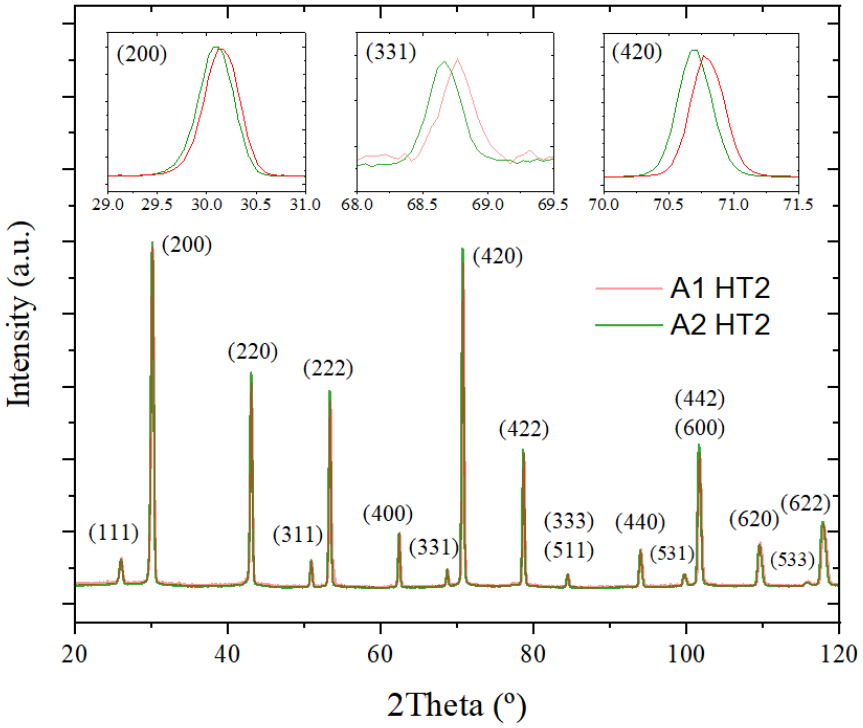

Figure 4.7. *Powder neutron diffractograms obtained at 423K for A1 HT2 (orange) and A2 HT2 (green) samples, alongside with insets of the (111), (200) and (420) peaks zoomed.*

The aforementioned variations in the crystal structure are responsible for the variation in the magnetic and structural behaviour of the alloys (see **Figures 4.1 and 4.3**, respectively). By comparing the same-composition different heat-treated samples (A1 noHT, A1 HT1 and A1 HT2), it can be concluded that a longer heat treatment results in a less stressed sample with a higher T_M and a narrower thermal hysteresis across the MT, as the martensitic transformation has been fully accomplished (i.e. there is no retained austenite phase at low temperatures). This may lead to an enhanced IMCE[33], as will be discussed in the next section. Regarding the different composition samples that underwent HT2, the slight increase in the T_M in A2 sample is attributed to a the higher amount of Mn on different sites, due to the reduced presence of Co at the 8c sites. As the Mn content of the A2 HT2 sample is higher than that of sample A1 HT2, an increase in both magnetization saturation and T_C should be expected only if the extra Mn-Mn interactions are ferromagnetic[21,31]. In order to investigate if this is the case, their magnetic structures are analysed via Rietveld refinements.

The patterns measured at magnetic phases (ferromagnetic austenite, at 323 K) for the samples after being subjected to HT2 show an increase of intensity in some of

the peaks belonging to pure nuclear (structural) scattering events, namely the (200) and the (111) reflections. This is due to the magnetic ordering induced in the structure when the transition from paramagnetic to ferromagnetic austenite occurs. As no purely magnetic peaks appear, it indicates that all samples present a ferromagnetic state. The Rietveld refinements of the magnetic structures (see **Figure 4.8**) give us information about the magnetic moments at each Wyckoff position (see **Table 4.4**).

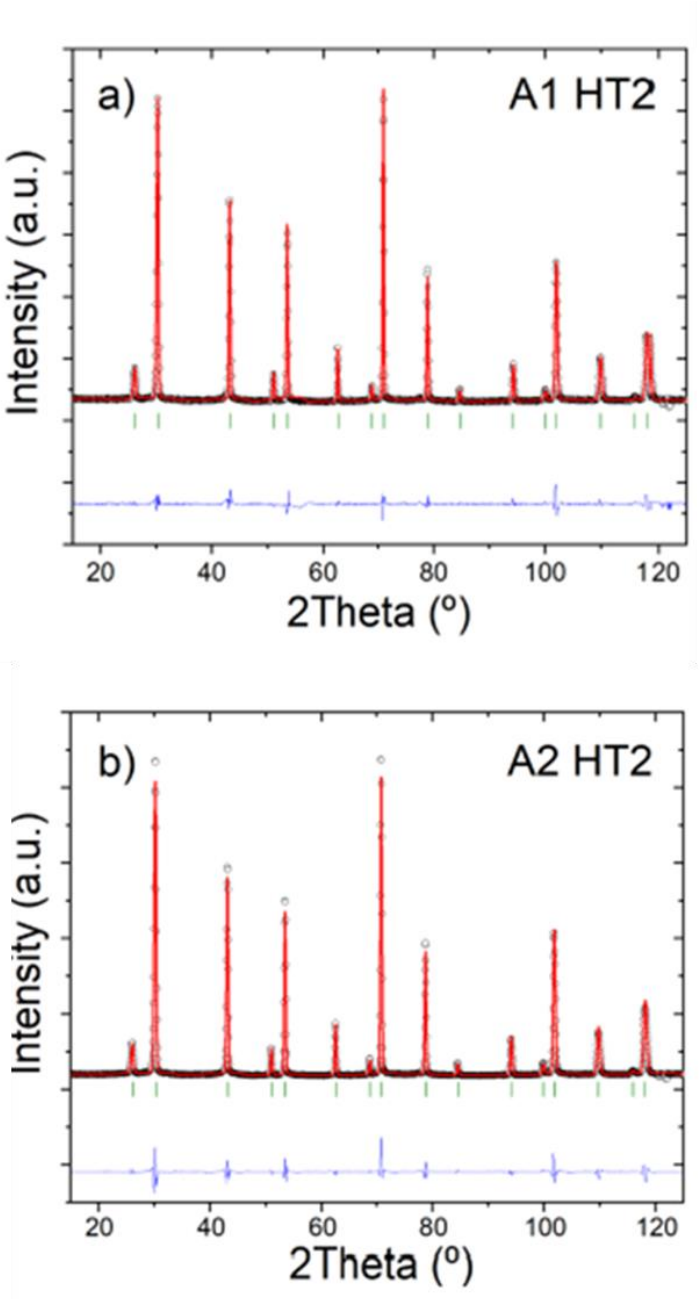

Figure 4.8 *Powder neutron diffraction patterns in the ferromagnetic austenite state (323K) of a) A1 HT2 and b) A2 HT2. Black open circles are the experimental data, red and blue lines represent the calculated and difference patterns respectively, and green marks indicate the Bragg reflections.*

In the A1 sample, where the Mn atoms are located mainly in the 4a positions and the Mn in excess goes to 4b sites, the magnetic coupling between 4a and 4b-placed atoms is ferromagnetic, with magnetic moments of 2.77μ_B and 0.85μ_B, respectively. The presence of Co atoms in the 8c positions results into an increase of the magnetic interactions between 4a and 4b sites, leading to a ferromagnetic coupling[31,34–36]. For the A2 sample, as seen in **Table 4.3**, Mn and Co atoms are located in all crystallographic positions, leading to a somewhat disordered *L21* phase. However, as previously reported[31,34–36],the presence of Mn atoms in 8c positions leads to a considerable increase of the localized magnetic moment in these sites. In this case, the presence of Mn atoms in all crystallographic positions increases the magnetic moment on the 4b site by 18% (see **Table 4.4**), resulting an increase of the total magnetic moment of the alloy and the overall saturation magnetization of the sample. The latter is compared to the experimentally measured saturation magnetization by Arrot method[37] (see **Figure 4.9**) in **Table 4.4**, supporting the accuracy of the magnetic structure analysis. For this analysis, the magnetic moments of Ni and Co are fixed to 0.2 and 1 μB, respectively[21].

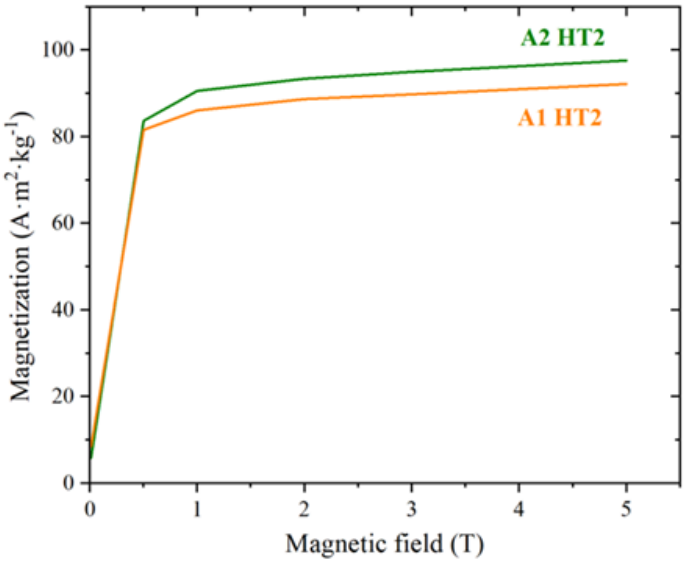

Figure 4.9 *Magnetic field evolution of the magnetization for A HT2 and A2 HT2 at* 323K.

***Table 4.4**. Magnetic moment determined for each atomic site in the ferromagnetic austenite (323 K) phases of the A1 HT2 and A2 HT2 alloys, alongside with the experimental (μ_{exp}) and obtained via Rietveld refinement (μ_{Riet}) total magnetic moments.*

Alloy	μ per site (μB)			μ total (μB/FU)	
	4a	4b	8c	μ_{Riet}	μ_{exp}
A1 HT2	2.77	0.85	0.31	4.24	4.39
A2 HT2	2.8	1.04	0.35	4.53	4.63

4.4. MAGNETOCALORIC EFFECT

As previously stated, ΔS, T_M and T_C are intimately related to the magnetocaloric performance of this kind of alloys. By studying the influence different heat treatments and slight compositional variations have on the structure and atomic site occupancies, their effect on the characteristic transition temperatures was determined, as presented in the previous section. In this section we will discuss the influence they have on ΔS associated to jumps in the magnetization, ΔM, on these alloys and, therefore, on their magnetocaloric performance. All the work presented in this section was done as part of a collaboration.

By looking at the temperature evolution of the magnetization when high magnetic fields are applied (Figure 4.9), it can be observed that the magnetization jump at MT, ΔM, is critically affected by the heat treatments, being doubled for the alloys that underwent a heat treatment with respect to the non-heat-treated one. ΔM values are related to the entropy change by **Equation 4.2**[38], what, in turn is directly linked to the magnetocaloric performance.[33] Therefore, the entropy change of this set of alloys was evaluated by **Equation 4.2** and the ΔM values derived from **Figure 4.1**.

$$\Delta S_m(T,H) = S_m(T,H) - S_m(T,0) = \mu_0 \int_0^H \frac{\delta' M(T,H')}{\delta T} \delta H' \qquad \textit{Equation 4.2}$$

The results of applying Equation 4.2 to the data shown in **Figure 4.2** are presented in **Figure 4.9a**. A remarkable difference in the entropy change between the heat-treated and the non-heat-treated powders can be appreciated, as expected from the less abrupt *M(T)* curve with much smaller ΔM. While the heat-treated samples exhibit values of $\Delta S_{m,max} \approx 35$ J·kg^{-1}·K^{-1} at 5T, the non-heat-treated sample value is $\Delta S_{m,max} \approx 10$ J·kg^{-1}·K^{-1}, about three time smaller. While there is almost no difference

in entropy change between A1 HT1 and A1 HT2, A1 HT1 presents a slightly higher value than A2 HT2.

To properly evaluate the magnetocaloric performance of this set of alloys, their refrigeration capacity, *RC*, defined as the amount of heat transferred between hot and cold reservoirs in a single refrigeration cycle, must be calculated.[39] With this aim, **Equation 4.3**[39] was applied to the previously calculated ΔS_m data, obtaining the results presented in **Figure 4.9b**

$$RC \approx \int_{T_{cold}}^{T_{hot}} |\Delta S_M(T,H)| \delta T \qquad \textbf{Equation 4.3}$$

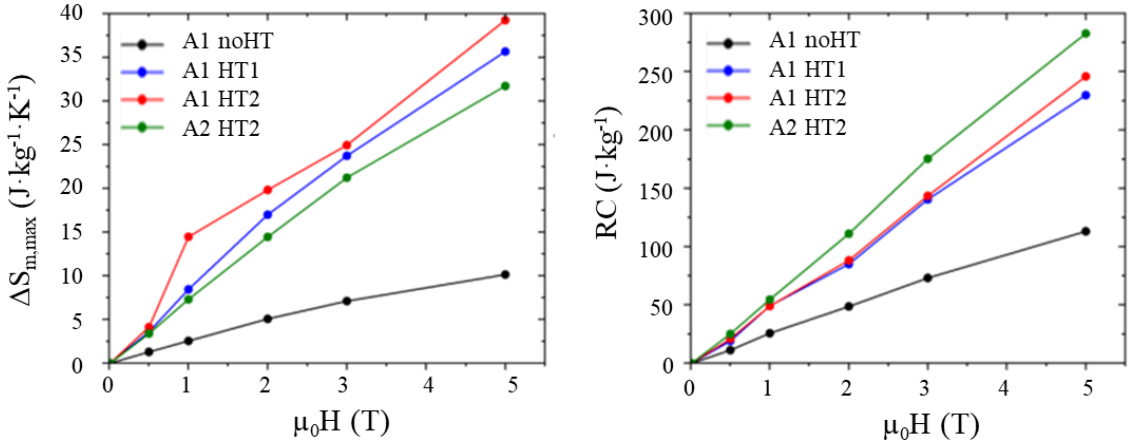

Figure 4.10 *a) Entropy change dependence with the applied magnetic field for every studied alloy. b) Refrigeration capacity evolution dependence with the applied magnetic field for every studied alloy.*

With these results, it can be concluded that the refrigeration capacity is highly influenced by the heat treatments, being around three times higher in the heat-treated samples, compared to the non-treated one.

4.5 SUMMARY AND CONCLUSIONS

In the present work we have studied the effect of different heat treatments on the crystalline and magnetic structures of the alloys and, subsequently, on their magnetocaloric performance.

For the preparation of the Heusler-type magnetocaloric $Ni_{43}Co_7Mn_{39}Sn_{11}$(at.%) powders, a technologically simple method of preparation was

used: grinding melt-spun ribbons from the master bulk alloy. This method allowed minimizing the content of residual stresses, defects or segregations in the material. The transformation behaviour, crystal structure, magnetic and magnetocaloric properties of the powder samples after undergoing different heat treatments were systematically studied by DSC, neutron powder diffraction and magnetic characterization measurements.

We have proven that different heat-treatments induce changes in the crystal structures of both the austenite and martensite phases of the studied alloys. It was concluded that the *Fm-3m* austenite phase of the non-heat-treated powder exhibited internal stresses which relaxed upon the application of both intermediate and complete heat treatments. The martensite phases exhibited a 3M modulated P2/m monoclinic structure that, in the case of the non-heat-treated sample, coexists with the cubic austenite even at 123 K. This retained austenite phase was not observed in the heat-treated samples, what draws the conclusion that the presence of residual internal stresses in the as-received melt-spun ribbon prevents a complete MT. The heat treatment at 1173 K (HT1), usually carried out to improve the composition homogeneity and to induce and maintain the desired phases in MMSMAs, was enough to relieve the presence of the internal stresses. No further stress relief was found with a subsequent annealing at 723 K (HT2). This behaviour is responsible for the difference in T_M between the same composition samples.

The analysis of the atomic site occupancy revealed an increased amount of Mn atoms in the 4b sites and a tendency of the Co and Mn atoms to occupy all available sites in the A2 alloy. This increases the unit cell disorder compared to the A1 alloy, where the Co atoms occupy only the 8c and 4b sites and the Mn atoms the 4a and 4b ones. The presence of Mn and Co in all crystallographic positions enhance the magnetic interactions between 4a and 4b sites, resulting in an increase of the local magnetic moment of the 4b site coupling ferromagnetically with 4a and 8c sites. This higher percentage of displaced Mn atoms interacting ferromagnetically explains the higher magnetization saturation and T_C values in A2, due to the higher content in Mn.

The results of the thermal, structural and magnetic properties of the four powdered MMSMAs ribbons studied unveiled a crucial role of the heat treatments in

their properties. The analysis of these results has evidenced a remarkable improvement of the magnetocaloric performance when the alloys undergo specific post-annealing treatments, related to the fact that the martensitic transformation can be completely accomplished. Further, the values of $\Delta S_{m,max}$ for the heat treated samples obtained in the present work are comparable to those ones of well-known magnetocaloric materials under similar applied fields[40–42] (see **Table 4.5**), which is of great importance for their implementation in future solid-state refrigeration devices based on the magnetocaloric effect.

Table 4.5. *Comparison of the maximum magnetic entropy ($\Delta S_{m,max}$) of the A1 HT2 used in this work and well-known magnetocaloric materials, under an applied field close to 2T.*

Alloy	$\Delta S_{m,max}$ ($J \cdot kg^{-1} \cdot K^{-1}$)
A1 HT2	20
$Ni_{40}Mn_{42.5}Sn_{9.5}Co_8$	25
$Gd_5(Si_2Ge_2)$	18.5
$LaFe_{11.4}Si_{1.6}$	19.4

4.6. BIBLIOGRAPHY

1. Ullakko K, Huang JK, Kantner C, Handley RCO. Large magnetic-field-induced strains in Ni2MnGa single crystals Large magnetic-field-induced strains in Ni 2 MnGa single crystals. *Appl Phys Lett*. 2013;69(13):1966-1998.

2. Umetsu RY, Ito W, Ito K, et al. Anomaly in entropy change between parent and martensite phases in the Ni50Mn34In16 Heusler alloy. *Scr Mater*. 2009;60(1):25-28. doi:10.1016/j.scriptamat.2008.08.022

3. Monroe JA, Karaman I, Basaran B, et al. Direct measurement of large reversible magnetic-field-induced strain in Ni-Co-Mn-In metamagnetic shape memory alloys. *Acta Mater*. 2012;60(20):6883-6891. doi:10.1016/j.actamat.2012.07.040

4. Rodríguez-Crespo B, Salazar D, Lanceros-Méndez S, Chernenko V. Development and magnetocaloric properties of Ni(Co)-Mn-Sn printing ink. *J*

Alloys Compd. 2022;917:165521. doi:10.1016/j.jallcom.2022.165521

5. Aguilar-Ortiz CO, Camarillo-García JP, Vergara J, et al. Effect of solidification rate on martensitic transformation behavior and adiabatic magnetocaloric effect of Ni 50 Mn 35 In 15 ribbons. *J Alloys Compd*. 2018;748:464-472. doi:10.1016/j.jallcom.2018.03.074

6. Stevens E, Kimes K, Salazar D, et al. Mastering a 1.2 K hysteresis for martensitic para-ferromagnetic partial transformation in Ni-Mn(Cu)-Ga magnetocaloric material via binder jet 3D printing. *Addit Manuf*. 2021;37(August 2020). doi:10.1016/j.addma.2020.101560

7. Webster PJ, Ziebeck KRA, Town SL, Peak MS. Magnetic order and phase transformation in Ni2MnGa. *Philos Mag B Phys Condens Matter; Stat Mech Electron Opt Magn Prop*. 1984;49(3):295-310. doi:10.1080/13642817408246515

8. Nambiar SS, Murthy BRN, Sharma S, Prasanna AA, Chelvane AJ. Microstructure and Mechanical Properties of Annealed Quinary Ni-Mn-Sn-Fe-In Heusler Alloy. *Eng Sci*. 2022;17:303-308. doi:10.30919/es8d632

9. Esakki Muthu S, Rama Rao N V., Manivel Raja M, Raj Kumar DM, Mohan Radheep D, Arumugam S. Influence of Ni/Mn concentration on the structural, magnetic and magnetocaloric properties in Ni50-xMn37+xSn13 Heusler alloys. *J Phys D Appl Phys*. 2010;43(42). doi:10.1088/0022-3727/43/42/425002

10. Zhukova V, Ipatov M, Granovsky A, Zhukov A. Magnetic properties of Ni-Mn-In-Co Heusler-type glass-coated microwires. *J Appl Phys*. 2014;115(17):10-13. doi:10.1063/1.4868919

11. Seguí C, Torrens-Serra J, Cesari E, Lázpita P. Optimizing the caloric properties of Cu-doped Ni-Mn-Ga alloys. *Materials (Basel)*. 2020;13(2). doi:10.3390/ma13020419

12. Cong DY, Roth S, Schultz L. Magnetic properties and structural transformations in Ni-Co-Mn-Sn multifunctional alloys. *Acta Mater*.

2012;60(13-14):5335-5351. doi:10.1016/j.actamat.2012.06.034

13. Liu J, Scheerbaum N, Kauffmann-Weiss S, Gutfleisch O. NiMn-based alloys and composites for magnetically controlled dampers and actuators. *Adv Eng Mater*. 2012;14(8):653-667. doi:10.1002/adem.201200038

14. Sokolovskiy V, Grünebohm A, Buchelnikov V, Entel P. Ab initio and Monte Carlo approaches for the magnetocaloric effect in Co- and in-doped Ni-Mn-Ga Heusler alloys. *Entropy*. 2014;16(9):4992-5019. doi:10.3390/e16094992

15. Luo HB, Li CM, Hu QM, et al. First-principles investigations of the five-layer modulated martensitic structure in Ni2Mn(AlxGa1-x) alloys. *Acta Mater*. 2011;59(15):5938-5945. doi:10.1016/j.actamat.2011.06.002

16. Soto D, Hernández FA, Flores-Zúñiga H, et al. Phase diagram of Fe-doped Ni-Mn-Ga ferromagnetic shape-memory alloys. *Phys Rev B - Condens Matter Mater Phys*. 2008;77(18):1-7. doi:10.1103/PhysRevB.77.184103

17. Xiao HB, Yang CP, Wang RL, Marchenkov V V., Bärner K. Effect of alloying element Al substitution on Ni-Mn-Sn shape memory alloy by first-principle calculations. *J Appl Phys*. 2012;112(12). doi:10.1063/1.4772618

18. Kihara T, Xu X, Ito W, Kainuma R, Tokunaga M. Direct measurements of inverse magnetocaloric effects in metamagnetic shape-memory alloy NiCoMnIn. *Phys Rev B - Condens Matter Mater Phys*. 2014;90(21):1-6. doi:10.1103/PhysRevB.90.214409

19. Chernenko VA, L'vov VA, Cesari E, Barandiaran JM. Fundamentals of magnetocaloric effect in magnetic shape memory alloys. In: *Handbook of Magnetic Materials*. Vol 28. Elviser; 2019:1-45. doi:10.1016/bs.hmm.2019.03.001

20. Kalbfleisch AS, Matthews G, Jacques PJ. On the influence of the cooling rate on the martensitic transformation of Ni-Mn-Sn Heusler alloys. *Scr Mater*. 2016;114:121-124. doi:10.1016/j.scriptamat.2015.12.005

21. Umetsu RY, Sheikh A, Ito W, et al. The effect of Co substitution on the magnetic properties of the Heusler alloy Ni50Mn33Sn17. *Appl Phys Lett*. 2011;98(4):10-13. doi:10.1063/1.3548558

22. Nguyen T, Zarudi I, Zhang LC. Grinding-hardening with liquid nitrogen: Mechanisms and technology. *Int J Mach Tools Manuf*. 2007;47(1):97-106. doi:10.1016/j.ijmachtools.2006.02.010

23. Wang Y, Salas D, Duong TC, et al. On the fast kinetics of B2–L21 ordering in Ni-Co-Mn-In metamagnetic shape memory alloys. *J Alloys Compd*. 2019;781:479-489. doi:10.1016/j.jallcom.2018.12.034

24. Bruno NM, Salas D, Wang S, et al. On the microstructural origins of martensitic transformation arrest in a NiCoMnIn magnetic shape memory alloy. *Acta Mater*. 2018;142:95-106. doi:10.1016/j.actamat.2017.08.037

25. Nazmunnahar M, Ryba T, Del Val JJ, et al. Half-metallic Ni2MnSn Heusler alloy prepared by rapid quenching. *J Magn Magn Mater*. 2015;386:98-101. doi:10.1016/j.jmmm.2015.03.066

26. Gutfleisch O, Yan A, Müller KH. Large magnetocaloric effect in melt-spun LaFe 13-x Si x. *J Appl Phys*. 2005;97(10):8-11. doi:10.1063/1.1847871

27. Porro Azpiazu JM, Petrenko V, Rodriguez Crespo B, Rodriguez Velamazan JA, Salazar D. Magnetic, structural and atomic ordering insight of metamagnetic shape memory alloys. Published online 2021. doi:10.5291/ILL-DATA 5-31-2804

28. Delaire F, Raphanel JL, Rey C. Plastic heterogeneities of a copper multicrystal deformed in uniaxial tension: Experimental study and finite element simulations. *Acta Mater*. 2000;48(5):1075-1087. doi:10.1016/S1359-6454(99)00408-5

29. Ji V, Zhang YG, Chen CQ. The non-destructive estimation of the superficial mechanical properties of components in the INCONEL 600 alloy by X-ray diffraction peak width. *Surf Coatings Technol*. 2000;130(1):95-99.

doi:10.1016/S0257-8972(00)00683-6

30. Ortiz AL, Tian JW, Villegas JC, Shaw LL, Liaw PK. Interrogation of the microstructure and residual stress of a nickel-base alloy subjected to surface severe plastic deformation. *Acta Mater*. 2008;56(3):413-426. doi:10.1016/j.actamat.2007.10.003

31. López-García J, Sánchez-Alarcos V, Recarte V, et al. Routes for enhanced magnetism in Ni-Mn-In metamagnetic shape memory alloys. *Scr Mater*. 2019;167:21-25. doi:10.1016/j.scriptamat.2019.03.025

32. Sánchez-Alarcos V, López-García J, Unzueta I, et al. Magnetocaloric effect enhancement driven by intrinsic defects in a Ni45Co5Mn35Sn15 alloy. *J Alloys Compd*. 2019;774:586-592. doi:10.1016/j.jallcom.2018.10.016

33. Biswas A, Chandra S, Samanta T, et al. Universality in the entropy change for the inverse magnetocaloric effect. *Phys Rev B - Condens Matter Mater Phys*. 2013;87(13):1-7. doi:10.1103/PhysRevB.87.134420

34. Lázpita P, Barandiarán JM, Gutiérrez J, Feuchtwanger J, Chernenko VA, Richard ML. Magnetic moment and chemical order in off-stoichiometric Ni-Mn-Ga ferromagnetic shape memory alloys. *New J Phys*. 2011;13:1-14. doi:10.1088/1367-2630/13/3/033039

35. Pérez-Checa A, Porro JM, Feuchtwanger J, et al. Role of Fe addition in Ni–Mn–Ga–Co–Cu–Fe ferromagnetic shape memory alloys for high-temperature magnetic actuation. *Acta Mater*. 2020;196:549-555. doi:10.1016/j.actamat.2020.07.007

36. Yang MJ, Bai J, Li Z, Qiu TF. Crystal structure, phase stability and magnetic properties of Cu-doped Ni2MnGa alloys from first-principles calculations. *Mater Sci Forum*. 2016;873:3-7. doi:10.4028/www.scientific.net/MSF.873.3

37. Arrott A. Criterion for ferromagnetism from observations of magnetic isotherms. *Phys Rev*. 1957;108(6):1394-1396. doi:10.1103/PhysRev.108.1394

38. López-García J, Khanna DLR, Sanchez Llamazares JL, et al. Magnetic structure analysis of the L21-type austenite in Ni–Mn–In alloys. *Intermetallics*. 2024;168:108242. doi:10.1016/j.intermet.2024.108242

39. Gschneider KA. Recent develompents in magnetic refrigeration. 1999;317:69-76. doi:10.4028/www.scientific.net/MSF.315-317.69

40. Hu FX, Shen BG, Sun JR, Cheng ZH, Rao GH, Zhang XX. Influence of negative lattice expansion and metamagnetic transition on magnetic entropy change in the compound LaFe11.4Si1.6. *Appl Phys Lett*. 2001;78(23):3675-3677. doi:10.1063/1.1375836

41. Sánchez-Alarcos V, Recarte V, Pérez-Landazábal JI, Cuello GJ. Correlation between atomic order and the characteristics of the structural and magnetic transformations in Ni-Mn-Ga shape memory alloys. *Acta Mater*. 2007;55(11):3883-3889. doi:10.1016/j.actamat.2007.03.001

42. Pecharsky VK, Gschneidner K. A. J. Giant Magnetocaloric Effect in Gd5Si2Ge2. *Phys Rev Lett*. 1997;78(23):4494-4497. doi:10.1103/PhysRevLett.78.4494

CHAPTER 5

Effect of Cu-doping on polycrystalline Ni-Mn-Ga alloys

5.1. INTRODUCTION

As stated in previous chapters, Ni-Mn-X (X = In, Sn, Sb, Ga…) Heusler alloys have been widely studied due to their promising solid-state refrigeration applications [1–3]. These applications are dependent on their magnetocaloric effect, that, in turn, is dependent on T_M, ΔS and ΔM (as described in **Equation 4.1**).[4–6]

Therefore, for magnetocaloric materials to be used in practical applications, controlling the entropy change and the structural and magnetic transition temperatures, as well as reducing the thermal hysteresis of the first order transformation, is key[7–11]. These factors are greatly influenced not only by the heat treatments, as demonstrated in **Chapter 4**, but also by the composition and presence of doping elements, giving rise to different behaviours both at the structural and magnetism levels.[12–14]

In previous studies[9,15–17] in $Ni_{50}Mn_{25-x}Ga_{25}Cu_x$ (x=3-11) systems, it was concluded that alloys with less than 5.5at% of Cu present a paramagnetic to ferromagnetic transition in the austenitic phase ($T_C^A > T_M$) and a ferromagnetic martensite, while those with a Cu content above 7.5at% show this magnetic transition in the martensitic phase ($T_C^M < T_M$), being the austenite always ferromagnetic. The domain of compositions x=5.5-7.5 presents a metamagnetic behaviour, arising from a magneto-structural transition from paramagnetic austenite to ferromagnetic martensite phase (See **Figure 5.1**). The variations in the structural and magnetic properties of the alloys arise from structural differences, including both the presence of different crystal lattices and different preferential atomic orderings depending on

the Cu at.% present in the alloy. This leads to changes in the magnetic coupling in the austenite and martensite phases and, consequently, in the resulting magnetization change (ΔM) across the MT. Therefore, a proper understanding of the crystalline structure of these compounds is critical to elucidate the mechanisms responsible of the magnetostructural transformation, the magnetic coupling and their possible aforementioned magnetocaloric response

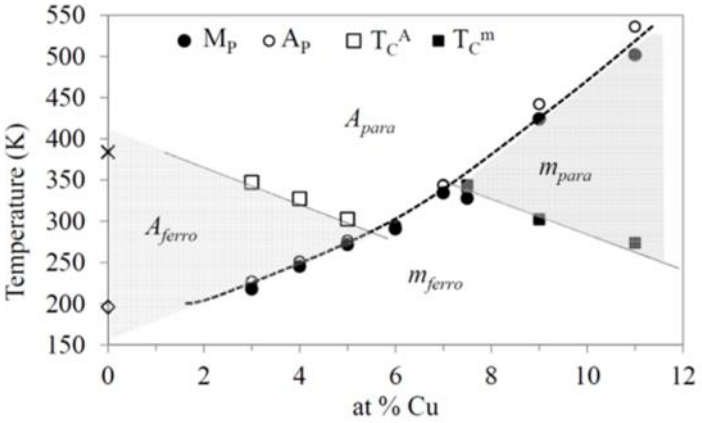

Figure 5.1. *Temperatures of the magnetic and structural transitions as a function of at % Cu. M_p and A_p correspond to the direct and inverse austenite→martensite transformation, respectively. The regions corresponding to different crystallographic and magnetic states of the alloys are indicated. Figure adapted from* [9]

In the work presented in this chapter, a set of powder alloys ($Ni_{50}Mn_{25-x}Ga_{25}Cu_x$; x=5, 6, 9) was studied via standard structural and magnetic characterization techniques, combined with powder neutron diffraction experiments, with the aim of drawing a connection between the atomic order and the magnetic and structural behaviour of the alloys.

5.2. EXPERIMENTAL PART

5.2.1. Fabrication of Ni-Mn-Ga-Cu alloys

A polycrystalline alloy series ($Ni_{50}Mn_{25-x}Ga_{25}Cu_x$, x=5, 6, 9, hereafter denoted as Cu_5, Cu_6 and Cu_9, respectively) was prepared in collaboration with colleagues from the UIB. The preparation consisted on induction melting under argon atmosphere, followed by several subsequent meltings by the arc-melting technique to homogenize the composition and structure of the alloys and minimize the Mn evaporation[18]. The

obtained alloy ingots were heat treated for 24 hours at 1170 K in a vacuum quartz tube, and subsequently quenched in water at room temperature[19,20]. This post-annealing process was done to relieve the internal stress and enhance a complete martensitic transformation (see **Chapter 4**). Finally, the alloys were manually grinded to obtain polycrystalline powders.

5.2.2. Characterisation techniques

The structural (martensitic) transformation temperatures (T_M, T_A) of the alloys were studied by Differential Scanning Calorimetry (DSC), while their magnetic transformation temperatures (T_C^A, T_C^M) and saturation magnetization values (μ_{sat}) were measured by Superconducting Quantum Interference Device (SQUID) magnetometry, in which the temperature evolution of the magnetization was measured under a 5 mT applied external magnetic field. The alloy compositions were studied by means of a desktop Scanning Electron Microscope (SEM) equipped with an Energy-Dispersive X-ray detector (EDX).

The powder neutron diffraction experiments were carried out at the D2B instrument of the Institute Laue-Langevin neutron source, with a neutron wavelength (λ) of 1.60 Å.[21] Neutron diffractograms at specific temperatures were measured in order to examine the crystal structures in the austenite and martensite phases. The acquired data was analysed to determine the crystalline structure using LeBail and Rietveld refinements in a complementary way. For these analyses, the Fullprof suite software was employed.

5.3. STRUCTURAL BEHAVIOUR

5.3.1. Composition and transformation characteristics

As previously stated, the goal of the work presented in this chapter was to study the effect of Cu content on Ni-Mn-Ga-Cu alloys with different composition. With this aim, three samples were prepared and their structure and magnetic behaviour studied.

Table 5.1 presents the denotation and measured compositions of the investigated alloys and their corresponding calculated[22] *e/a* relations, accompanied by the austenite ↔ martensite transformation temperatures (T_M and T_A, denoting direct

and reverse martensitic transformation temperatures, respectively), the martensitic transformation hysteresis temperatures (T_A-T_M), as well as the Curie temperatures in both austenite and martensite phases (T_C^A and T_C^M, respectively).

***Table 5.1**. Measured compositions, calculated electronic concentrations (e/a), representative transition temperatures and thermal hysteresis values of the studied alloys.*

Alloy	Composition	T_M (K)	T_A (K)	T_A-T_M (K)	T_C^M (K)	T_C^A (K)	e/a
Cu_5	$Ni_{50.4}Mn_{18.9}Ga_{25.8}Cu_{4.9}$	272	276	4	–	303	6.668
Cu_6	$Ni_{49.4}Mn_{19.1}Ga_{25.9}Cu_{5.6}$	282	291	9	–	–	6.715
Cu_9	$Ni_{49.1}Mn_{16.2}Ga_{25.2}Cu_{9.5}$	426	444	18	307	–	6.863

Since the structural transformation temperatures correspond to the points where the highest heat flow exchange occurs during the DSC measurements, the maximum and minimum peaks in the measured curves were used to determine T_M and T_A, respectively (See **Figure 5.2**). The unusual aspect of the MT in the Cu_6 sample is attributed to the presence of an intermartensitic transformation, as will be detailed later. T_C^A and T_C^M were determined by applying the previously explained (in **Section 4.3.1**) derivative method in the thermomagnetization curves presented in **Figure 5.3**. The MT occurring in sample Cu_5 is also appreciable in the magnetic measurement, alongside with the Hopkinson peak[23] present at around 300 K.

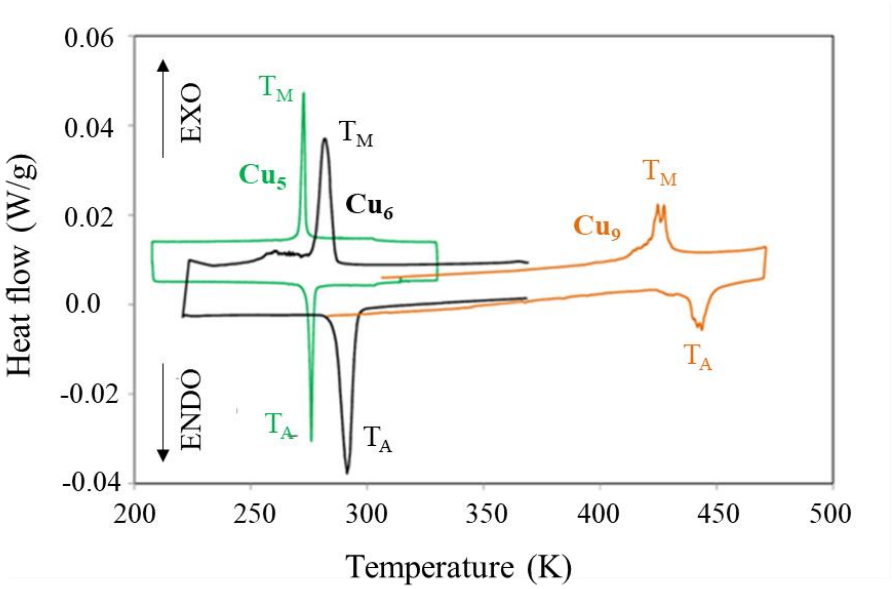

***Figure 5.2**. Normalized differential scanning calorimetry (DSC) curves obtained during cooling/heating cycles for the complete set of Cu_5, Cu_6 and Cu_9 alloys. T_M temperatures correspond to the exothermic (positive) peaks, while T_A temperatures are associated with the endothermic (negative) ones.*

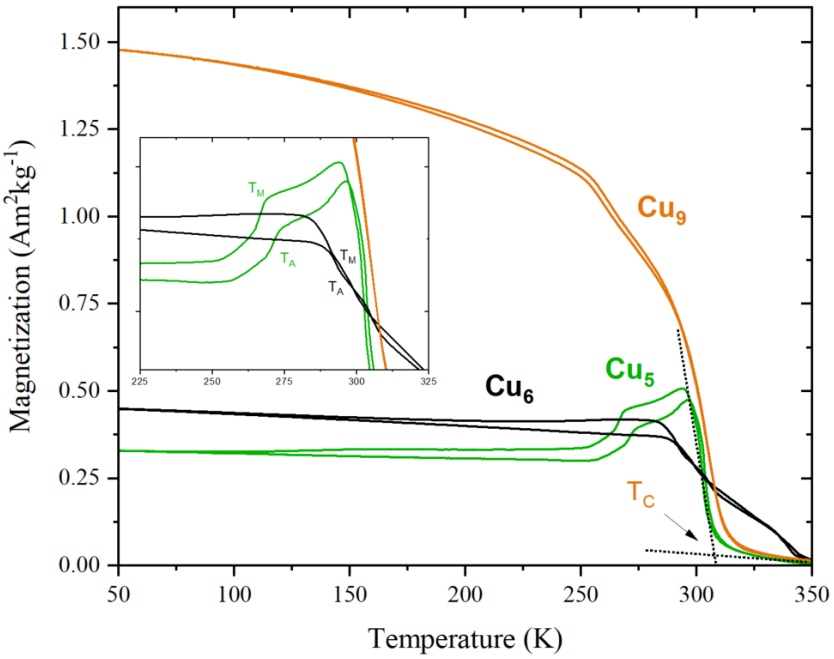

***Figure 5.3**. Temperature evolution of the magnetization for the Cu_5, Cu_6 and Cu_9 alloys, measured with a 0.005 T applied magnetic field. The inset shows the detailed martensitic and austenitic transformations for the Cu_5 and Cu_6 samples.*

An evident increase in T_M and a negligible change in T_C, associated with a higher content of Cu, can be appreciated. This results in the magnetic transition occurring either within the austenite phase (Cu_5), the martensite phase (Cu_9), or simultaneously with the MT (Cu_6), being the latter the reason for not having included a specific T_C in **Table 5.1.** This simultaneity, alongside with the small thermal hysteresis it displays, makes this alloy composition the most suitable for magnetocaloric related applications[10].

5.3.2. Powder neutron diffraction

Previous studies[24,25] have correlated an increasing T_M with a higher *e/a* value. However, that is not the case in this work, since there is no lineal relationship between both factors. Therefore, the explanation must arise from the crystalline structure and atomic ordering[26], reason why a powder neutron diffraction study was performed. As previously mentioned, several diffractograms were obtained at different temperatures, showing paramagnetic austenite, ferromagnetic austenite, weak magnetic martensite phases, or a mix of two of those phases, as summarized in **Table 5.2**.

***Table 5.2**. Powder neutron diffractograms acquisition temperatures and phases measured at these temperatures.*

Alloy	Temperature (K)	Phases
Cu_5	315	Paramagnetic austenite
	280	Ferromagnetic austenite + Ferromagentic martensite
	265	Ferromagnetic austenite + Ferromagentic martensite
	230	Ferromagnetic austenite + Ferromagentic martensite
Cu_6	335	Paramagnetic austenite + Ferromagentic martensite
	300	Paramagnetic austenite + Ferromagentic martensite
	240	Ferromagentic martensite
	205	Ferromagentic martensite
Cu_9	501	Paramagnetic austenite + Paramagnetic martensite
	466	Paramagnetic austenite + Paramagentic martensite
	394	Paramagnetic martensite
	359	Ferromagentic martensite

LeBail refinements were performed at the higher and lower temperatures measured for each alloy, resulting in the fittings presented in **Figures A.2.1 – A.2.3** (see **Figure 5.4** for a representative). Out of these fittings, the space groups and lattice parameters shown in **Table 5.3** are obtained

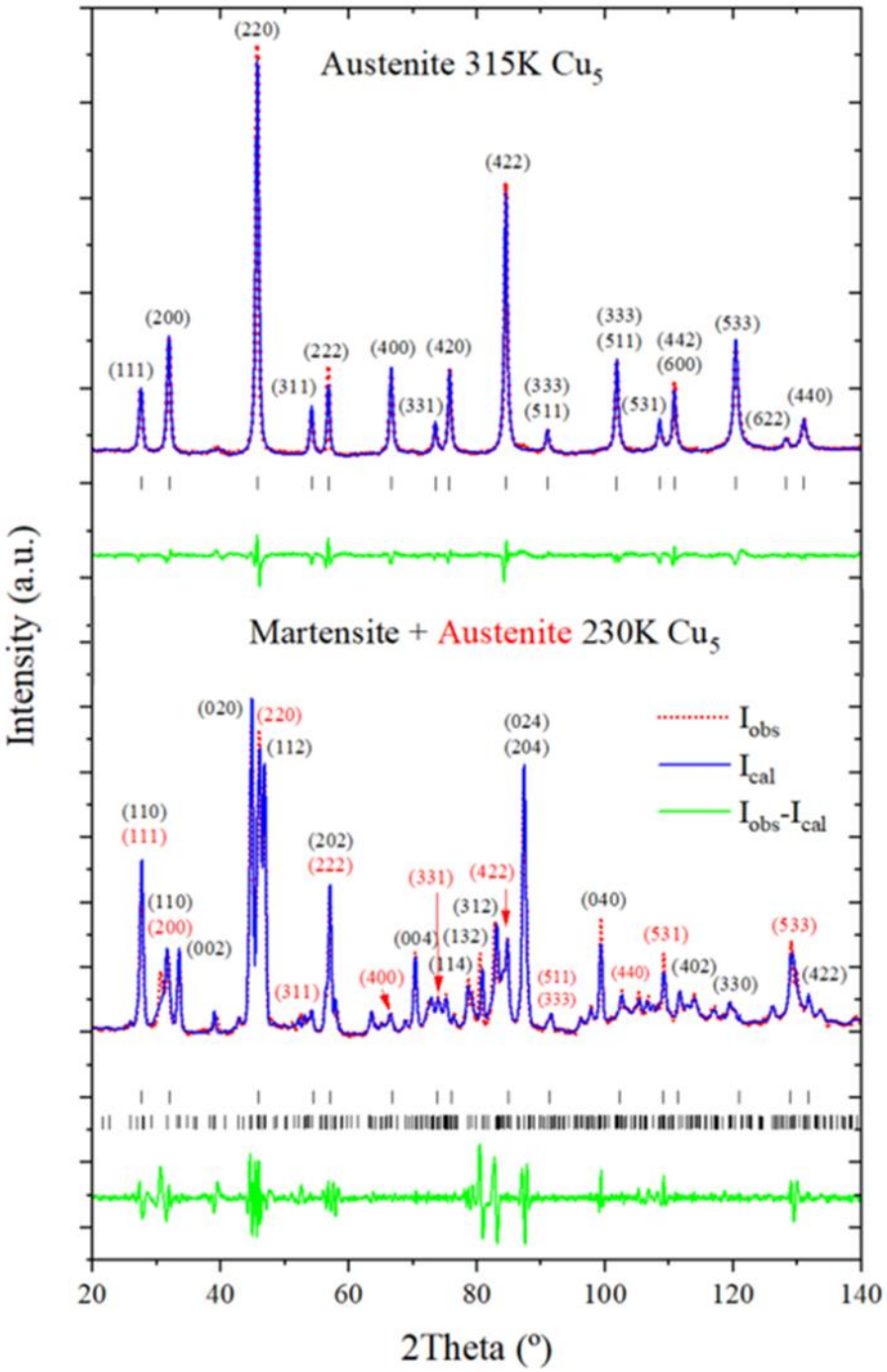

***Figure 5.4**. Neutron diffraction patterns and LeBail refinements for the Cu_5 cubic austenite + tetragonal martensite at 501K and tetragonal martensite at 359K. Red dots represent experimental points; blue lines are the LeBail fittings; and green lines correspond to the difference between the measurements and the fittings. The Miller indices corresponding to each reflection are indicated with a black line and indexed above each peak, with its colour indicating its correspondence to the austenite or martensite phases.*

***Table 5.3**. Lattice parameters, space groups and predominating (main) phase at the highest and lowest measured temperatures for Cu_5, Cu_6 and Cu_9 alloys.*

Alloy	Temperature (K)	Main Phase	Space group	Lattice (Å)
Cu_5	315	Austenite	Fm-3m	a = 5.81
	230	Martensite	Immm 5M	a = 4.12, b = 4.19, c = 5.54
Cu_6	335	Austenite	Fm-3m	a = 5.81
	205	Martensite	Immm 5M	a =4.10, b = 4.18, c = 5.53
		Martensite	I4/mmm NM	a = 3.87, c = 6.46
Cu_9	501	Austenite	Fm-3m	a = 5.81
	359	Martensite	I4/mmm NM	a = 3.86, c = 6.54

From these results, several observations were made, which are in concordance to previous studies[9]:

- The Cu_5 alloy shows a partial structural transformation from a $L2_1$ cubic austenite (space group *Fm-3m*, common to all austenite phases in these alloys) to a *5M* modulated orthorhombic martensite (space group *Immm*).
- The Cu_6 alloy undergoes a MT from a $L2_1$ phase to a *5M* modulated orthorhombic, followed by an intermartensitic transformation, from a *5M* modulated orthorhombic (space group *Immmm*) to a non-modulated tetragonal, $L1_0$, (space group *I4/mmm*) martensitic phase. It must be mentioned that, even though no sign of this intermartensitic transformation is appreciated in the magnetic measurements, a slight peak, corresponding to the heat exchange associated to this transformation, can be observed at 260 K in the DSC measurements.
- The Cu_9 alloy shows a complete structural transformation from the $L2_1$ cubic austenite phase to a non-modulated tetragonal $L1_0$ martensite.

When the pattern matching fittings are performed in the remaining measured diffractograms at different temperatures, the lattice parameters' evolution with temperature can be disclosed (see **Figure 5.5**). A nearly constant austenitic cubic lattice parameter (a_C) is observed, irrespective of the Cu-doping amount. This is similar to what happens with the value of the lattice

parameters ($a_{O,T}$, $b_{O,T}$ *and* $c_{O,T}$) in the martensite phases, meaning that the unit cell remains almost unaltered upon temperature changes within the temperature ranges measured.

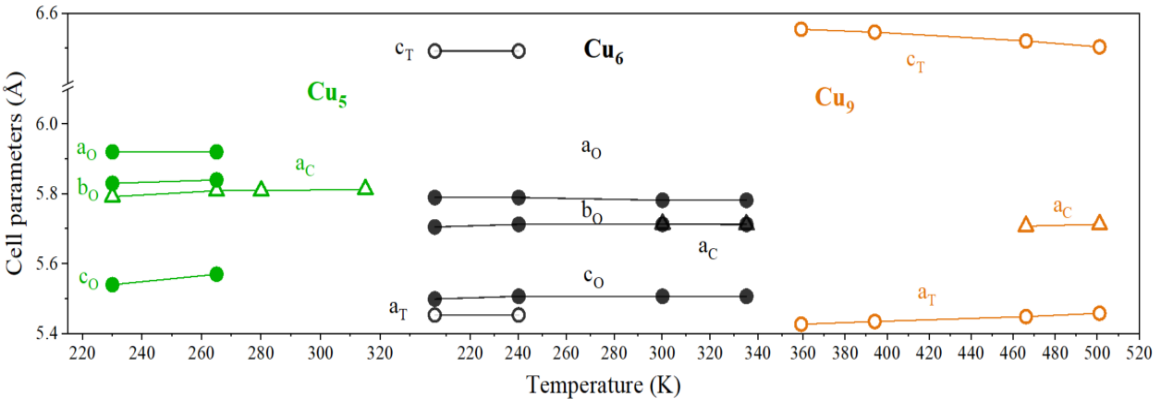

Figure 5.5*: Lattice parameters evolution with temperature, using the fcc cell as reference. Triangles represent the austenitic parameters, bold dots correspond to the orthorhombic martensite, and circles to the tetragonal martensite.*

With this crystallographic analysis, and as previously anticipated, the increase of T_M with the increasing Cu content can be explained. These results lead to conclude that the higher the Cu content, the more structurally different austenite and martensite phases are, resulting into a higher *c/a* distortion associated to the lower temperature martensite. The structural difference between the austenite and the martensite is physically represented by the *c/a* relationship: *c/a* = 0.95, 0.95(Immm5M)/1.18(I4/mmm) and 1.20 for Cu_5, Cu_6 and Cu_9, respectively.Due to this increasing distortion, more energy is needed to induce the structural transformation, and the MT occurs at higher temperatures. These results are in line with previous studies, where Fe is employed as dopant and a reduced martensitic structural distortion, with its subsequent decrease in T_M, was reported.[27]

Once the origin of the evolution of T_M as a function of Cu % has been explained, Rietveld fittings (see **Figure 5.6**) were employed to unravel the atomic site occupancies and to explain the evolution of T_C and $\mu_{sat,}$ being the latter highly dependant on the magnetic interactions between atoms and, hence, on the atomic site occupancies. The results, presented in **Table 5.4**, were obtained by performing the Rietveld refinements on those diffractograms displaying a single phase: the highest temperature austenite for Cu_5 (315 K) and the lowest temperature martensite for Cu_9

(359 K). Nevertheless, no diffractogram measured in the Cu_6 alloy shows a single phase, so the analysis was performed in an austenite and martensite mixed phase measured at 335 K. The atomic site occupancies were ascertained by using them for subsequent Rietveld fittings performed in the other phase measured for each alloy (austenite for Cu_9, martensite for Cu_5 and a mix of martensite and austenite at 205K for Cu_6)

Table 5.4. *Atomic site occupancies (at%) of the studied alloys obtained via Rietveld refinements.*

Alloy	Position	Ni	Mn	Ga	Cu
Cu_5	(0.25, 0.25, 0.25) - 8c	50	–	–	–
	(0, 0, 0) - 4a	0.4	18.9	5.7	–
	(0.5, 0.5, 0.5) - 4b	–	–	20.1	4.9
Cu_6	(0.25, 0.25, 0.25) - 8c	49.4	0.6	–	–
	(0, 0, 0) - 4a	–	17.7	7.2	–
	(0.5, 0.5, 0.5) - 4b	–	0.8	18.6	5.6
Cu_9	(0.25, 0.25, 0.25) - 8c	49.1	0.9	–	–
	(0, 0, 0) - 4a	–	13.9	11.1	–
	(0.5, 0.5, 0.5) - 4b	–	1.4	14.1	9.5

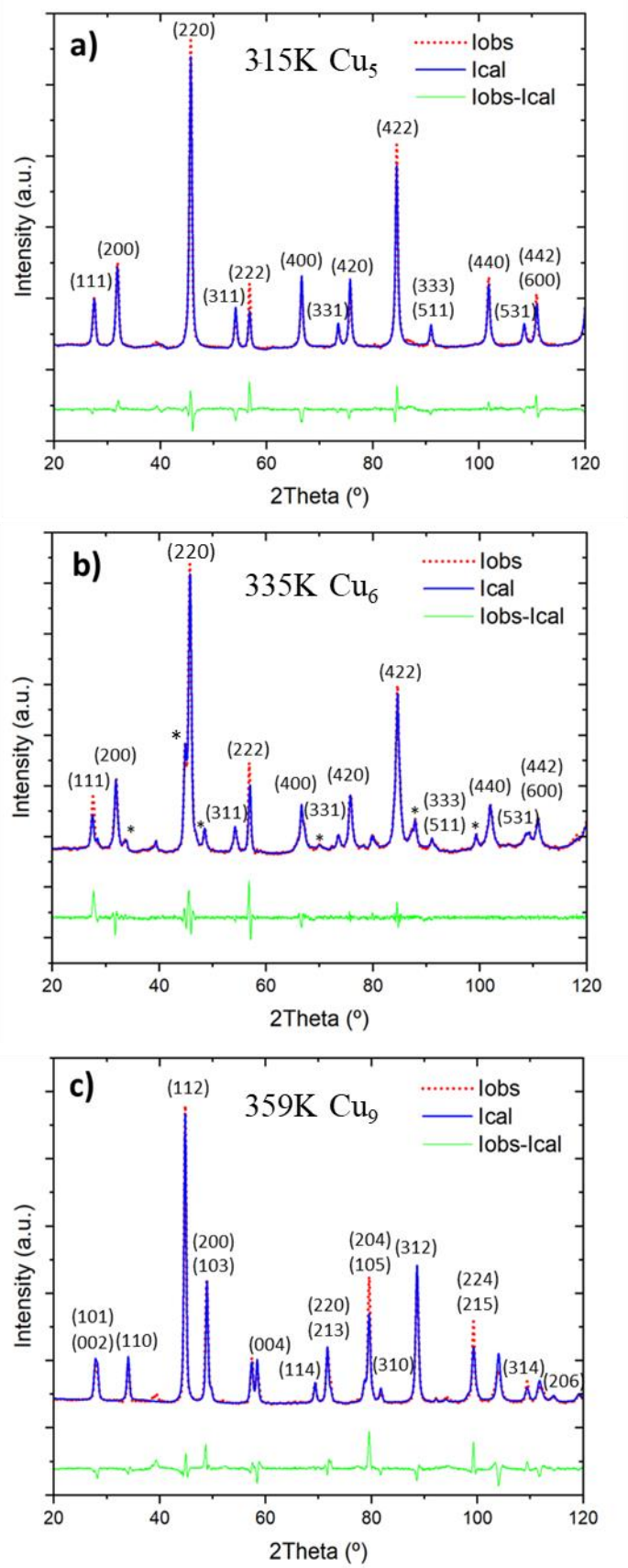

Figure 5.6. *Neutron diffraction patterns and Rietveld refinements for the a) Cu_5 cubic austenite at 315K b) Cu_6 cubic austenite + orthorhombic martensite (indicated with an asterisk) at 335K and c) Cu_9 tetragonal martensite at 359K. Red dots represent experimental points; blue*

lines are the Rietveld fittings; and green lines correspond to the difference between the measurements and the fittings. The Miller indices corresponding to each reflection are indicated with a black line and indexed above each peak of the main phase.

As more than two different atomic species can be present in a specific crystallographic site, the analysis of the occupancies cannot be solved fully experimentally, and therefore some assumptions should be made. The model employed for the refinements was based on the approaches available on literature for Cu-doped Ni-Mn-Ga alloys [28], where the atoms follow the $L2_1$ order in the austenite phase (see **Section 1.2.3**). Besides this, it was assumed that Cu atoms occupy 4a Wyckoff positions, since this is a clear tendency shown by Cu as dopant in $Ni_{50}Mn_{25-x}Ga_{25}Cu_x$ systems[28–30]. This, together with the Ga in excess also taking 4a sites, leads to Mn atoms being displaced to 8c and 4b sites in the alloys with an atomic percentage of Cu greater than 5, whereas for the 5 % Cu content sample the Mn atoms remain at 4a positions, due to the small amount of displaced Ga.

5.4. MAGNETIC INTERACTIONS AND STRUCTURE

The atomic site occupancies are highly correlated with the magnetic coupling, since it has been demonstrated that the main contribution to the magnetism of the Ni–Mn-based FeOrromagnetic SMAs comes from the Mn atoms moments and Mn–Mn exchange interactions, with further contributions coming from the Mn-Ni coupling[26,27,31]. We may anticipate the presence of antiferromagnetic exchange interactions between displaced Mn atoms (placed on 8c or 4b Wyckoff sites), due to a particular, RKKY-type relation between the nature of the exchange coupling[32,33], and the interatomic distances (ferromagnetic above 3.32 Å and antiferromagnetic below 2.92 Å)[26,31]

Using the phases at each temperature and the corresponding lattice parameters (see **Table 5.2**), together withd the information provided by the atomic orderings (see **Table 5.3**), the type of exchange coupling between Mn atoms in this particular system of alloys can be elucidated, making it possible to calculate the total magnetic moment per unit formula and to compare it to the experimentally measured one. The experimental magnetic moments were determined by the Arrot plot method[34] from

magnetization curves, which will be presented and discussed later, obtained at 5 K with applied magnetic fields up to 7 T, to make sure that every alloy is in the ferromagnetic martensite phase. Therefore, the atomic distances employed to determine the nature of the magnetic interactions (i.e. ferromagnetic or antiferromagnetic) correspond to those calculated for the orthorhombic (Cu_5) and the tetragonal martensite (Cu_6 and Cu_9) unit cells.

The equations employed to determine the interatomic distances in the orthorhombic cell are shown in **Figure 5.7**, while the **Equations 5.2 – 5.5**[27] were used to determine the interatomic distances within the tetragonal unit cell. While the employed Wyckoff denotations 8c, 4a, 4b correspond to the austenitic cell, rather than to the martensitic one, the notation is kept also for the martensite, due to the fact that the martensitic transformation is diffusionless and the atomic sites, equivalent, as previously explained in the **Section 1.2** of the **Chapter 1**.

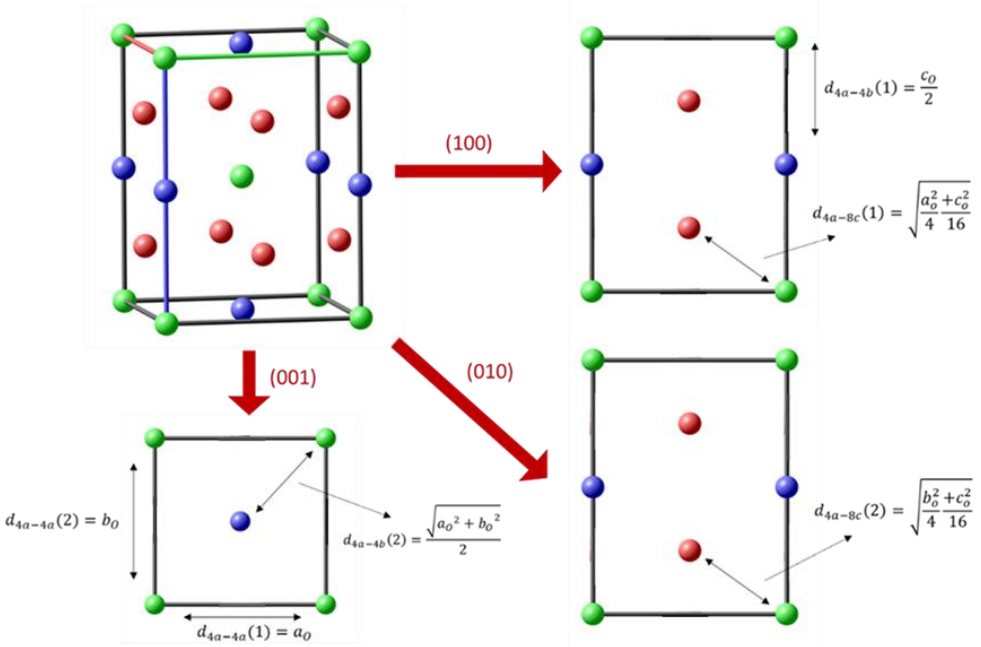

***Figure 5.7**. 3D representation of the martensitic orthorhombic Immm structure, where red, green, and blue balls represent the equivalent 8c, 4a and 4b Wyckoff sites of the austenite phase, respectively. (100), (010) and (001) planes are shown, together with their corresponding interatomic distances.*

$$d_{4a-4b}(1) = \frac{c_T}{2} \qquad \textbf{Equation 5.2}$$

$$d_{4a-4a} = a_T \qquad \textbf{Equation 5.3}$$

$$d_{4a-4b}(2) = \frac{a_T\sqrt{2}}{2} \qquad \textbf{Equation 5.4}$$

$$d_{4a-4c} = \sqrt{\frac{{a_T}^2}{4} + \frac{{c_T}^2}{16}} \qquad \textbf{Equation5.5}$$

The calculated interatomic distances in the martensite phases of all the alloys, employing the corresponding tetragonal or orthorhombic cell parameters, are shown in **Table 5.5**.

***Table 5.5**: Interatomic distances within the martensite phases calculated for each of the measured alloys, referred to the atomic species located at the Wyckoff sites specified as subscripts for each distance. (1) and (2) represent different possible distances between positions in the orthorhombic cell, as depicted in Figure 5.6.*

Alloy	$d_{4a\text{-}4a}(1)$ (Å)	$d_{4a\text{-}4a}(2)$ (Å)	$d_{4a\text{-}4b}(1)$ (Å)	$d_{4a\text{-}4b}(2)$ (Å)	$d_{4a\text{-}4c}(1)$ (Å)	$d_{4a\text{-}4c}(2)$ (Å)
Cu_5	4.120	4.190	2.770	2.940	2.480	2.510
Cu_6	3.863	–	3.261	2.731	2.528	–
Cu_9	3.855	–	3.271	2.725	2.528	–

As previously mentioned, in this work we aimed to determine the type of interatomic magnetic interactions by comparing the experimentally measured magnetization saturaton, μ_{sat}, with the calculated one based on the obtained atomic site occupancies. For this purpose, three different models, accounting for the different nature of magnetic interactions between atoms, are proposed hereafter. This is an alternative method to the magnetic Rietveld analysis, performed in **Chapter 4.**

Every model starts with the assumption that the Mn atoms contribute with 3.51 μ_B/atom and Ni with 0.33 μ_B/atom [35,36], while Cu and Ga present a null magnetic moment[26]. Model 1 assumes only ferromagnetic interactions between every Mn atom, and a ferromagnetic coupling with Ni atoms. Models 2 and 3 take into consideration the previously mentioned possible antiferromagnetic coupling between Mn atoms when they are apart from each other less than 2.92 Å, assuming partial (model 2) and total (model 3) antiferromagnetic coupling between displaced (Mn in 8c and 4b positions) and properly placed (Mn in 4a positions) Mn atoms. For every model, the contribution of the excess Ni atoms was considered to be ferromagnetic.[35]

Model 2 assumes that Mn atoms placed in their own 4a sites are coupled ferromagnetically with the Ni magnetic moments, while the Mn atoms displaced to 4b positions present an antiferromagnetic or ferromagnetic coupling depending on the nature of their first neighbours. The interaction between Mn atoms in 4a sites and those in 8c sites is always antiferromagnetic as their interatomic distances are below

2.92 Å. However, the Mn placed at 4b sites presents an antiferromagnetic coupling when their closest neighbours are Ni on 8c sites, but it becomes ferromagnetic for Mn atoms at the 8c sites, which overcome the antiferromagnetic coupling between Mn atoms in their proper sites (4a) and Mn displaced to the Ga sites (4b). The percentage of ferromagnetic and antiferromagnetic interactions occurring in these positions can be calculated by **Equations 5.6 and 5.7** respectively, based on those employed in previous similar works[26,35]

$$\%at\ Mn/4b_{FM} = (\%at\ Mn/4b)\cdot(\%at\ Mn/8c)/2 \qquad \textbf{Equation 5.6}$$

$$\%at\ Mn/4b_{AFM} = (\%at\ Mn/4b) - \%at\ Mn/4b_{FM} \qquad \textbf{Equation 5.7}$$

And the total magnetic moment can be calculated by using the next equation:

$$\mu(\mu_B/FU) = 4/100((\%at\ Ni\cdot m_{NI} + (\%at\ Mn/4a + \%at\ Mn/4b_{FM})\cdot m_{Mn})- (\%at\ Mn/4b_{AFM} + (\%atMn/8c)/2)\cdot m_{Mn})) \qquad \textbf{Equation 5.8}$$

Since Model 3 assumes that Mn atoms placed at 4a positions present ferromagnetic coupling with Ni atoms and antiferromagnetic coupling with both Mn atoms displaced to 4b and 8c positions, the total magnetic moment is calculated by **Equation 8**:

$$\mu(\mu_B/FU) = 4/100((\%at\ Ni\cdot m_{Ni} + \%at\ Mn/4a\cdot m_{Mn})- ((\%atMn/8c)/2) + (\%atMn/4b)\cdot m_{Mn}) \qquad \textbf{Equation 5.9}$$

Table 5.6 shows the calculated values of the total magnetic moment per formula unit by each of the three models used, accompanied by the experimentally measured ones.

Table 5.6*. Magnetization saturation moments, per formula unit, of the studied alloys, obtained experimentally (from Figure 7a) and calculated based on the atomic site occupancies obtained via Rietveld refinements (Table 3). The number after μ_{cal} corresponds to the model used for the calculations.*

Alloy	M_S (emu/g)	μ_{exp} (μ_B/FU)	μ_{cal} 1 (μ_B/FU)	μ_{cal} 2 (μ_B/FU)	μ_{cal} 3 (μ_B/FU)
Cu_5	77.0	3.37	3.32	3.31	3.31
Cu_6	67.0	2.93	3.33	2.94	2.97
Cu_9	54.9	2.41	2.92	2.35	2.34

The comparison between the experimental and calculated magnetic moments allows us to distinguish three different situations, one for each of the alloys studied:

- Cu_5 alloy: there are no displaced Mn atoms out of the 4a positions, so every Mn-Mn distance is roughly 4.2Å, implying that there are no antiferromagnetic interactions.
- Cu_6 alloy: since it is Ni-deficient and there is Mn atoms displaced to both 8c and 4b positions, the distances between properly placed and displaced Mn atoms are close to 2.5 and 2.7Å, respectively. The interaction between Mn atoms in 4a sites and those in 8c sites is antiferromagnetic, whereas it is partially ferromagnetic between Mn atoms in 4a and in 4b sites, meaning a partial ferromagnetic-to-antiferromagnetic interaction crossover between Mn atoms.
- Cu_9 alloy: while it is also Ni-deficient with Mn atoms displaced to both 8c and 4b positions, the modest difference between the μ_{cal} obtained with models 2 and 3 hinders to determine whether the partial magnetic crossover happens.

Based on this, we demonstrated not only that the atomic ordering hypothesis obtained via Rietveld analysis is consistent with the physical behaviour of the alloy, but also the presence of antiferromagnetic exchange coupling between Mn atoms out of the 4a positions. It cannot be concluded whether the Mn atoms displaced to 4b suffer a partial magnetic interaction crossover (from ferromagnetic to antiferromagnetic), due to the antiferromagnetic coupling between Mn atoms in their own positions and in 8c positions, as discussed within the previous models. This allows us to conclude that these particular interactions are not the most relevant in this set of alloys.

The correlation between T_C and μ_{sat} was also drawn by the data presented in Figure 5.8. In Figure **5.8a**, the decrease of the latter with increasing Cu content is evident, while in **Figure 5.8b** the decrease is correlated with the decrease in the Mn atoms interacting ferromagnetically (assuming ferromagnetic interactions between the Mn atoms in their own sites and those in Ga sites, see **Table 5.3**), rather than to the percentage of total Mn atoms. The competence between the percentage of total

Mn atoms and the percentage of Mn atoms interacting ferromagnetically is the reason of the barely changing T_C, what comes together with the bibliographically reported correlation between the decrease in T_C and the increasing Cu content in this system.[9]

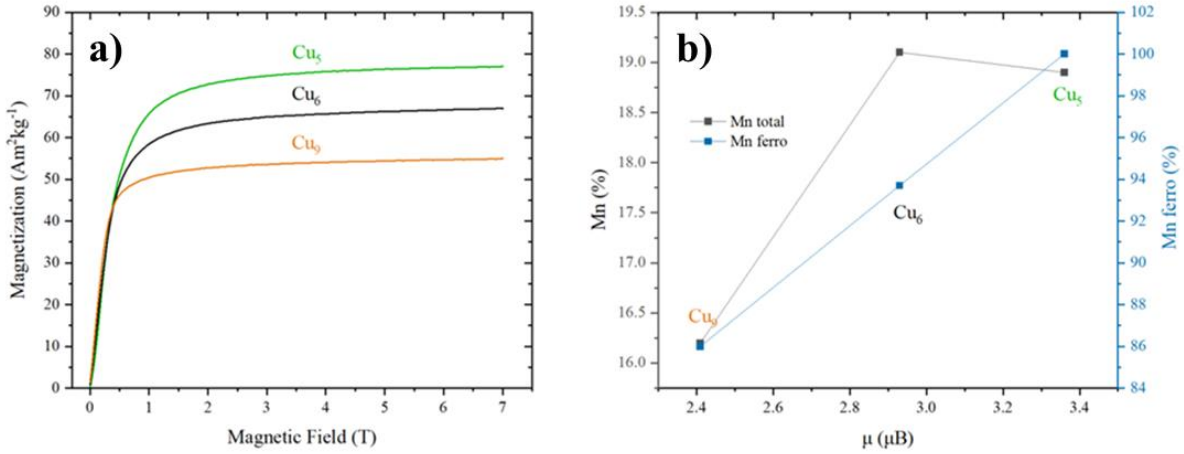

Figure 5.8 *a) Magnetic field evolution of the magnetization for Cu_5, Cu_6 and Cu_9 at* 5K. *b) Correlation between the saturation magnetization, the percentage of Mn atoms in each alloy and the percentage of Mn atoms interacting ferromagnetically.*

5.5. SUMMARY AND CONCLUSIONS

In the present work we have analysed the transformation behaviour, crystal structure and magnetic properties of the powder samples as a function of the Cu content, with the aim of understanding its effect on potential magnetocaloric applications.

For the preparation of the $Ni_{50}Mn_{25-x}Ga_{25}Cu_x$ powders, arc-melting furnace was used to fabricate bulk alloys that were subsequently grinded to obtained powders. The transformation behaviour, crystal structure and magnetic properties of the powder samples as a function of the Cu content were systematically studied by neutron powder diffraction and magnetic characterization measurements.

The changes in the crystal structures of both the austenite and martensite phases induced via Cu doping were studied by LeBail fittings. We have found that, even when there are no significant changes in the *Fm-3m* austenite phase upon Cu doping, the martensitic transformation is greatly affected. In the Cu_5 alloy, the MT leads to a 5M modulated *Immm* orthorhombic martensite, while in the Cu_9 alloy, the resultant martensite is a non-modulated *I4/mmm* tetragonal one. The intermediate

composition (Cu_6) alloy suffers from an intermartensitic transformation, from a 5M modulated *Immm* to a non-modulated *I4/mmm* one. The explanation of the higher T_M as the Cu content increases can be found in this more distorted martensite, implying a more energetic MT.

Analogously to the variation in T_M being explained by the observed structural changes, the explanation for the evolution of T_C and μ_{sat} is linked to the atomic site occupancies, which were unravelled via Rietveld refinements. The key role of Mn-Mn interactions in these alloys has been fully disclosed, finding that the magnetization saturation is dependent on the presence of ferromagnetic and/or antiferromagnetic interactions between Mn atoms, which depend on the interatomic distances that, in turn, are deduced from the different martensite phases stabilized in the alloys. Due to the less number of ferromagnetic interactions and Mn content, a lower T_C was expected with the increasing Cu content, this magnetic transition occurring in either the austenite or the martensite led to barely changing values

These studies follow the line towards a systematic design of MMSMA alloys for possible magnetocaloric applications, in a similar way to the Ni-Mn-Sn-Co alloys studied in **Chapter 4**. More specifically, these alloys pave the way to create systems with optimized properties to be used as possible heat exchangers in technological applications, where the determinant specific magnetic interactions between atoms can be tailored through custom-made Cu doping of the alloys.

5.6. BIBLIOGRAPHY

1. Ullakko K, Huang JK, Kantner C, Handley RCO. Large magnetic-field-induced strains in Ni2MnGa single crystals Large magnetic-field-induced strains in Ni 2 MnGa single crystals. *Appl Phys Lett*. 2013;69(13):1966-1998.

2. Umetsu RY, Ito W, Ito K, et al. Anomaly in entropy change between parent and martensite phases in the Ni50Mn34In16 Heusler alloy. *Scr Mater*. 2009;60(1):25-28. doi:10.1016/j.scriptamat.2008.08.022

3. Monroe JA, Karaman I, Basaran B, et al. Direct measurement of large reversible magnetic-field-induced strain in Ni-Co-Mn-In metamagnetic shape memory

alloys. *Acta Mater*. 2012;60(20):6883-6891. doi:10.1016/j.actamat.2012.07.040

4. Nambiar SS, Murthy BRN, Sharma S, Prasanna AA, Chelvane AJ. Microstructure and Mechanical Properties of Annealed Quinary Ni-Mn-Sn-Fe-In Heusler Alloy. *Eng Sci*. 2022;17:303-308. doi:10.30919/es8d632

5. Esakki Muthu S, Rama Rao N V., Manivel Raja M, Raj Kumar DM, Mohan Radheep D, Arumugam S. Influence of Ni/Mn concentration on the structural, magnetic and magnetocaloric properties in Ni50-xMn37+xSn13 Heusler alloys. *J Phys D Appl Phys*. 2010;43(42). doi:10.1088/0022-3727/43/42/425002

6. Zhukova V, Ipatov M, Granovsky A, Zhukov A. Magnetic properties of Ni-Mn-In-Co Heusler-type glass-coated microwires. *J Appl Phys*. 2014;115(17):10-13. doi:10.1063/1.4868919

7. Sandeman KG. Magnetocaloric materials: The search for new systems. *Scr Mater*. 2012;67(6):566-571. doi:10.1016/j.scriptamat.2012.02.045

8. Franco V, Blázquez JS, Ipus JJ, Law JY, Moreno-Ramírez LM, Conde A. Magnetocaloric effect: From materials research to refrigeration devices. *Prog Mater Sci*. 2018;93:112-232. doi:10.1016/j.pmatsci.2017.10.005

9. Seguí C, Torrens-Serra J, Cesari E, Lázpita P. Optimizing the caloric properties of Cu-doped Ni-Mn-Ga alloys. *Materials (Basel)*. 2020;13(2). doi:10.3390/ma13020419

10. Stevens E, Kimes K, Salazar D, et al. Mastering a 1.2 K hysteresis for martensitic para-ferromagnetic partial transformation in Ni-Mn(Cu)-Ga magnetocaloric material via binder jet 3D printing. *Addit Manuf*. 2021;37(August 2020). doi:10.1016/j.addma.2020.101560

11. Gutfleisch O, Gottschall T, Fries M, et al. Mastering hysteresis in magnetocaloric materials. *Philos Trans R Soc A Math Phys Eng Sci*. 2016;374(2074). doi:10.1098/rsta.2015.0308

12. Río-lópez NA, Lázpita P, Salazar D, et al. Neutron scattering as a powerful tool to investigate magnetic shape memory alloys: A review. *Metals (Basel)*.

2021;11(5):1-21. doi:10.3390/met11050829

13. L'vov VA, Chernenko VA, Barandiaran JM. Magnetic shape memory materials with improved functional properties: Scientific aspects. In: *Springer Series in Materials Science*. Vol 231. .) Novel f. Springer International Publishing; 2016:1-40. doi:10.1007/978-3-319-26106-5_1

14. Billinge SJL, Levin I. The problem with determining atomic structure at the nanoscale. *Science (80-)*. 2007;316(5824):561-565. doi:10.1126/science.1135080

15. Sokolovskiy V, Grünebohm A, Buchelnikov V, Entel P. Ab initio and Monte Carlo approaches for the magnetocaloric effect in Co- and in-doped Ni-Mn-Ga Heusler alloys. *Entropy*. 2014;16(9):4992-5019. doi:10.3390/e16094992

16. Kataoka M, Endo K, Kudo N, et al. Martensitic transition, ferromagnetic transition, and their interplay in the shape memory alloys Ni2 Mn1-x Cux Ga. *Phys Rev B - Condens Matter Mater Phys*. 2010;82(21):1-14. doi:10.1103/PhysRevB.82.214423

17. Stadler S, Khan M, Mitchell J, et al. Magnetocaloric properties of Ni 2Mn 1-xCu xGa. *Appl Phys Lett*. 2006;88(19). doi:10.1063/1.2202751

18. Alijani F, Reihanian M, Gheisari K, Edalati K, Miyamoto H. Effect of Homogenization on Microstructure and Hardness of Arc-Melted FeCoNiMn High Entropy Alloy During High-Pressure Torsion (HPT). *J Mater Eng Perform*. 2022;31(6):5080-5089. doi:10.1007/s11665-021-06573-8

19. Rodríguez-Crespo B, Salazar D, Lanceros-Méndez S, Chernenko V. Development and magnetocaloric properties of Ni(Co)-Mn-Sn printing ink. *J Alloys Compd*. 2022;917:165521. doi:10.1016/j.jallcom.2022.165521

20. Rodríguez-Crespo B, Río-López N., Lázpita P, et al. Impact of magnetic, atomic and microstructural ordering on the magnetocaloric performance of powdered NiCoMnSn metamagnetic shape memory ribbons. *Mater Des*. Published online 2024:113279. doi:10.1016/j.matdes.2024.113279

21. PORRO AZPIAZU Jose Maria; CESARI Eduard; J. Gutierrez; LAZPITA Patricia;

MONDELLI Claudia; A. Perez-Checa; RODRIGUEZ VELAMAZAN Jose Alberto and Segui C. Influence of Cu addition on structural and magnetic properties of Ni50Mn25-xGa25Cux (x = 3, 6 and 9) metamagnetic shape memory alloys. *Inst Laue-Langevin*. Published online 2020. doi:10.5291/ILL-DATA.5-31-2707

22. Chernenko V. Compositional instability of B—phase in Ni—Mn-Ga alloys. *Scr Mater*. 1999;40(5):523-527. http://scholar.google.com/scholar?hl=en&btnG=Search&q=intitle:COMPOSITIONAL+INSTABILITY+OF+b-PHASE+IN+Ni-Mn-Ga+ALLOYS#0

23. Geshev J, Popov O, Mikhov M, Sanchez Ll JL, Suarez N, Leccabue F. The Hopkinson effect in a BaFe12O19 fine particle system: demagnetization field effects. *J Magn Magn Mater*. 1992;117(1-2):190-194. doi:10.1016/0304-8853(92)90310-K

24. Enkovaara J, Heczko O, Ayuela A, Nieminen RM. Coexistence of ferromagnetic and antiferromagnetic order in Mn-doped Ni2MnGa. *Phys Rev B - Condens Matter Mater Phys*. 2003;67(21):14-17. doi:10.1103/PhysRevB.67.212405

25. Jin X, Marioni M, Bono D, Allen SM, O'Handley RC, Hsu TY. Empirical mapping of Ni-Mn-Ga properties with composition and valence electron concentration. *J Appl Phys*. 2002;91(10 I):8222-8224. doi:10.1063/1.1453943

26. Lázpita P, Barandiarán JM, Gutiérrez J, Feuchtwanger J, Chernenko VA, Richard ML. Magnetic moment and chemical order in off-stoichiometric Ni-Mn-Ga ferromagnetic shape memory alloys. *New J Phys*. 2011;13:1-14. doi:10.1088/1367-2630/13/3/033039

27. Pérez-Checa A, Porro JM, Feuchtwanger J, et al. Role of Fe addition in Ni–Mn–Ga–Co–Cu–Fe ferromagnetic shape memory alloys for high-temperature magnetic actuation. *Acta Mater*. 2020;196:549-555. doi:10.1016/j.actamat.2020.07.007

28. Li CM, Luo H Bin, Hu QM, Yang R, Johansson B, Vitos L. Site preference and elastic properties of Fe-, Co-, and Cu-doped Ni 2MnGa shape memory alloys from first principles. *Phys Rev B - Condens Matter Mater Phys*. 2011;84(2):1-10. doi:10.1103/PhysRevB.84.024206

29. Yang MJ, Bai J, Li Z, Qiu TF. Crystal structure, phase stability and magnetic properties of Cu-doped Ni2MnGa alloys from first-principles calculations. *Mater Sci Forum*. 2016;873:3-7. doi:10.4028/www.scientific.net/MSF.873.3

30. Zelený M, Sozinov A, Straka L, Björkman T, Nieminen RM. First-principles study of Co- and Cu-doped Ni2MnGa along the tetragonal deformation path. *Phys Rev B - Condens Matter Mater Phys*. 2014;89(18):1-9. doi:10.1103/PhysRevB.89.184103

31. Lázpita P, Barandiarán JM, Chernenko VA, et al. Magnetic properties of Ni40+xMn39-xSn21 (x = 0, 2, 4, 6 and 8 at.%) Heusler alloys. *J Alloys Compd*. 2014;594:171-174. doi:10.1016/j.jallcom.2014.01.142

32. Himmetoglu B, Katukuri VM, Cococcioni M. Origin of magnetic interactions and their influence on the structural properties of Ni 2 MnGa and related compounds. 185501. doi:10.1088/0953-8984/24/18/185501

33. Ruderman M., Kittel C. Indirect Exchange Coupling of Nuclear Magnetic Moments by Conduction Electrons. 1954;96(3):72-75.

34. Arrott A. Criterion for ferromagnetism from observations of magnetic isotherms. *Phys Rev*. 1957;108(6):1394-1396. doi:10.1103/PhysRev.108.1394

35. Richard ML, Feuchtwanger J, Allen SM, et al. Chemical order in off-stoichiometric Ni-Mn-Ga ferromagnetic shape-memory alloys studied with neutron diffraction. *Philos Mag*. 2007;87(23):3437-3447. doi:10.1080/14786430701297582

36. Webster PJ, Ziebeck KRA, Town SL, Peak MS. Magnetic order and phase transformation in Ni2MnGa. *Philos Mag B Phys Condens Matter; Stat Mech Electron Opt Magn Prop*. 1984;49(3):295-310. doi:10.1080/13642817408246515

CHAPTER 6

Effect of Fe-doping on polycrystalline Ni-Mn-Ga-Co-In alloys

6.1. INTRODUCTION

Ni-Mn-Ga alloys have been attracting great interest for decades[1–5], partly due to the contactless deformation they can undergo when subjected to an external magnetic field, making them highly suitable for magnetostrictive-related applications, such as sensors and actuators[6–8]. Since this deformation is driven by the movement of twin variants or by the magnetic field induced MT, the potential applications are greatly conditioned by the structural and magnetic transition temperatures (T_M and T_C, respectively).

Following this line, doped Ni-Mn-Ga alloys have been extensively studied due to the interesting alteration of T_C and T_M induced through compositional variations, making them versatile materials towards their use in industrial applications, as discussed throughout different parts of this thesis. The use of Co as dopant has attracted particular attention due to inducing not only changes in the transition temperatures, but also because it remarkably improves the magnetocaloric properties in these alloys[9–11]. In a recent study[12], an interesting martensitic transformation-related volumetric change was found in Ni-Mn-Ga-Co-In alloys, in addition to considerably good magnetocaloric properties. More specifically, the $Ni_{41.7}Mn_{32.3}Ga_{14.1}Co_{8.6}In_{3.3}$ composition presents a ~1.2% volumetric deformation upon the martensitic transformation and a $\Delta S_{m,max} = 13.4$ J·kg^{-1}K^{-1}, close to other well-known magnetocaloric materials[13–15].

The goal of the work presented in this chapter is to develop a set of alloys combining these magnetocaloric and magnetostrictive properties associated to the martensitic transformation, in addition to an easily controlled actuation temperature

range. With this aim, the aforementioned composition was tuned by Fe-doping, since it has proven to dramatically affect both structural and magnetic transformation temperatures[3,16]. Although the prospective sensor and actuator applications are improved by the use of single crystals, due to the greater magnetostrictive behaviour arising from the lack of grain boundaries[17–19] this study was performed employing polycrystalline materials. The reason lies in their significantly easier fabrication method and accessibility of the characterization techniques.

Therefore, a set of $Ni_{41}Mn_{32-x}Ga_{15}Co_9In_3Fe_x$ powder alloys (x = 0, 1, 2, 4, 6) was prepared and studied via standard structural and magnetic characterization techniques, combined with powder neutron diffraction experiments, with the aim of not only studying the evolution of T_C and T_M with the Fe content, but also to understand the structural changes that lead to the aforementioned temperatures evolution.

6.2. EXPERIMENTAL PART

6.2.1. Fabrication of Ni-Mn-Ga-Co-In-Fe alloys

A polycrystalline alloy series ($Ni_{41}Mn_{32-x}Ga_{15}Co_9In_3Fe_x$, x=0, 1, 2, 4, 6, hereafter denoted as Fe_0, Fe_1, Fe_2, Fe_4 and Fe_6 respectively) was prepared by using an induction melting furnace under argon atmosphere, followed by several subsequent meltings of each alloy by the arc-melting technique, in order to obtain a more compositional and structurally homogenized alloy while minimizing the stoichiometric Mn loses due to evaporation[20]. The obtained alloy ingots were heat treated for 24 hours at 1170 K in a vacuum quartz tube, and subsequently quenched in water at 273 K. Finally, the alloys were manually grinded to obtain polycrystalline powders. The reasons behind using these specific heat treatments are detailed and referenced in previous chapters (see **Sections 4.2.1 and 5.2.1**).

6.2.2. Characterization techniques

The composition of the alloys was determined via Energy Dispersive X-Ray Spectroscopy (EDX). For the determination of the structural and magnetic transformation temperatures (T_M and T_C) Superconducting Quantum Interference

Device (SQUID) magnetometry and Vibrating Sample Magnetometry (VSM) were employed, studying the temperature evolution of the magnetization under a 5 mT applied magnetic field.

Powder neutron diffraction measurements were carried out at the D1B diffractometer of the Institute Laue-Langevin, ILL, using the λ = 1.28 Å configuration[21]. Thermodiffractograms were acquired upon sweeping the temperature from 50 K to 500 K for the low-Fe content samples, and from 300 K to 500 K for the higher Fe content samples. High resolution diffractograms were collected at selected temperatures, corresponding to specific structural and magnetic phases that will be discussed hereafter. To unravel the crystalline structures, LeBail and Rietveld refinements were performed via Fullprof software[22].

6.3. STRUCTURAL BEHAVIOUR

6.3.1. Composition and transformation characteristics

With the aim of understating the effect Fe-doping has on the crystalline structure and properties of Ni-Mn-Ga-Co-In alloys, a set of six samples were prepared and their structure and magnetic properties, studied. Their measured composition and calculated[23] *e/a* are presented in **Table 6.1**, together with the structural (T_M and T_A) and magnetic (T_C^A and T_C^M) transition temperatures. The temperature dependence of the low-field magnetization, *M(T)*, shown in **Figure 6.1**, was used to determine these characteristic temperatures, employing the derivative method (see **Sections 4.3.1 and 5.3.1** for the explanation).

Table 6.1. *Measured compositions, calculated electronic concentrations (e/a) and representative transition temperatures of the studied alloys.*

Alloy	Composition (at%)	T_M (K)	T_A (K)	T_C^A (K)	T_C^M (K)	e/a
Fe_0	$Ni_{40.7}Mn_{31.2}Ga_{16.7}Co_{8.7}In_{2.7}$	397	409	422	139	7.62
Fe_1	$Ni_{40.7}Mn_{30.8}Ga_{16.2}Co_{8.5}In_3Fe_{0.8}$	371	389	420	224	7.63
Fe_2	$Ni_{41.8}Mn_{30.2}Ga_{14.6}Co_{9.1}In_{2.9}Fe_{1.4}$	–	–	424	–	7.75
Fe_4	$Ni_{41.3}Mn_{26.8}Ga_{15.4}Co_{8.9}In_3Fe_{4.6}$	–	–	478	–	7.73
Fe_6	$Ni_{41.8}Mn_{27.9}Ga_{13.5}Co_{8.4}In_{2.5}Fe_{5.8}$	–	–	533	–	7.83

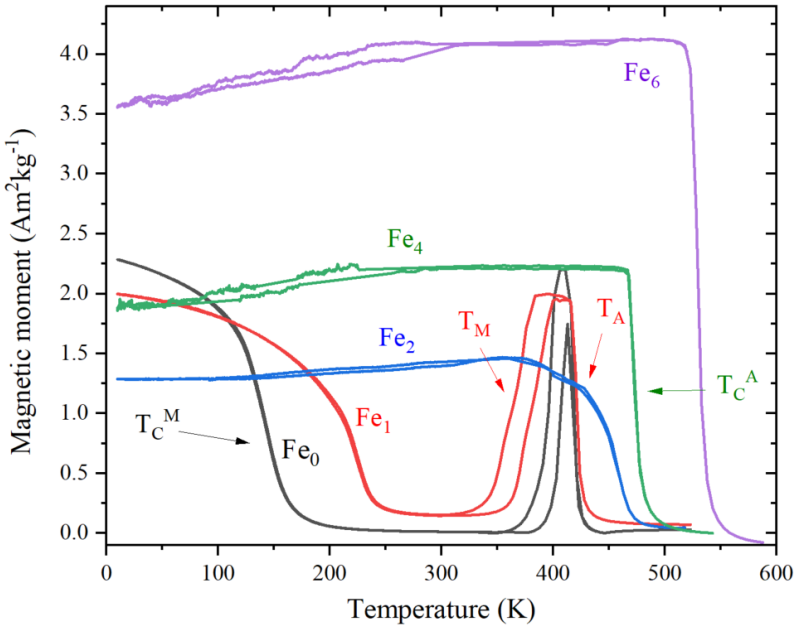

***Figure 6.1**. Magnetization evolution with temperature of the studied alloys, measured at 0.005T, alongside with an example of the approximate position of T_C^A, T_C^M, T_M and T_A. in some of the alloys studied.*

The study of the magnetization evolution with the temperature reveals the absence of a complete martensitic transformation in Fe_2, Fe_4 and Fe_6 samples, being that the reason why T_M and T_A could only be determined for the Fe_0 and Fe_1 alloys derived from the M(T) curves. Due to the parallelism with previous works[24], the uncomplete martensitic transformation in the higher-Fe content samples is attributed to the presence of secondary phases inhibiting the formation of the martensite.

Already with just a nearly 1at% of Mn substitution by Fe, an evident decrease in the martensitic temperature with respect to the non-doped one can be observed. Even though previous studies correlate this decrease with a lower electronic

concentration[23,25], the calculated *e/a* values for these two alloys are remarkably similar. Therefore, the underlying explanation should lie on the microstructure. This will be discussed in the next section, together with the evident increase in T_C^A with the higher Fe content, and the presence of T_C^M in the Fe_0 and Fe_1 alloys.

6.3.2. Powder neutron diffraction

For the determination of the austenitic and martensitic structures, the diffractograms obtained at specific temperatures were analysed. Since Fe_0 and Fe_1 alloys undergo three different transitions (paramagnetic to ferromagnetic austenite, ferromagnetic austenite to paramagnetic/weak-magnetic martensite and paramagnetic/weak-magnetic to ferromagnetic martensite), four temperatures were selected to measure the different structural and magnetic phases (see **Table 6.2**). For the Fe_2, Fe_4 and Fe_6 alloys, isothermal diffractograms were acquired at 500K, plus an additional one at 250K for the first one.

Table 6.2. *Powder neutron diffractograms acquisition temperatures and their corresponding phases measured at them.*

Alloy	Temperature (K)	Phase
Fe_0	500	Paramagnetic austenite
	450	Ferromagnetic austenite
	300	Paramagnetic martensite
	50	Magnetic martensite
Fe_1	500	Paramagnetic austenite
	400	Ferromagnetic austenite
	300	Weak magnetic martensite
	50	Magnetic martensite
Fe_2	500	Paramagnetic austenite
	250	Austenite + Martensite
Fe_4	500	Paramagnetic austenite
Fe_6	500	Paramagnetic austenite

LeBail refinements were performed in the isotherm diffractograms to determine the lattice parameters and space groups for the austenitic and martensitic

phases. Two representative LeBail refinement are shown in **Figure 6.2**, while the rest of fittings are presented in the appendix (**Figures A.3.1 – A.3.3**) to avoid overcrowding the discussion with figures. In this refinement one can observe the presence of four unfitted peaks in the martensitic phase of those samples undergoing a complete martensitic transition. Due to the parallelism with the magnetic structure unravelled by Orlandi et al.[26], we attribute them to a magnetic phase modulation which will be discussed later in **Section 6.4**.

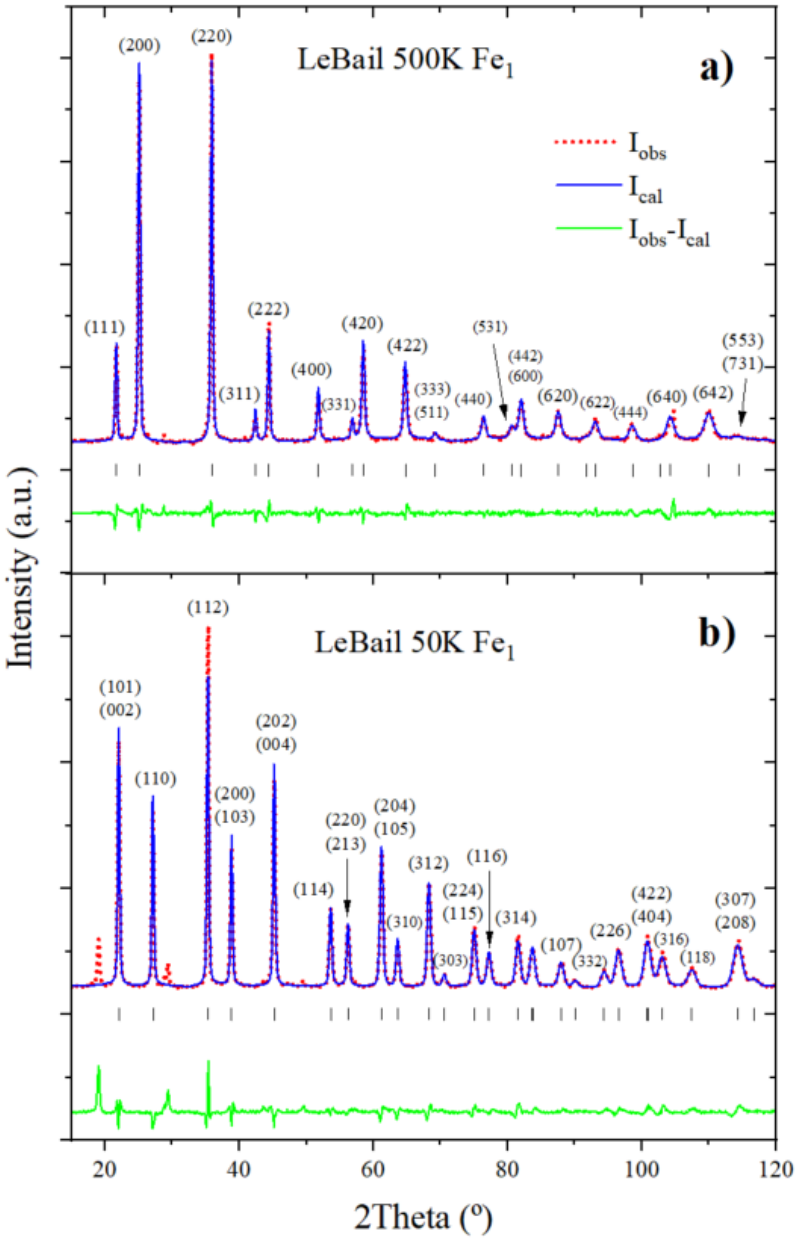

***Figure 6.2**. Neutron diffraction patterns and LeBail refinements for the a) austenite at 500K and b) martensite at 50K of the Fe_1 alloy. Red dots represent experimental points; blue lines are the LeBail fittings; and green lines correspond to the difference between the*

measurements and the fittings. The Miller indices corresponding to each reflection are indicated with a black line and indexed above each peak.

The results of these fittings are shown in **Table 6.3**. From them we can conclude that the cubic *Fm-3m* austenitic phases display an invariant (within the error) *a* parameter as the Fe content increases. A tetragonal *I4/mmm* martensite was observed both in the alloys undergoing a complete martensitic transformation (Fe_0 and Fe_1) and in Fe_2, which displays a mixture of cubic austenite and tetragonal martensite phases at 250K.

Table 6.3. *Lattice parameters, space groups and phases at the highest and lowest measured temperatures for Fe_0, Fe_1, Fe_2, Fe_4 and Fe_6 alloys.*

Alloy	Phase	Temperature (K)	Space group	Lattice parameters (Å)
Fe_0	Austenite	500	Fm-3m	a = 5.84
	Martensite	50	I4/mmm	a = 3.82, c = 6.65
Fe_1	Austenite	500	Fm-3m	a = 5.84
	Martensite	50	I4/mmm	a = 3.83, c = 6.63
Fe_2	Austenite	500	Fm-3m	a = 5.84
	Austenite	250	Fm-3m	a = 5.84
	Martensite		I4/mmm	a = 3.88, c = 6.65
Fe_4	Austenite	500	Fm-3m	a = 5.84
Fe_6	Austenite	500	Fm-3m	a = 5.84

As the diffractograms were acquired not only isothermally at the previously specified temperatures but also while continuously sweeping the temperature (**Figure 6.3**), the evolution of the lattice parameters and *c/a* relation with temperature may be disclosed via sequential LeBail fittings in these measurements. The results, displayed in **Figure 6.4**, show that Fe_0 and Fe_1 alloys present a remarkable increase in the a_T and a decrease of the c_T as the temperature rises. The evolution of the Fe_2 lattice parameters is not presented, since the range of temperatures where the presence of tetragonal martensite is appreciated (around 60K) is insufficient to analyse its evolution with temperature. An evident reduction in *c/a* as the at% Fe increases is observed for the Fe_0 and Fe_1 alloys.

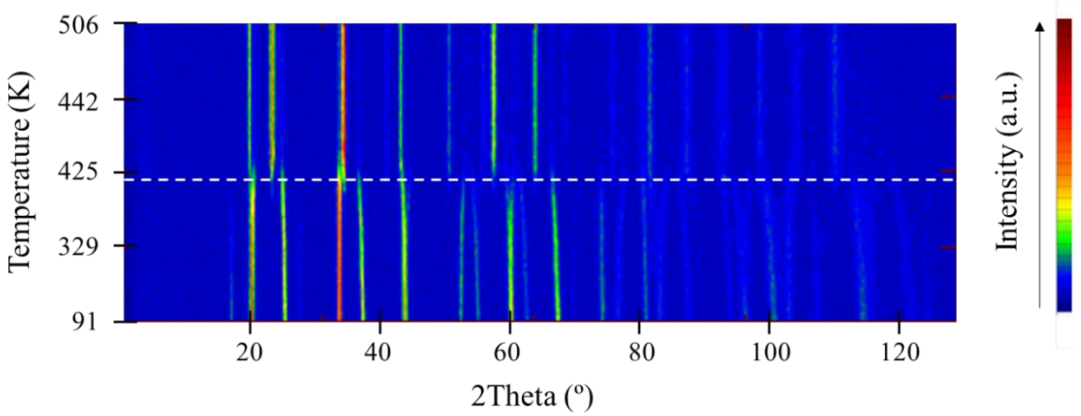

***Figure 6.3**. Thermodiffractogram obtained by PND on the Fe_1 sample. The lines represent the diffraction peaks and the colour, their intensity. The dashed line indicates the martensitic transformation.*

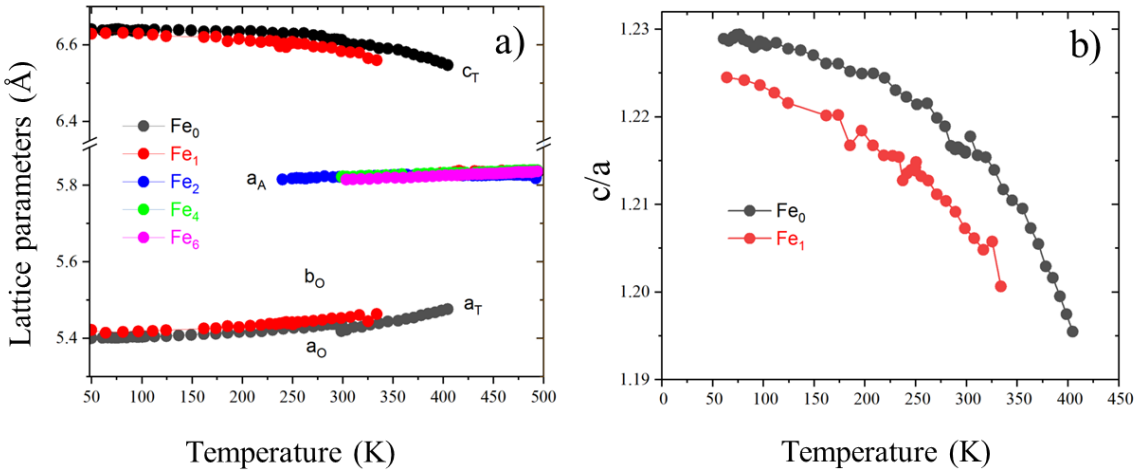

***Figure 6.4**. Thermal evolution of the a) lattice parameters for every alloy in the austenite, and for the Fe0 and Fe1 in the martensite, and b) c/a relation for Fe_0, Fe_1 and alloys, using the fcc cell as reference.*

From the evolution of the lattice parameters with temperature (**Figure 6.4**), the volumetric contraction associated with the martensitic transformation was calculated for those alloys displaying a complete MT. At the martensitic temperature, the martensitic lattice parameters for the Fe_0 alloy, using the *fcc* cell as a reference, are a = 5.47 Å and c = 6.55 Å, while for the Fe_1 alloy they are a = 5.46 Å and c = 6.56 Å. This implies a martensitic volume of roughly 196 and 195 $Å^3$, respectively. Since at the same temperature the austenitic volume is close to 198 $Å^3$, the transformation leads to a volumetric change of ~1% in the non-doped alloy and ~1.5% in the Fe-doped one, making these alloys promising for potential magnetostrictive-related applications.

It was previously suggested that the differences in the microstructure of the alloys are the reason behind the observed evolution of T_M in the alloy series, rather than the electronic concentration, *e/a*. As deduced from the presented crystallographic analysis, the lower T_M associated with higher Fe contents can be attributed to the *c/a* reduction. This observation is in line with previous studies[3,27], where a less distorted, more cubic-like martensitic structure is correlated with a decreasing T_M, due to an easier and, hence, less energy-demanding martensitic transformation.

6.4. RELATION BETWEEN MAGNETIC INTERACTIONS AND STRUCTURE

To understand the underlying mechanism for the increasing T_C with the Fe content, a more detailed study of the crystalline structure was performed. It is well known that the atomic ordering has a strong correlation with the magnetic behaviour of the alloys[25,28–30], since it is extremely dependent on the magnetic interactions between atoms that, in turn, depend on their interatomic distances.

With this purpose, the atomic site occupancies of the five studied alloys were obtained via Rietveld refinements of the high intensity diffractograms measured at 500 K (see **Figures A.3.4 - A.3.8**), to ensure every alloy is in its paramagnetic austenite phase. A representative of the fitting is presented in **Figure 6.5**, while the results are summarized in **Table 6.4**, in which all the alloys present the $L2_1$ ordered, *Fm-3m* cubic unit cell. As previously stated in **Section 5.3.2,** more than two different atomic species can be present in a specific crystallographic site, implying that several assumptions need to be made to perform successful fittings. The assumptions, based on similar works[3,26,31,32] are listed below:

- The totality of the Ni and Ga atoms are placed in the 8c and 4b Wyckoff sites, respectively.
- Co is placed either solely at 8c sites or distributed between 8c and 4a positions.
- Fe is located either solely at 4a sites or distributed between 8c and 4a positions.

Table 6.4. *Atomic site occupancies (at%) of the studied samples obtained via Rietveld refinements performed in the diffractograms measured at 500K (paramagnetic austenite).*

Alloy	Position - Wyckoff site	Ni	Mn	Ga	Co	In	Fe
	(0.25, 0.25, 0.25) - 8c	40.7	0.6	–	8.7	–	–
Fe_0	(0, 0, 0) - 4a	–	22.3	–	–	2.7	–
	(0.5, 0.5, 0.5) - 4b	–	8.3	16.7	–	–	–
	(0.25, 0.25, 0.25) - 8c	40.7	0	–	8.4	–	0.9
Fe_1	(0, 0, 0) - 4a	–	22	–	–	3	–
	(0.5, 0.5, 0.5) - 4b	–	8.8	16.2	–	–	–
	(0.25, 0.25, 0.25) - 8c	41.8	3.4	–	5.8	–	1
Fe_2	(0, 0, 0) - 4a	–	21.7	–		2.9	0.4
	(0.5, 0.5, 0.5) - 4b	–	5.1	14.6	3.3	–	–
	(0.25, 0.25, 0.25) 8c	41.3	3.4	–	3.8	–	1.5
Fe_4	(0, 0, 0) - 4a	–	18.9	–	–	3	3.1
	(0.5, 0.5, 0.5) - 4b	–	4.5	15.4	5.1	–	–
	(0.25, 0.25, 0.25) - 8c	41.8	2.8	–	1.6	–	3.8
Fe_6	(0, 0, 0) - 4a	–	20.4	–	–	2.5	2
	(0.5, 0.5, 0.5) - 4b	–	4.7	13.5	6.8	–	–

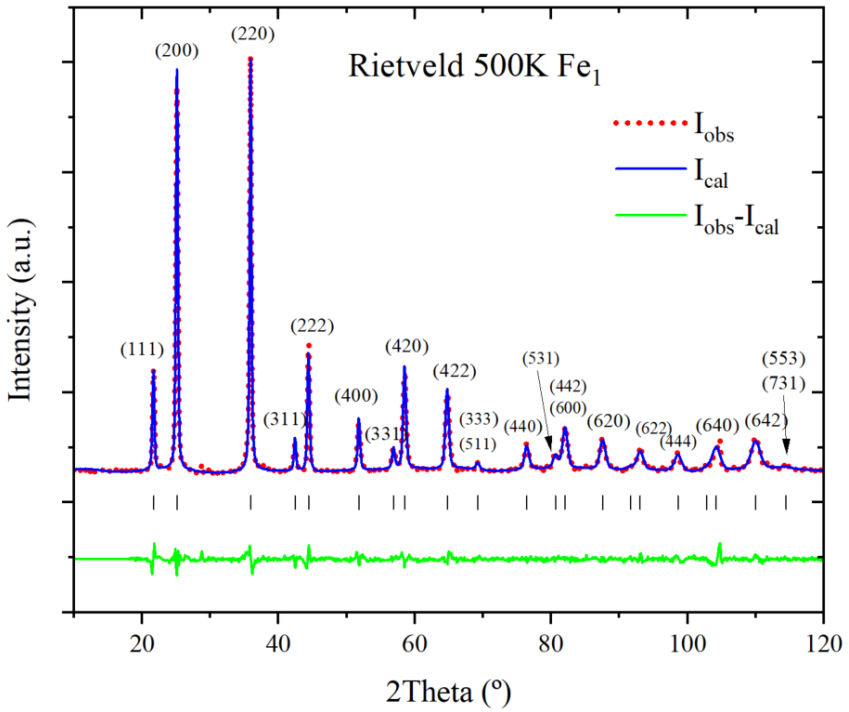

Figure 6.5. *Neutron diffraction pattern, together with its corresponding Rietveld refinement, measured at 500K for the Fe_1 alloy. Red dots represent experimental points; blue lines are the Rietveld fittings; and green lines correspond to the difference between the measurements and the fittings. The Miller indices corresponding to each reflection are indicated with a black line and indexed above each peak.*

As derived from the Rietveld refinements, the following tendencies for the different elements forming the alloys to occupy various positions are revealed:

- In the Fe_0 sample the totality of Ni and Co atoms are placed at 8c sites, similarly to what happens with Ga atoms in the 4b sites and with In atoms in the 4a sites. Nevertheless, Mn atoms are distributed among all sites, and not only in their preferential 4a positions.
- In the Fe_1 sample, Fe atoms are exclusively located in the 8c sites, saturating it together with Ni and Co, forcing Mn atoms to be displaced to the remaining 4a and 4b sites.
- For the alloys with a Fe content above 2 at%, Fe is placed at 4a and 8c sites. As a consequence of the increasing amount of Fe in the alloy series, Co atoms are displaced to the 4b sites, partially displacing Mn to the 8c sites. Consequently, a more crystallographically disordered structure is formed.

In previous chapters, the dependence of the RKKY-type Mn-Mn magnetic exchange interactions in Ni-Mn-based alloys was extensively used and discussed.[30] Connected to this, and to properly associate the atomic distributions with the magnetic behaviour of the alloys, the distances between atomic positions should be calculated, in an analogous way to the work presented in **Section 5.4.** For the austenitic structure, the distances between atomic sites where Mn atoms are present are the following: d_{4a-4a}= 4.13 Å, d_{4a-4b}=2.92 Å, d_{4a-8c}=2.53 Å, calculated with the equations proposed by Perez-Checa et al.[3] (**Equations 6.1-6.3**)

$$d_{4a-4a} = \frac{a\sqrt{2}}{2} \qquad \textit{Equation 6.1}$$

$$d_{4a-4b} = \frac{a}{2} \qquad \textit{Equation 6.2}$$

$$d_{4a-8c} = \frac{a\sqrt{3}}{4} \qquad \textit{Equation 6.3}$$

Since Mn-Mn interactions at distances below 2.92 Å have been proven to be antiferromagnetic (AFM), the presence of AFM interactions between the 4a and the 8c Mn atoms is deduced. However, there is limited information about the interaction in the range between 2.92 Å and 3.32 Å, so the nature of the interactions between the

4a and the 4b atoms cannot be easily assumed. For the sake of simplicity, and analogously to the hypothesis make on **Section 5.4**, we assume antiferromagnetic interactions. We considered the other magnetic elements of the alloys to present purely ferromagnetic exchange interactions, as no studies have proven otherwise. **Figure 6.6** displays the evolution of the percentage of atoms interacting antiferromagnetically with the %Fe, alongside with the evolution of T_C^A. The increasing value of the latter is correlated with the lower number of antiferromagnetic interactions.

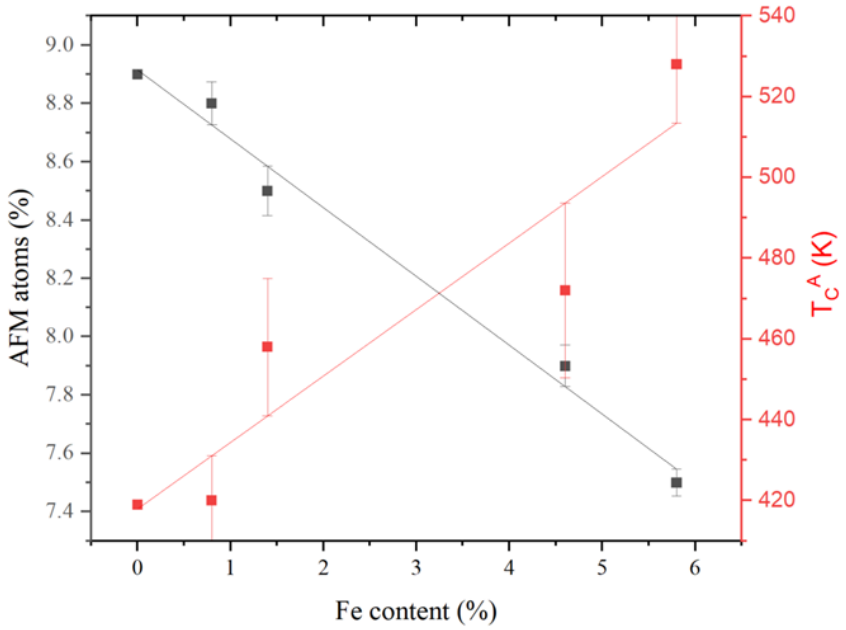

Figure 6.6 *Correlation between the Fe content, the austenitic magnetic transition temperature (red) and the percentage of atoms interacting antiferromagnetically (black).*

The almost linear relation between the increasing T_C^A and the decreasing AFM interactions in the first situation leads to two main conclusions:

- The interactions between Mn atoms at 4a positions and those displaced to 4b sites is antiferromagnetic.
- The dependence between the antiferromagnetic interactions and the magnetic transition temperatures is confirmed: the lower the percentage of Mn atoms interacting antiferromagnetically, the more enhanced the ferromagnetism is, what is physically observed as an increase in T_C^A.

Besides this well-known paramagnetic to ferromagnetic transition in the austenite phase, an additional magnetic transformation was observed in the Fe_0 and

Fe_1 alloys within their martensite phases. The temperature at which it occurs is denoted as T_C^M and shown in **Figure 6.1** and **Table 6.1**. In line with the previously discussed ferromagnetic and antiferromagnetic interactions between Mn atoms, the reason behind the differences in T_C^M may be related to the nature of the magnetic interactions. The presence of purely magnetic peaks in the diffractograms acquired in the martensitic phase implies an antiferromagnetic ordering[26,33]. In order to confirm this, magnetic Rietveld fittings, which are shown in **Figure 6.7**, were performed in the diffractograms acquired at 50 K.

The symmetry analysis of the magnetic structure reveals an antiferromagnetic ordering in a P_I4_2/mnm magnetic space group, with the totality of the magnetic moment densities located at the position equivalent to the austenitic 8c (**see Figure 6.8**), in a similar fashion to what is observed elsewhere in literature[26]. From the fittings, the magnetic moment densities (expressed in Bohr magnetrons, μ_B) per site of the unit cell can be calculated. The total magnetic moment (equivalent to the density at the 8c site) is displayed in **Table 6.5**, and compared with the ones obtained experimentally employing the Arrot plot method[34] in the M(T) curves (**Figure 6.9**). The similarity between both values confirms that the fittings are consistent with the physical behaviour of the alloys.

As previously anticipated, the temperature at which this antiferromagnetic ordering starts to occur (T_C^M) is remarkably higher in the Fe-doped alloy. This may also be attributed to the same reason leading to the previously stated correlation between the Fe content and the increased in the austenitic Curie temperature.

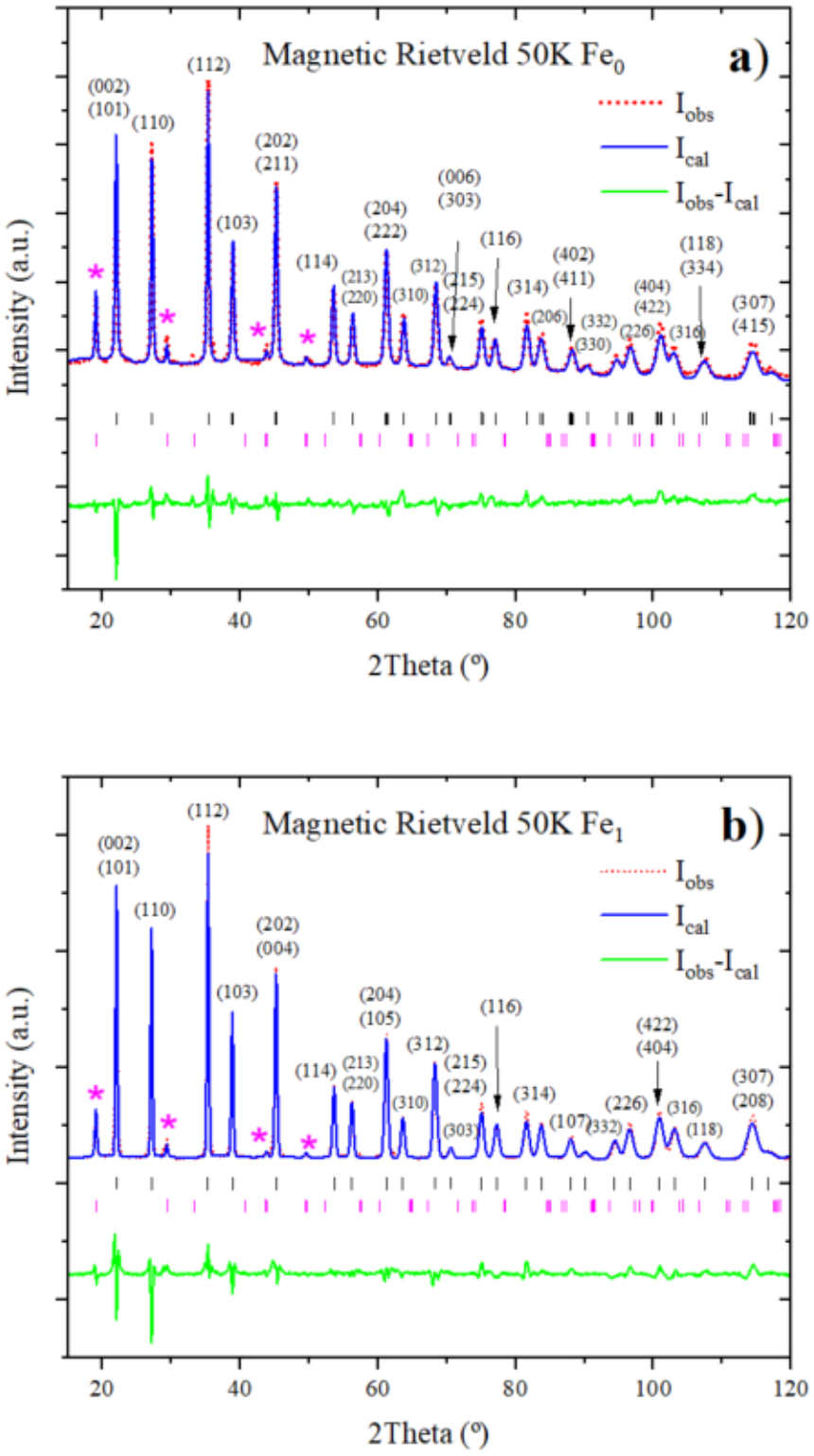

Figure 6.7. *Neutron diffraction patterns measured at 50K, together with their corresponding magnetic Rietveld refinements for the a) Fe_0 and b) Fe_1 alloys. Red dots represent experimental points; blue lines are the Rietveld fittings; and green lines correspond to the difference between the measurements and the fittings. The structural reflections are indicated with a black line and the magnetic ones with a pink line. The purely magnetic peaks are represented with an asterisk.*

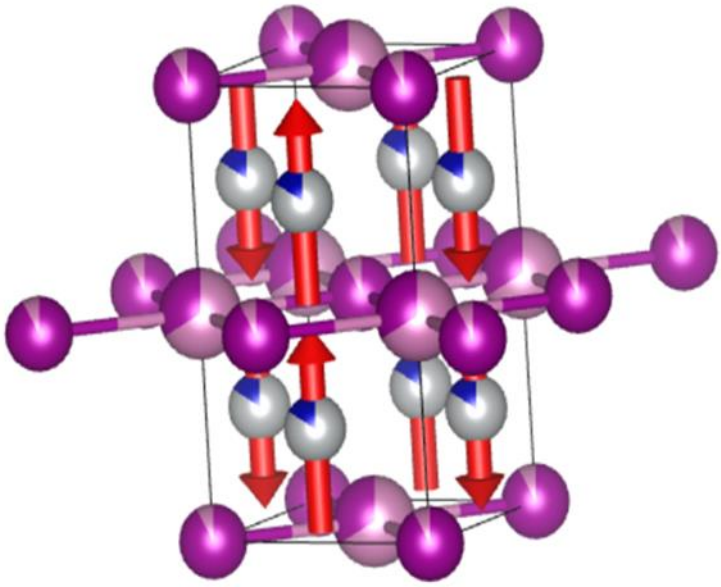

Figure 6.8. *Graphical representation of the antiferromagnetic ordering the Fe_0 single crystal unit cell, based on the data acquired at 50K.*

Table 6.5. *Calculated (μ_{Riet}) and experimental (μ_{exp}) total magnetic moments in the magnetic martensite (50 K) of the Fe_0 and Fe_1 alloys.*

Alloy	μ_{Riet} (μ_B)	μ_{exp} (μ_B)
Fe_0	0.89	0.91
Fe_1	0.87	1.20

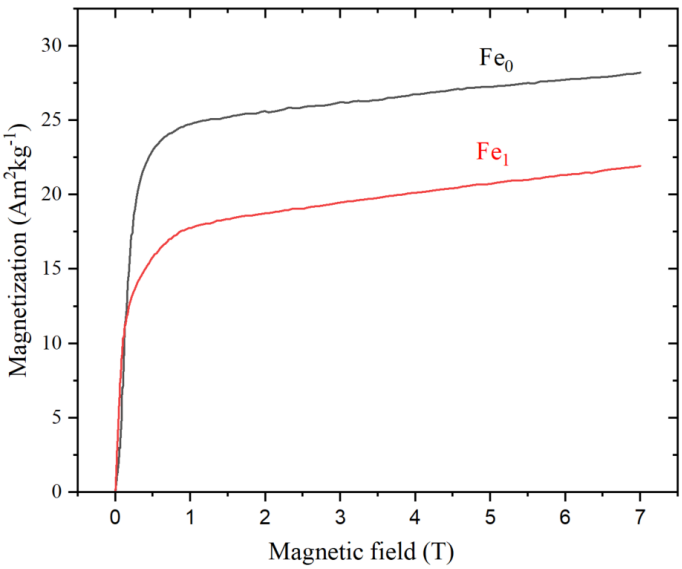

Figure 6.9 *Magnetic field evolution of the magnetization for the Fe_0 and Fe_1 alloys at 50K.*

6.5. SUMMARY AND CONCLUSIONS

In the present work we have studied the transformation behaviour, crystal structure and magnetic properties of the Fe-doped powder Ni-Mn-Ga-Co-In-Fe alloys as a function of the dopant content. The aim was to obtain a better understanding of the effect that Fe doping on these alloys has on the temperature actuation ranges of the materials for potential magnetostrictive and magnetocaloric related applications.

For the fabrication of the powder samples, a combination of induction and arc-melting furnaces was employed, followed by heat treatments and subsequent grinding of the alloys to obtain them in powder form. Their transformation behaviour, crystalline structure and magnetic properties as a function of the Fe content were analysed via neutron powder diffraction and magnetic characterization measurements.

Both the austenitic and martensitic structures were studied via LeBail refinements, finding that even when there are no significant changes in the cubic *Fm-3m* austenite phase upon Fe doping, the martensitic transformation is greatly affected. We observed a decreasing T_M with the Fe content in Fe_0 and Fe_1 samples, while in those samples with a Fe content higher than 2 at% (Fe_2, Fe_4, Fe_6) the MT is not completed, probably due to the formation of secondary phases, which have been observed for the Fe_2 alloy. This alloy presents a partial martensitic transformation, and the martensite phases observed after both the total (Fe_0, Fe_1) or partial (Fe_2) martensitic transformation present *I4/mmm* tetragonal structures. The explanation of the lower T_M as the Fe content increases can be attributed to less distorted martensites as the Fe content increases, implying a less energetic MT, in an analogous behaviour to the Cu doped alloy series presented in **Chapter 5**.

The atomic site occupancies of the studied alloys were unravelled via Rietveld refinements, endorsing the nature of the Mn-Mn exchange interactions between the 4a and the 8c and 4b positions.

The key role Mn-Mn interactions play in the evolution of T_C^A in this system was also established. Analogously to the effect demonstrated for other alloys, as well as in **Chapters 4 and 5** of this thesis, the lower percentage of atoms interacting antiferromagnetically is physically seen as a higher T_C^A.

We observed the occurrence of an interesting magnetic transition in the martensite in samples displaying a complete martensitic transformation (Fe_0 and Fe_1). This phenomenon is attributed to the presence of antiferromagnetic ordering at low temperatures, resulting into the presence of a P_I4_2/mnm magnetic space group at 50K. The increase of T_C^M with the Fe % aligns with the similar behaviour observed in T_C^A.

Similarly to the studies presented in **Chapters 4 and 5**, this work follows the line of systematic design of MMSMAs for magnetocaloric applications, adding up a potential use of these materials in magnetostrictive related applications. More specifically, the tuning of the actuation temperature ranges of the alloys was discussed upon Fe doping.

6.5. BIBLIOGRAPHY

1. Murray SJ, Marioni M, Allen SM, Handley RCO. in ferromagnetic Ni – Mn – Ga. *Appl Phys Lett*. 2000;77(6):886-888. doi:10.1063/1.1306635

2. Chernenko VA, L'vov VA, Cesari E, Barandiaran JM. Fundamentals of magnetocaloric effect in magnetic shape memory alloys. In: *Handbook of Magnetic Materials*. Vol 28. Elviser; 2019:1-45. doi:10.1016/bs.hmm.2019.03.001

3. Pérez-Checa A, Porro JM, Feuchtwanger J, et al. Role of Fe addition in Ni–Mn–Ga–Co–Cu–Fe ferromagnetic shape memory alloys for high-temperature magnetic actuation. *Acta Mater*. 2020;196:549-555. doi:10.1016/j.actamat.2020.07.007

4. Río-lópez NA, Lázpita P, Salazar D, et al. Neutron scattering as a powerful tool to investigate magnetic shape memory alloys: A review. *Metals (Basel)*. 2021;11(5):1-21. doi:10.3390/met11050829

5. Straka L, Heczko O, Seiner H, et al. Highly mobile twinned interface in 10 M modulated Ni-Mn-Ga martensite: Analysis beyond the tetragonal approximation of lattice. *Acta Mater*. 2011;59(20):7450-7463. doi:10.1016/j.actamat.2011.09.020

6. Dunand DC, Müllner P. Size effects on magnetic actuation in Ni-Mn-Ga shape-memory alloys. *Adv Mater*. 2011;23(2):216-232. doi:10.1002/adma.201002753

7. Auernhammer D, Kohl M, Krevet B, Ohtsuka M. Intrinsic position sensing of a Ni – Mn – Ga microactuator. Published online 2009. doi:10.1088/0964-1726/18/10/104016

8. Glavatskyy I, Glavatska N, Dobrinsky A, Hoffmann JU, Söderberg O, Hannula SP. Crystal structure and high-temperature magnetoplasticity in the new Ni-Mn-Ga-Cu magnetic shape memory alloys. *Scr Mater*. 2007;56(7):565-568. doi:10.1016/j.scriptamat.2006.12.019

9. Liang L, Tong W, Xu J, et al. Acta Materialia Evidence for austenite to non-modulated martensite transformation crystallography and variant organization in Ni-Mn-Ga-Co ferromagnetic shape memory alloys. 2023;254(April). doi:10.1016/j.actamat.2023.119022

10. Cong DY, Wang S, Wang YD, Ren Y, Zuo L, Esling C. Martensitic and magnetic transformation in Ni – Mn – Ga – Co ferromagnetic shape memory alloys. 2008;473:213-218. doi:10.1016/j.msea.2007.03.088

11. Sánchez-Alarcos V, Pérez-Landazábal JI, Recarte V, Gómz-Polo C, Rodríguez-Velamazan JA. Correlation between composition and phase transformation temperatures in Ni – Mn – Ga – Co ferromagnetic shape memory alloys. 2008;56:5370-5376. doi:10.1016/j.actamat.2008.07.017

12. Cugini F, Porcari G, Fabbrici S, Albertini F, Solzi M. Influence of the transition width on the magnetocaloric effect across the magnetostructural transition of Heusler alloys. *Philos Trans R Soc A Math Phys Eng Sci*. 2016;374(2074). doi:10.1098/rsta.2015.0306

13. Hu FX, Shen BG, Sun JR, Cheng ZH, Rao GH, Zhang XX. Influence of negative lattice expansion and metamagnetic transition on magnetic entropy change in the compound LaFe11.4Si1.6. *Appl Phys Lett*. 2001;78(23):3675-3677. doi:10.1063/1.1375836

14. Sánchez-Alarcos V, Recarte V, Pérez-Landazábal JI, Cuello GJ. Correlation between atomic order and the characteristics of the structural and magnetic transformations in Ni-Mn-Ga shape memory alloys. *Acta Mater*. 2007;55(11):3883-3889. doi:10.1016/j.actamat.2007.03.001

15. Pecharsky VK, Gschneidner K. A. J. Giant Magnetocaloric Effect in Gd5Si2Ge2. *Phys Rev Lett*. 1997;78(23):4494-4497. doi:10.1103/PhysRevLett.78.4494

16. Chen F, Wang HB, Zheng YF, Cai W, Zhao LC. Effect of Fe addition on transformation temperatures and hardness of NiMnGa magnetic shape memory alloys. *J Mater Sci*. 2005;40(1):219-221. doi:10.1007/s10853-005-5712-3

17. Yu Q, Jauregui LA, Wu W, et al. Control and characterization of individual grains and grain boundaries in graphene grown by chemical vapour deposition. *Nat Mater*. 2011;10(6):443-449. doi:10.1038/nmat3010

18. Hansen N, Huang X, Winther G. Effect of grain boundaries and grain orientation on structure and properties. *Metall Mater Trans A Phys Metall Mater Sci*. 2011;42(3):613-625. doi:10.1007/s11661-010-0292-5

19. Hobza A, Patrick CL, Ullakko K, Rafla N, Lindquist P, Müllner P. Sensors and Actuators A : Physical Sensing strain with Ni-Mn-Ga. *Sensors Actuators A Phys*. 2018;269:137-144. doi:10.1016/j.sna.2017.11.002

20. Alijani F, Reihanian M, Gheisari K, Edalati K, Miyamoto H. Effect of Homogenization on Microstructure and Hardness of Arc-Melted FeCoNiMn High Entropy Alloy During High-Pressure Torsion (HPT). *J Mater Eng Perform*. 2022;31(6):5080-5089. doi:10.1007/s11665-021-06573-8

21. RIO-LOPEZ Natalia Ahiova, CHERNENKO Volodymyr, GONCALVES Bruna F, LAZPITA Patricia, PLAZAOLA MUGURUZA Fernando, PORRO AZPIAZU Jose Maria, PUENTE ORENCH Ines RVJA. Magnetostrictive behaviour and crystal structure of Fe-doped Ni-Mn-Ga-Co-In-Fe Metamagnetic Shape Memory Alloys. Published online 2023. doi:doi:10.5291/ILL-DATA.5-23-784

22. Rodríguez-Carvajal J. FullProf. Published online 2001.

23. Chernenko V. Compositional instability of B—phase in Ni—Mn-Ga alloys. *Scr Mater*.1999;40(5):523-527.

24. Lázpita P, Sasmaz M, Barandiarán JM, Chernenko VA. Effect of Fe doping and magnetic field on martensitic transformation of Mn-Ni(Fe)-Sn metamagnetic shape memory alloys. *Acta Mater*. 2018;155:95-103. doi:10.1016/j.actamat.2018.05.052

25. Barandiarán JM, Chernenko VA, Lázpita P, Gutiérrez J, Fdez-Gubieda ML, Kimura A. Neutron and synchrotron studies of structure and magnetism of Shape Memory Alloys. *J Phys Conf Ser*. 2015;663(1). doi:10.1088/1742-6596/663/1/012014

26. Orlandi F, Fabbrici S, Albertini F, Manuel P, Khalyavin DD, Righi L. Long-range antiferromagnetic interactions in Ni-Co-Mn-Ga metamagnetic Heusler alloys: A two-step ordering studied by neutron diffraction. *Phys Rev B*. 2016;94(14):1-5. doi:10.1103/PhysRevB.94.140409

27. Seguí C, Torrens-Serra J, Cesari E, Lázpita P. Optimizing the caloric properties of Cu-doped Ni-Mn-Ga alloys. *Materials (Basel)*. 2020;13(2). doi:10.3390/ma13020419

28. Richard ML, Feuchtwanger J, Allen SM, et al. Chemical order in off-stoichiometric Ni – Mn – Ga ferromagnetic shape-memory alloys studied with neutron diffraction. 2007;6435. doi:10.1080/14786430701297582

29. Roy S, Blackburn E, Valvidares SM, et al. Delocalization and hybridization enhance the magnetocaloric effect in Cu-doped Ni2 MnGa. *Phys Rev B - Condens Matter Mater Phys*. 2009;79(23):1-5. doi:10.1103/PhysRevB.79.235127

30. Lázpita P, Barandiarán JM, Gutiérrez J, Feuchtwanger J, Chernenko VA, Richard ML. Magnetic moment and chemical order in off-stoichiometric Ni-Mn-Ga ferromagnetic shape memory alloys. *New J Phys*. 2011;13:1-14. doi:10.1088/1367-2630/13/3/033039

31. Cong DY, Wang YD, Lin Peng R, et al. Crystal structures and textures in the hot-forged Ni-Mn-Ga shape memory alloys. *Metall Mater Trans A Phys Metall Mater Sci*. 2006;37(5):1397-1403. doi:10.1007/s11661-006-0084-0

32. Orlandi F, Çaklr A, Manuel P, Khalyavin DD, Acet M, Righi L. Neutron diffraction and symmetry analysis of the martensitic transformation in Co-doped Ni2MnGa. *Phys Rev B*. 2020;101(9):1-13. doi:10.1103/PhysRevB.101.094105

33. Aksoy S, Acet M, Deen PP, Mañosa L, Planes A. Magnetic correlations in martensitic Ni-Mn-based Heusler shape-memory alloys: Neutron polarization analysis. *Phys Rev B - Condens Matter Mater Phys*. 2009;79(21):1-4. doi:10.1103/PhysRevB.79.212401

34. Arrott A. Criterion for ferromagnetism from observations of magnetic isotherms. *Phys Rev*. 1957;108(6):1394-1396. doi:10.1103/PhysRev.108.1394

CHAPTER 7

Polarized neutron diffraction on Ni-Mn-Ga-Co-(In,Fe) Single crystal alloys

7.1. INTRODUCTION

In the previous chapter (**Chapter 6**), the effect Mn substitution by Fe in MMSMA alloys has on their structural and magnetic transition temperatures was analysed, in relation to a possible use of doped Ni-Mn-Ga alloys for magnetostrictive related applications. For the sake of simplicity and accessibility, the study was performed on polycrystalline powders, even though an enhanced magnetostrictive behaviour arising from the lack of grain boundaries makes single crystals more interesting for this kind of applications.[1–3] In line with this, in the present chapter we discuss a continuation of the aforementioned study consisting in investigating the structural and magnetic characterization of selected single crystals with similar compositions to those studied in the powders of **Chapter 6**.

Alongside with the temperature actuation range of the alloy, determined by T_C and T_M, the volumetric change undergone by the crystal plays an important role towards its use in possible industrial applications[4–6]. Being the volumetric change due to either a magnetic field-induced martensitic transformation or a twin variants reorientation, the martensitic transformation and the resultant martensite phase are key factors for the alloy composition design. Since it is well known the effect the single crystal training, introduced in **Section 1.2.2**, has on the alloy performance[7–10], the study was completed by testing different trainings and investigating the effect they have on the elastic/plastic behaviour of the resultant martensite.

In this regard, two suitable alloy compositions showing promising properties towards prospective applications, were selected after analysing the conclusions drawn in **Section 6.5**: $Ni_{41}Mn_{32-x}Ga_{15}Co_9In_3Fe_x$, x = 0 and 2 (thereafter denoted Fe_0 and Fe_2,

respectively). Fe_0 presents compelling entropy and volumetric change properties, associated to the ferromagnetic austenite to paramagnetic martensite transformation (see **Figure 6.1**), making it a potential candidate for both magnetocaloric and magnetostrictive applications. Fe_2 was selected with the goal of testing an analogous effect Fe doping has on the properties of polycrystalline Ni-Mn-Ga-Co-In-Fe alloys in single crystal alloys.

For a full understanding of the structural changes and magnetic interactions affecting the evolution of the characteristic temperatures (T_C and T_M) of the alloys, both polarized and unpolarized single crystal neutron diffraction experiments were performed. The results were used to correlate the atomic structure and magnetic site densities with the measured bulk magnetic behaviour of the single crystals. Different trainings were performed in each crystal, with the aim of testing their effect on the martensitic transformation and on the resultant martensitic structure. Additionally, compression tests were also performed in the single crystals to evaluate their mechanical properties and to observe their shape memory effect.

Besides the well-known effect compositional variations and training methods have in the actuation of single crystal MSMAs[11–14], previous studies have investigated the effect that surface modifications have on the actuation properties of these alloys[11,15]. These alterations, such as patterning, create internal stresses analogous to the ones obtained by training that, in turn, act as nucleation points for the formation of variants[16,17]. In order to study this effect in our alloys, both the Fe_0 and Fe_2 single crystals were patterned via micropeening, followed by measurements of their mechanical properties to observe how they vary with respect to the fresh, non-patterned single crystals.

7.2. EXPERIMENTAL PART

7.2.1. Fabrication of Ni-Mn-Ga-Co-(In,Fe) master alloys

Two polycrystalline alloys ($Ni_{41}Mn_{32-x}Ga_{15}Co_9In_3Fe_x$, x= 0, 2) were prepared via induction melting under argon atmosphere, followed by a heat treatment of 24 hours at 1170 K in a vacuum quartz tube and a subsequent quenching in water at 273

K. As explained in **Chapters 4 and 5**, the aim of this post-annealing process was to relieve the internal stresses and to allow for a complete martensitic transformation to occur. These polycrystalline alloys were the master alloys for the subsequent single crystal growth, resulting into the single crystal alloys named Fe_0 and Fe_2.

7.2.2. Growth of Ni-Mn-Ga-Co-(In,Fe) single crystals

The single crystals were grown employing a modified optical floating zone furnace, whose operation process is described in **Section 2.1**. A (100) oriented stoichiometric Ni_2MnGa single crystal was employed as seed for the growth of our alloys, together with the following conditions selected for the growth process: starting base pressure of ~10^{-4} MPa, working pressure of 0.25 MPa of high purity argon atmosphere, to minimise the evaporation of the melt (Mn exhibits a high vapour pressure), and a growth speed of 2 mm/hour, in order to create a dendritic free structure. Both the master alloys fabrication and the single crystal growths were done in collaboration with colleagues from FZU and Universita Karlova, in Prague, Czech Republic.

7.2.3 Structural and magnetic characterization techniques

The structural (T_M and T_A) and magnetic (T_C^A) transformation temperatures of all polycrystalline and single crystal alloys were studied by Vibrating Sample Magnetometry (VSM), under a 10 mT magnetic field. The alloy compositions were studied by means of X-Ray Fluorescence spectroscopy (XRF). To orient the single crystals for the neutron diffraction experiments, a Laue Diffractometer was employed.

The polarized and unpolarized single neutron diffraction experiments were carried out at the D9 and D3 single crystal diffractometers of the Institute Laue-Langevin neutron source, respectively, with a neutron wavelength of 0.83 Å. The data was acquired at selected temperatures in the austenite phase of the material, in an attempt to measure above, during and below the T_C. In D3, a magnetic field of 8T was applied. Laue neutron diffraction measurements, acquired at the Orient express instrument of the ILL, were employed to orient the sample. To determine the crystalline structure, Rietveld refinements were performed on the obtained data, employing Fullprof suite software[18]. In order to adjust the flipping ratios measured in

D3 and obtain the magnetic site densities, Mag2Pol[19] was employed, making use of the least-squares method to fit the data.

7.2.4 Surface patterning and single crystal mechanical testing

The effect different mechanical trainings have on the induced martensite phases was investigated. For this study, single crystal pieces of approximately 1 x 2 x 7 mm^3 from each grown alloy were heated up to 900 K, to make sure that a complete reset of the structure has occurred and that the alloy is in the austenitic phase, and were subsequently cooled down to room temperature under a variable weight load applied on the larger surface. This heating-cooling process was repeated 3 consecutive times to obtain trained single crystals (see **Section 1.2.2**).

From this training processes, different working loads lead to different final martensite phases in the single crystals. In order to compare the effect the different trainings (i.e. different working loads) have on the resulting martensite, compression tests were performed in the single crystals as a method to disclose the presence or absence of martensitic twin variants after the training. A homemade micromechanical testing device was employed to apply stress on the samples and, via stress-strain curves, to correlate the applied stress with the induced residual deformation, the movement of twin variants and the elastic or ductile behaviour displayed by the alloy.

Surface patterning processes were performed in the pieces of single crystals by micropeening, consisting in hitting the surface with glass nanoparticles in a controlled manner. In order to do the patterning, a homemade micropeening station with variable air pressures (the employed ones in our study were 1, 2.5 and 5 MPa) was used to propel the nanoparticles, resulting into different induced surface patternings. To compare the effect of the different patternings obtained with the aforementioned pressures on the actuation of the martensite, a micromechanical testing process was employed, analogously to the previously described one for the training results.

Both the patterning and the mechanical tests were done in collaboration with colleagues from the Boise State University, in Idaho, USA.

7.3. STRUCTURAL BEHAVIOUR

7.3.1. Composition and transformation characteristics

As stated in the previous section, the composition and characteristic transformation temperatures (T_M, T_A and T_C^A) were determined by different techniques, obtaining the values summarized in **Table 7.1**.

Table 7.1. *Alloys studied, including the master and single crystal alloy compositions, the calculated electronic concentrations (e/a) and the characteristic transformation temperatures.*

Alloy		Composition	T_M (K)	T_A (K)	T_C^A (K)	e/a
Fe_0	Master Alloy	$Ni_{42.7}Mn_{31.0}Ga_{14.1}Co_{8.6}In_{3.6}$	442	445	447	7.75
	Single Crystal	$Ni_{43.0}Mn_{30.8}Ga_{14.6}Co_{8.6}In_{3.0}$				
Fe_2	Master Alloy	$Ni_{42.1}Mn_{29.8}Ga_{14.3}Co_{7.9}In_{3.6}Fe_{2.3}$	318	335	467	7.89
	Single Crystal	$Ni_{45.4}Mn_{28.3}Ga_{16.0}Co_{8.1}Fe_{2.2}$				

Due to the fact that the compositions are not completely homogeneous along the single crystal rods (see **Figure 7.1**), the single crystals were cut along the most-homogeneous central region of the rods, from which all the analysis presented here is deducted. The temperature dependence of the magnetization, *M(T)*, curves measured at 1T are shown in **Figure 7.2**. From these curves we can determine the characteristic structural and magnetic transition temperatures employing the derivative method, i.e., calculating the derivative curve of *M(T)* in a similar way as in previous chapters.

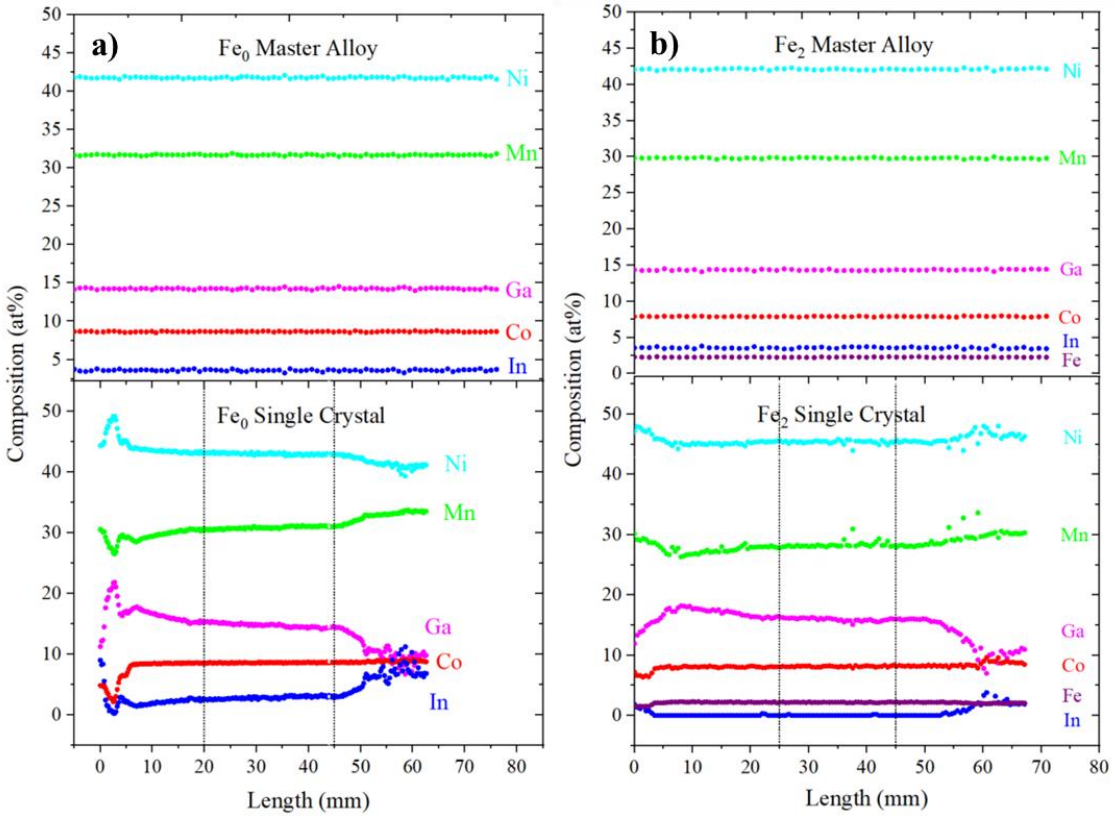

Figure 7.1. *Composition of the a) Fe_0 and b) Fe_2 master alloys (up) and single crystals (down) along the rod, measured by XRF. Grey lines mark the beginning and the end of the most compositionally homogeneous region of the rods, from which the single crystals are cut.*

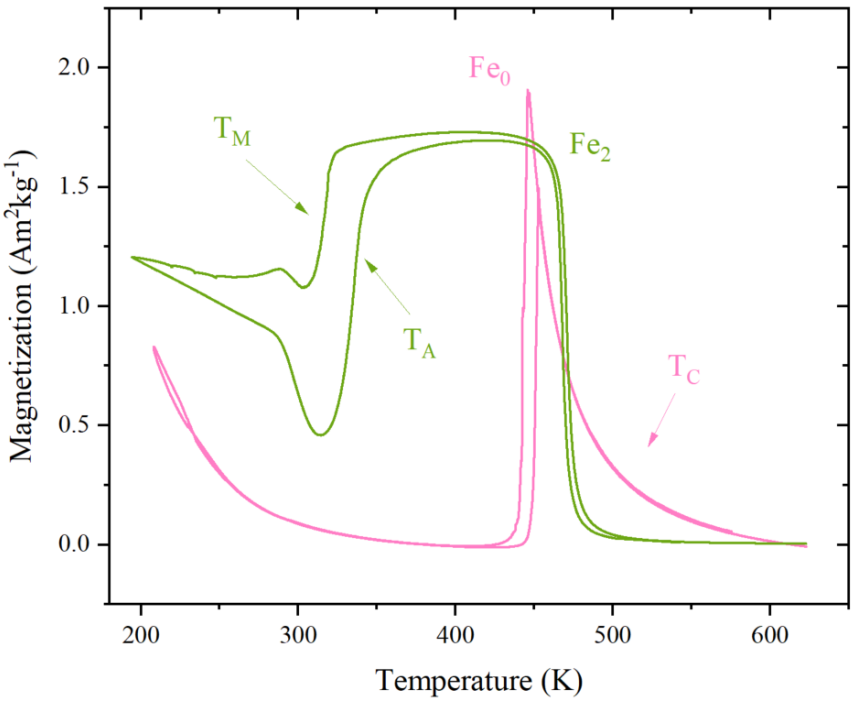

Figure 7.2. *Magnetization versus temperature (M(T)) curves for the Fe_0 (pink) and Fe_2 (green) single crystals, measured at 1 T, alongside with an example of the approximate positions of T_C^A, T_A and T_M for the Fe_2 alloy.*

From the data presented in **Figures 7.1** and **7.2**, the following observations can be made:

- The growth of the Fe_2 single crystal was partially unsuccessful, resulting into an inhomogeneous crystal, with all the Indium in the extremes of the rod, and a higher proportion of the remaining elements in the central parts of the single crystal.

- The unusual aspect of the MT in the Fe_2 crystal can be attributed either to the simultaneity of T_M and a potential T_C^M or to the inhibition of the MT due to the Fe content being higher than 2 at%, as compared to the corresponding polycrystalline alloy presented in the previous chapter. Although the latter assumption is in line with the behaviour of the Fe-doped polycrystalline samples, further characterization needs to be performed at lower temperatures to confirm this hypothesis.

- T_M is lower and T_C^A, higher, in the single crystal with Fe (Fe_2), in line with the discussion presented in **Chapter 6.**

To further characterize the behaviour of the Fe_0 single crystal, the macroscopical change in the shape associated to the evolution of the temperature (including the one associated to the MT) was characterized via dilatometry measurements along the *c* axis. As shown in **Figure 7.3**, the austenite-to-martensite transformation involves a 35µm (~ 0.05 %) expansion at 452K, while the reverse transition leads to a 25µm (~ 0.04 %) contraction at 464K. The martensite transformation temperatures are consistent with the structural transformation temperatures determined by the *M(T)* measurements presented in **Figure 7.2**.

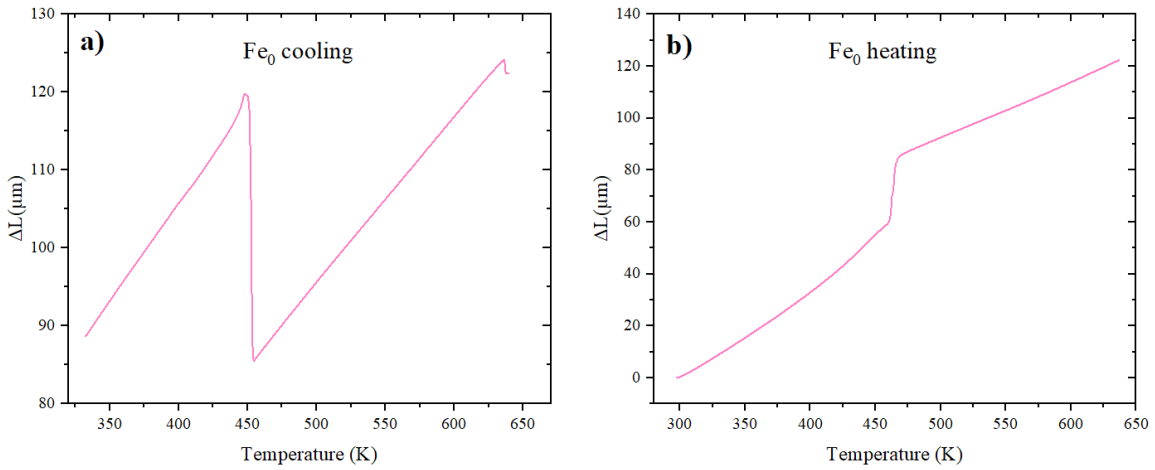

Figure 7.3. *Thermal expansion of the Fe_0 single crystal along the c axis upon a) cooling and b) heating.*

To ascertain the hypothesis behind the increasing T_C^A (higher number of ferromagnetic interactions, in line with the conclusions drawn in **Section 6.5** of the previous chapter) the crystalline and magnetic structures of the single crystals must be unravelled. In order to do so, single crystal neutron diffraction measurements were performed in the two alloys.

7.3.2. Single crystal neutron diffraction

As previously mentioned, single crystal neutron diffraction experiments have been performed at the D9 (unpolarized) and D3 (polarized) diffractometers of the ILL, where three measurements at specific temperatures were acquired in the austenitic phase of each alloy. The measurement temperatures, alongside with their relation to T_C^A, known as reduced temperatures, are the following:

- Fe_0 single crystal: 650K, 560K and 510K (T/T_C^A = 1.45, 1.25 and 1.14, respectively)
- Fe_2 single crystal: 600K, 430K and 390K (T/T_C^A = 1.27, 0.92 and 0.83, respectively)

The great number of dubious reflexions measured at every temperature in the Fe_2 sample is a consequence of the fact that this alloy presents multiple crystal grains with relatively similar orientations, rather than being a pure single crystal. This was confirmed by measuring the Fe_2 Laue neutron diffraction pattern at the Orient Express

instrument (ILL) at room temperature, which is presented in **Figure 7.4**, where multiple reflections close to each other can be observed for each Bragg spot corresponding to specific crystallographic planes.

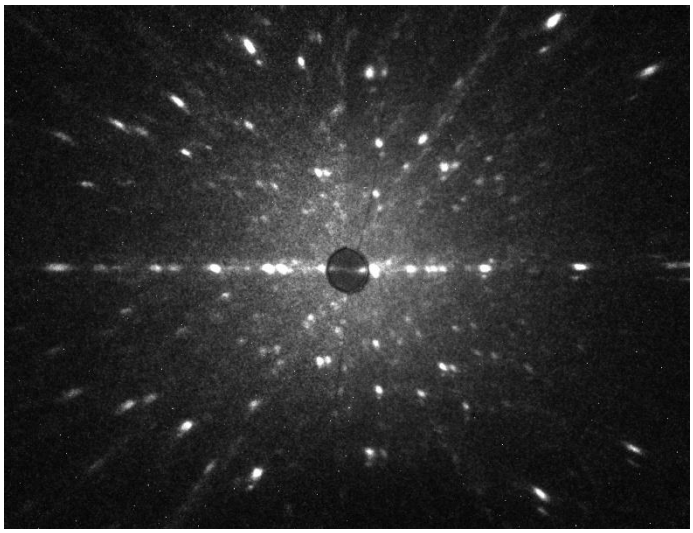

Figure 7.4. Laue diffraction patterns acquired from the Fe_2 crystal at room temperature.

The crystal structure is determined from the measurements on the D9 instrument, where the structural form factors corresponding to nuclear scattering events are obtained for each Bragg reflection measured. The magnetic site densities (graphically represented in **Figures A.4.1 and A.4.2**) are determined from the measurements on the D3 instrument, where the magnetic form factor is added to the structural form factor for each Bragg reflection measured, leading to the flipping ratio measured at each reflection. Therefore, for the analysis of the D3 data the input from the fittings of the nuclear form factors measured from D9 is needed. From the D9 measurements the lattice parameters, which are displayed in **Table 7.2**, and the atomic site occupancies, shown in **Table 7.3**, were obtained via Rietveld refinements.

Table 7.2. *Lattice parameters and space groups obtained from the Rietveld refinements of the* measurements performed at the specified temperatures for the Fe_0 and Fe_2 single crystals.

Alloy	Temperature (K)	Space group	Lattice (Å)
Fe_0	650	Fm-3m	5.86
	560	Fm-3m	5.86
	510	Fm-3m	5.86
Fe_2	600	Fm-3m	5.86
	430	Fm-3m	5.84
	390	Fm-3m	5.84

Analogously to the work presented in previous chapters, the Rietveld refinements (**Figures A.4.3 and A.4.4,** with a representative in **Figure 7.5**) were performed employing initial assumptions based on successful previous refinements[20–23]. The results, depicting the atomic site occupancies of the single crystals in the austenite phase, are summarized in **Table 7.3**.

Table 7.3. *Atomic site occupancies (at%) of the single crystals obtained via Rietveld refinements performed in the highest temperature measurements for each alloy.*

Alloy	Position - Wyckoff site	Ni	Mn	Ga	Co	In	Fe
Fe_0	(0.25, 0.25, 0.25) - 8c	43.0	1.9	–	5.1	–	–
	(0, 0, 0) - 4a	–	22.0	–	–	3.0	–
	(0.5, 0.5, 0.5) - 4b	–	6.9	14.6	3.5	–	–
Fe_2	(0.25, 0.25, 0.25) - 8c	45.4	1.1	–	3.5	–	–
	(0, 0, 0) - 4a	–	22.8	–	–	–	2.2
	(0.5, 0.5, 0.5) - 4b	–	4.4	16	4.6	–	–

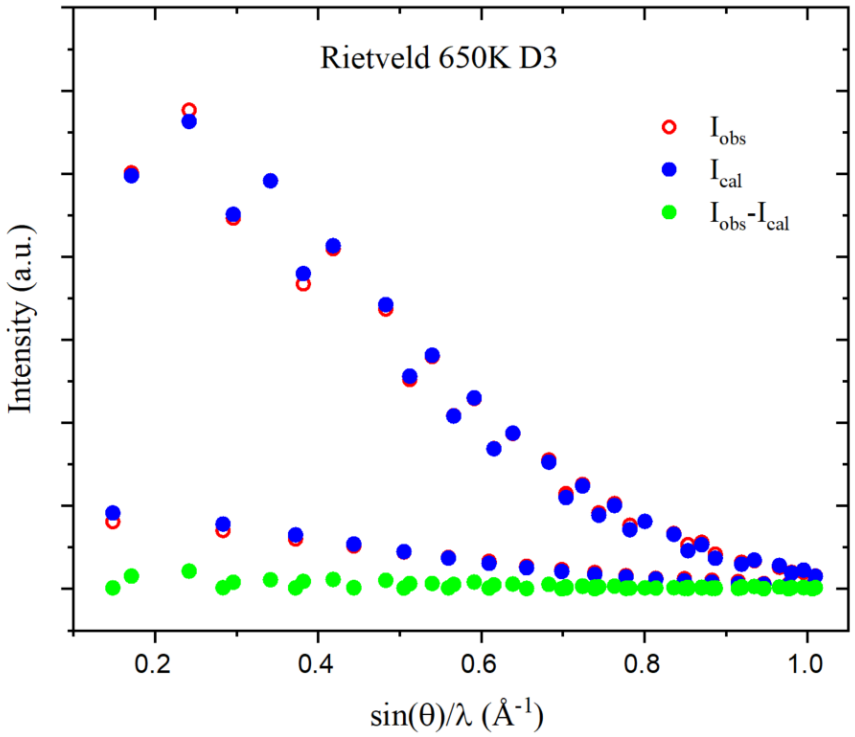

Figure 7.5 *Neutron diffraction reflections measured at 650K, with the corresponding Rietveld refinement for the Fe_0 alloy. Red dots represent experimental reflections; blue bots are the Rietveld fittings; and green ones correspond to the difference between the measurements and the fittings. The Miller indices corresponding to each reflection are indexed above each reflection. Fittings performed employing the data acquired at other temperatures are shown in* ***Figures A.4.3 and A.4.4***

The Rietveld fittings in the Fe_2 single crystal cannot be considered successful, due to the aforementioned presence of multiple reflections for each Bragg peak arising from the multiple grains with similar but slightly different orientations. Nevertheless, the atomic structure shown in **Table 7.3**, deduced from both the previously mentioned works and the information obtained from the polycrystalline samples (see **Table 6.4**) was employed for the following subsequent magnetic analysis. The similarity of the atomic site occupancies within the non-doped polycrystalline and single crystal alloys supports this assumption (**see Table 7.2 and 6.3**). Nonetheless, from the average position of each of the observed Bragg reflections for the Fe_2 single crystal it is still possible to deduct the lattice parameter of the austenite phase. Both samples present the expected *Fm-3m* cubic symmetry in the measured austenitic phase, with a neglectable difference in the lattice parameter between them. It must be mentioned that, while the Fe_2 sample presents a slight decrease in the lattice parameter with the temperature, no change can be appreciated in the Fe_0 crystal.

The mechanism behind the evolution of T_M could not be experimentally demonstrated, since no martensitic measurements were done. Nevertheless, the important role the martensite structure plays in T_M has been widely referenced and discussed in this dissertation. Continuing this line, the lower T_M upon Fe-doping could be attributed to a less-distorted martensite which, as mentioned, is yet to be experimentally confirmed.

For the fittings of the flipping ratios measured for each Bragg reflection at D3, employing an 8T magnetic field, the use of the least-square refinement method (see **Figure 7.6** for the measurements at 560K) allowed the determination of the magnetic moment density in each atomic position of the crystal lattice. The results, presented in **Table 7.3**, evidence an increase of the magnetic moment as the temperature lowers, corresponding to the transition from a paramagnetic to a ferromagnetic behaviour.

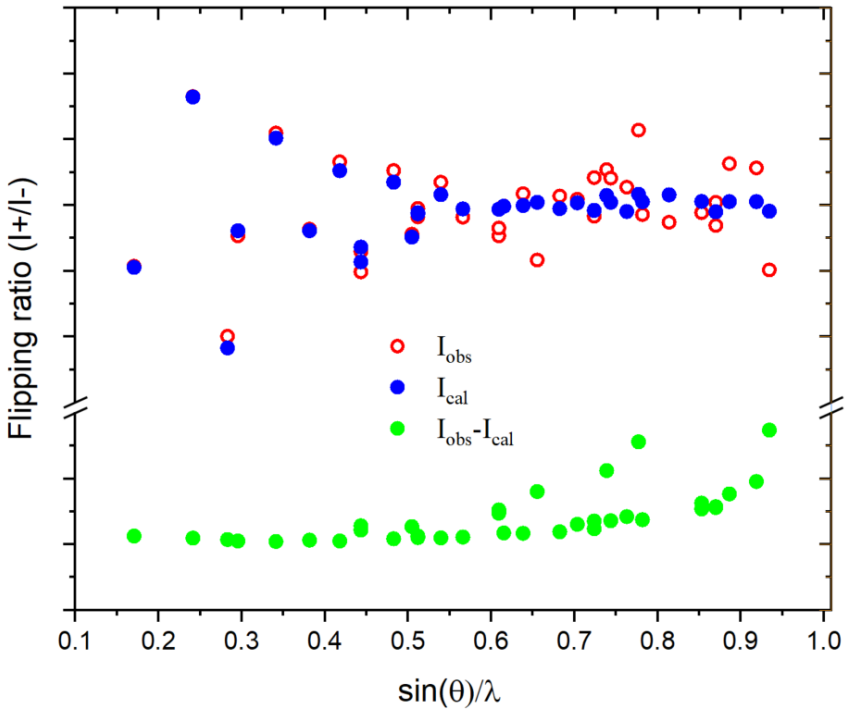

Figure 7.6. *Representative measurement of the flipping ratios obtained at specific Bragg reflections measured at 560K, with its corresponding Magnetic Rietveld refinement, for the Fe_0 alloy. Red dots represent experimental flipping ratios; blue bots are the Rietveld fittings; and green ones correspond to the difference between the measurements and the fittings. The Miller indices corresponding to each reflection are indexed above each reflection. Fittings performed employing the data acquired at other temperatures and for the Fe_2 alloy are shown in* ***Figures A.4.5 and A.4.6****.*

Table 7.3 *Magnetic site densities obtained from the refinements of the measurements of the Fe_0 and Fe_2 alloys at every measured temperature. The atomic sites are named following the Wyckoff notation.*

Alloy	Temperature (K)	μ_{8c} (μ_B)	μ_{4a} (μ_B)	μ_{4b} (μ_B)
Fe_0	650	0.03	0.20	0.04
	560	0.06	0.36	0.04
	510	0.09	0.63	0.06
Fe_2	600	0.10	0.48	0.07
	460	0.29	1.72	0.14
	390	0.33	2.93	1.64

The remarkable lower total value of the magnetic moments in the Fe_0 crystal is due to the totality of the data been acquired above T_C^A. Therefore, every measurement was performed in the paramagnetic state of the crystal. On the contrary, the data acquired for Fe_2 corresponds to temperatures above, near and below T_C^A. Thus, a much higher increase of the obtained magnetic site densities with the temperature is expected, attributed to the transition from a paramagnetic to a ferromagnetic behaviour.

As an approach to explain the differences in T_C^A for the two alloys, the magnetic moment densities obtained at similar reduced temperatures are compared. Therefore, the measurements selected for the Fe_0 and Fe_2 crystals are 560 and 600K, respectively ($T/T_C \sim 1.25$). The higher moment densities obtained in the Fe_2 alloy can be attributed to an increasing number of ferromagnetic exchange interactions, what is in line with the results presented in **Section 6.4**. As widely discussed in previous chapters[20,24], the magnetic exchange interactions are greatly dependant on the interatomic distances between sites where Mn atoms are present. For this reason, the distances between the atomic sites are quantified, employing the equations proposed in the previous chapter (**Equations 6.1-6.3**) for the austenite. For the two $T/T_C \sim 1.25$ measurements (Fe_0 at 560K and Fe_2 at 600K), the calculated distances are $d_{4a\text{-}4a}$= 4.14 Å, $d_{4a\text{-}4b}$=2.92Å, $d_{4a\text{-}8c}$=2.53 Å.

With this information, a correlation between the atomic site occupancies (**Table 7.2**) and the magnetic moment distribution (**Table 7.3**) can be established:

- The significant increase of the magnetic moment in the 4a position of Fe_2 single crystal is associated to the presence of Fe atoms, instead of In, and, therefore, to the increasing number of magnetic atoms in 4a sites.
- The higher magnetic moment in the 4b and 8c positions upon Fe doping can be attributed to the reduced amount of Mn and the increased number of Co atoms in these positions. Following the approach established in **Chapters 5 and 6,** where Mn-Mn magnetic interactions in the distance range of 2.92 Å and below are considered to present antiferromagnetic behaviour, we assume the same occurrence between 4a and displaced (4b and 8c) Mn atoms in this set of samples.

7.4. EFFECT OF TRAINING ON THE MARTENSITIC ELASTICITY

After characterizing the austenitic phase of the crystals and correlating the results with their magnetic behaviour, to further characterize the properties of the single crystals they were trained by the procedure explained in **Section 7.2** (heating and allowing to cool until room temperature under an applied stress). To elucidate whether the resultant martensite is influenced by the applied stress and, thus, by the different loads applied during each training process, mechanical compression tests were performed at room temperature.

The pressures (loads) applied to each sample while cooling down are listed below, and the resulting measured stress-strain curves shown collectively in **Figure 7.7** and separately in **Figure A.4.7**).

- Fe_0: 2.5, 5, 7.5, 10, 12.5, 15, 17.5 and 20 MPa.
- Fe_2: 7.5, 10, 12.5 and 17.5 MPa.

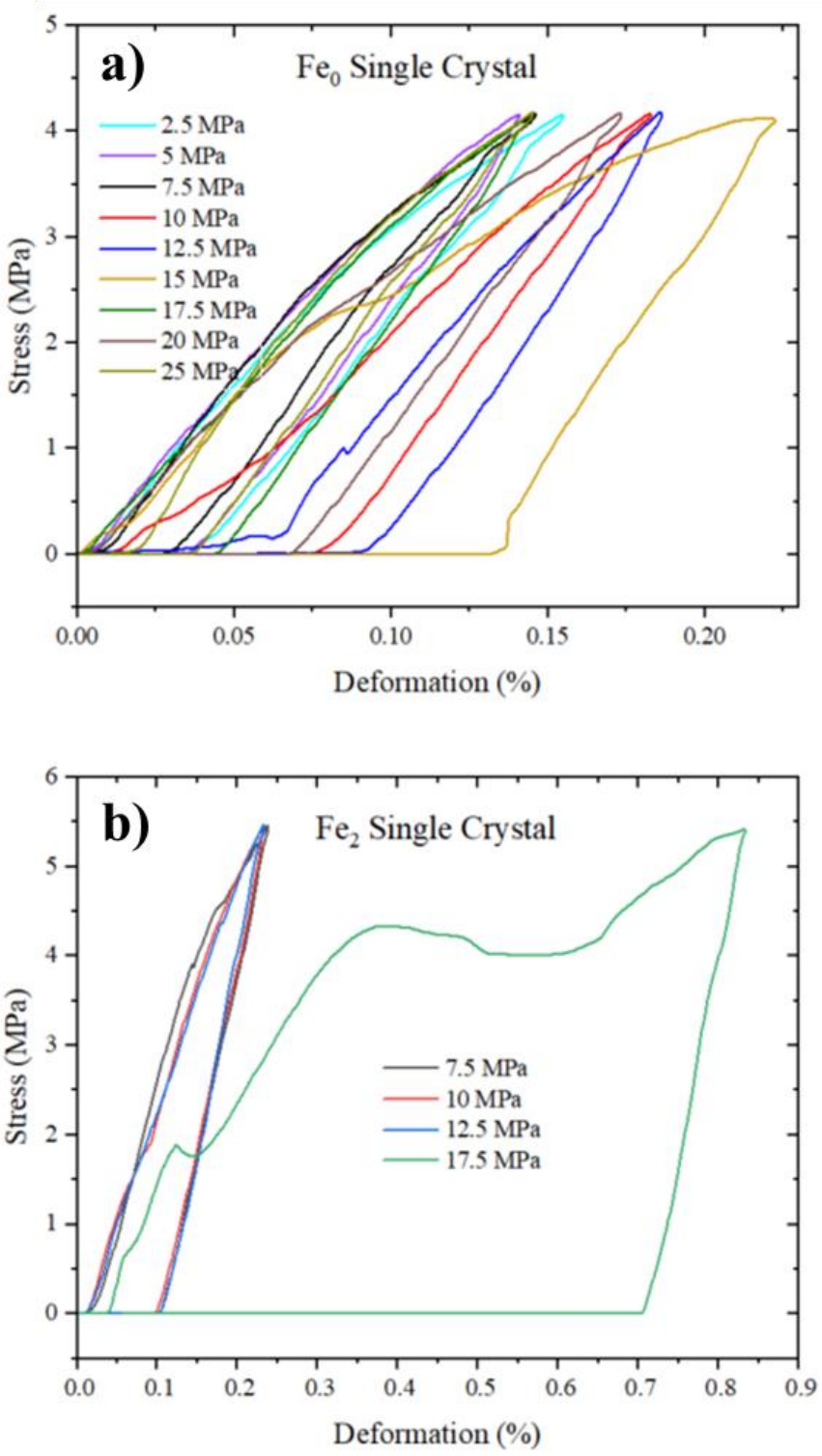

Figure 7.7. *Stress-strain curves obtained via micromechanical testing at room temperature after training the a) Fe_0 and b) Fe_2 crystals under different stresses. See* ***Figure A.4.7*** *in the Annex for a separate graph of each Fe_0 curve.*

The remarkable different aspect of the stress-strain curves infers a great dependence of the loads applied during cooling on the compressive behaviour. In

particular, four main observations can be deduced from the measurements performed in the Fe_0 single crystal:

- The residual deformation remaining in the alloy after the compression test is ~ 0.05% for the martensites induced upon cooling under stresses below 10 MPa (see **Figure 7.8**). The linear relation between deformation and stress implies a non-oriented twinned martensite, which implies a purely elastic behaviour of the alloy[25,26].
- The application of a 12.5 MPa stress during cooling results in a twinned martensite and a residual deformation close to 0.1%. This assumption is based on the region of the stress-strain curve where the undergoing deformation does not increase the stress in the detector, leading to conclude that it is not caused by an elastic deformation[16,27,28].
- After a 10 MPa stress was applied upon cooling, the measured stress-strain curve presents a hybrid aspect between the 12.5 MPa and the ones below 10 MPa. This can be attributed to the formation of a partially oriented twinned martensite.
- The stress-strain curves corresponding to the martensitic phases obtained upon cooling under 15 MPa or higher loads present a residual deformation comparable to the twinned martensite one, in addition to a non-lineal relation between deformation and stress, although no clear motion of twin variants is appreciated. This effect can be attributed to a martensite with the ordered twin variants moving collectively, what is physically seen as a slight but noticeable deviation from the linear behaviour in the elastic region of the curve.

Besides these observations, it should be remarked that the presence of deformations arising from the reorientation of twin variants is of great interest for the prospective applications of the Ni-Mn-Ga-Co-In single crystals as sensors and/or actuators. This interest originates from the fact that the alloys undergo deformations as a result from two different mechanisms and, thus, at two different temperature ranges: at the MT and from the twin variants reorientation.

A narrower range of loads was used for the systematic study of the Fe_2 crystal, since the study on Fe_0 sample infers no significant differences for working loads below 7.5 MPa, and plastic deformation is induced in the alloy employing 17.5 MPa. Following these measurements, useful information can be extracted by inspecting the results presented in **Figure 7.7b** for this alloy, such as the appearance of a non-linear behaviour in the training with a 17.5 MPa load. Analogously to the explanation drawn for the Fe_0 single crystal, this effect can be attributed to either the collective motion of twin variants or to a partially oriented twinned martensite. As a consequence, further tests need to be performed to elucidate the mechanism behind it. The absence of clear twin variants movement can be attributed to it being inhibited by grain boundaries arising from the different crystal orientations present in this alloy, as evidenced by the Laue diffraction pattern at room temperature shown in **Figure 7.4**.

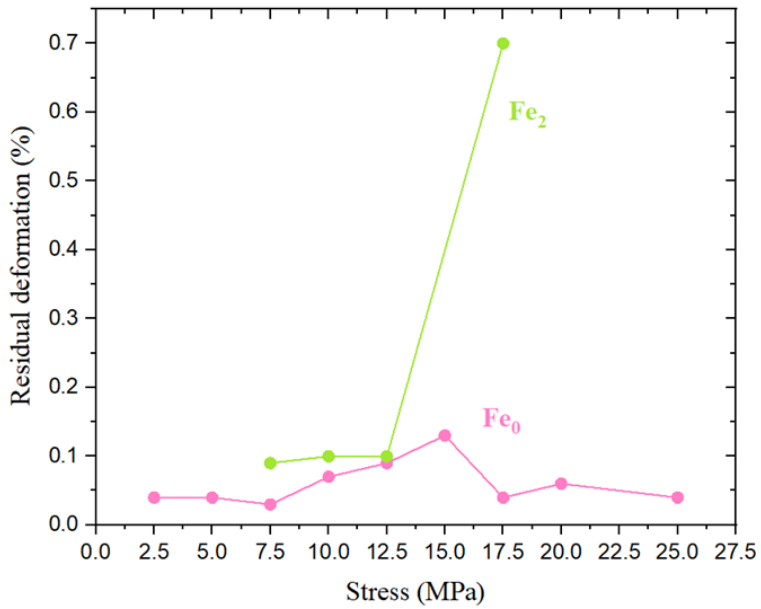

***Figure 7.8**. Dependence of the residual deformation after each compression test on the stress applied in each crystal during training.*

The ~ 0.1% residual deformation under the lowest stresses means that the Fe doping favours a more ductile, less elastic behaviour in the martensite[25]. This assumption is supported by the permanent, plastic deformation induced in the sample by the micromechanical testing of the sample after a 17.5MPa stress. It should be mentioned that this more ductile behaviour, along with the lack of twin variant movement, may be derived from the same reason mentioned in the previous

paragraph; i.e. the imperfection of this single crystal, which presents smaller crystallites with slightly different crystal orientations.

7.5. EFFECT OF PATTERNING ON THE ELASTICITY OF THE MARTENSITE

In the previous section, we explained that the movement of the twin variants was easily appreciated in the Fe_0 crystal after being heated up to 900 K and cooled down under a 12.5 MPa stress. Therefore, a Fe_0 single crystal trained under a 12.5MPa load was subjected to surface patterning, with the aim of studying how it affects the mechanical behaviour of the alloys by interfering with the motion of the twin variants[29]

As previously mentioned, the surface patterning was performed by hitting the single crystal with glass nanoparticles, resulting into a surfaced patterned with small, randomly distributed dots. Three different patternings were created in the single crystal, as a result of ejecting these particles with pressures of 1, 2.5 and 5 MPa, hereafter denoted Patterning 1, 2 and 3, respectively. Compression tests, analogous to the ones presented in **Figure 7.7**, were performed in each sample, resulting in the stress-strain curves presented in **Figure 7.9.**

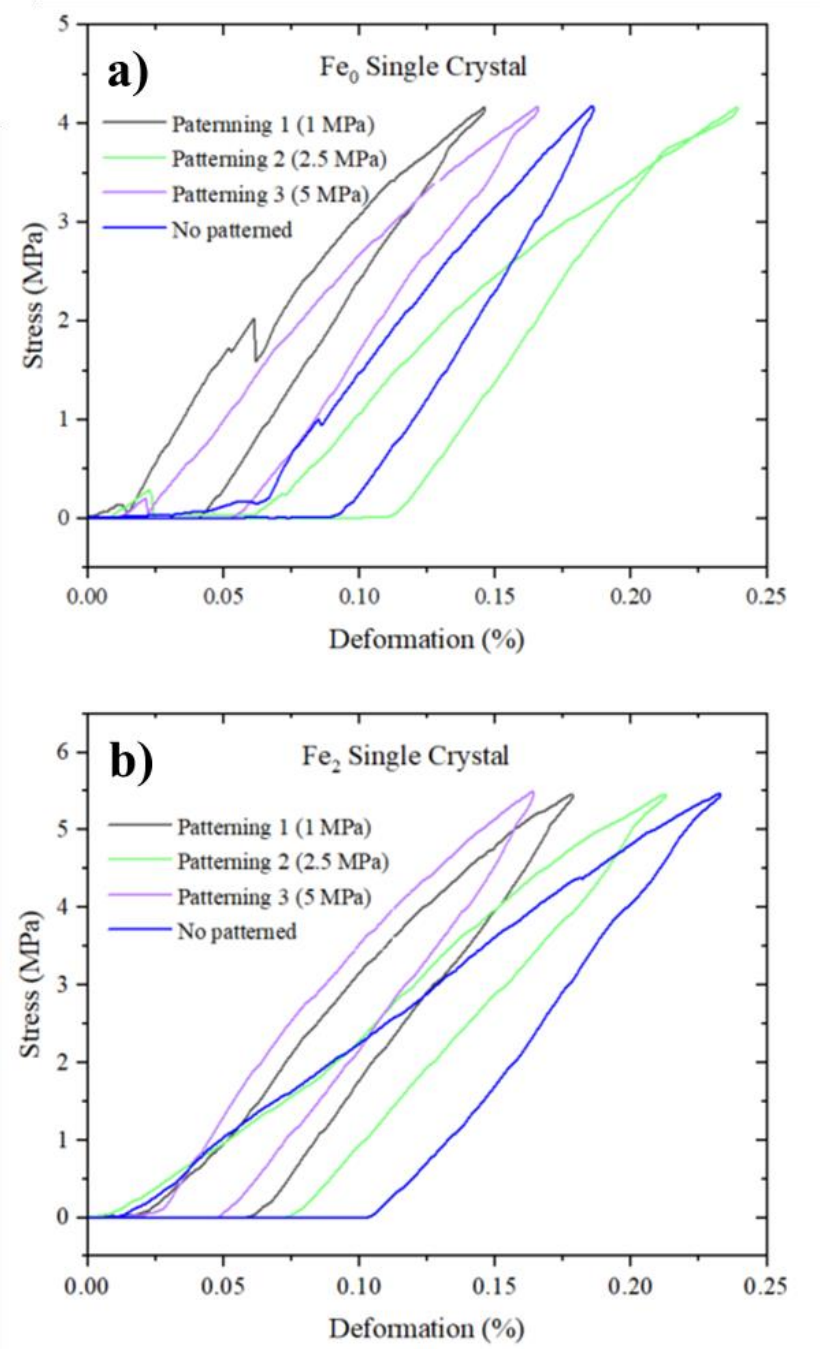

Figure 7.9. *Stress-strain curves obtained via micromechanical testing at room temperature after patterning the trained a) Fe_0 and b) Fe_2 crystals employing different air pressures.*

By comparing the non-patterned, 1 (patterning 1) and 2.5 (patterning 2) MPa patterned Fe_0 crystals, the presence of a peak in the middle of the elastic region (between 0.05 – 0.10% deformation) is clearly evidenced. This can be attributed to the interference caused by the interaction of several variants movement. The sample patterned under 2.5 MPa (patterning 2) displays the twin variants-related deformation also shown by the non-patterned sample, although presenting a greater residual

deformation, as it can be appreciated in **Figure 7.10**. Further measurements and analysis need to be gathered to be able to explain this behaviour. The stress-strain curve obtained after the patterning employing 5 MPa (patterning 3) displays a purely elastic behaviour. This phenomenon can be attributed to the inhibition of the movement of twin variants due to the strains induced by the patterning.

Regarding the Fe_2 crystal, a similar analysis to that presented for the patterned Fe_0 crystal can be drawn. For the sake of comparison, the same training (heating up to 900 K and cooling down under a 12.5 MPa stress) and patterning pressures were employed in both samples. The behaviour of the 2.5 MPa (patterning 2) sample is comparable to the non-patterned sample, while the 1 MPa (patterning 1) and 5 MPa (patterning 3) samples appear to present pure elastic deformations. Analogously to the explanations given for the Fe_0 sample, this behaviour cannot be explained or attributed to the twin variants movement being inhibited by the induced strains. Therefore, from the measurements available up to the writing of this thesis, we can only attribute the smaller residual deformation found in every patterned sample to a patterning-enhanced SME. Further measurements are yet to be performed in order to confirm this hypothesis.

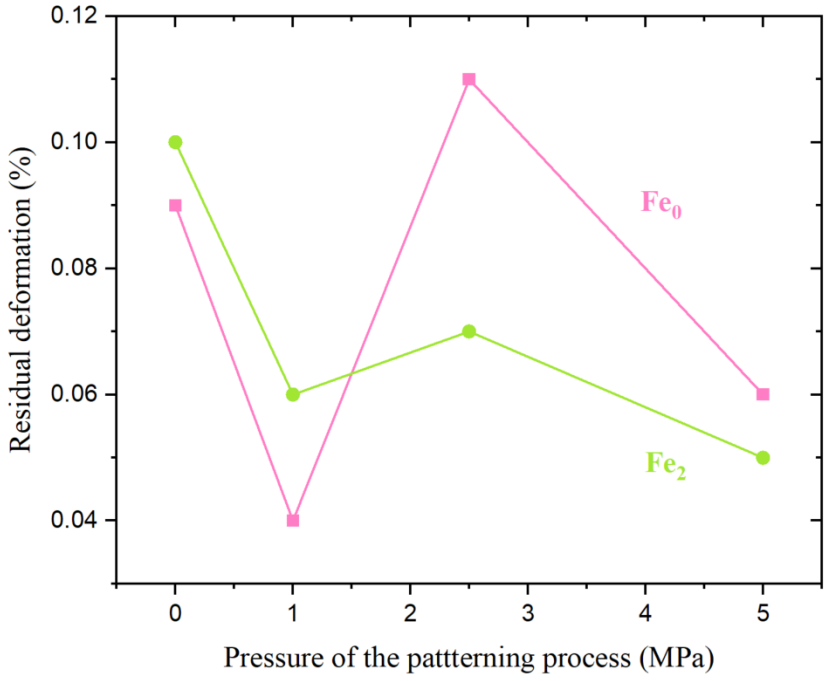

Figure 7.10. *Residual deformation after compression test dependence on the pressure employed for the patterning in each crystal.*

7.6. SUMMARY AND CONCLUSIONS

The present chapter continues the work started in the previous one, where the effect Fe doping has on the transformation behaviour, crystal structure and magnetic properties of powder Ni-Mn-Ga-Co-In-Fe alloys was investigated. That work has been continued by growing and characterizing single crystals of selected compositions displaying interesting entropy and volumetric change properties, since the lack of grain boundaries makes them more interesting from an industrial point of view towards their use in applications such as sensors and actuators.

Ni-Mn-Ga-Co-In and a Ni-Mn-Ga-Co-Fe single crystals were grown using the modified optical floating zone technique. Volumetric changes of ~ 0.05 % were measured upon undergoing martensitic transformations. Their crystal and magnetic structures have been characterized via polarized and non-polarized single crystal neutron diffraction experiments.

The Rietveld fittings of the data acquired in the non-polarized neutron diffraction measurements reveal a *Fm-3m* structure in both crystals. The atomic site occupancies obtained for the Fe_0 sample resemble the ones that the similar composition polycrystalline alloy studied in **Chapter 6** shows. The magnetic refinements performed on the data obtained in the polarized neutron diffraction experiments evidence an increase of the magnetic moment in each atomic site upon Fe-doping. This is attributed to the nature of the Mn-Mn interactions in a similar fashion to what was discussed in previous chapters, that in these alloys results in an increase of ferromagnetic exchange interactions between Mn atoms upon Fe doping. The key role these interactions play in the evolution of T_C explains its higher value in the Fe doped alloy.

As we have not measured yet the single variant martensite phases of the two studied crystals, we cannot explain yet the underlying mechanism of the decrease in T_M upon Fe doping. Nevertheless, the parallelism with previous works lets us hypothesize that it may be associated with a more distorted martensite.

The effect of training in the martensite of the alloys studied here was analysed by inducing the martensitic transformation with an applied pressure upon cooling

from the austenite, and subsequently testing the elasticity and twin variants movement on the resultant martensite via compression tests. A martensite with oriented twin variants was revealed to be induced when the training was performed with an applied pressure of 12.5 MPa and above in the Fe_0 crystal, although the movement of the variants is inhibited by the strains created when training under pressures higher than 15 MPa. In the Fe_2 crystal, a slight hint of a martensite with oriented twins is appreciated upon training with 12.5 MPa loads, together with a remarkable increase in the ductility compared to the non-doped one. The greater ductility is seen not only in the higher residual deformation, but also in the plastic deformation induced by training under a 17.5 MPa stress.

As previously introduced in **Section 7.1,** the motion of twin variants can be enhanced in surface-patterned samples, due to the increase in the nucleation points the superficial strains induce in the alloy. In the current status of investigation of this work at the time of writing this dissertation, this effect was not found. Instead, we found that the created strains either do not affect or hinder the twin variants movement. Nevertheless, an improvement in the shape recovery can be appreciated due to the patterning, what could be interesting for potential sensor and actuator applications.

7.6. BIBLIOGRAPHY

1. Yu Q, Jauregui LA, Wu W, et al. Control and characterization of individual grains and grain boundaries in graphene grown by chemical vapour deposition. *Nat Mater*. 2011;10(6):443-449. doi:10.1038/nmat3010

2. Hansen N, Huang X, Winther G. Effect of grain boundaries and grain orientation on structure and properties. *Metall Mater Trans A Phys Metall Mater Sci*. 2011;42(3):613-625. doi:10.1007/s11661-010-0292-5

3. Hobza A, Patrick CL, Ullakko K, Rafla N, Lindquist P, Müllner P. Sensors and Actuators A : Physical Sensing strain with Ni-Mn-Ga. *Sensors Actuators A Phys*. 2018;269:137-144. doi:10.1016/j.sna.2017.11.002

4. Chernenko VA, L'Vov VA, Cesari E, Kosogor A, Barandiaran JM. Transformation volume effects on shape memory alloys. *Metals (Basel)*.

2013;3(3):237-282. doi:10.3390/met3030237

5. Naresh C, Bose PSC, Rao CSP. Shape memory alloys: A state of art review. *IOP Conf Ser Mater Sci Eng*. 2016;149(1). doi:10.1088/1757-899X/149/1/012054

6. Hornbogen E. Review Thermo-mechanical fatigue of shape memory alloys. *J Mater Sci*. 2004;39(2):385-399. doi:10.1023/B:JMSC.0000011492.88523.d3

7. Asadian M, Seyedein SH, Aboutalebi MR, Maroosi A. Optimization of the parameters affecting the shape and position of crystal-melt interface in YAG single crystal growth. *J Cryst Growth*. 2009;311(2):342-348. doi:10.1016/j.jcrysgro.2008.10.045

8. Chulist R, Czaja P. On the role of atomic shuffling in the 4O, 4M and 8M martensite structures in Ni-Mn-Sn single crystal. *Scr Mater*. 2020;189:106-111. doi:10.1016/j.scriptamat.2020.08.007

9. Chernenko VA, Villa E, Besseghini S, Barandiaran JM. Giant two-way shape memory effect in high-temperature Ni-Mn-Ga single crystal. *Phys Procedia*. 2010;10:94-98. doi:10.1016/j.phpro.2010.11.081

10. Zheludev A, Shapiro S, Wochner P, Tanner L. Precursor effects and premartensitic transformation inMnGa. *Phys Rev B - Condens Matter Mater Phys*. 1996;54(21):15045-15050. doi:10.1103/PhysRevB.54.15045

11. Chmielus M, Rolfs K, Wimpory R, Reimers W, Müllner P, Schneider R. Effects of surface roughness and training on the twinning stress of Ni-Mn-Ga single crystals. *Acta Mater*. 2010;58(11):3952-3962. doi:10.1016/j.actamat.2010.03.031

12. Maziarz W, Czaja P, Szczerba MJ, Lityńska-Dobrzyńska L, Czeppe T, Dutkiewicz J. Influence of Ni/Mn concentration ratio on microstructure and martensitic transformation in melt spun Ni-Mn-Sn Heusler alloy ribbons. *J Alloys Compd*. 2015;615(S1):S173-S177. doi:10.1016/j.jallcom.2013.12.164

13. Barandiarán JM, Chernenko VA, Lázpita P, Gutiérrez J, Fdez-Gubieda ML, Kimura A. Neutron and synchrotron studies of structure and magnetism of Shape Memory Alloys. *J Phys Conf Ser*. 2015;663(1). doi:10.1088/1742-6596/663/1/012014

14. Richard ML, Feuchtwanger J, Allen SM, et al. Chemical order in off-

stoichiometric Ni-Mn-Ga ferromagnetic shape-memory alloys studied with neutron diffraction. *Philos Mag*. 2007;87(23):3437-3447. doi:10.1080/14786430701297582

15. Chmielus M, Witherspoon C, Ullakko K, Müllner P, Schneider R. Effects of surface damage on twinning stress and the stability of twin microstructures of magnetic shape memory alloys. *Acta Mater*. 2011;59(8):2948-2956. doi:10.1016/j.actamat.2011.01.035

16. Lázpita P, Villa E, Villa F, Chernenko V. Temperature dependent stress–strain behavior and martensite stabilization in magnetic shape memory ni51.1 fe16.4 ga26.3 co6.2 single crystal. *Metals (Basel)*. 2021;11(6):1-11. doi:10.3390/met11060920

17. Singh S, Kushwaha P, Scheibel F, et al. Residual stress induced stabilization of martensite phase and its effect on the magnetostructural transition in Mn-rich Ni-Mn-In/Ga magnetic shape-memory alloys. *Phys Rev B - Condens Matter Mater Phys*. 2015;92(2):1-6. doi:10.1103/PhysRevB.92.020105

18. Rodríguez-Carvajal J. FullProf. Published online 2001.

19. Qureshi N. Mag2pol: A program for the analysis of spherical neutron polarimetry, flipping ratio and integrated intensity data. *J Appl Crystallogr*. 2019;52:175-185. doi:10.1107/S1600576718016084

20. Pérez-Checa A, Porro JM, Feuchtwanger J, et al. Role of Fe addition in Ni–Mn–Ga–Co–Cu–Fe ferromagnetic shape memory alloys for high-temperature magnetic actuation. *Acta Mater*. 2020;196:549-555. doi:10.1016/j.actamat.2020.07.007

21. Cong DY, Wang YD, Lin Peng R, et al. Crystal structures and textures in the hot-forged Ni-Mn-Ga shape memory alloys. *Metall Mater Trans A Phys Metall Mater Sci*. 2006;37(5):1397-1403. doi:10.1007/s11661-006-0084-0

22. Orlandi F, Fabbrici S, Albertini F, Manuel P, Khalyavin DD, Righi L. Long-range antiferromagnetic interactions in Ni-Co-Mn-Ga metamagnetic Heusler alloys: A two-step ordering studied by neutron diffraction. *Phys Rev B*. 2016;94(14):1-5. doi:10.1103/PhysRevB.94.140409

23. Orlandi F, Çaklr A, Manuel P, Khalyavin DD, Acet M, Righi L. Neutron

diffraction and symmetry analysis of the martensitic transformation in Co-doped Ni2MnGa. *Phys Rev B*. 2020;101(9):1-13. doi:10.1103/PhysRevB.101.094105

24. Lázpita P, Barandiarán JM, Gutiérrez J, Feuchtwanger J, Chernenko VA, Richard ML. Magnetic moment and chemical order in off-stoichiometric Ni-Mn-Ga ferromagnetic shape memory alloys. *New J Phys*. 2011;13:1-14. doi:10.1088/1367-2630/13/3/033039

25. Roylance D. STRESS-STRAIN CURVES. Published online 2001:1-14.

26. Villa E, Villa F, Crespo BR, et al. Shape memory and elastocaloric properties of melt-spun NiMn-based Heusler alloys. *J Alloys Compd*. 2023;965(May):171437. doi:10.1016/j.jallcom.2023.171437

27. Müllner P, King AH. Deformation of hierarchically twinned martensite. *Acta Mater*. 2010;58(16):5242-5261. doi:10.1016/j.actamat.2010.05.048

28. Aaltio I, Söderberg O, Ge Y, Hannula SP. Twin boundary nucleation and motion in Ni-Mn-Ga magnetic shape memory material with a low twinning stress. *Scr Mater*. 2010;62(1):9-12. doi:10.1016/j.scriptamat.2009.09.012

29. Zhang Q, Semperlotti F. Nonlinear damping characteristics of shape-memory-alloy hybrid composite plates: The synergistic role of patterning and pre-straining SMA layers. *Mech Syst Signal Process*. 2024;218(February). doi:10.1016/j.ymssp.2024.111545

CHAPTER 8

Conclusions and future work

8.1. CONCLUSIONS

The main goal of the work endured in this thesis was to draw a connection between the microstructure and the properties of selected magnetic shape memory alloys, following the path towards the obtention of materials with tailored properties for a variety of implementations, such as solid-state refrigeration or sensors and actuators, among other possible ones.

A deep study of the influence of different post annealing heat treatments and compositional variations, through specific element doping, on the structural, magnetic, and mechanical properties of both polycrystalline and single crystal magnetic shape memory alloys was performed. The general conclusions of the work are summarized as follows.

The particular goal of **Chapter 4** was to study the effect of different heat treatments on the structure and magnetocaloric performance of Co-doped Ni-Mn-Sn metamagnetic shape memory alloys. The neutron diffraction experiments concluded that the cubic *Fm-3m* structure transforms to a modulated monoclinic one (3M *P2/m*) upon the martensitic transition. The presence of retained austenite in the martensitic range of temperatures in non-heat-treated alloy is evidenced. We attributed this coexistence of phases to an incomplete martensitic transformation due to the stresses induced during the fabrication process. The relaxation of the stresses and, thus, a total MT was observed after both previous (HT1) and intermediate (HT2) heat treatments.

Additionally, the analysis of the atomic site occupancies of the two different-composition alloys that underwent similar heat treatments revealed a higher percentage of Mn atoms interacting ferromagnetically in the alloy with higher Mn and lower Co contents, what explains the higher T_C and μ_{sat} values obtained for this alloy.

We also observed that, after the post-annealing heat treatments, the magnetocaloric performance of the alloys is noticeably improved, being comparable to recognized magnetocaloric materials studied in literature ($\Delta Sm.max \approx 20$ J·kg-1K-1 under a 2T magnetic field).

Chapters 5 and 6 focus on the influence different doping elements have on the austenitic and martensitic structure of Ni-Mn-Ga-based alloys, to pursuit a better understanding of the underlying mechanism behind the evolution of the characteristic temperatures (T_C and T_M) controlling the temperature actuation range of the alloys.

The study of the influence Cu-doping has on Ni-Mn-Ga-Cu alloys enables to deduce the occurrence of an interesting intermartensitic transition (from an orthorhombic 5M modulated *Immm* to a tetragonal non-modulated *I4/mmm*) when the Cu doping is 6%, while lower Cu-content alloys present a 5M modulated *Immm* orthorhombic martensite and higher Cu-content ones present a non-modulated *I4/mmm* tetragonal martensite. The explanation of the increase in T_M as the Cu content increases is attributed to more distorted martensite structures. Additionally, we associate the higher Cu content with a decrease in the number of ferromagnetic interactions between Mn atoms, which are responsible for the observed evolutions of μ_{sat} and T_C in the alloy series.

A relatively similar study exploring the effect Fe-doping has on the properties of Ni-Mn-Ga-Co-In alloys endorsed the established correlation between the lower percentage of Mn atoms displaying antiferromagnetic exchange interactions and the increasing T_C both in the austenite and martensite phases. We observed an inhibition of the MT in the alloys with 2 at% Fe doping or higher in the selected set of samples (between 0 and 6 at% content of Fe), which may be attributed to the presence of secondary phases in these alloys. The structural analysis unravelled the usual cubic *Fm-3m* austenitic structure and a tetragonal non modulated *I4/mmm* symmetry in every martensite analysed. The evolution of the cell parameters evidences less distorted martensite phases as the Fe content increases, what explains the observed decrease of T_M with increased Fe content in the alloys that display a MT. An interesting martensitic magnetic transition was observed in those alloys undergoing a

full MT (Fe_0 and Fe_1), in which antiferromagnetic ordering was found at low temperatures (50K).

While the majority of the work presented in this dissertation was conducted employing polycrystalline materials, **Chapter 7** summarized the study performed on Ni-Mn-Ga-Co-(In,Fe) single crystals. Unpolarized single crystal neutron diffraction experiments revealed the expected cubic *Fm-3m* austenitic structure. Polarized neutron diffraction experiments allowed us to perform magnetic refinements that evidence an increase of the magnetic moment in each atomic site of the crystal lattice in the Fe-doped single crystal, attributed to the nature of the Mn-Mn interactions. This is in line with the conclusions obtained in previous chapters, and is also responsible for the increase in T_C as compared to the single crystal without Fe.

Besides the determination of the crystal and magnetic structures of the austenite phases of the two studied single crystals, in this work we also disclosed the effect of mechanical training in the low-temperature martensite structure. The results evidence that a martensite with more mobile twin variants is induced upon cooling the Fe_0 crystal from the austenite under an applied pressure (load) of 12.5 MPa. In the Fe-doped crystal, which we found to display a greater ductility, a hint of twin variants mobility was appreciated when cooling under a 17.5 MPa load, although plastic deformation was generated after that training. Finally, the effect of surface patterning on the two crystals, by employing micropeening processes, on their mechanical properties was studied. The motion of twin variants was observed to be either not affected or hindered by surface patterning, although it was proven to improve the shape memory effect of the studied crystals.

8.2. FUTURE WORK

As this thesis progressed, some future works have already been identified, offering promising opportunities to further expand and corroborate the results presented here.

First of all, the Ni-Mn-Ga-Co-(In,Fe) single crystals study is worth to be completed with the characterization of the martensite phases of the alloys. SCND

studies should be performed at temperatures lower than T_M to characterize the martensitic magnetic and nuclear structures, analogously to the work performed in the austenite. The single crystal growth method should be optimized, and a Fe-doped crystal with the desired composition, grown. The presented SCND studies, dilatometry, training and patterning processes should be extended to an optimized Fe_2 crystal that displays no crystallites, to be able to extract the magnetic and crystal structures of the austenite and martensite phases, as well as its mechanical behaviour without the grain boundaries interference. The results obtained by polarized neutron diffraction experiments can be complemented by performing X-ray magnetic circular dichroism (XMCD) experiments. In this way, the average magnetic moment contribution for each type of atom will be obtained, leading to a full understanding of the contribution to the magnetic site density of each element at each specific site.

As a result of a future optimization of the single crystal growth method, Ni-Mn-Ga-Co-In-Fe and Ni-Mn-Sn-Co single crystals can be grown, as these have shown interesting properties towards prospective applications. In particular, mechanical tests and measurements of the adiabatic temperature change across the structural and magnetic phase transitions will tell us if these single crystals are suitable for sensing/actuating and magnetocaloric applications, respectively.

When aiming to use these materials for magnetic refrigeration, through the exploitation of the magnetocaloric effect they display, increasing the surface-to-volume ratio would allow us to increase the effective surface through which the heat exchange takes place. Therefore, exploring paths towards an increase of this surface-to-volume ratio is an interesting path to follow. In this regard, we are starting to investigate the possibility to use patterning techniques to modify the surface of single crystals of MSMAs in the micro- and nano-scales through Focused Ion Beam (FIB) milling. An example of this initial work can be observed in **Figure 8.1**. These pillars correspond to a preliminary testing, part of an ongoing project with CICNanogune, in San Sebastián, Spain.

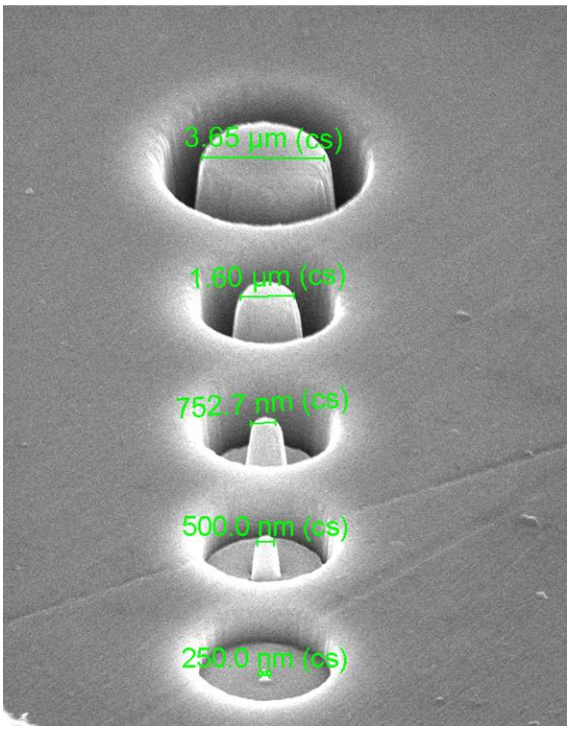

Figure 8.1. Nanopillars patterned in a Ni-Mn-Ga single crystal´s surface.

Finally, another path to follow in the future may be to perform magnetic Rietveld refinements in the ferromagnetic austenite of each alloy, pursuing the determination of the magnetic structure and magnetic site densities of all the alloys studied. Although these fittings have already been accomplished in Ni-Mn-Sn-Co polycrystals and Ni-Mn-Ga-Co-(In,Fe) single crystals, the polycrystalline Ni-Mn-Ga-Cu and Ni-Mn-Ga-Co-In-Fe studies are missing it. These measurements will further demonstrate the validity of the proposed model and amplify the comprehension of the correlation between structure and magnetic behaviour in these MSMAs.

Appendix – Supporting Images

A.1. CHAPTER 4 SUPPORTING IMAGES

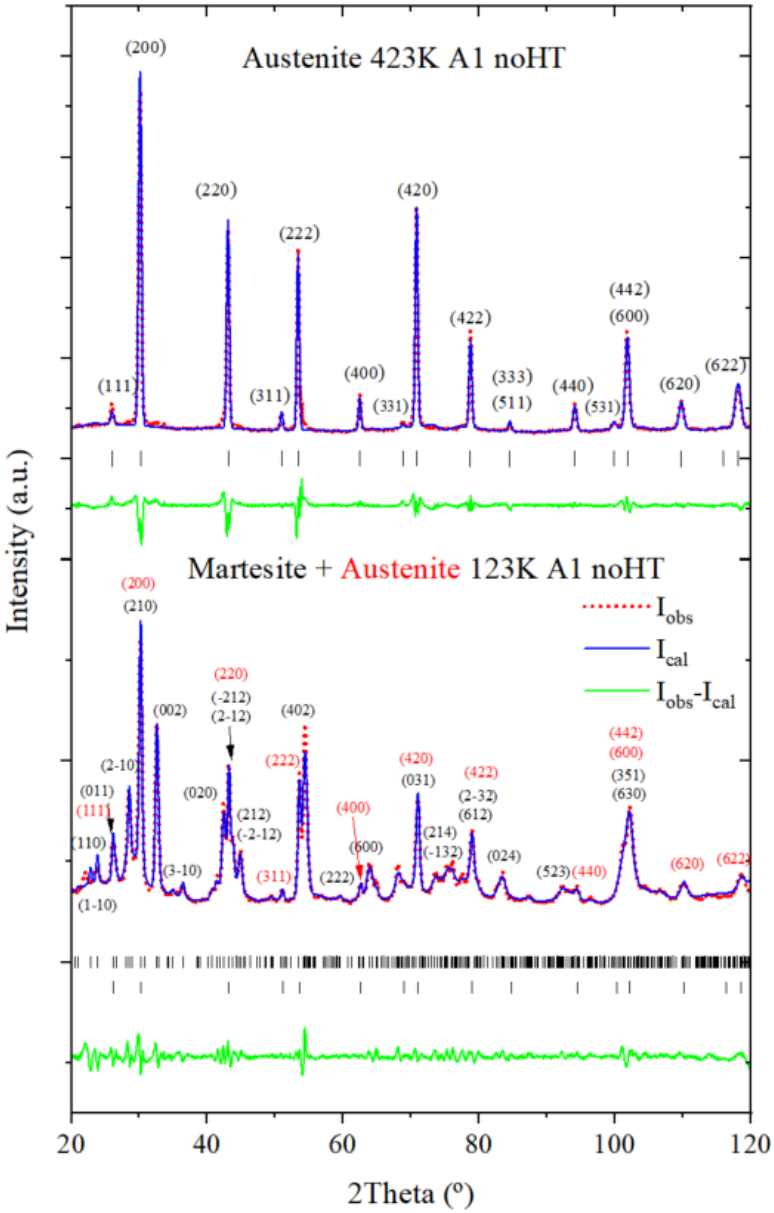

Figure A.1.1. *Neutron diffraction patterns and LeBail refinements at 423 and 123 K of the A1 noHT alloy. Red dots represent experimental points; blue lines are the LeBail fittings; and green lines correspond to the difference between the measurements and the fittings. The Miller indices corresponding to each reflection are indicated with a black line and shown above each main peak, with the colour indicating the phase they correspond to.*

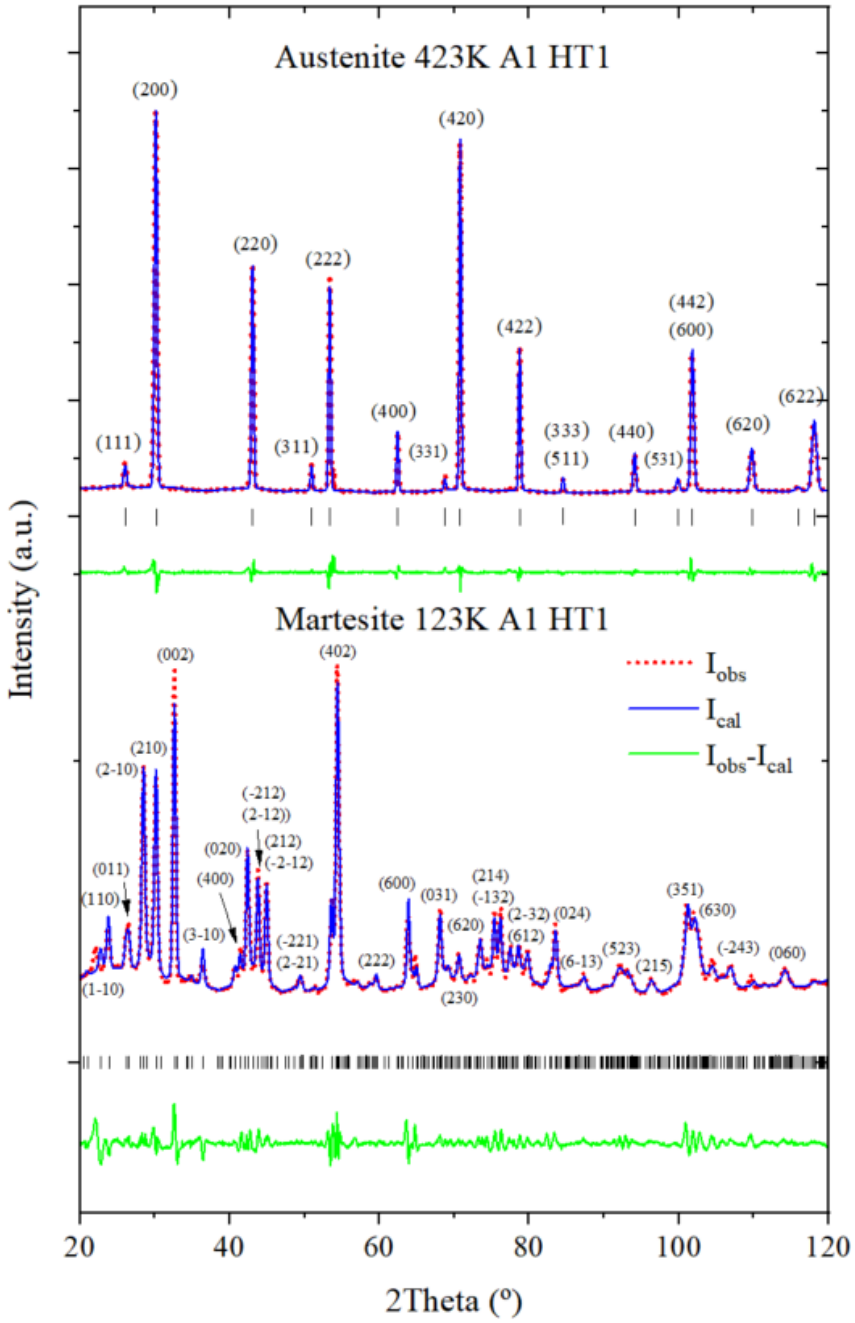

Figure A.1.2. *Neutron diffraction patterns and LeBail refinements at 423 and 123 K of the A1 HT1 alloy. Red dots represent experimental points; blue lines are the LeBail fittings; and green lines correspond to the difference between the measurements and the fittings. The Miller indices corresponding to each reflection are indicated with a black line and shown above each main peak.*

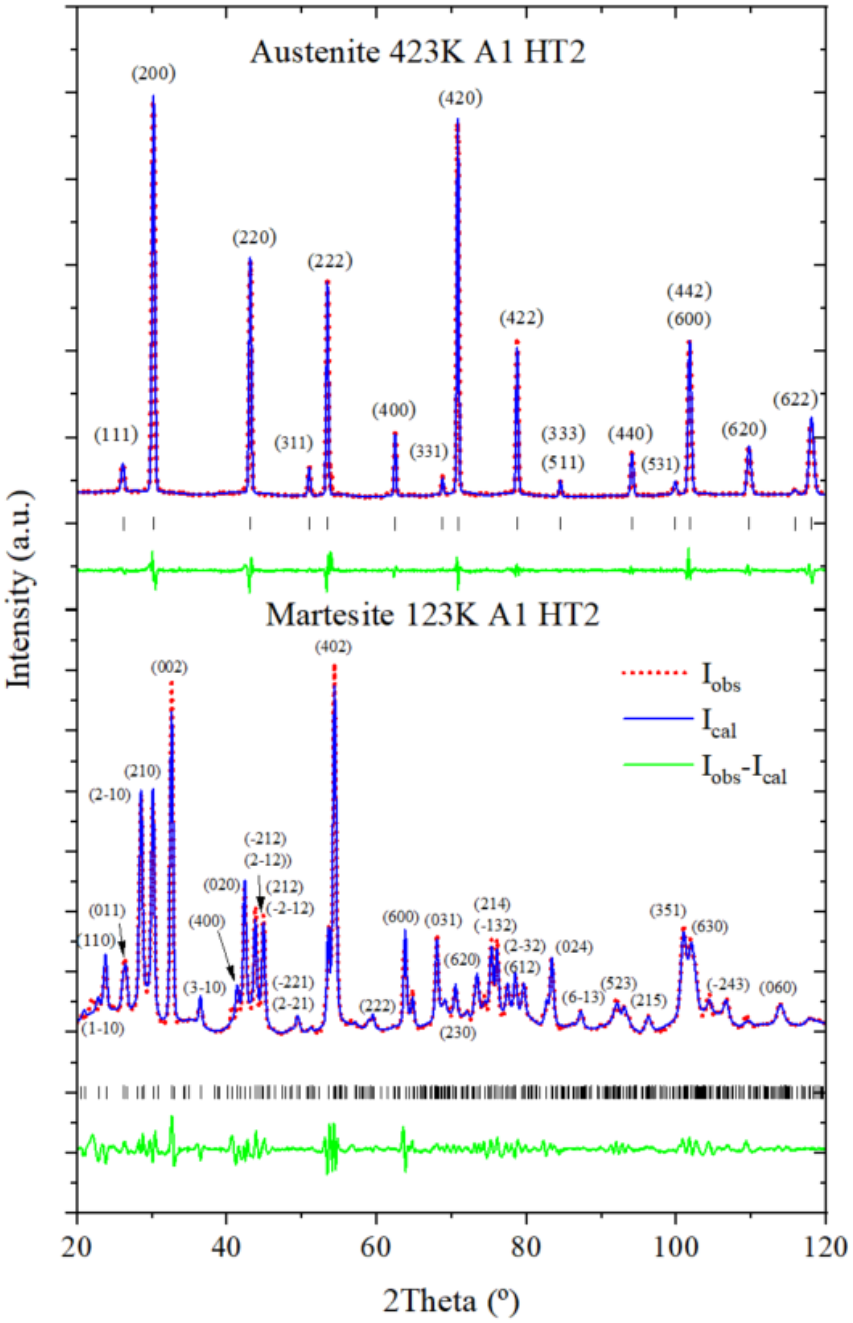

Figure A.1.3. *Neutron diffraction patterns and LeBail refinements at 423 and 123 K of the A1 HT2 alloy. Red dots represent experimental points; blue lines are the LeBail fittings; and green lines correspond to the difference between the measurements and the fittings. The Miller indices corresponding to each reflection are indicated with a black line and shown above each main peak.*

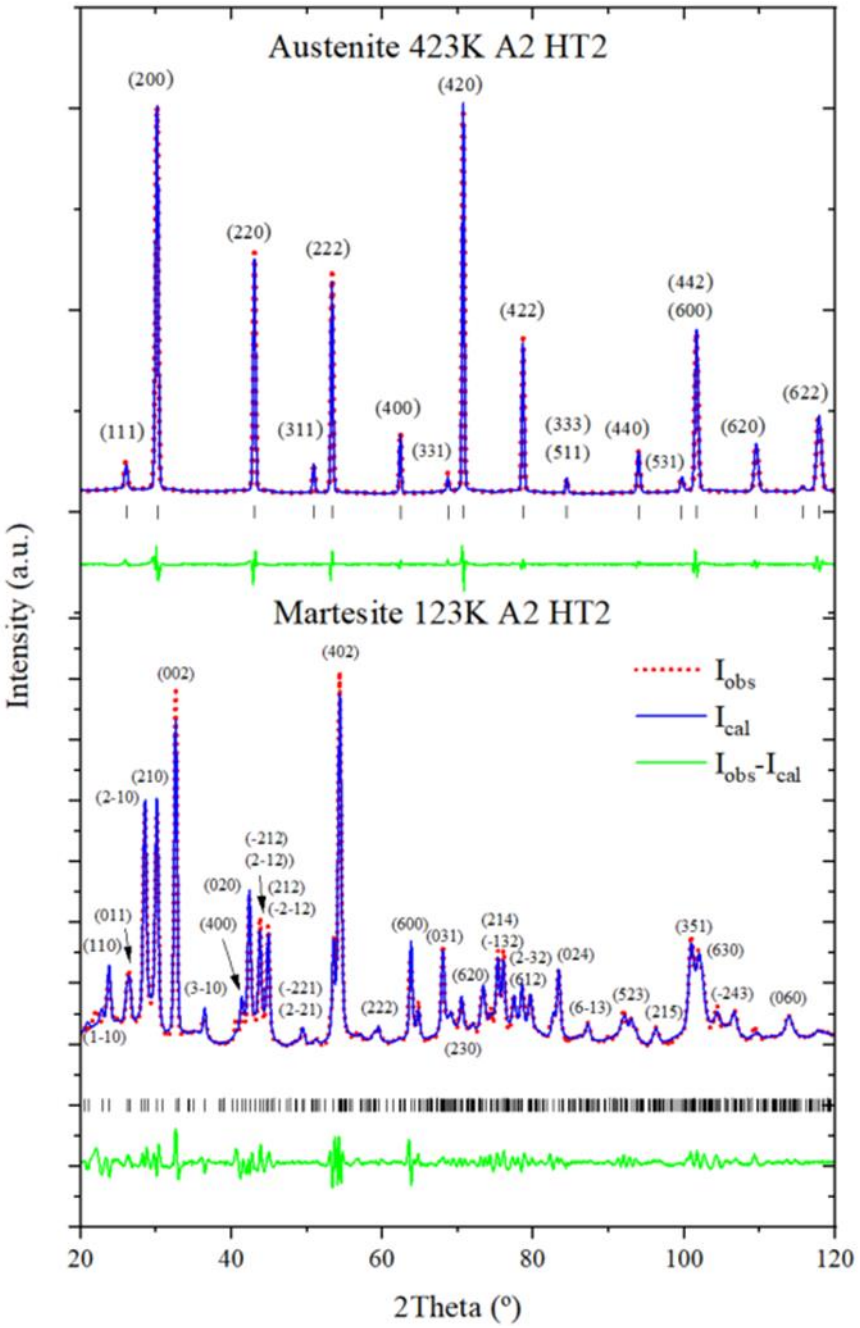

Figure A.1.4. *Neutron diffraction patterns and LeBail refinements at 423 and 123 K of the A2 HT2 alloy. Red dots represent experimental points; blue lines are the LeBail fittings; and green lines correspond to the difference between the measurements and the fittings. The Miller indices corresponding to each reflection are indicated with a black line and shown above each main peak.*

A.2. CHAPTER 5 SUPPORTING IMAGES

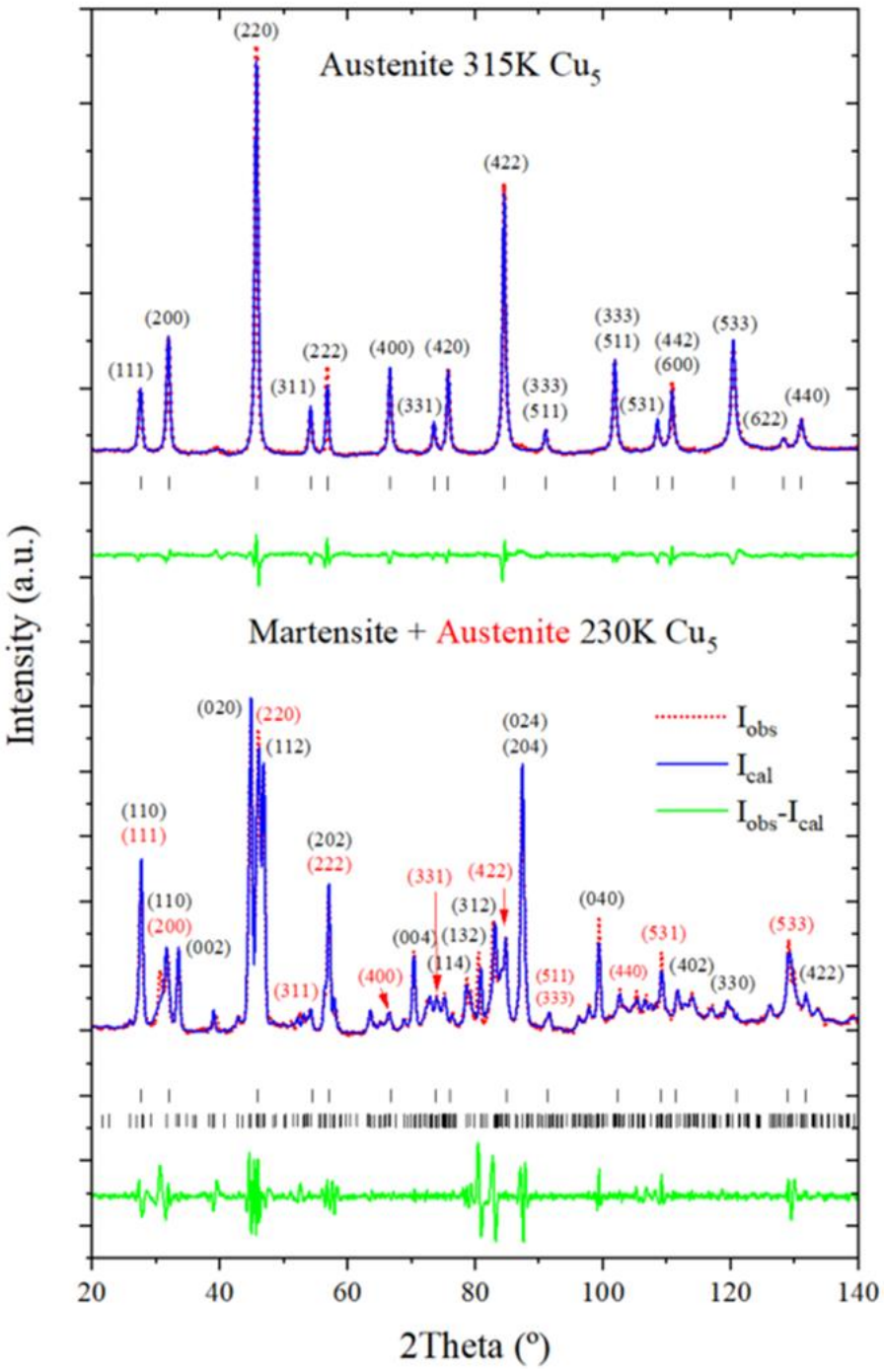

Figure A.3.1. *Neutron diffraction patterns and LeBail refinements at 315 and 230 K of the Cu_5 alloy. Red dots represent experimental points; blue lines are the LeBail fittings; and green lines correspond to the difference between the measurements and the fittings. The Miller indices corresponding to each reflection are indicated with a black line and shown above each main peak, with its colour indicating its correspondence to the austenite or martensite phases.*

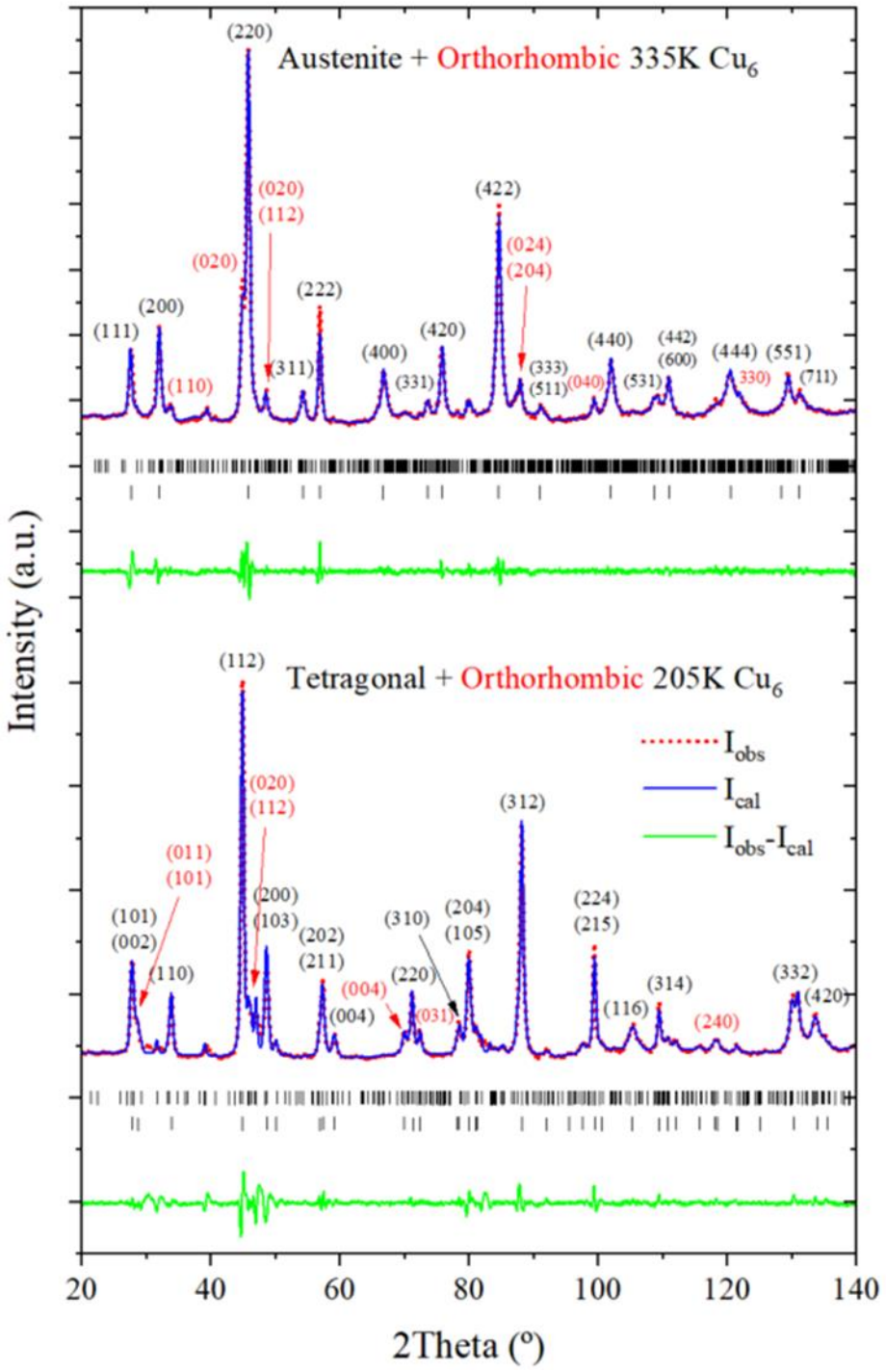

Figure A.3.1. *Neutron diffraction patterns and LeBail refinements at 335 and 205 K of the Cu6 alloy. Red dots represent experimental points; blue lines are the LeBail fittings; and green lines correspond to the difference between the measurements and the fittings. The Miller indices corresponding to each reflection are indicated with a black line and shown above each main peak, with its colour indicating its correspondence to the austenite or martensite phases.*

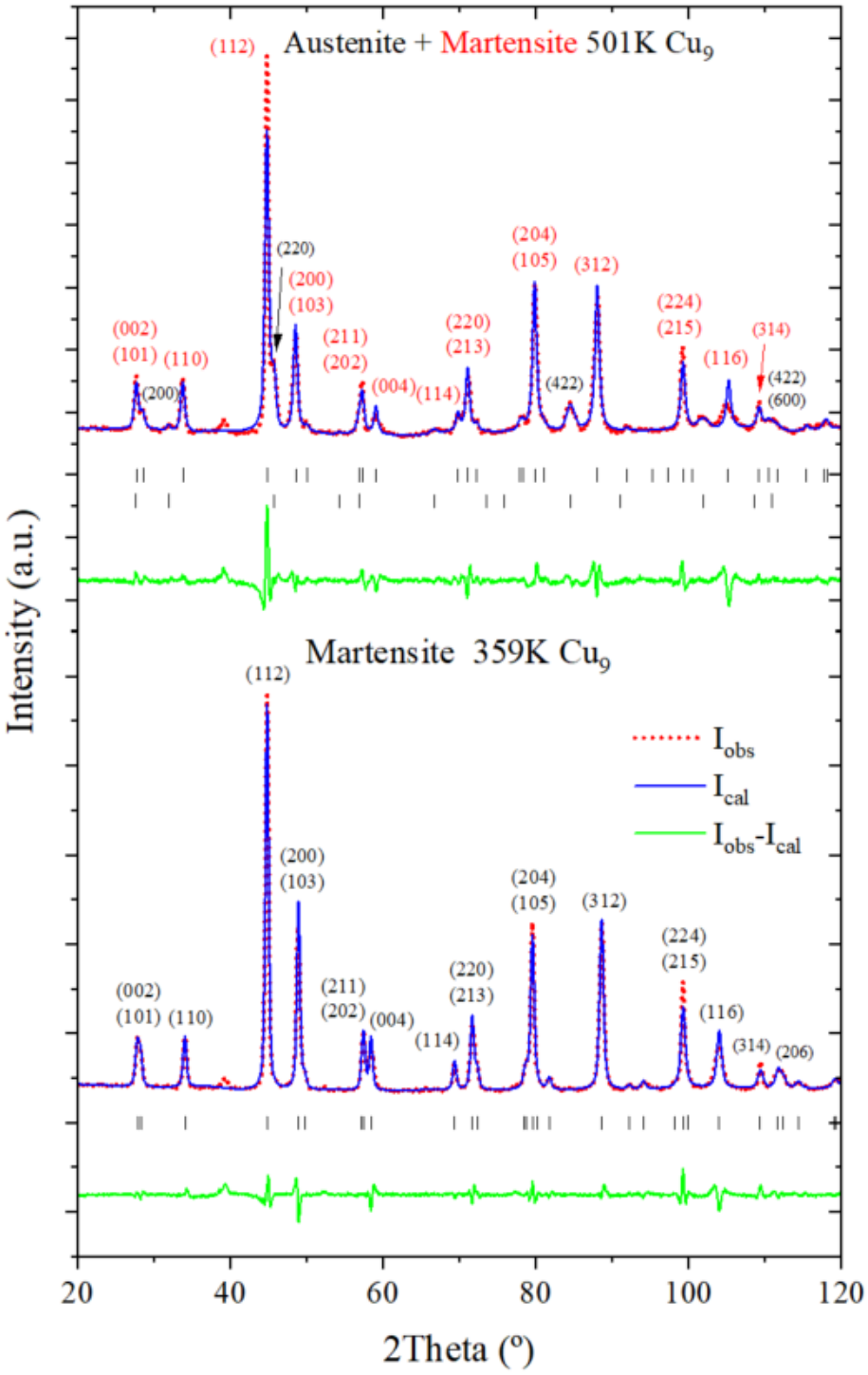

Figure A.3.1. *Neutron diffraction patterns and LeBail refinements at 501 and 359 K of the Cu_9 alloy. Red dots represent experimental points; blue lines are the LeBail fittings; and green lines correspond to the difference between the measurements and the fittings. The Miller indices corresponding to each reflection are indicated with a black line and shown above each main peak, with its colour indicating its correspondence to the austenite or martensite phases.*

A.3. CHAPTER 6 SUPPORTING IMAGES

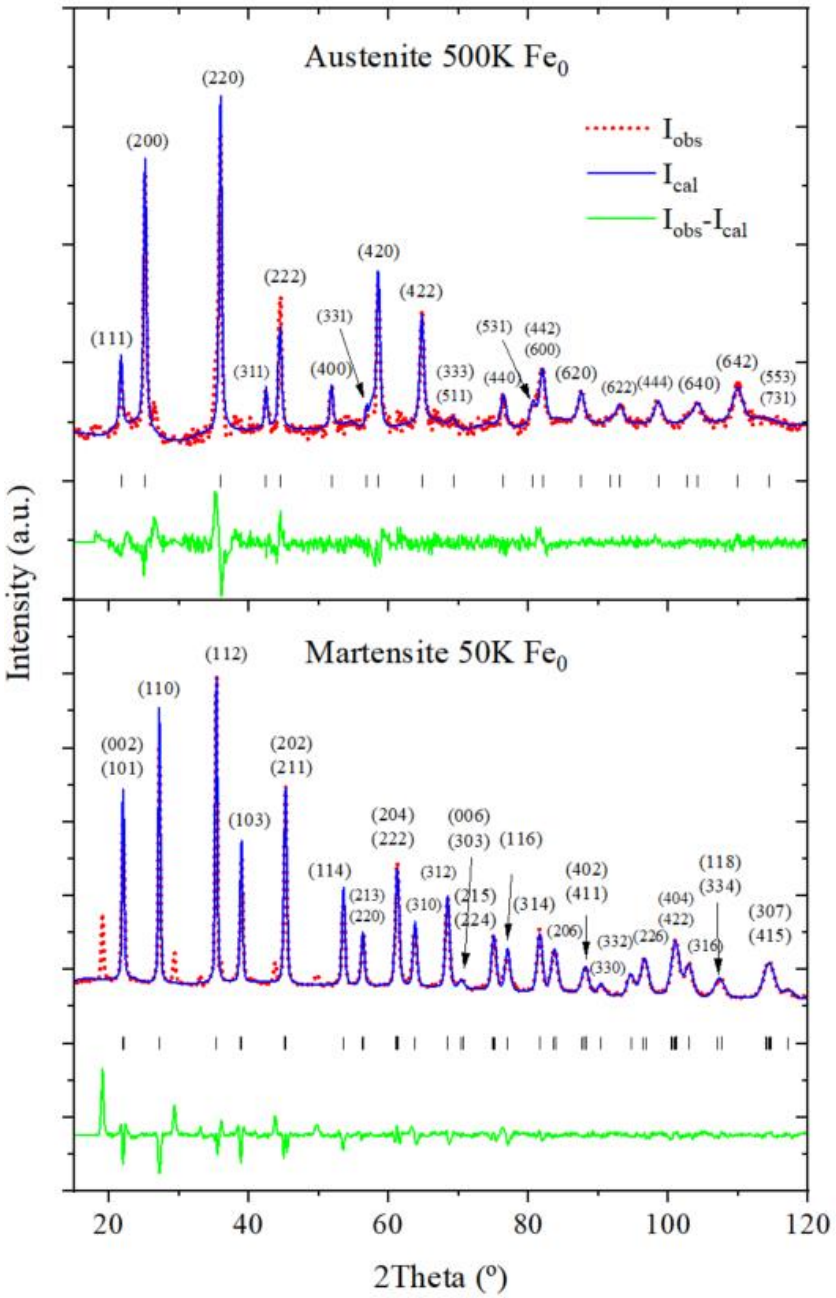

Figure A.3.1. *Neutron diffraction patterns and LeBail refinements at 500 and 50 K of the Fe_0 alloy. Red dots represent experimental points; blue lines are the LeBail fittings; and green lines correspond to the difference between the measurements and the fittings. The Miller indices corresponding to each reflection are indicated with a black line and shown above each main peak.*

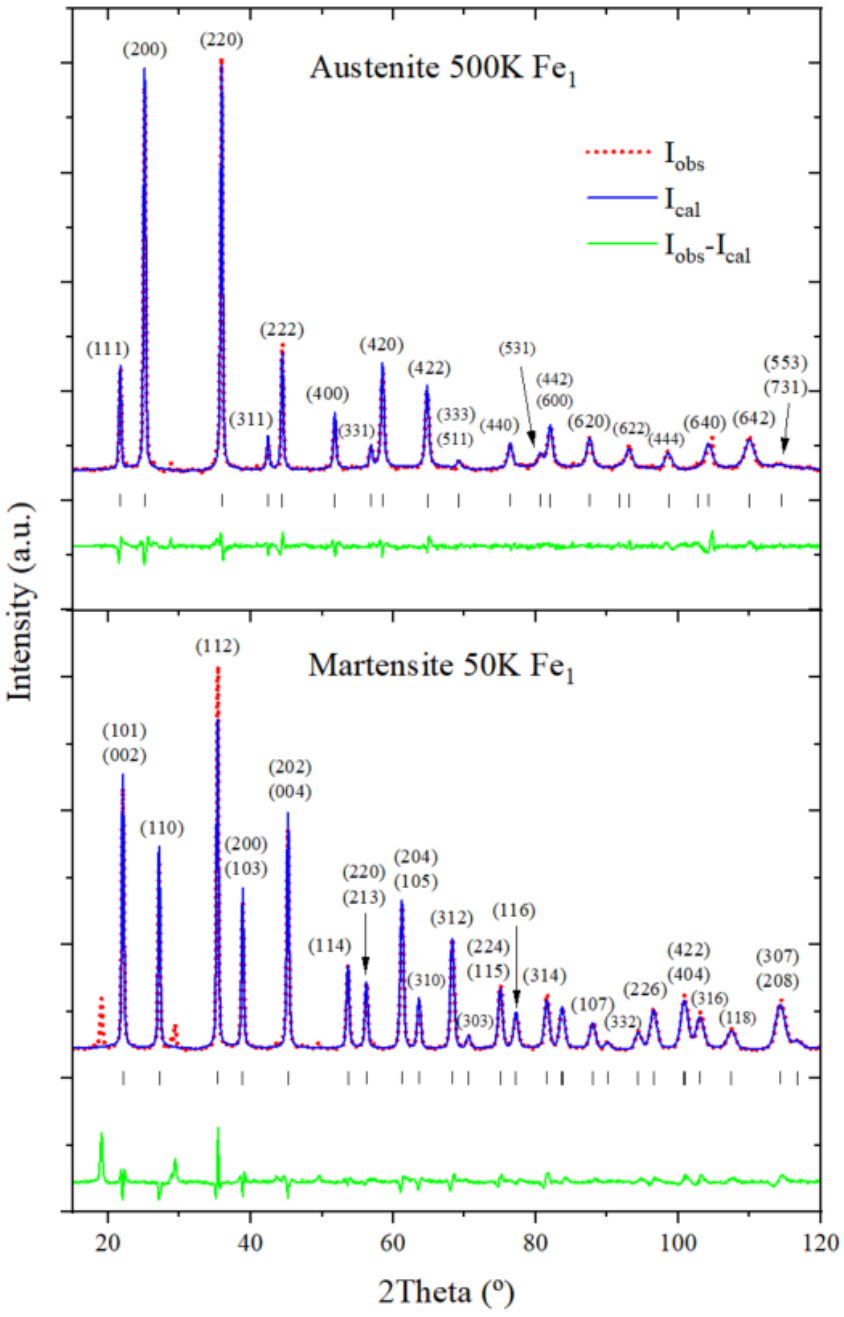

Figure A.3.2. *Neutron diffraction patterns and LeBail refinements at 500 and 50 K of the Fe_1 alloy. Red dots represent experimental points; blue lines are the LeBail fittings; and green lines correspond to the difference between the measurements and the fittings. The Miller indices corresponding to each reflection are indicated with a black line and shown above each main peak*

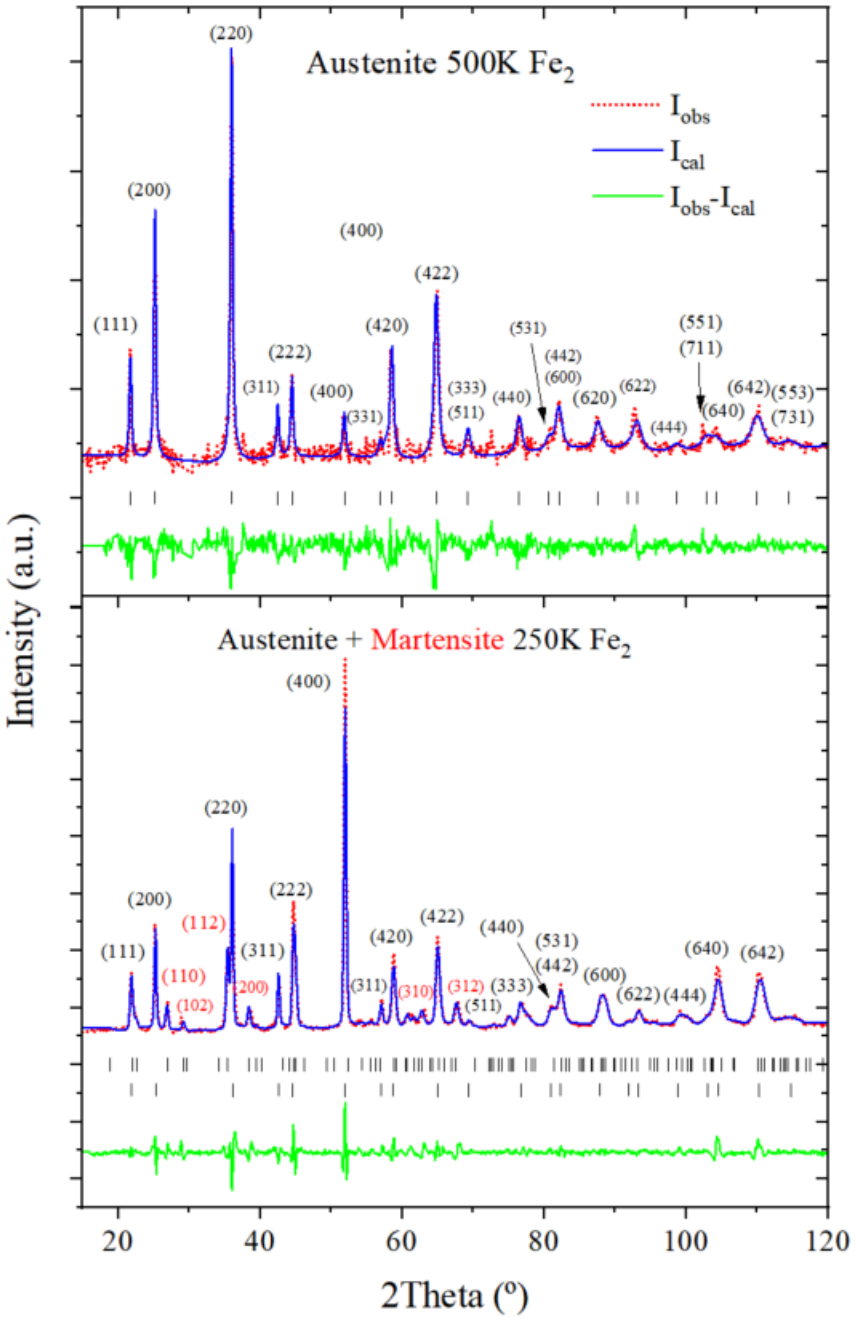

Figure A.3.3. *Neutron diffraction patterns and LeBail refinements at 500 and 250 K of the Fe_{1} alloy. Red dots represent experimental points; blue lines are the LeBail fittings; and green lines correspond to the difference between the measurements and the fittings. The Miller indices corresponding to each reflection are indicated with a black line and shown above each main peak., with the colour indicating the phase they correspond to.*

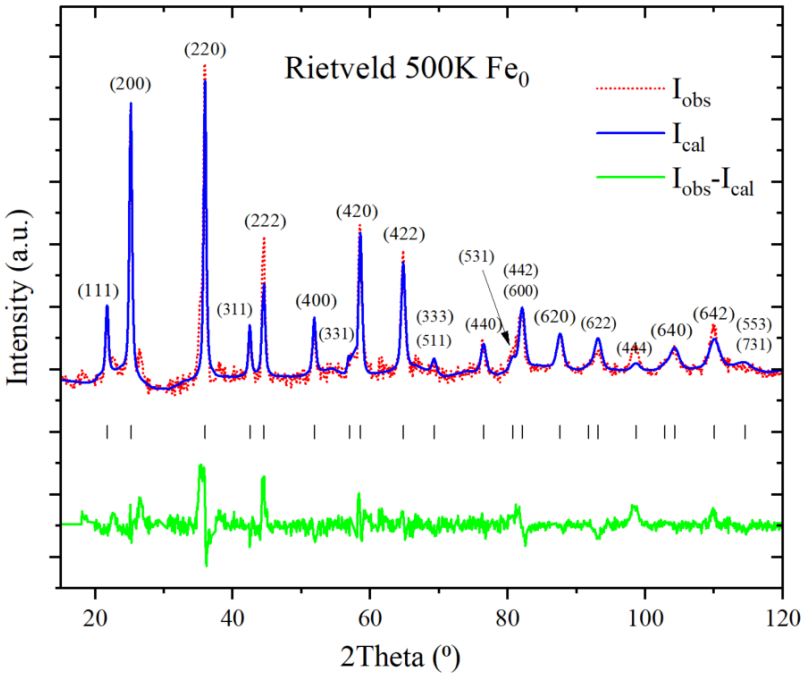

Figure A.3.4. *Neutron diffraction patterns and Rietveld refinements at 500 K of the Fe_0 alloy. Red dots represent experimental points; blue lines are the LeBail fittings; and green lines correspond to the difference between the measurements and the fittings. The Miller indices corresponding to each reflection are indicated with a black line and shown above each main peak., with the colour indicating the phase they correspond to.*

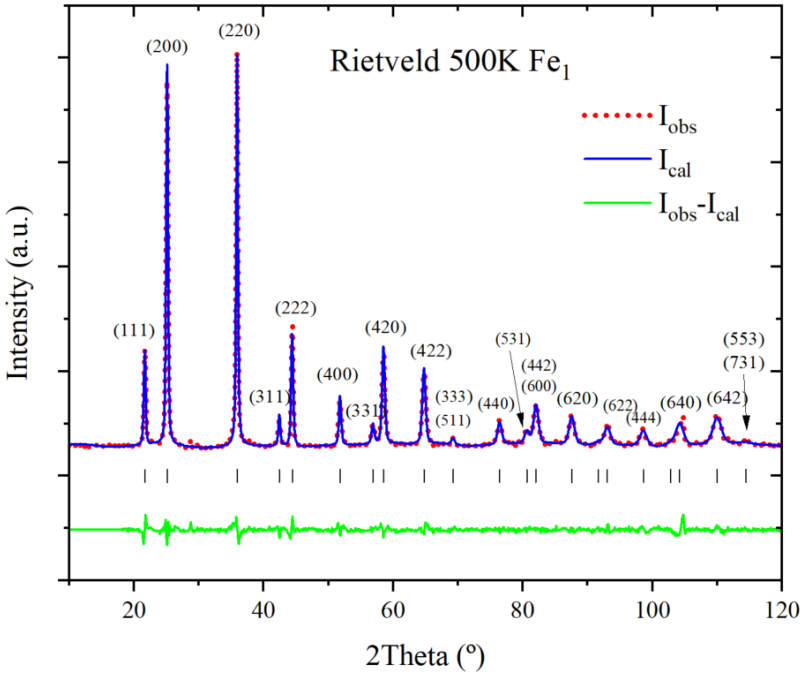

Figure A.3.5. *Neutron diffraction patterns and Rietveld refinements at 500 K of the Fe_1 alloy. Red dots represent experimental points; blue lines are the LeBail fittings; and green lines correspond to the difference between the measurements and the fittings. The Miller indices corresponding to each reflection are indicated with a black line and shown above each main peak., with the colour indicating the phase they correspond to.*

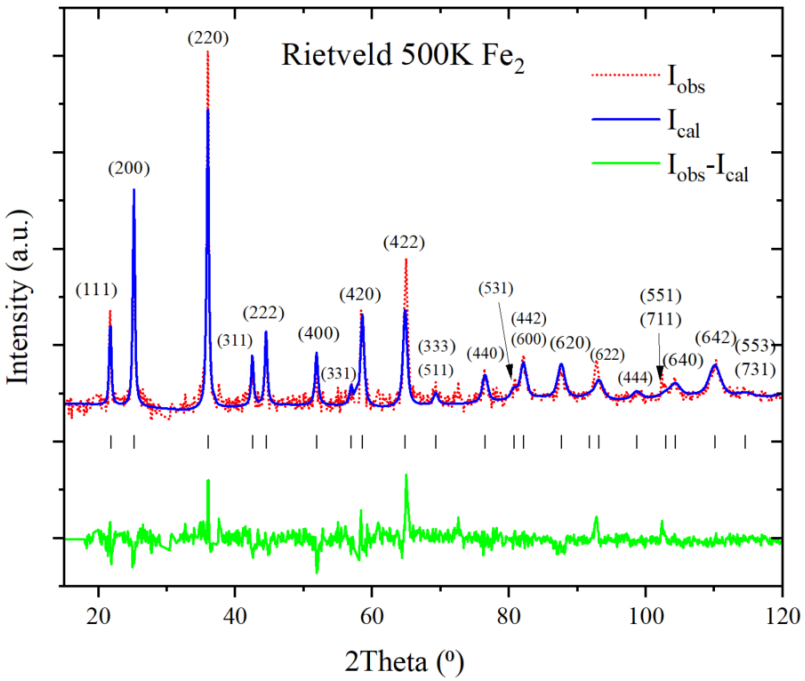

Figure A.3.6. *Neutron diffraction patterns and Rietveld refinements at 500 K of the Fe_2 alloy. Red dots represent experimental points; blue lines are the LeBail fittings; and green lines correspond to the difference between the measurements and the fittings. The Miller indices corresponding to each reflection are indicated with a black line and shown above each main peak., with the colour indicating the phase they correspond to.*

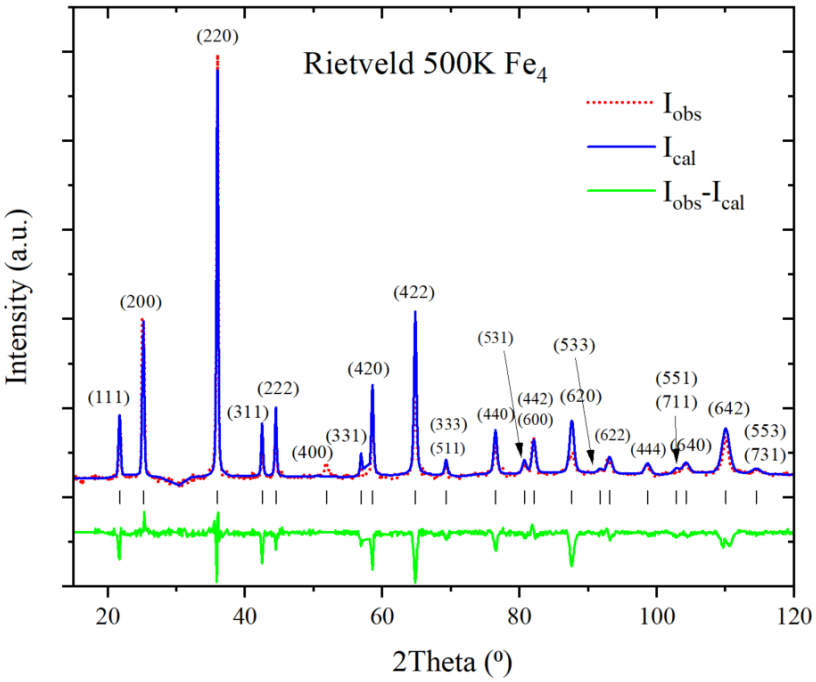

Figure A.3.7. *Neutron diffraction patterns and Rietveld refinements at 500 K of the Fe_4 alloy. Red dots represent experimental points; blue lines are the LeBail fittings; and green lines correspond to the difference between the measurements and the fittings. The Miller indices corresponding to each reflection are indicated with a black line and shown above each main peak., with the colour indicating the phase they correspond to.*

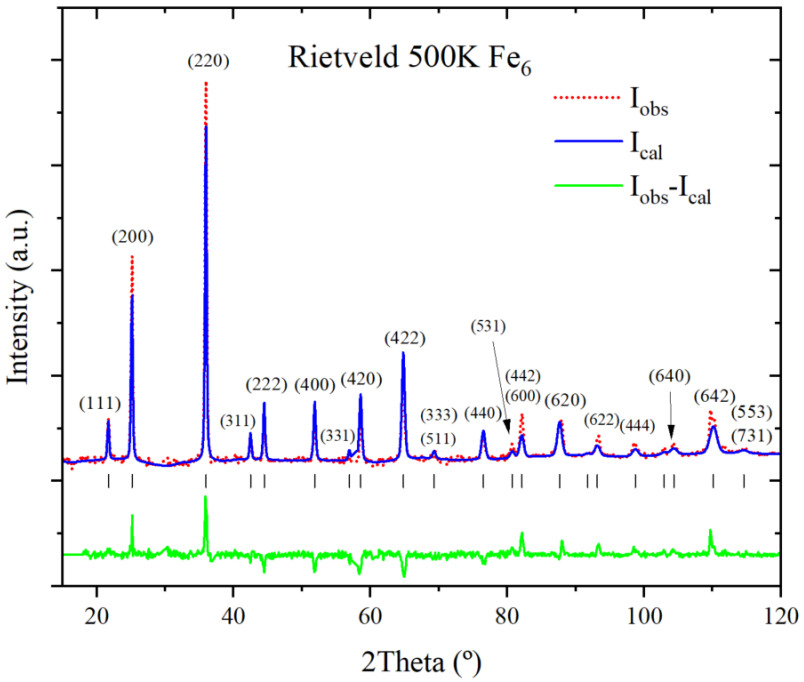

Figure A.3.8. *Neutron diffraction patterns and Rietveld refinements at 500 K of the Fe_6 alloy. Red dots represent experimental points; blue lines are the LeBail fittings; and green lines correspond to the difference between the measurements and the fittings. The Miller indices corresponding to each reflection are indicated with a black line and shown above each main peak., with the colour indicating the phase they correspond to.*

A.4. CHAPTER 7 SUPPORTING IMAGES

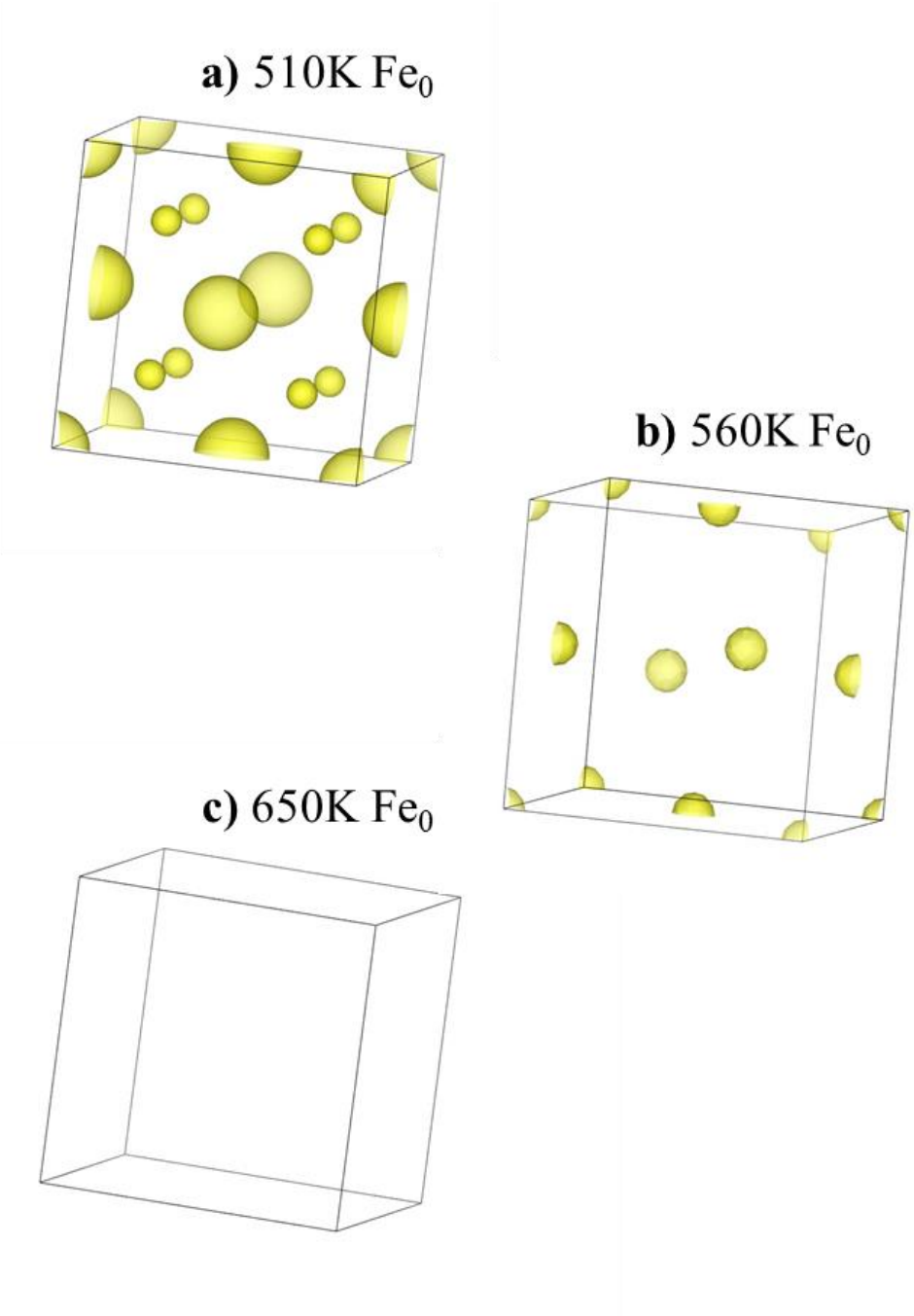

Figure A.4.1. *Graphical representation of the magnetic moment distribution in each site of the Fe_0 single crystal unit cell, based on the data acquired at a)510K, b) 560K and c) 650K.*

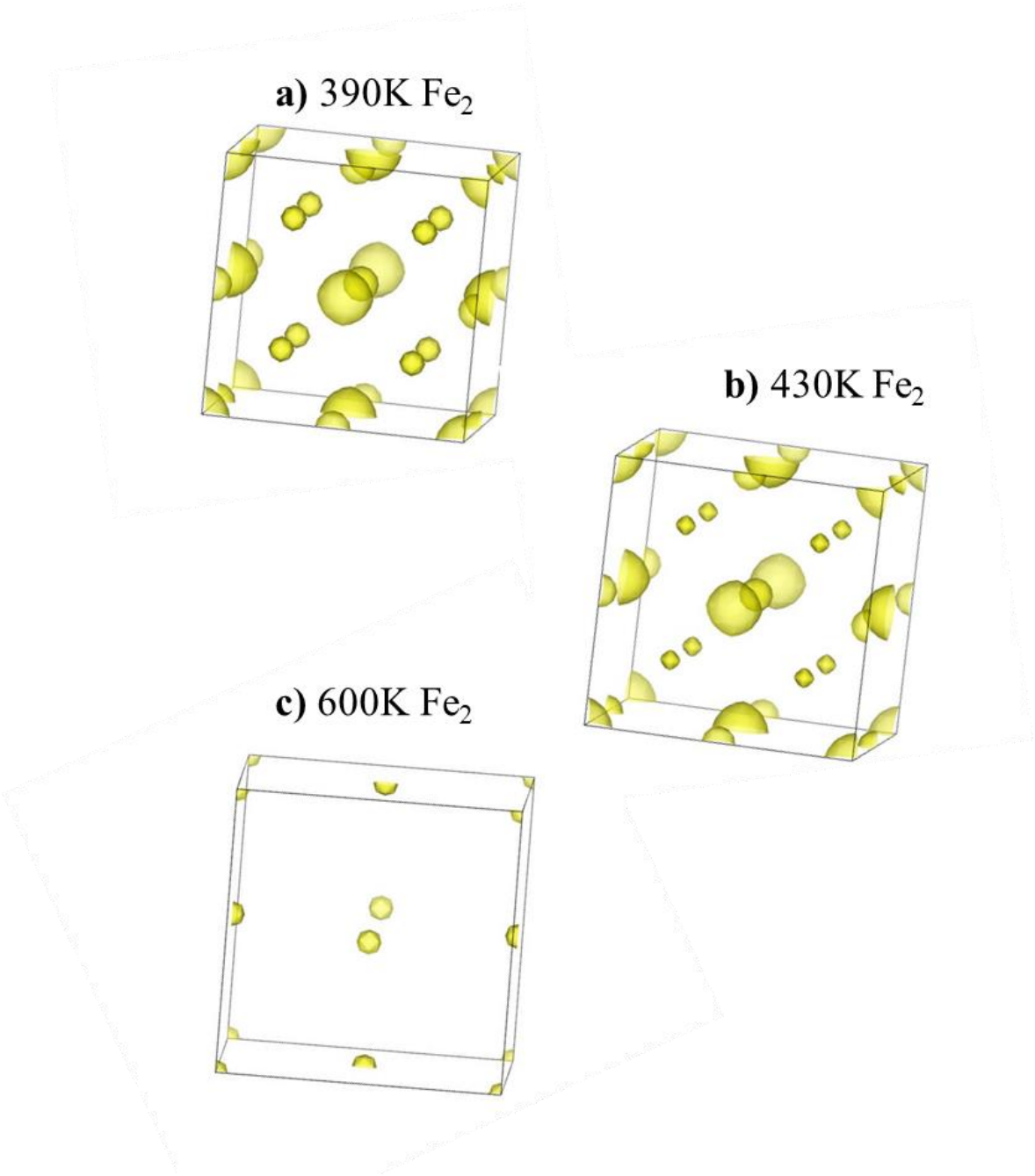

Figure A.4.2. *Graphical representation of the magnetic moment distribution in each site of the Fe_2 single crystal unit cell, based on the data acquired at a)390K, b) 430K and c) 600K.*

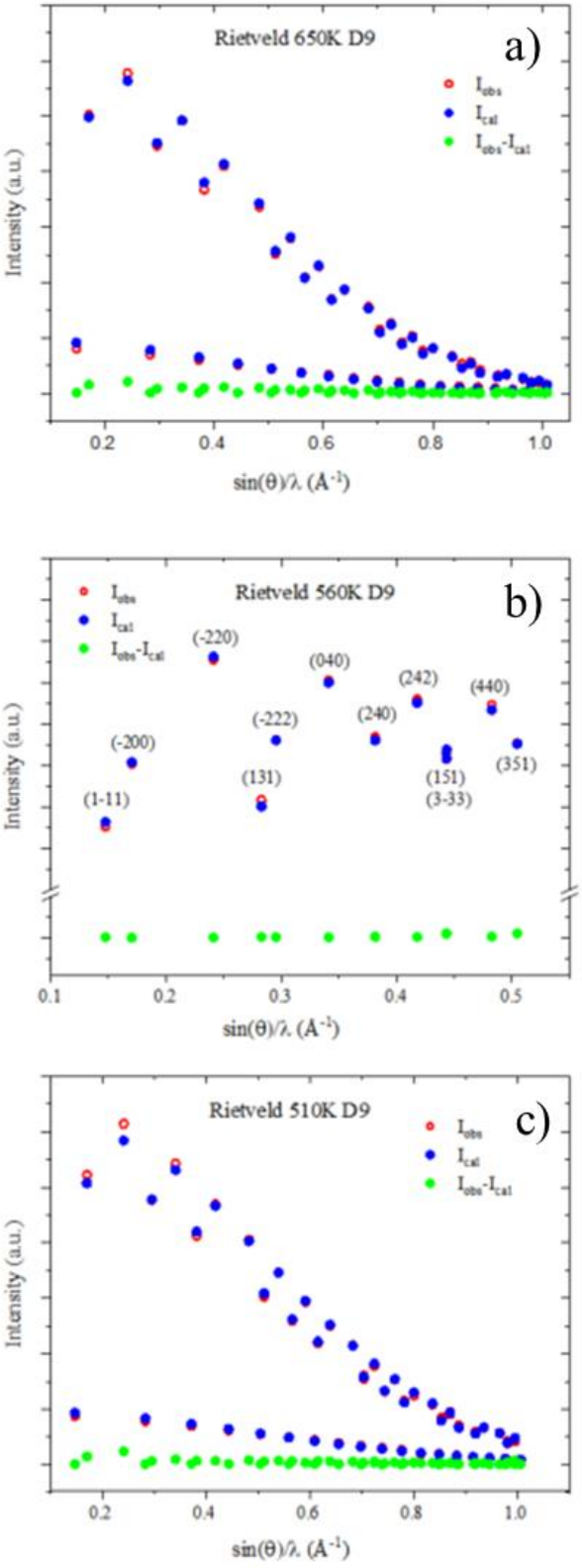

Figure A.4.3 *Neutron diffraction reflections measured at a) 510K, b) 560K and c) 650K, with its corresponding Rietveld refinement for the $\underline{Fe_0\ alloy}$. Red dots represent experimental reflections; blue bots are the Rietveld fittings; and green ones correspond to the difference between the measurements and the fittings. The Miller indices corresponding to each reflection are indexed above each reflection.*

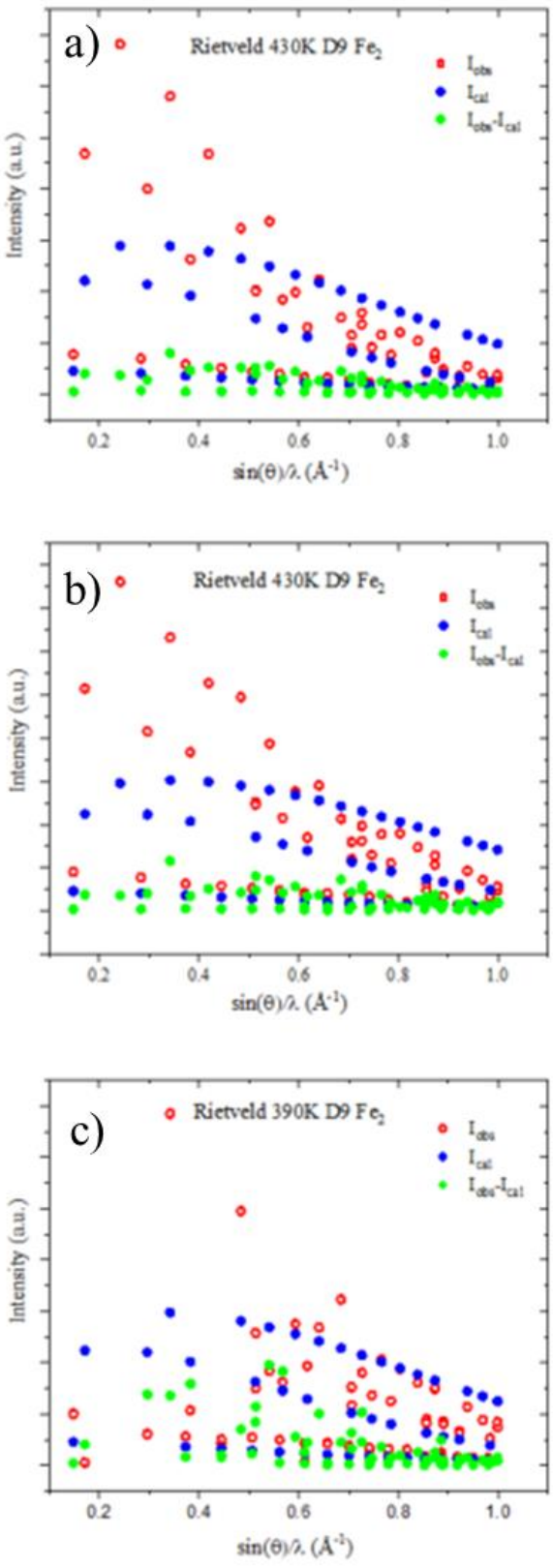

Figure A.4.4. *Neutron diffraction reflections measured at a) 390K, b) 460K and c) 600K, with its corresponding Rietveld refinement for the Fe_2 alloy. Red dots represent experimental reflections; blue bots are the Rietveld fittings; and green ones correspond to the difference between the measurements and the fittings. The Miller indices corresponding to each reflection are indexed above each reflection*

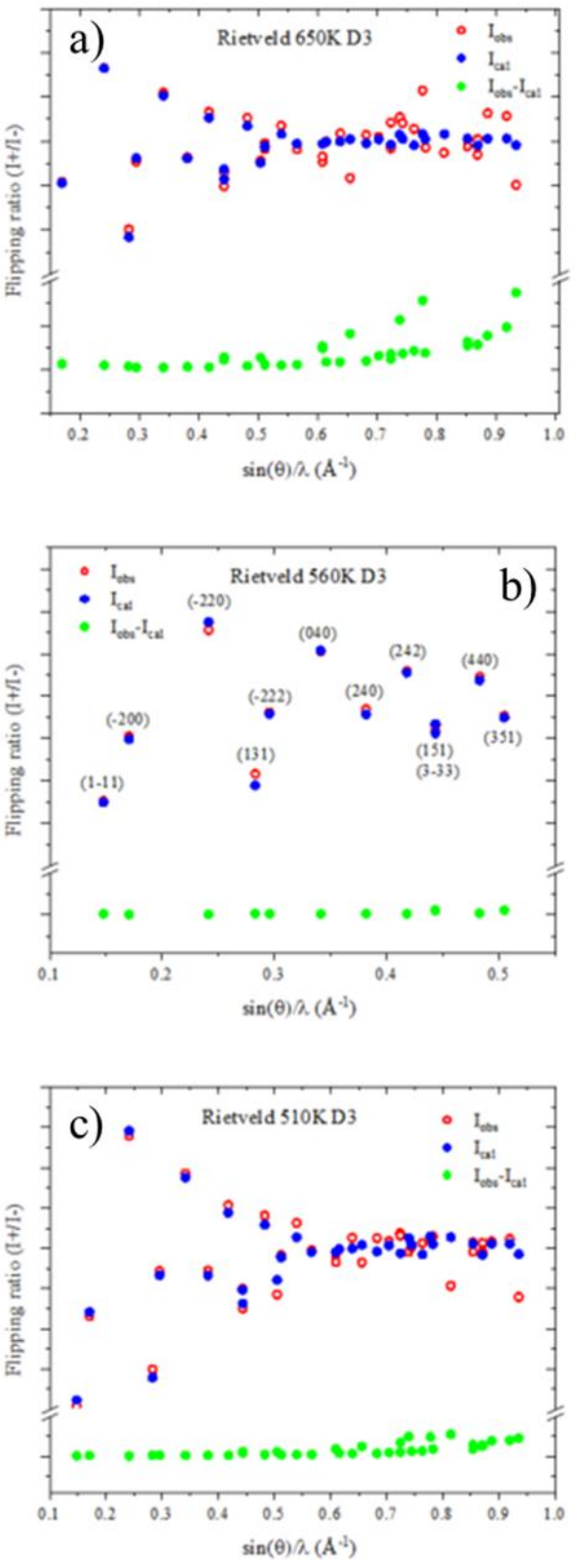

Figure A.4.5. *Flipping ratios measured at a) 510K, b) 560K and c) 650K, with its corresponding Rietveld refinement for the* $\underline{Fe_0\ alloy}$*. Red dots represent experimental reflections; blue bots are the Rietveld fittings; and green ones correspond to the difference between the measurements and the fittings. The Miller indices corresponding to each reflection are indexed above each reflection.*

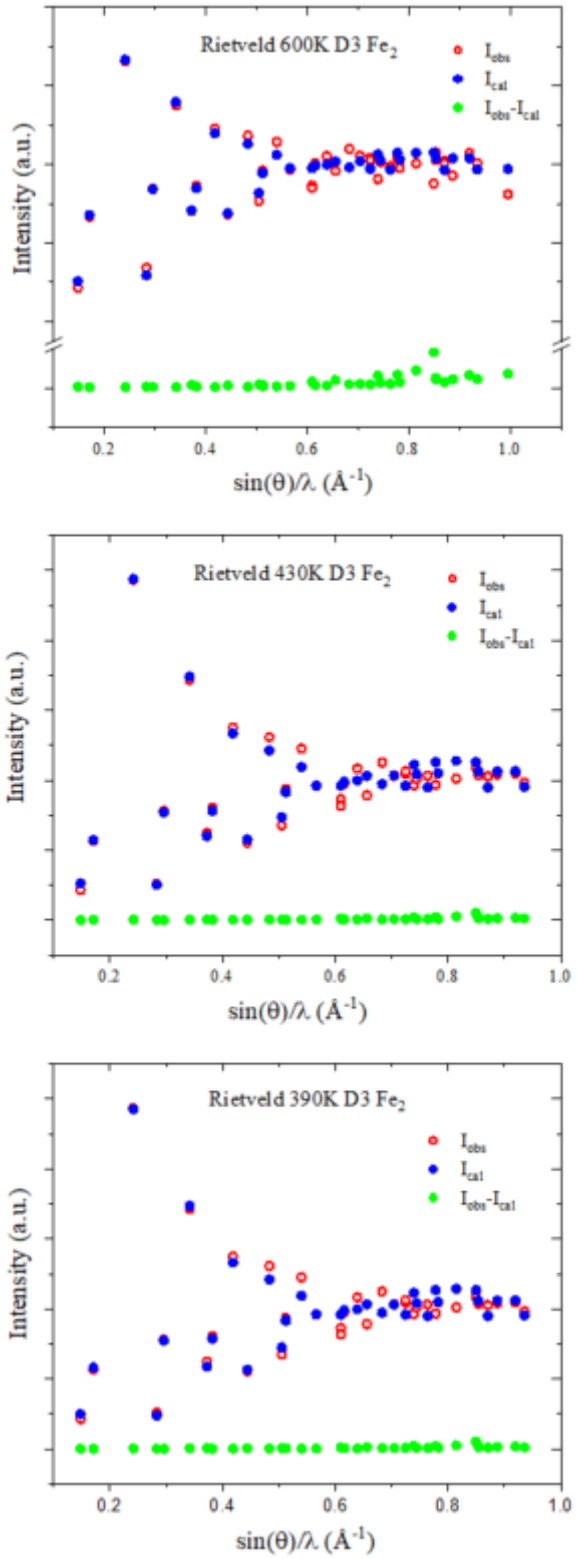

Figure A.4.6. *Flipping ratios measured at a) 390K, b) 460K and c) 600K, with its corresponding Rietveld refinement for the Fe_2 alloy. Red dots represent experimental reflections; blue bots are the Rietveld fittings; and green ones correspond to the difference between the measurements and the fittings. The Miller indices corresponding to each reflection are indexed above each reflection*

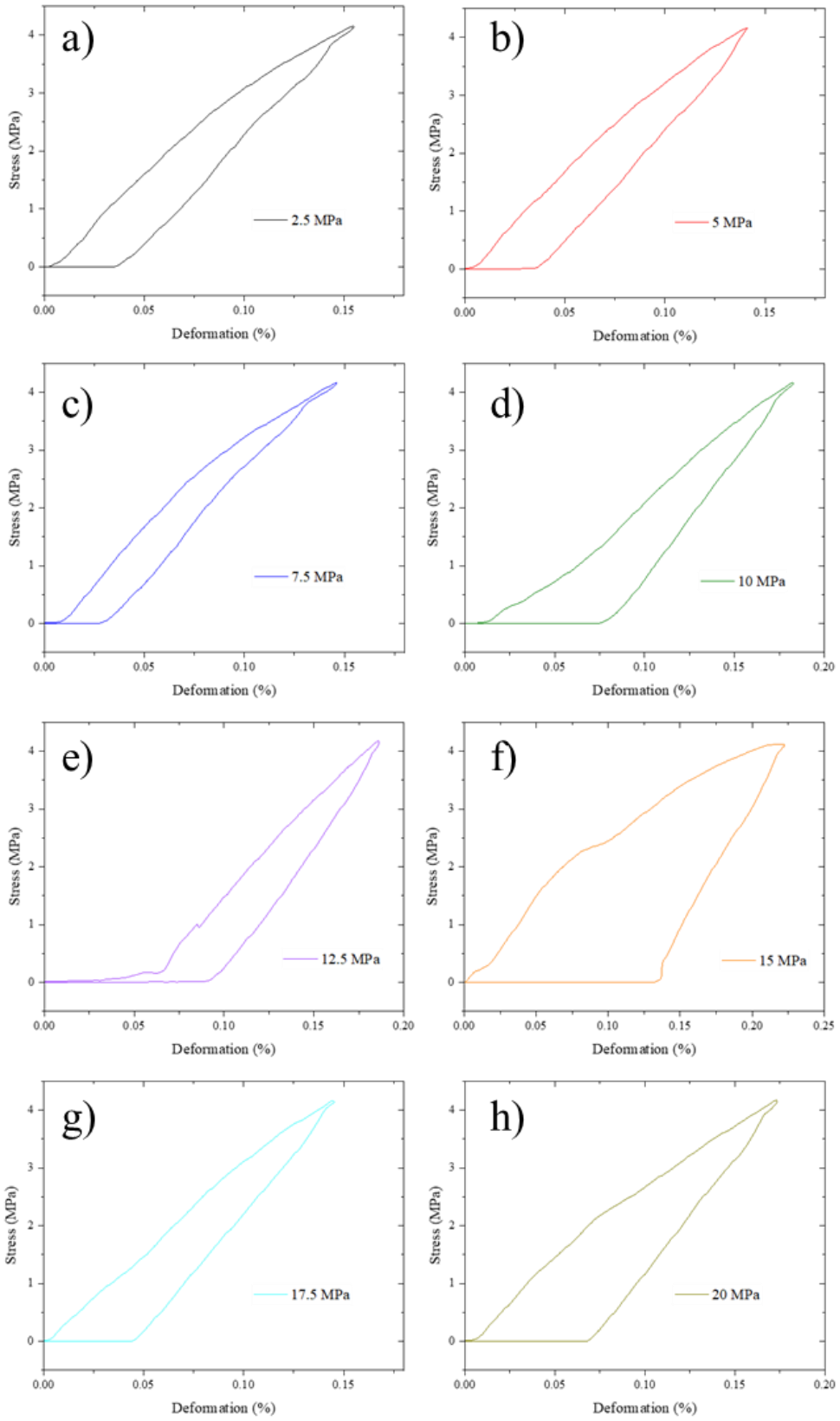

Figure A.4.7. *Stress-strain curves obtained via micromechanical testing at room temperature after training the Fe_0 crystal under a) 2.5 Mpa, B) 5 MPa, c) 7.5 MPa, d) 10 MPa, e) 12.5 MPa, f) 15 MPA, g) 17.5 MPa and h) 20 MPa stresses*